

**Scanning Probe Microscopy  
from the  
Perspective of the Sensor**

Julian Stirling

Thesis submitted to the University of Nottingham for the  
degree of Doctor of Philosophy

March 2014

# Abstract

The class of instruments considered in this thesis, scanning probe microscopes (SPM), raster scan a sensory probe over a surface to form both high resolution images and quantitative interaction measurements. Understanding and extracting information from SPM data has been considered extensively in the three decades since the first SPM. Major developments tend to be greeted with their own theory and data analysis techniques. The more gradual evolution of equipment has not, however, attracted the same level of theoretical consideration.

In this thesis we consider the SPM from an instrumentation perspective, concentrating on two specific types of microscope: the scanning tunnelling microscope (STM) and the atomic force microscope (AFM). Both of these microscopes rely on a sensory probe or sensor to induce and measure the desired interaction. We have carefully considered a range of experiments from a ‘sensor-eye-view’, both theoretically and experimentally.

We first consider the effect of the geometry of AFM sensors on quantitative force measurements, identifying that the length of tips that the length of tips can induce an unwanted coupling of lateral and normal forces. We go further by developing methods to experimentally correct these force measurements along with designing a sensor which exploits symmetry to separate lateral and normal forces.

We also consider the ways to automatically optimise the apex of the sensory probe of an STM to give the desired imaging resolution using a combination of prescribed routines and genetic algorithms. Image analysis techniques developed for this work have been developed into an open-source toolbox to automatically process and analyse SPM images.

Finally, we use control theory to analyse the feedback controlling the SPM probe. We find that the methods used in the literature do not fully consider the method with which the control loop is implemented in SPM. We employ a modified approach which results in more realistic simulated SPM operation.

## List of Publications

R. A. J. Woolley, J. Stirling, A. Radocea, N. Krasnogor, and P. Moriarty, “*Automated probe microscopy via evolutionary optimization at the atomic scale*”, Appl. Phys. Lett., **98** (25), 253104 (2011)

J. Stirling and G. A. Shaw, “*Calculation of the effect of tip geometry on noncontact atomic force microscopy using a qPlus sensor*”, Beilstein J. Nanotechnol., **4**, 10, (2013)

J. Stirling, “*Optimal geometry for a quartz multipurpose SPM sensor*”, Beilstein J. Nanotechnol., **4**, 370, (2013)

J. Stirling, R. A. J. Woolley, and P. Moriarty, “*Scanning probe image wizard: A toolbox for automated scanning probe microscopy data analysis*”, Rev. Sci. Instrum., **84** (11), 113701 (2013)

J. Stirling, “*Control theory for scanning probe microscopy revisited*”, **Submitted**, (2013)

J. Stirling, I. Lekkas, A. Sweetman, P. Djuranovic, D. G. Fernig, Q. Guo, J. Granwehr, R. Lèvy, and P. Moriarty, “*Critical assessment of the evidence for striped nanoparticles*”, **In preparation**, (2013).

## Acknowledgements

At the end of my PhD, looking back I am overwhelmed by the number of people who I need to thank for help and support.

First and foremost I want to thank my supervisor, Phil. One could not hope for a supervisor who is more generous with time spent to answer any question, nor one with a more encyclopedic knowledge of the literature. Most of all I would like to thank Phil for supporting my research even as it diverged from his research interests, for selflessly refusing to be an author when he felt that he had not had enough input on a publication, and for still investing the time to carefully proofread this work anyway.

Secondly, I want to thank Gordie for the interest he showed in my verbose early work on AFM calibration, and for inviting me to collaborate with him at NIST. The results we achieved in just one month would not have been possible without the time he invested in both preparation and experimentation.

Next, I have to mention the contribution Rich made to getting me adjusted to PhD life and motivating me to do my best. We have had many disagreements down the line about almost everything, but still my PhD would be very different without the help and guidance he has given me.

On to more general thanks. Much of this work would not have been possible without the discussions with Pete and Sam. Other experimental endeavours would have not been possible without the support of the Nottingham technical staff, particularly from Paul Munday, George White, Ian Taylor, Steve Booth, and Dave Laird.

On a more personal note I want to thank Sanda, Alex, Lozz, and my family for their emotional support. Also Simon, Lozz, Caroline, Dave, and Rob for helping with all of the little details which arose from me writing my thesis in another country. I am in debt to Angelo Moriondo and Milanese Luigi Bezzera for inventing the espresso, the most tasty and efficient way to ingest my favourite xanthine alkaloid. And to the staff of Flowers Tea House in Cluj for providing me with excellent *espressi* and friendly service during my write up.

*“To those who do not know mathematics it is difficult to get across a real feeling as to the beauty, the deepest beauty, of nature. . . If you want to learn about nature, to appreciate nature, it is necessary to understand the language that she speaks in.”*

Richard Feynman

# Contents

<b>Abstract</b>	<b>i</b>
<b>List of Publications</b>	<b>ii</b>
<b>Acknowledgements</b>	<b>iii</b>
<b>Contents</b>	<b>v</b>
<b>1 Introduction</b>	<b>1</b>
<b>2 Instrumental Techniques</b>	<b>4</b>
2.1 STM Theory . . . . .	4
2.2 AFM Theory . . . . .	14
2.2.1 Amplitude-Modulated AFM . . . . .	15
2.2.2 Frequency-Modulated AFM . . . . .	16
2.2.3 Force spectroscopy . . . . .	17
2.3 SPM Instrumentation . . . . .	24
2.3.1 Vibration Isolation . . . . .	24
2.3.2 Scanning Unit . . . . .	26
2.3.3 Coarse Positioning Motors . . . . .	28
2.3.4 Feedback Controllers . . . . .	29
2.3.5 STM Electronics . . . . .	31
2.3.6 AM-AFM Electronics . . . . .	33
2.3.7 FM-AFM Electronics . . . . .	34
<b>3 Literature Review</b>	<b>40</b>
3.1 Materials . . . . .	41

## Contents

3.1.1	Highly Oriented Pyrolytic Graphite (HOPG) . . . . .	41
3.1.2	Silicon(111) . . . . .	42
3.1.3	C <sub>60</sub> . . . . .	45
3.2	The Evolution of AFM Sensors . . . . .	49
3.3	AFM Sensor Calibration . . . . .	53
3.3.1	Cleveland Method . . . . .	55
3.3.2	Thermal Tuning . . . . .	56
3.3.3	Sader Method . . . . .	57
3.3.4	Other Methods of Calibration . . . . .	57
3.3.5	Comparisons . . . . .	59
<b>4</b>	<b>Calculation of the Effect of Tip Geometry on ncAFM Measure-</b>	
	<b>ments with a qPlus Sensor</b> . . . . .	<b>60</b>
4.1	Introduction . . . . .	61
4.2	Effects on dynamic properties . . . . .	63
4.3	Resulting lateral motion . . . . .	67
4.3.1	Experimental validation . . . . .	69
4.3.2	Effect on frequency shift . . . . .	70
4.3.3	Effect on calibration . . . . .	72
4.3.4	Effect on imaging and spectroscopy . . . . .	72
4.4	Conclusion . . . . .	75
<b>5</b>	<b>3D force mapping of C<sub>60</sub>–C<sub>60</sub> interactions</b> . . . . .	<b>76</b>
5.1	Introduction . . . . .	76
5.2	Calculation of sensor properties . . . . .	78
5.2.1	Measuring tip geometry from optical images . . . . .	78
5.2.2	Calculating angle of apex motion from tip geometry . . . . .	80
5.2.3	Other experimental considerations: spring constant and sensitivity . . . . .	81
5.3	Measuring 3D potentials . . . . .	83
5.3.1	Processing grid spectroscopy measurements . . . . .	84
5.3.2	Simulating grid spectroscopy measurements . . . . .	85
5.3.3	Correcting grid spectroscopy measurements . . . . .	86

## Contents

5.4	Results and Discussion . . . . .	87
5.5	Conclusion . . . . .	95
<b>6</b>	<b>Optimal geometry for a quartz multi-purpose SPM sensor</b>	<b>96</b>
6.1	Introduction . . . . .	96
6.1.1	Combining NC-AFM and DLFM . . . . .	97
6.2	Non-cantilever geometries . . . . .	100
6.2.1	Dynamic properties of symmetrical sensors . . . . .	101
6.2.2	Optimal geometry for a symmetrical sensor . . . . .	104
6.2.3	Experimental viability . . . . .	106
6.3	Conclusion . . . . .	107
<b>7</b>	<b>Automated Tip Conditioning</b>	<b>108</b>
7.1	Introduction . . . . .	108
7.2	Image Analysis for HOPG images . . . . .	111
7.2.1	Large Size Image Analysis . . . . .	111
7.2.2	Target-Driven Image Analysis . . . . .	112
7.3	Image Analysis for Silicon . . . . .	113
7.3.1	Analysing large scale images . . . . .	115
7.3.2	Target-Free Small Image Analysis . . . . .	115
7.4	Optimisation protocols . . . . .	117
7.4.1	Deterministic Coarse Conditioning . . . . .	118
7.4.2	Evolutionary Fine Tuning . . . . .	121
<b>8</b>	<b>SPIW: A toolbox for automated scanning probe microscopy data analysis</b>	<b>124</b>
8.1	Introduction . . . . .	125
8.2	Overview of capabilities . . . . .	126
8.2.1	Adaptive masking and flattening . . . . .	127
8.2.2	Step edge finding . . . . .	128
8.2.3	Atom/molecule recognition . . . . .	130
8.2.4	Generating image statistics . . . . .	133
8.2.5	Computer vision outputs . . . . .	134
8.3	Performance under different conditions . . . . .	134

## Contents

8.3.1	Step edges with atomic resolution . . . . .	134
8.3.2	Feature locating for molecular networks . . . . .	134
8.3.3	Known issues . . . . .	135
8.4	Conclusion . . . . .	136
<b>9</b>	<b>Control theory for scanning probe microscopy revisited</b>	<b>138</b>
9.1	Introduction . . . . .	138
9.2	Analytical Models for SPM Feedback . . . . .	139
9.2.1	Complete model of SPM feedback . . . . .	142
9.2.2	Feedback performance - without mechanical modelling . .	145
9.2.3	Feedback performance - with mechanical and electrical mod- elling . . . . .	147
9.3	Numerical implementation of feedback simulations . . . . .	150
9.4	Conclusion . . . . .	153
<b>10</b>	<b>Conclusion</b>	<b>155</b>
10.1	Future work . . . . .	156
10.1.1	Accuracy of force extraction . . . . .	156
10.1.2	Automated SPM image acquisition and analysis . . . . .	157
10.1.3	Feedback loop modelling . . . . .	158
	<b>Bibliography</b>	<b>159</b>
<b>A</b>	<b>Derivations of key equations in AFM</b>	<b>172</b>
A.1	Free simple harmonic oscillator . . . . .	172
A.2	Quality Factor . . . . .	173
A.3	Driving Amplitude . . . . .	175
A.4	The Cantilever . . . . .	175
A.4.1	Equation of Motion of a Cantilever . . . . .	175
A.4.2	Second moment of area . . . . .	177
A.4.3	Spring Constant . . . . .	177
A.4.4	Natural Frequencies . . . . .	179
A.4.5	Effective Mass of Cantilever . . . . .	182
A.5	Driven Cantilever . . . . .	183

## Contents

A.6	Full equations of motion for the cantilever. . . . .	186
A.7	Frequency shift in AFM . . . . .	187
A.7.1	First order frequency shift (Low amplitude) . . . . .	188
A.7.2	Frequency shift for arbitrary amplitudes . . . . .	189
<b>B</b>	<b>Derivations from Calculation of Effects of Tip Geometry</b>	<b>192</b>
B.1	Boundary Conditions of a Loaded Cantilever . . . . .	192
B.2	Elastic Potential Energy of a Loaded Cantilever . . . . .	193
B.3	Analytical Solution for $\Lambda_i$ . . . . .	194
<b>C</b>	<b>Full derivations of dynamic properties for a symmetrical sensor</b>	<b>201</b>
C.1	Harmonics of the symmetrical sensor . . . . .	201
C.1.1	Odd modes . . . . .	202
C.1.2	Even modes . . . . .	203
C.1.3	Odd modes - including tip . . . . .	203
C.1.4	Even modes - including tip . . . . .	204
C.2	Static Spring Constants . . . . .	205
C.2.1	Calculating $k_{\text{norm}}$ . . . . .	206
C.2.2	Calculating $k_{\text{lat}}$ . . . . .	207
<b>D</b>	<b>Computer Science Techniques</b>	<b>209</b>
D.1	Robust Mutual Information (RMI) . . . . .	209
D.1.1	Mutual Information (MI) . . . . .	209
D.1.2	Calculating RMI from MI . . . . .	210
D.2	Cellular Genetic Algorithms . . . . .	210
	<b>List of Figures</b>	<b>213</b>

# Chapter 1

## Introduction

*“In the beginning there was nothing, which exploded.”*

Terry Pratchett

Scanning probe microscopy (SPM) is arguably the most powerful and diverse tool in a nanoscientist’s toolbox. Depending on the type of SPM and the mode of operation a great range of surface data can be acquired. Usually this is in the form of topographical data, mapping out contours of a surface to keep a feedback parameter constant. This can be used as a first approximation of the true surface topography as is common for larger scale studies, with scans of microns in width. However, at the more fundamental atomic or molecular level the data can tell us much more. For scanning tunnelling microscopy (STM) [1] the feedback parameter is the tunnelling current. This is related not only to the tip-sample distance, but also the local density of states. For non-contact atomic force microscopy (AFM) the gradient of the tip-sample force [2], which modifies the eigenfrequency of the sensor, is tracked (directly or indirectly) during feedback. This force gradient depends on both the tip-sample distance and the chemical nature of surface under study. Other important SPM techniques include lateral force microscopy (LFM) [3], magnetic force microscopy [4], scanning near-field optical microscopy [5], and scanning capacitance microscopy [6].

SPM data has been key to a number of important scientific studies, across a range of fields. From the structure of the Si(111)  $7 \times 7$  reconstruction, finally solved using a diffraction techniques combined with STM data [7], to the first

## Introduction

true atomic resolution images of friction, produced with dynamic LFM [8] continuing the pioneering advances in nanotribology which LFM has provided [9]. In addition to its use in fundamental nanoscience, SPM has become a standard tool for surface characterisation of materials ranging from metal organic frameworks to cell components.

We can divide the SPM into three core components: the sample under study, the sensor detecting physical interactions, and the actuators with their associated electronics. SPM studies normally take a sample-centred approach to experiment design and analysis, often assuming the sensor and electronics perform perfectly within the confines of idealised models which describe how they react to the tip-sample interaction. Some exceptions to this generalisation exist: studies regularly consider the broadening of surface features, due to image showing a convolution of tip and surface structure [10–13]. Similarly, many papers note the effect of feedback loop artefacts on SPM experiments [14, 15]. This thesis, however, finds much of the theoretical modelling of these loops to be in need of adjustment (see Chapter 9).

In this thesis, AFM and STM experiments are studied with the behaviour of the instrumentation being the primary concern. From this it is possible to identify possible inaccuracies in SPM experiments and analysis. We go further to suggest methods to correct for or avoid such issues, including proposing a new design for a combined AFM/LFM/STM sensor. The questions of repeatability of SPM measurements and of wasted SPM researcher time are also considered. From this we have developed new methods to automatically coerce the tip-apex of SPM sensors into the desired state.

Chapter 4 discusses how the geometry of the tip of the qPlus sensor can result in lateral motion of the tip apex. This causes forces to be probed in a direction which is not normal to the surface, and how this affects force spectroscopy measurements. Chapter 5 details preliminary experimental work which aims to directly measure the effect of this lateral motion in 3D for the interaction between two  $C_{60}$  molecules, and discusses methods to correct for such motion. From this work Chapter 6 introduces a proposed sensor design which exploits symmetry to ensure a direction of oscillation which is purely normal to the sample surface. By exciting other eigenmodes of the sensor purely lateral motions

## Introduction

can also be generated allowing LFM operation. For the experiments described in Chapter 5 it was essential to engineer the tip apex into a specific condition. To address the time consumed by this activity in Chapter 7 we explore methods to automate tip conditioning. This conditioning is performed in STM due to its relative simplicity compared to AFM. The final aim, however, is to apply such methods to AFM. In Chapter 8 we discuss an open-source SPM image analysis toolbox which was created from the algorithms developed for the automated tip conditioning software to assess SPM images. We discuss the performance of this toolbox for automated SPM data processing. Finally, Chapter 9 derives improvements to the methods currently used in the literature to model SPM feedback loops. These models can be applied to understand both instrumental performance and SPM imaging artefacts.

# Chapter 2

## Instrumental Techniques

*“And you know why four plus minus one  
Plus ten is fourteen minus one?  
'Cause addition is commutative, right.  
And so you have thirteen tens,  
And you take away seven,  
And that leaves five...  
Well, six actually.  
But the idea is the important thing.”*

Tom Lehrer

### Chapter Overview

As this thesis is centred on instrumental influences on SPM measurements, a detailed explanation of the instrumental techniques is given before the literature review. This section discusses both scanning tunnelling microscopy and atomic force microscopy specifically along with instrumental concepts common to most scanning probe microscopes.

### 2.1 STM Theory

The scanning tunnelling microscope utilises the phenomenon of quantum tunnelling to control the separation of a monatomic tip and a conducting surface.

## Instrumental Techniques

The tip is raster scanned across the sample using piezoelectric actuators. As the number of electrons tunnelling is dependent on tip-sample separation, another piezoelectric actuator is used to adjust the height of the tip to keep the tunnelling current constant, see Figure 2.1. Hence it is possible to construct a three dimensional image of the surface by recording the tip's height as it is scanned.

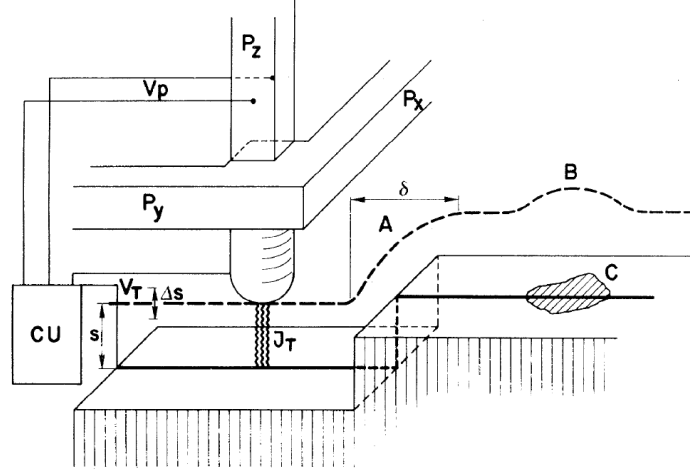


Figure 2.1: *Schematic diagram of an STM scan. The  $P_y$  and  $P_x$  actuators move the tip across the sample. The control unit (CU) adjusts the voltage  $V_P$  to the  $P_z$  actuator, to keep the tunnelling current  $J_T$  constant. The dashed line indicates path taken by the tip. Note the response to a step edge (A) is not directly proportional to the surface topography, and that the tip also responds (B) to changes in the work function of the surface (C). (Figure from reference [16].)*

Consider this tip-sample interaction in one dimension [17], see Figure 2.2(a), where the barrier of height  $E_{\text{vac}}$  arises from the vacuum<sup>1</sup> between the tip and the sample. We can calculate the dependence of the current on tip-sample separation by applying the Schrödinger equation, where  $E$  is the energy of the electron state:

$$\left( \frac{-\hbar^2}{2m} \frac{\partial^2}{\partial x^2} + E_{\text{vac}} \right) \psi = E\psi \quad (2.1)$$

$$\frac{\partial^2 \psi}{\partial x^2} = \frac{2m}{\hbar^2} (E_{\text{vac}} - E)\psi. \quad (2.2)$$

<sup>1</sup>While STM is not limited to vacuum, with many systems working in both ambient and liquid environments, this section will consider the system to be in vacuum for simplicity.

## Instrumental Techniques

The solution inside the barrier is

$$\psi = Be^{-\kappa x} + Ce^{\kappa x} \quad \text{where} \quad \kappa = \sqrt{\frac{2m}{\hbar^2}(E_{\text{vac}} - E)}. \quad (2.3)$$

As  $E_{\text{vac}} > E$ ,  $\kappa$  is real, and  $\psi$  is a combination of an exponentially increasing and an exponentially decreasing function. The second term is not physical for a tall and wide barrier, otherwise the electron would be more likely to be found on the far side of the barrier, which is clearly untrue.  $C$  must always be less than  $B$  for any size barrier for the probability to decrease across the barrier, as can clearly be seen by differentiating equation (2.3).

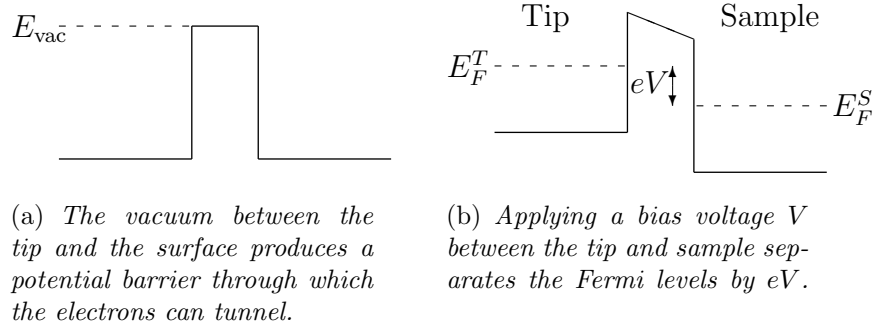


Figure 2.2: 1D representations of the tip-sample tunnel junction.

A good approximation for the tunnel current can be found by setting  $C = 0$ , justified by the barrier being tall and wide enough.  $\psi$  then becomes an exponentially decreasing function. Therefore the tunnelling current  $I_c$ , determined from the transmission probability, decays as a function of the separation  $d$ ,

$$I_c \propto e^{-2\kappa d}, \quad (2.4)$$

as previously mentioned.

For electrons at the Fermi level in the tip,  $E_{\text{vac}} - E$  is the work function of the tip material. Since most materials have a work function of 4–6 eV [18], we can calculate that  $2\kappa \sim 2 \text{ \AA}^{-1}$ . Hence, to reduce the tunnel current by an order of magnitude,  $d$  must increase by

$$\Delta d = \frac{-\ln(0.1)}{2\kappa} \sim 1 \text{ \AA}. \quad (2.5)$$

## Instrumental Techniques

A more thorough derivation of the tunnelling current can be done by matching the solutions both sides of the barrier with the solution inside the barrier [19]. Considering a barrier extending from  $x = 0$  to  $x = d$  we can say

$$\psi = \begin{cases} e^{ikx} + Ae^{-ikx} & x < 0 \\ Be^{-\kappa x} + Ce^{\kappa x} & 0 < x < d \\ De^{ikx} & d < x \end{cases} \quad (2.6)$$

where the wavefunction is normalised in terms of the incidence flux on the barrier. By matching the wave function and its derivative at the boundaries we get the following four simultaneous equations

$$B + C = 1 + A \quad (2.7)$$

$$Be^{-\kappa d} + Ce^{\kappa d} = De^{ikd} \quad (2.8)$$

$$-xBe^{-\kappa d} + xCe^{\kappa d} = ikDe^{iks} \quad (2.9)$$

$$-xB + xC = ik - Aik \quad (2.10)$$

By writing these as a matrix

$$\underline{\underline{M}} = \begin{pmatrix} -1 & 1 & 1 & 0 \\ 0 & e^{-\kappa d} & e^{\kappa d} & -e^{ikd} \\ 0 & -xe^{-\kappa d} & xe^{\kappa d} & -ike^{ikd} \\ 1 & \frac{-x}{ik} & \frac{x}{ik} & 0 \end{pmatrix} \begin{pmatrix} A \\ B \\ C \\ D \end{pmatrix} = \begin{pmatrix} 1 \\ 0 \\ 0 \\ 1 \end{pmatrix} \quad (2.11)$$

and using Gaussian elimination  $\underline{\underline{M}}$  can be reduced to

$$\begin{pmatrix} -1 & 1 & 1 & 0 \\ 0 & e^{-\kappa d} & e^{\kappa d} & -e^{ikd} \\ 0 & 0 & 2xe^{\kappa d} & -(ik + \kappa)e^{ikd} \\ 0 & 0 & 0 & -e^{ikd} \left( e^{\kappa d} \left( \frac{-\kappa}{ik} + 1 \right) \left( \frac{ik + \kappa}{2\kappa} - 1 \right) - e^{-\kappa d} \left( \frac{\kappa}{ik} + 1 \right) \left( \frac{ik + \kappa}{2\kappa} \right) \right) \end{pmatrix}. \quad (2.12)$$

## Instrumental Techniques

Hence, after some rearranging we can calculate  $D$  as

$$D = \frac{1}{e^{ikd} \left( \cosh(\kappa d) - \frac{i(k^2 - x^2)}{2kx} \sinh(\kappa d) \right)}. \quad (2.13)$$

From elementary quantum mechanics we can say the probability current density of the electrons incident on the barrier is

$$j_i = \frac{-i\hbar}{2m} \left( \psi_i^* \frac{d\psi_i}{dx} - \psi_i \frac{d\psi_i^*}{dx} \right) \quad \text{where } \psi_i = e^{ikx} \quad (2.14)$$

$$= \frac{\hbar k}{m} \quad (2.15)$$

and for the transmitted wave the probability current density is

$$j_t = \frac{-i\hbar}{2m} \left( \psi_t^* \frac{d\psi_t}{dx} - \psi_t \frac{d\psi_t^*}{dx} \right) \quad \text{where } \psi_t = D e^{ikx} \quad (2.16)$$

$$= \frac{\hbar k}{m} |D|^2 \quad (2.17)$$

hence the fraction of incident electrons transmitted,  $T$ , can be calculated as

$$T = \frac{j_i}{j_t} = \frac{1}{|D|^2} \quad (2.18)$$

$$= \frac{1}{1 + \frac{(k^2 + \kappa^2)^2}{4k^2\kappa^2} \sinh^2(\kappa d)} \quad (2.19)$$

For large  $\kappa d$ ,  $\sinh^2(\kappa d)$  tends to  $\frac{1}{4}e^{2\kappa d}$ , and this term will dominate the denominator. Thus, in this case

$$T \approx \frac{16k^2\kappa^2}{(k^2 + \kappa^2)^2} e^{-2\kappa d} \quad (2.20)$$

and as  $T \propto I_c$  this agrees with equation (2.4).

To justify this approximation it must be shown that  $\kappa d$  is large enough in STM. Evaluating  $\kappa$  from equation (2.3), gives

$$\kappa \approx 1.15 \text{ \AA}^{-1} \quad (2.21)$$

using a value of 5 eV for  $(E_{\text{vac}} - E)$ , since most materials have a work function of 4–6 eV [18]. A sensible value to use for  $k$  is  $k_F$ , the Fermi wave vector of the

## Instrumental Techniques

material, as most tunnelling happens near the Fermi level. As metals tend to have a Fermi wave vector of order  $0.5\text{--}2 \text{ \AA}^{-1}$  [18] a value of  $k = 1.25 \text{ \AA}^{-1}$  will be used.  $T$  has been plotted, using equations (2.19) and (2.20), for tip-sample separations of  $0\text{--}3 \text{ \AA}$  in Figure 2.3. The approximation gives good agreement for  $d > 1.5 \text{ \AA}$ , however, below  $0.6 \text{ \AA}$  the approximation is non-physical with  $T > 1$ , implying more electrons transmitted than incident on the barrier. For a typical tip-sample separation of  $5 \text{ \AA}$ , the approximation holds well.

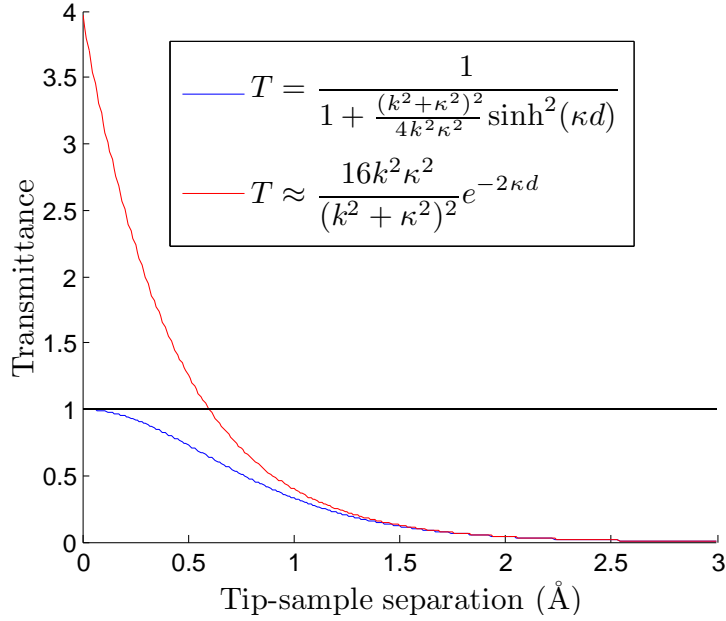


Figure 2.3: *Comparing calculated transmittance of a 1D potential barrier to exponentially decreasing approximation.*

The full transmittance equation, (2.19), is a time-independent solution for a single tunnelling electron. A many particle time-dependent approximation for tunnelling was calculated by Bardeen [20]. Here Fermi's golden rule is used to calculate the rate of transition from the incident state

$$T_{i \rightarrow t} = \frac{2\pi}{\hbar} |M_{it}|^2 \rho_f \quad (2.22)$$

where  $M_{it}$  is the matrix element of the electron transition from state  $i$  to state  $t$  and  $\rho_f$  is the density of final states. Instead of creating a simple approximate Hamiltonian with exact solutions, approximate solutions are found for the

## Instrumental Techniques

‘exact’ Hamiltonian. The wavefunction  $\psi_i$  is approximated as an oscillating solution on the left-hand-side of the barrier as before; inside the barrier and on the right-hand-side it is approximated as an exponentially decreasing solution. Similarly,  $\psi_f$  is an oscillating solution on the right-hand-side and an exponentially decreasing solution on both in and left of the barrier. So for a barrier of width  $d$ , we can say

$$\psi_i = \begin{cases} e^{ik_i x} + A_i e^{-ik_i x} & x < 0 \\ B_i e^{-\kappa x} & x > 0 \end{cases} \quad (2.23)$$

$$\psi_t = \begin{cases} A_t e^{ik_t x} & x > d \\ B_t e^{\kappa(x-d)} & x < d \end{cases} \quad (2.24)$$

Defining the left-hand-side of the barrier as region  $L$ , the right-hand-side as region  $R$ , and the barrier as region  $B$ , we can say  $\psi_i$  is a good solution in  $L$  and  $B$  with energy  $E_i$ , also  $\psi_t$  is a good solution in  $R$  and  $B$  with energy  $E_t$ . The matrix element can be written as

$$M_{it} = \langle \psi_t | \hat{\mathcal{H}}_T | \psi_i \rangle \quad (2.25)$$

where  $\hat{\mathcal{H}}_T = \hat{\mathcal{H}} - E_i$  is the Hamiltonian describing the tunnelling from state  $i$ . So

$$M_{it} = \langle \psi_t | \hat{\mathcal{H}} - E_i | \psi_i \rangle \quad (2.26)$$

writing separately in the regions  $L$ ,  $B$  and  $R$

$$= \int_L \psi_t^* (\hat{\mathcal{H}} - E_i) \psi_i dV + \int_B \psi_t^* (\hat{\mathcal{H}} - E_i) \psi_i dV + \int_R \psi_t^* (\hat{\mathcal{H}} - E_i) \psi_i dV \quad (2.27)$$

But in regions  $L$  and  $B$   $\hat{\mathcal{H}}\psi_i = E_i\psi_i$ , hence these integrals evaluate to zero

$$= \int_R \psi_t^* (\hat{\mathcal{H}} - E_i) \psi_i dV \quad (2.28)$$

## Instrumental Techniques

In regions  $R$ ,  $\psi_i \left( \hat{\mathcal{H}} - E_t \right) \psi_t^* = 0$ , so this can be subtracted from the integral for symmetry

$$= \int_R \left( \psi_t^* \left( \hat{\mathcal{H}} - E_i \right) \psi_i - \psi_i \left( \hat{\mathcal{H}} - E_t \right) \psi_t^* \right) dV \quad (2.29)$$

But as the perturbing Hamiltonian is time independent the scattering is elastic and  $E_i = E_t$ , thus

$$= \int_R \left( \psi_t^* \hat{\mathcal{H}} \psi_i - \psi_i \hat{\mathcal{H}} \psi_t^* \right) dV \quad (2.30)$$

Inserting  $\hat{\mathcal{H}} = -\frac{\hbar^2}{2m} \nabla^2 + U(r)$ , where  $U(r)$  is the potential.

$$= \int_R \left( -\frac{\hbar^2}{2m} \psi_t^* \nabla^2 \psi_i + \frac{\hbar^2}{2m} \psi_i \nabla^2 \psi_t^* + \psi_t^* U(r) \psi_i - \psi_i U(r) \psi_t^* \right) dV \quad (2.31)$$

Removing the last two terms inside the parentheses as  $U(r) = 0$  in the region  $R$ , and then applying the divergence theorem we get

$$= -\frac{\hbar^2}{2m} \int_{S_R} \left( \psi_t^* \nabla \psi_i - \psi_i \nabla \psi_t^* \right) \cdot d\mathbf{S} \quad (2.32)$$

where the integral is over is the surface enclosing the region  $R$ . However,  $\psi_i$  tends to zero quickly in region  $R$  hence the surface integral only needs to be evaluated at the surface of boundary of the tunnelling gap,  $B_T$

$$M_{it} = -\frac{\hbar^2}{2m} \int_{B_T} \left( \psi_t^* \nabla \psi_i - \psi_i \nabla \psi_t^* \right) d\mathbf{S} \quad (2.33)$$

Evaluating this in 1D removes the integral and inserting the barrier wavefunctions from equations (2.23) and (2.24), we get

$$M_{it} = -\frac{\hbar^2}{2m} \left\{ B_t e^{\kappa(x-d)} \frac{\partial}{\partial x} (B_i e^{-\kappa x}) \Big|_{x=d} - B_i e^{-\kappa x} \frac{\partial}{\partial x} (B_t e^{\kappa(x-d)}) \Big|_{x=d} \right\} \quad (2.34)$$

$$= \frac{\hbar^2}{m} \kappa B_t B_i e^{-\kappa d} \quad (2.35)$$

which is independent of  $x$ , thus, for thus uniform system the surface integral in

## Instrumental Techniques

equation (2.33) could be done over any surface in the barrier. Now by evaluating  $|M_{it}|^2$  we can say

$$T_{i \rightarrow t} \propto e^{-2\kappa d} \quad (2.36)$$

as calculated before in equations (2.4) and (2.20). However, by considering the Bardeen method we get  $T_{i \rightarrow t}$  is proportional to the density of states of the final state. As the number of electrons currently in the initial state depends on the density of states, we can conclude that the tunnel current is proportional to both the density of states in the initial and final state.

To obtain a tunnel current, a bias voltage  $V$  is applied between the tip and sample. Although the barrier potential is no longer constant, see Figure 2.2(b), the derivations above can still be used (by considering the average potential). A more thorough solution can be obtained by using the Wentzel–Kramers–Brillouin (WKB) approximation to solve the Schrödinger equation for the modified potential.

The bias voltage has the effect of separating the Fermi levels of the tip,  $E_F^T$ , and the sample,  $E_F^S$ , by an energy of  $eV$ .<sup>2</sup> At absolute zero, tunnelling can only occur between these two Fermi levels. This is because energies greater than  $E_F^T$  contain no electrons for tunnelling, and energies lower than  $E_F^S$  have no empty states to tunnel into<sup>3</sup>. At higher temperatures this energy window increases due to the thermal excitation of electrons above the Fermi level. However, as this happens in both materials it does not affect the net tunnelling current, instead leading to thermal noise.

As only the electrons (and empty electron states) within the  $eV$  energy window below (above) the Fermi level can tunnel, it is only the density of states of these states that affect the tunnelling. Hence, by sweeping the voltage at constant tip-sample distance we can probe the integral of the local density of states (LDOS) of the sample from  $E_F$  to  $E_F + eV$ , assuming the LDOS in the tip is unchanging in energy. In fact what is being probed is<sup>4</sup>

$$I_c(V) \propto \int_0^{eV} \rho_{\text{tip}}(E_F^T - E) \rho_{\text{sample}}(E_F^S + eV - E) dE. \quad (2.37)$$

<sup>2</sup>The elementary charge multiplied by the voltage, not to be confused with an electron volt.

<sup>3</sup>When applying a reverse bias, the same argument holds but with  $E_F^T$  and  $E_F^S$  reversed

<sup>4</sup>Assuming the matrix element is constant at all energies

## Instrumental Techniques

This equation allows us to understand the meaning of the varying contrast for different bias voltages.

The formalism derived above is similar to the derivation used by Tersoff and Hamann to describe the theory of the STM [21], however their method goes further by including a simplistic model for the tip shape and solving the equation in three dimensions. Tersoff-Hamann, however, relies on Equation 2.33 being valid for any smooth plane enclosed inside the barrier region. While this is true for tunnelling between two infinite planes, or when reduced to a 1D system (as above), this is not true for arbitrary geometries [22]. No proof of the validity of this assertion for the geometry used by Tersoff-Hamann is given. The proposed geometry is a spherical tip apex (with radius  $R$ ) with an  $s$ -wave wavefunction for a constant barrier potential. This  $s$ -wave is expanded as a 2D Fourier series in the sample plane. This approximation is not covered in detail in this thesis due to the complexity of the derivation. Instead the result:

$$I_c = \frac{32\pi e^2 V (E_{\text{vac}} - E_F)^2 \rho_t(E_F) R^2}{\hbar \kappa^4} e^{2\kappa R} \sum_i |\psi_i(\mathbf{r}_0)|^2 \delta(E_i - E_F), \quad (2.38)$$

will be considered qualitatively (where  $\mathbf{r}_0$  is the coordinate of the centre of the spherical tip). It is important to note that while current is proportional to  $e^{-2\kappa d}$  the distance  $d$  is defined from the planar surface in which the Bloch surface states exist. Therefore, to produce resolution one relies on the LDOS of the surface wave function at the centre of the tip. As the corrugations in the LDOS are too small to be observed at the distances used by Tersoff-Hamann, their approximations do not explain atomic resolution imaging [22], and (more importantly for this thesis) the dependence of image morphology on tip structure. Improvements to the theory explain atomic corrugations on surfaces such as graphite [23]. A more complete theory for STM in three dimensions, by considering a modified Bardeen approach at the interface of a hyperbolic tip, is provided by Chen [22,24]. These more detailed approaches are not covered as they provide little intuitive insight into image formation. Instead these formalisms provide models for image simulations which are outside the scope of this thesis.

## 2.2 AFM Theory

Atomic force microscopy uses a sharp (ideally terminated with a single atom) tip attached to a force sensor to measure the force between the tip and the sample. This thesis only considers non-contact AFM where tip-sample forces are measured by their effect on the sensor's mechanical resonance.

As most AFMs use a force sensor of cantilever geometry this section will concentrate on this geometry. Due to the detail in which the results chapters utilise and reapply the full derivations for the mechanics of AFM sensors these derivations are provided in Appendix A. This section will cover how these results apply to imaging, and will refer the reader to full derivations where appropriate.

In Appendix A.4.4 we derive the fundamental eigenfrequency of a freely oscillating cantilever to be

$$\omega_0 = 3.516015 \sqrt{\frac{EI}{mL^3}} \quad (2.39)$$

where  $E$  is the Young's modulus of the material,  $m$  is the mass of the cantilever,  $I$  is the second moment of area of the cantilever (Appendix A.4.2), and  $L$  the length. This can also be written in terms of the spring constant,  $k$ , and effective mass,  $m_{\text{eff}}$ , of the cantilever (see Appendices A.4.5 and A.4.3), as

$$\omega_0 = \sqrt{\frac{k}{m_{\text{eff}}}}. \quad (2.40)$$

As the AFM tip is approached to the sample the resulting force of the tip-sample interaction,  $F_{\text{ts}}$ , is felt by the cantilever. Under the assumption that the amplitude of oscillation is small enough that the gradient of the tip sample interaction is constant throughout the oscillation cycle, the resonant frequency shifts by

$$\Delta\omega = -\frac{\omega_0}{2k} \frac{\partial F_{\text{ts}}}{\partial z}, \quad (2.41)$$

as derived in Appendix A.7.1. However, this approximation is not accurate for the amplitude under which AFMs normally operate. For arbitrary amplitudes of oscillation the frequency shift is proportional to the average force over the

oscillation instead of the force gradient

$$\Delta\omega = -\frac{\omega_0}{A^2k}\langle F_{ts}(z_0 - q')q'\rangle, \quad (2.42)$$

where  $A$  is the amplitude of oscillation and  $q' = A\cos(\omega t)$ , as derived in Appendix A.7.2. Equation 2.42 is of particular importance for making quantitative measurements. This is discussed in detail in Section 2.2.3.

AFM images are usually taken using one of two modes: either amplitude-modulated (AM-AFM) or frequency-modulated (FM-AFM). In these modes a feedback controller adjusts the tip-sample separation to maintain either a constant amplitude of oscillation at a particular frequency or a constant resonant frequency while always driving on resonance.

### 2.2.1 Amplitude-Modulated AFM

The amplitude of an oscillating cantilever, with a particular driving amplitude,  $A_{\text{drive}}$ , varies for different drive frequencies  $\omega$  as

$$|A| = \frac{|A_{\text{drive}}|}{\sqrt{\left(1 - \frac{\omega^2}{\omega_0^2}\right)^2 + \frac{1}{Q^2} \frac{\omega^2}{\omega_0^2}}}, \quad (2.43)$$

where  $\omega_0$  is the resonant frequency of the cantilever and  $Q$  its quality factor.<sup>5</sup> By driving the cantilever just off resonance, any shift in resonant frequency of the cantilever due to a tip-sample interaction will shift the resonance either closer to the driving frequency or further from the driving frequency. This will cause the amplitude to rise or fall respectively (see Figure 2.4). By comparing the measured amplitude with a setpoint amplitude and using a feedback loop to adjust the tip-sample separation the amplitude of the oscillation can be kept constant as the tip is scanned across the surface. Assuming no change in non-conservative forces, which lead to damping and hence a lower  $Q$ , this means the tip will follow a contour of constant force gradient. By recording the path taken by the tip an image of the surface can be constructed.

---

<sup>5</sup>See Appendices A.5 and A.2

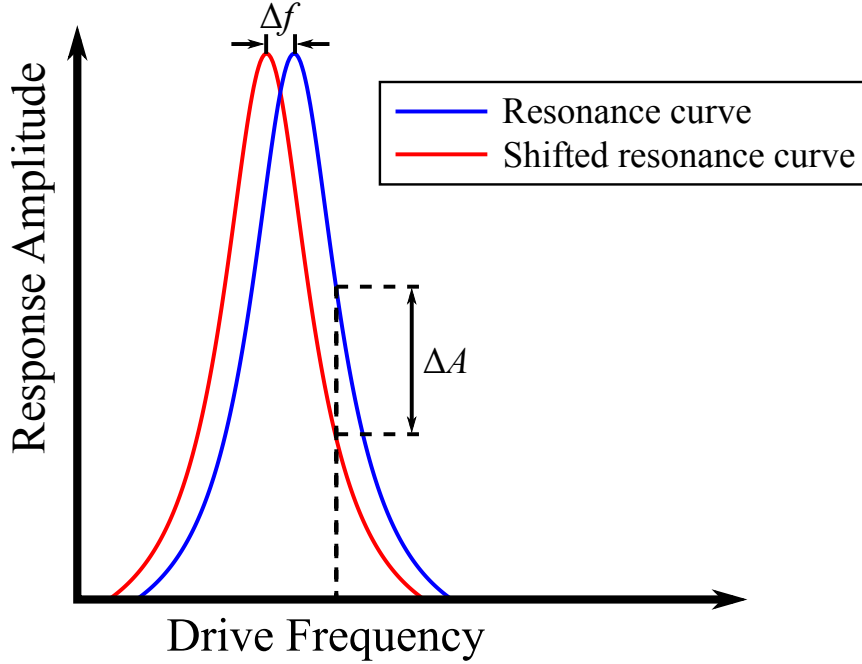


Figure 2.4: *Response of a free cantilever (Blue) and a cantilever experiencing an attractive potential (Red) to being externally driven. By exciting a cantilever just off resonance any frequency shift will result in a change in the amplitude with different sign for positive and negative frequency shifts.*

### 2.2.2 Frequency-Modulated AFM

For frequency modulated AFM the cantilever needs to always be excited on resonance, even as the resonance changes due to the tip-sample forces. By considering the phase relationship between a cantilever and its driving frequency<sup>6</sup>

$$\phi = \arctan \left( -\frac{\omega}{Q\omega_0 \left(1 - \frac{\omega^2}{\omega_0^2}\right)} \right) \quad (2.44)$$

clearly when the cantilever is excited on resonance  $\frac{\omega^2}{\omega_0^2} = 1$  and therefore  $\phi = \arctan(-\infty) = -\frac{\pi}{2}$ . Thus, the resonance condition is that the driving force must be quarter of a cycle ahead of the cantilever's response. To keep the cantilever on resonance the AFM electronics use the response signal of the cantilever, either phase shifted or locked to by a PLL to excite the cantilever (See Sections 2.3.6

<sup>6</sup>See Appendix A.5

and 2.3.7). A feedback controller adjusts the amplitude of this signal to maintain a constant excitation amplitude. The output of this feedback controller is also proportional to the damping due to non conservative forces. A second feedback controller compares the frequency shift (relative to the free resonance of the cantilever) with a setpoint and adjusts the tip-sample separation to maintain this. Just as with AM-AFM the tip's path is recorded as it is scanned over the surface, maintaining a constant force gradient.

### 2.2.3 Force spectroscopy

Force spectroscopy is a technique used to obtain quantitative force measurements from an FM-AFM. The method relies on inverting Equation 2.42. Considering that the frequency shift is proportional to  $\langle F_{ts}(z_0 - q')q' \rangle$ , and that  $q'$  is sinusoidal, one realises that  $\Delta f$  is unchanged for a constant offset in  $F$ . Thus, any method used to deconvolve  $F_{ts}$  from  $\Delta f$  only produces the relative difference in force rather than an absolute force.

To overcome this, measurements are taken using the following method. The feedback loop is disabled, and  $z$  is directly controlled while  $\Delta f$  is recorded.  $\Delta f$  readings are taken at the same  $x$ - $y$  coordinate at a large number of  $z$  positions moving away from the surface. These are recorded until the force is negligible. The point furthest from the surface is taken to have a force of zero and the force for each subsequent measurement can be calculated relative to the previous measurement, and thus the absolute force at each  $z$  position can be calculated. By performing numerical integration one can further calculate the potential between the tip and the surface.

In practice, using this process to directly measure the absolute force or potential between the tip apex and a surface feature is far from simple. First, the interaction of interest is not the only contribution to the frequency shift. Other, longer range, interactions such as the van der Waals interaction of the surface with the macroscopic tip structure often dominate the frequency shift. Thus, to measure a particular interaction one must first calculate a short range frequency shift. This is dealt with in Section 2.2.3.1. Secondly, as Equation 2.42 is a convolution, to invert the formula to calculate the force a deconvolution

## Instrumental Techniques

operation is required. Analytical deconvolutions are rarely intuitive to derive, and numerical deconvolutions necessarily result in an approximation. Sections 2.2.3.2 and 2.2.3.3 deal with the methods which can be used to deconvolve  $\Delta f$  data into absolute force measurements.

### 2.2.3.1 Calculating the Short Range Chemical Interaction

To separate long range van der Waals interactions from short range interactions under study one must find a way to estimate the long range contribution to the frequency shift and subtract this from the measured frequency shift. This is analogous to background subtraction performed regularly in optical spectroscopy techniques [25]. In early force spectroscopy measurements the predominant method for long range subtraction was to take the force spectra over a very large  $z$  range ( $\sim 10$  nm) until even the long range interactions become negligible [26]. One then defines the first  $\sim 0.5$  nm as the short interaction area, and the other  $\sim 9.5$  nm as the long range interaction area. By fitting a power law to the long range interaction and extrapolating this power law into the short interaction area one can subtract the long range interaction. This method, however, presents significant problems as fitting power laws to experimental data is very imprecise [27]. Thus, changes in noise level or in the arbitrary choice of cut-off between long and short range interaction can have a significant effect on the numerical quantities obtained.

A more appropriate method, though sometimes experimentally challenging, is to perform an equivalent force spectroscopy measurement, but without the interaction of interest. For example if one is studying the interaction of the tip termination with a molecule adsorbed on the surface one can perform identical measurements over the molecule and over the surface near the molecule. As the molecule is spatially higher in  $z$  than the surface, provided that the “off” spectrum does not approach close enough to the surface such that chemical interactions are probed, this spectrum should provide an accurate measurement of the long range interaction contribution to the frequency shift. For studies of surface features rather than adsorbed molecules this method may not be possible. However, some surfaces such as the silicon (111)  $7\times 7$  reconstruction have recessed

## Instrumental Techniques

features above which suitable “off” spectra can be taken.

### 2.2.3.2 Force Deconvolution: Giessibl Matrix Method

Giessibl introduced a very intuitive and neat method for deconvolving the force from the measured frequency shift [28]. This method starts by rewriting Equation 2.42 as an integral (See Appendix A.7.2) applying a change of variables to remove time dependence

$$\Delta f(z_0) = -\frac{f_0}{\pi k A^2} \int_{-A}^A \frac{F_{ts}(z_0 - q')q'}{\sqrt{A^2 - q'^2}} dq'. \quad (2.45)$$

In this form it becomes apparent that  $\Delta f$  is truly a convolution which can be written in the form

$$\Delta f(z) = -\frac{f_0}{\pi k A^2} (F * G)(z), \quad \text{where } G(q') = \frac{q'}{\sqrt{A^2 - q'^2}}. \quad (2.46)$$

To deconvolve the data Giessibl exploits the discrete nature of data acquisition to approximate the measured frequency shifts as a matrix equation, acting on a vector of forces. Under this formalism inversion is simple under the laws of linear algebra. To construct the matrix equation a further change of variables applied to write the integral in terms of a normalised quantity  $\tau = q'/A$ . Further, the integral is written approximately as a sum of  $2\alpha + 1$  integrals. Here  $\alpha$  is an integer quantity calculated as

$$\alpha = \text{int} \left( \frac{A}{\Delta z} \right), \quad (2.47)$$

where int is an operation to round to the nearest integer and  $\Delta z$  is the distance in  $z$  between adjacent  $\Delta f$  measurements. We can now write the  $m$ th frequency shift (where  $m = 1$  is the frequency shift measured furthest from the surface) as

$$\Delta f_m \approx -\frac{f_0}{\pi k A} \sum_{n=0}^{2\alpha} \int_{\frac{2(n+1)}{2\alpha+1}-1}^{\frac{2n}{2\alpha+1}-1} \frac{\tau}{\sqrt{1-\tau^2}} d\tau F_{m+n}. \quad (2.48)$$

Note here that the force is not a function of  $\tau$  due to it being discretely measured at only one point in the integrated region. We can now construct the following

## Instrumental Techniques

equation with the matrix  $\underline{\underline{M}}$ ,

$$\begin{pmatrix} \Delta f_1 \\ \Delta f_2 \\ \vdots \\ \Delta f_{2\alpha+1} \\ \Delta f_{2\alpha+2} \\ \vdots \\ \Delta f_N \end{pmatrix} \approx \begin{pmatrix} M_{11} & 0 & \cdots & 0 \\ M_{21} & M_{22} & \cdots & 0 \\ \vdots & \vdots & \ddots & \vdots \\ M_{(2\alpha+1)1} & M_{(2\alpha+1)2} & \cdots & 0 \\ 0 & M_{(2\alpha+2)2} & \cdots & 0 \\ \vdots & \vdots & \ddots & \vdots \\ 0 & 0 & \cdots & M_{NN} \end{pmatrix} \begin{pmatrix} F_1 \\ F_2 \\ \vdots \\ F_{2\alpha+1} \\ F_{2\alpha+2} \\ \vdots \\ F_N \end{pmatrix}, \quad (2.49)$$

where the matrix elements can be derived simply from Equation 2.48 as

$$M_{ij} = \begin{cases} \text{if } 0 \leq (j - i) \leq 2\alpha, & \int_{\frac{2(j-i+1)-1}{2\alpha+1}}^{\frac{2(j-i)-1}{2\alpha+1}} \frac{\tau}{\sqrt{1-\tau^2}} d\tau \\ \text{else,} & 0 \end{cases}. \quad (2.50)$$

It is now clear that the vector of force values can be simply calculated as

$$\begin{pmatrix} F_1 \\ F_2 \\ \vdots \\ F_N \end{pmatrix} = \underline{\underline{M}}^{-1} \begin{pmatrix} \Delta f_1 \\ \Delta f_2 \\ \vdots \\ \Delta f_N \end{pmatrix}. \quad (2.51)$$

Although this formalism is simple to derive, the accuracy is highly dependent on  $\alpha - \frac{A}{\Delta z}$ , and fails entirely if  $\frac{A}{\Delta z} < 0.5$ . This is due to the discrete nature under which the formalism is derived.

In practice, the method is very computationally efficient as only  $2\alpha + 1$  terms need to be calculated to build the matrix  $\underline{\underline{M}}$ . As often  $\sim 1000$  measurements are taken for a force spectroscopy experiment one intuitively expects inverting a  $1000 \times 1000$  element matrix will be computationally expensive. However, as  $\underline{\underline{M}}$  is triangular the calculation is extremely efficient.

### 2.2.3.3 Force Deconvolution: Sader-Jarvis Method

Despite the discrete nature of the data acquisition it is arguably better to solve the deconvolution in a continuous fashion. This way the discretisation of the deconvolution cannot mismatch the discretisation of the measurement. In 2004 Sader and Jarvis derived a continuous method to approximate force deconvolution [29] (henceforth the Sader-Jarvis method).

Starting with Equation 2.46 and applying an inverse Laplace Transform and using the convolution theorem we get

$$\mathcal{L}^{-1} \left\{ \frac{\Delta f}{f_0} \right\} = \frac{1}{\pi k A^2} B(\lambda) T(\lambda), \quad (2.52)$$

where  $B(\lambda)$  and  $T(\lambda)$  are the inverse Laplace transforms of  $F(z)$  and  $-G(z)$  respectively. By simply rearranging and applying a Laplace transform we arrive at

$$F(z) = \mathcal{L} \left\{ \frac{\pi k A^2}{T(\lambda)} \mathcal{L}^{-1} \left\{ \frac{\Delta f}{f_0} \right\} \right\}. \quad (2.53)$$

At this point Sader and Jarvis construct an approximate form for  $T(\lambda)$  using a Padé power series approximation with three terms. Two terms are derived from the limiting behaviour of  $T(\lambda)$  and a third *ad hoc* term numerically derived to improve the approximation. Due to the difficulty of numerically solving Laplace or inverse Laplace transforms these are rewritten as Riemann-Liouville fractional integrals. From this they obtain their final form for the force to be

$$F(z) = \frac{2k}{f_0} \int_z^\infty \left( 1 + \frac{A^{1/2}}{8\sqrt{\pi(\tau-z)}} - \frac{A^{3/2}}{\sqrt{2(\tau-z)}} \frac{d}{d\tau} \right) \Delta f(\tau) d\tau, \quad (2.54)$$

where  $\tau$  is a dummy integration variable. By integrating we obtain a method to directly calculate the interaction potential,  $U(z)$  from the recorded data:

$$U(z) = \frac{2k}{f_0} \int_z^\infty \left( (\tau-z) - \frac{A^{1/2}}{4} \sqrt{\frac{\tau-z}{\pi}} + \frac{A^{3/2}}{\sqrt{2(\tau-z)}} \right) \Delta f(\tau) d\tau. \quad (2.55)$$

The Sader-Jarvis method and the Giessibl matrix method have been compared via numerical solutions of simulated  $\Delta f$  data for a Morse potential [30].

## Instrumental Techniques

Both results provide similar accuracy, although the study of Ref. [30] does not consider the effect of random noise on the experimental data.

Recent work [31] has shown that as Equation 2.55 is an improper integral with the third bracketed term diverging to infinity at the limit  $\tau = z$ , a more appropriate integral for numerical implementation can be derived by substituting  $u = \sqrt{\tau - z}$  into the integral giving

$$U(z) = \frac{4k}{f_0} \int_0^\infty \left( u^3 + \sqrt{\frac{A}{16\pi}} u^2 + \sqrt{\frac{A^3}{2}} \right) \Delta f(u^2 + z) du. \quad (2.56)$$

As numerical integrals are effectively low-pass filters converting straight to interaction potential reduces experimental noise, compared to calculating the potential by integrating Equation 2.54, where the noise has been amplified by the differential term. Forces can then be calculated from the results of Equation 2.56 via Lanczos low-noise differentiation which essentially applies a boxcar average during the differentiation [32].

### 2.2.3.4 Grid Spectroscopy

Grid spectroscopy is an extension of force spectroscopy in which multiple force spectra are taken above a grid of positions on the  $x$ - $y$  (imaging) plane [26]. As multiple measurements in  $z$  are taken for each force spectrum the final data represents a three dimensional array of spatially separated  $\Delta f$  measurements. By applying previously discussed methods to extract the interaction potential from each spectrum, one can calculate the potential landscape in three dimensions. By differentiating this grid in any direction of interest the force in this direction can be calculated. Thus, by differentiating in three orthogonal directions the full force vector felt by the tip is known for all sampled areas. A similar method has been used in 2D to calculate the force needed for lateral manipulations [33, 34], however, for this method the order of  $\Delta f$  measurements is modified as the tip moves parallel to the surface at a range of different heights.

Grid spectroscopy measurements take a considerable time. To improve the accuracy of force deconvolution the spacing in  $z$  should ideally be much smaller than the amplitude of oscillation, and the  $z$  range needs to extend far enough

## Instrumental Techniques

that the chemical interaction is zero. So if we assume a  $z$  range of 1.5 nm and a  $z$  step of 1.5 pm (as AFM measurements with amplitudes of order 20 pm are possible [35]), this results in 1000 points in  $z$ . Spectroscopy measurements are normally recorded during the movement in both directions as this allows the hysteresis in the measurement caused by either piezoelectric creep or tip/sample changes to be detected. If we assume a very sparse grid in the  $x$ - $y$  plane of only  $30 \times 30$  spectra, a total of 1.8 million individual  $\Delta f$  measurements are required. Assuming a short integration time for each measurement of only 10 ms and ignoring the time the tip takes moving between the measurements, the entire grid would take 5 hours to complete. Unless the AFM system is operating at only a few kelvin in this time thermal drift can have a considerable effect on the measurement. Increasing the density of the  $x$ - $y$  grid to  $45 \times 45$  and doubling the integration time, the experiment will now take over 22 hours, probably over 24 once the time for the tip to move is factored in.

With such long experiments it is important to introduce some method to compensate for drift of the sample relative to the tip. For this we use the concept of atom tracking [36]. Atom tracking is a method where the tip is positioned over a local maximum or minimum on the surface. Assuming that the maximum is radially symmetric, if the tip motion is set to circle the maxima in  $x$  and  $y$ , with  $z$  feedback off, the frequency shift should remain constant. If the sample drifts relative to the tip in the  $x$ - $y$  plane the frequency shift will no longer remain constant. The direction of tip movement to compensate for this drift can be calculated very simply by considering that to apply the circular motion sinusoidal signals are applied in  $x$  and  $y$  with a phase difference of  $90^\circ$ . The magnitude of the variation in  $\Delta f$  which is in-phase with the  $x$  component corresponds to the drift in  $x$ . Similarly the  $\Delta f$  variation  $90^\circ$  out of phase with  $x$  corresponds to drift in  $y$ . Thus, the drift in the  $x$ - $y$  plane can be compensated with two feedback loops (See Section 2.3.4) acting on the in-phase and quadrature outputs of a two-phase lock-in amplifier, with  $\Delta f$  as the input and the  $x$  dither signal as the reference input.

Atom tracking was originally used not to compensate for drift but to, as the name suggests, track adsorbed atoms [37] (or dimers [38,39]) diffusing across the sample surface in STM. The idea was then extended to AFM for drift compen-

sation [40]. To combine drift compensation with other measurements the drift is measured above a stable point of interest for a set time. The drift in  $z$  is also calculated by setting low gain to the  $z$  feedback rather than switching it off. The  $z$  feedback should be too slow to react to the changes in  $\Delta f$  induced by the tip dither (these being corrected by the  $x$  and  $y$  loops), instead correcting for tip sample drift in  $z$ . By applying linear fits to the motion in  $x$ ,  $y$ , and  $z$  the drift rate can be calculated, and compensated for during the measurement. As drift rates, however, are non-linear one must regularly pause long experiments to re-calculate drift rates and update the drift compensation. For grid spectroscopy measurements presented in this thesis atom tracking was performed to update the drift rate between each spectra using specialised instrumentation designed by Rahe *et al.* [41].

## 2.3 SPM Instrumentation

This section gives an overview of design considerations for SPM instrumentation. It focuses on vacuum STM and AFM as this is most relevant to experimental chapters. However, ambient SPM is also considered.

### 2.3.1 Vibration Isolation

As discussed in Section 2.1 a displacement of 1 Å between the tip and the sample in STM changes the tunnel current by approximately an order of magnitude. Due to this strong dependence on position, vibrational isolation is vital to collecting accurate scan data in STM. Ideally, vibrations should be reduced to an amplitude of less than 5 pm [17], and as floor vibrations are of the order of 0.5  $\mu\text{m}$  this requires a vibrational isolation factor of  $10^{-5}$ . Similarly, vibrations can excite an AFM cantilever so any vibrations must have a much smaller amplitude than the tip oscillation.

In vacuum SPM a first level vibrational isolation is often provided by pneumatic feet on the vacuum chamber, which houses the system. Further vibrational isolation can be provided by suspending the main stage of the SPM from springs and damping any vibrations with eddy current damping, see Section 2.3.1.1. In

## Instrumental Techniques

ambient SPM vibrational isolation is often provided passively by suspending the main stage of the SPM from bungee cords. Alternatively some systems use active vibrational isolation stages which use an accelerometer to sense vibrations and an actuator to move the stage to counter the vibration.

An important design consideration is the resonant frequency of any passive vibrational isolation stage. The damped vibrational isolation stage needs to have a low resonant frequency, as a damped oscillator does not attenuate vibration below its resonant frequency [19], see Figure 2.5(b). In contrast to this, the scanning unit (see Section 2.3.2) and sample experience the same vibrations, thus the tip-sample junction is only affected by vibrations which are either amplified or attenuated by the scanning unit. For this reason the tip-sample is less affected by vibrations below the resonant frequency of the scanning unit, thus a high resonant frequency is optimal, see Figure 2.5(a). By meeting these resonance conditions the combined frequency response becomes significantly lower, Figure 2.5(c) [17].

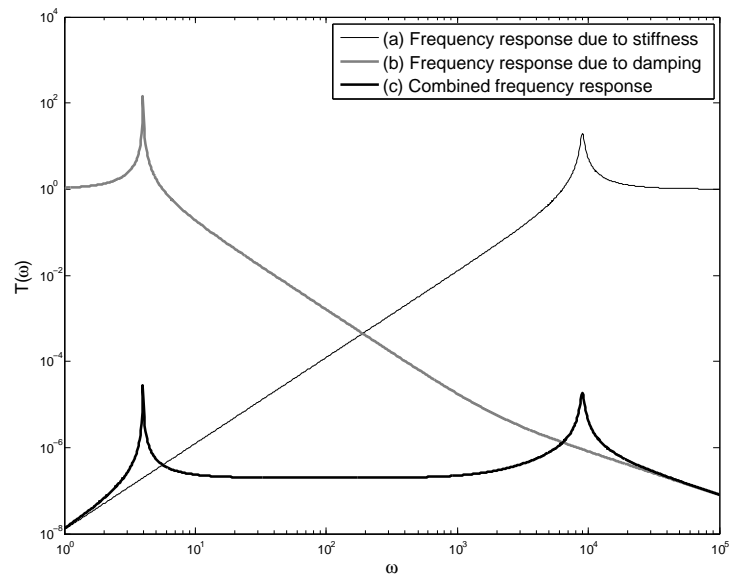


Figure 2.5: *The frequency response of vibrational isolation due to mechanical vibration. By combining stiff scanning components with high resonant frequencies (a), and damped vibrational isolation with low resonant frequencies (b), the combined frequency response (c) can be reduced significantly.*

### 2.3.1.1 Eddy Current Damping

A method commonly used to produce a low frequency, well-damped main SPM stage in vacuum systems is to suspend the stage from soft springs. The main stage is then damped by attaching copper plates to the stage, such that as the stage oscillates the plates are move through a magnetic field produced by fixed magnets located between the plates. These magnets are mechanically coupled to the outer vacuum system, not to the stage. The motion of the plates relative to the magnetic field induces small circulating currents in to the copper [42]. These currents, due to Faraday's Law<sup>7</sup>

$$\oint_C \mathbf{E} \cdot d\mathbf{l} = -\frac{\partial \Phi_{B,S}}{\partial t}, \quad (2.57)$$

cause two important effects. First, by Lenz's law, the induced current creates a magnetic field opposing the magnetic field inducing it. The opposing magnetic field increases the restoring force, reducing the amplitude of oscillation. Secondly, the resistance of the copper causes Joule heating, thus dissipating energy from the system.

The damping coefficient  $\gamma$  for eddy current damping is given by [17]

$$\gamma = \frac{B^2 S d C_0}{\rho}, \quad (2.58)$$

where  $B$  is the magnetic field,  $S$  and  $d$  are the cross-sectional area and thickness of the plate respectively and  $\rho$  is the resistivity of the plate.  $C_0$  is a dimensionless constant that is dependent on the plate's geometry. Therefore, to maximize eddy current damping it is important to maximize flux cut by the plates, see Equation (2.57). This is often achieved by having each plate in between two closely spaced permanent magnets, mounted on a ring adjacent to the sample stage.

### 2.3.2 Scanning Unit

An SPM needs to be able to move the tip in three dimensions, with sub-Angstrom resolution to collect an image with atomic resolution. There are multiple methods

---

<sup>7</sup> $d\mathbf{l}$  is an infinitesimal segment of the path  $C$  enclosing the area  $S$ .

## Instrumental Techniques

for making scanning units, but this report will concentrate on the piezoelectric tube scanner. This will be compared with the more intuitive method of the piezoelectric tripod, demonstrated in Figure 2.1.

Early STMs used tripod scanners. Typical tripod scanners have a lowest resonant frequency of 5 kHz [43]. This resonance limits the maximum scan speed, as well as affecting vibrational isolation. The tube scanner was designed as a scanning unit with a higher resonant frequency. This is achieved by building the scanner out of a single piezoelectric tube.

The outer surface of the piezoelectric tube is covered by four electrodes, see Figure 2.6. By applying equal and opposite biases (with respect to the internal electrode) to opposite electrodes the tube can be bent sideways. By applying an equal bias to all electrodes the tube can be elongated.

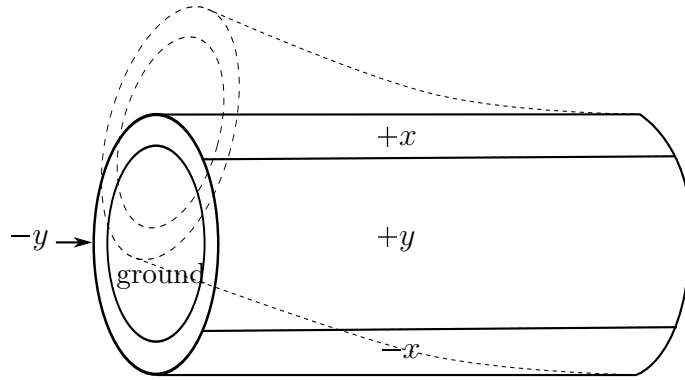


Figure 2.6: *Diagram of a piezoelectric tube scanner.*

The tip deflection can be calculated as [44]

$$\Delta x = 2\sqrt{2} d_{31} \frac{l^2}{\pi D t} V_x, \quad (2.59)$$

where  $\Delta x$  is the  $x$  deflection<sup>8</sup>,  $l$  is the length of the tube,  $D$  is the internal diameter of the tube,  $t$  is the thickness of the tube wall, and  $\pm V_x$  is the voltage applied to the  $x$  electrodes.  $d_{31}$  is the piezoelectric voltage conversion factor.

<sup>8</sup> $y$  deflection calculated using same equation, replacing  $V_x$  with  $V_y$ .

## Instrumental Techniques

The tube extension can be calculated as for a normal piezoelectric tube by [19]

$$\Delta l = d_{31} \frac{l}{t} V. \quad (2.60)$$

### 2.3.3 Coarse Positioning Motors

For an SPM to attain atomic or molecular resolution, the tip must be less than a nanometre from the surface. As a typical tube scanner has a range of about 1–2  $\mu\text{m}$ , the user must be able to move the tip relative to the sample with a very high degree of accuracy. This is made more complicated as the range of movement must be of the order of a few millimeters to allow procedures such as replacing the sample. While only one dimensional coarse positioning normal to the surface is strictly required, it is useful to be able to move the sample in two or three dimensions so different areas of the sample can be scanned.

There are many methods for coarse positioning, ranging from a very simple manual screw approach to complicated piezoelectric walkers which can walk around the isolation stage. A common method, used on all SPM systems used in this thesis, is the inertial slider.

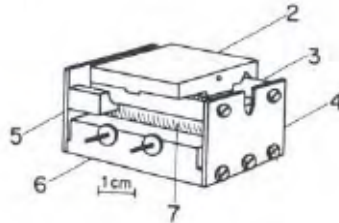


Figure 2.7: *Design of an inertial slider. Showing the top plate(2), rods (3), leaf springs (4) and (5), motor base (6) and piezoelectric tubes (7). (Diagram from reference [45])*

The inertial slider is a remarkably ingenious and simple design that can move with steps as small as 5 nm, and typically has a range of up to a centimetre [46]. The original inertial slider design [45] consists of a top plate sitting on two support rods, which are held in place by a holder, see Figure 2.7. This rod holder is connected to the motor base by two leaf springs. Both the rod holder and the base are attached to the ends of a pair of piezoelectric tubes. As the

## Instrumental Techniques

tubes are elongated (or contracted) the rods move relative to the fixed motor base. If acceleration of the rods is low, the static friction will hold the top plate on the rods, moving it with them. However, if the acceleration of the rods is high enough, the inertial force will overcome the static friction and the top plate will remain stationary as the rods move below it. Hence, by using a saw tooth signal to control the piezoelectric tubes, the top plate can gradually be shunted across the rods. By using three connected inertial sliders it is possible to produce a three dimensional coarse positioning motor with resolution of a few nanometres and range of a few millimetres in each dimension.

### 2.3.4 Feedback Controllers

As mentioned in Section 2.1, the topography is mapped in SPM by feedback loops adjusting the tip-sample separation to keep the tunnel current constant. Similarly, in AFM the topography is mapped by feeding back on either the amplitude or frequency shift constant, for AM-AFM and FM-AFM respectively. A detailed theoretical account of feedback is given in Chapter 9, this section covers the basics of the feedback controller in the context of understanding SPM instrumentation.

The simplest feedback controller is a “bang-bang” controller which has only two possible states, normally referred to as ‘On’ and ‘Off’. In the case of the SPM feedback loop they would relate to either approaching or retracting the tip one ‘step’ depending on if the measured interaction is below or above the set-point. This feedback method is not appropriate for SPM. If the step is ‘small’ then it will take many steps (and therefore a long time) to reach the set-point. If, on the other hand, the step is ‘large’ then the set-point cannot be accurately reached as the system will be constantly stepping forward and back over the set-point.

Another simple feedback loop is the proportional controller. In this feedback loop the difference between the measured and set-point interaction is multiplied by a constant and added to the tip-sample separation. Proportional feedback controllers provide a much smoother response than “bang-bang”, however they are vulnerable to producing steady state errors, where the system tends towards a value which is not the set-point (See Section 2.3.4.1).

## Instrumental Techniques

A common method for improving feedback loops is called a proportional-integral-derivative (PID) controller. A PID controller adjusts the process variable, or tip sample separation in the case of the SPM, under the following formula

$$\delta h(t) = K_p E(t) + K_i \int_0^t E(\tau) d\tau + K_d \frac{d}{dt} E(t), \quad (2.61)$$

where  $\delta h(t)$  is the separation change at time  $t$ ,  $E$  is the difference between the set-point current and measured tunnel current, and  $\tau$  is a dummy integration variable.  $K_p$ ,  $K_i$  and  $K_d$  are the system gains for the proportional, integral and derivative components respectively.

The integral term sums all previous errors. This both speeds up the feedback response and, more importantly, eliminates steady state errors (see Section 2.3.4.1). However, the integral term causes the tip to overshoot the set-point position. The result is that the interaction approaches the set-point by oscillating above and below it.

The derivative term is proportional to the rate of change of the error, acting to reduce the overshoot introduced by the integral term. However, the disadvantage of the derivative term is that it amplifies rapidly varying noise, and hence is only suitable for controlling systems with a high single-to-noise ratio. For this reason the derivative term is rarely implemented in SPM systems. For this reason SPM feedback controllers are referred to as proportional-integral (PI) controllers.

### 2.3.4.1 Steady State Errors

As an explanation for steady state error we consider an SPM trying to maintain constant interaction using a simple proportional feedback loop, meanwhile thermal expansion is causing the tip to drift from the sample at a rate  $d_{\text{drift}}$  per feedback iteration. Then each iteration ( $n$ ) of the feedback loop the tip-sample separation  $d_{\text{ts}}^n$  will be

$$d_{\text{ts}}^n = d_{\text{ts}}^{n-1} + d_{\text{drift}} + d_{\text{feedback}} \quad (2.62)$$

where  $d_{\text{feedback}}$  is the distance moved due to feedback. Due to the proportional relationship between  $d_{\text{feedback}}$  and  $E(t)$  this will eventually hit a steady state

## Instrumental Techniques

where

$$d_{\text{drift}} = -d_{\text{feedback}} = -E(t)K_p \quad (2.63)$$

However, if the feedback also contains an integral term then this steady state error is integrated, causing the feedback to compensate for the constant error. This is shown graphically in Figure 2.8.

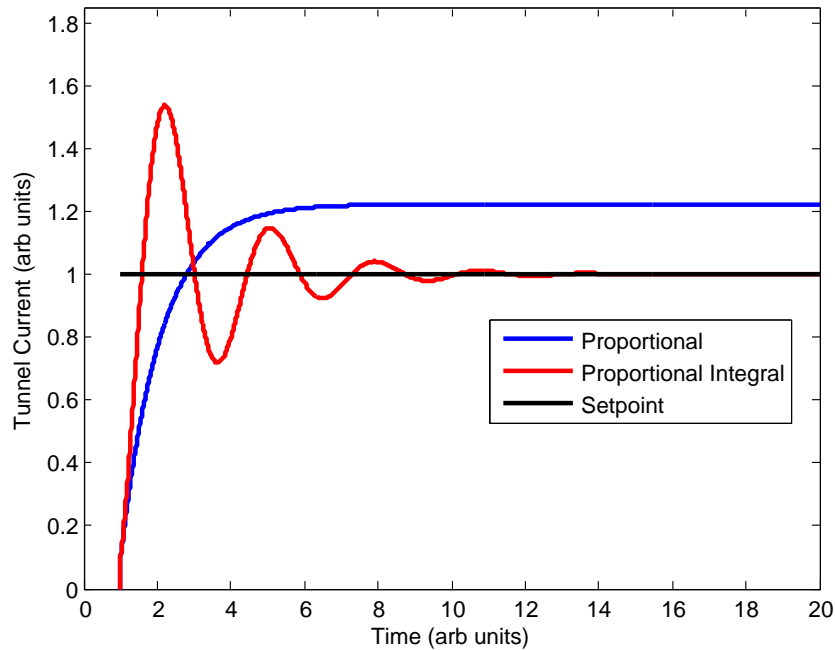


Figure 2.8: Path taken by proportional, and PI (proportional integral) controllers, feeding back to a setpoint while experiencing a constant drift. The proportional controller reaches equilibrium when the feedback term equals the drift term leading to a steady state error. However, the PI controller eliminates steady state error by integrating the error signal.

### 2.3.5 STM Electronics

In STM the electronics are divided into two independent circuits. One circuit contains the HV (high voltage) electronics for operating the piezoelectric actuators used for scanning and coarse positioning. The other circuit contains the LV (low voltage) electronics for controlling the sample bias, and amplifying the

tunnel current. A schematic of the wiring has been provided in Figure 2.9.

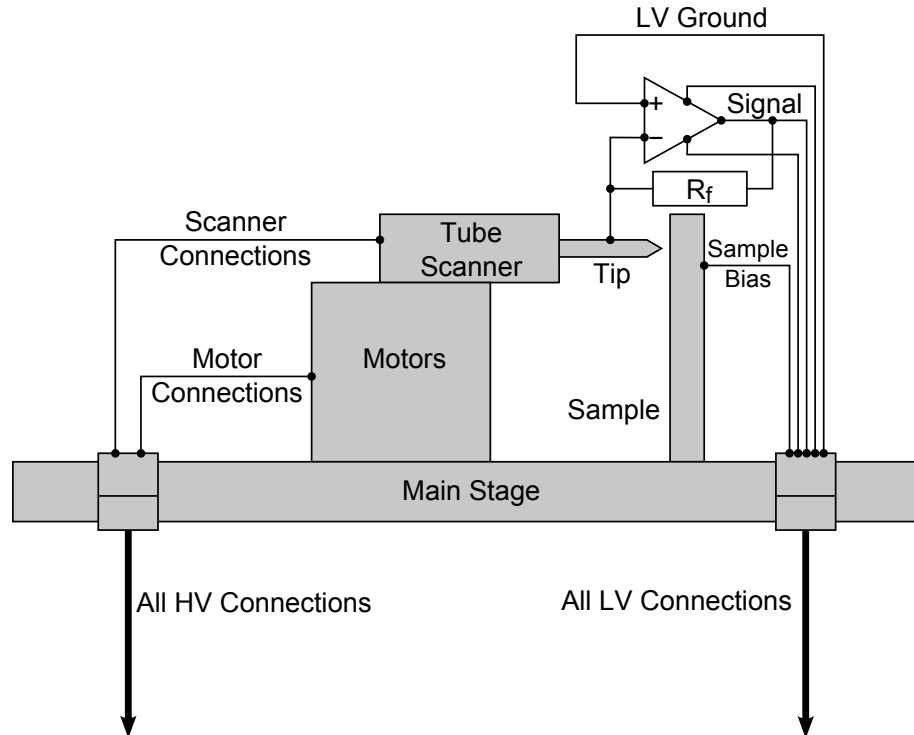


Figure 2.9: *Schematic of STM electronics. Note, the motor and scanner connections are multiple wires. Generally all wires shown are twisted pairs, or occasionally coaxial cables depending on the exact design of the STM head.*

### 2.3.5.1 Low Voltage Electronics

This section will explain the electronics for an STM where the sample is biased and the tip is at virtual ground. Other implementations with virtual biases and real ground, or biased tips are possible, but the concepts remain unchanged. The STM tip is connected to the inverting input of an op-amp held at LV virtual ground by the feedback resistor, as the non-inverting input is connected directly to LV ground. This op-amp is used as a current-to-voltage amplifier (See Figure 2.9). As the tunnel current is of the order of nanoamps it is important to protect the signal from noise as much as possible by using either twisted pairs or coaxial cables. It is also important to position the preamp spatially as close as possible to the tip to reduce the length of wire the tunnel current has to pass down.

## Instrumental Techniques

The feedback resistor of the op-amp ( $R_f$ ) determines the gain of the current-to-voltage preamp. As no current passes through the op-amp the output voltage can be calculated simply from Ohm's law

$$V_{\text{out}} = I_c R_f, \quad (2.64)$$

where  $I_c$  is the tunnel current. The feedback resistor is often of order 100 M $\Omega$ –1 G $\Omega$ , which will produce a signal of 0.1–1 V for 1 nA of current. This signal can then be fed into the control electronics for the STM.

### 2.3.5.2 High Voltage Electronics

The HV electronics control the piezoelectric actuators for coarse positioning and scanning. These are on a completely separate circuit to the LV electronics to reduce the coupling of noise onto the sensitive LV electronics. Importantly, the grounds are kept separate as the current flowing in a ground loop from the HV to LV ground could be detected by the current to voltage preamp, and mistaken for a tunnel current. Similar high voltage electronics are present in AFM systems, but the need for complete isolation, while ideal, is less vital as the low voltage signals are generally larger and thus are less sensitive to noise.

### 2.3.6 AM-AFM Electronics

For amplitude modulation the circuitry needs to excite the cantilever slightly off resonance. This can simply be performed by a function generator. The tip deflection signal is fed into a lock-in amplifier, with the excitation signal as a reference signal. From the lock-in amplifier the amplitude of the cantilever can be compared to a set-point amplitude and a PID controller adjusts the tip sample separation to minimise the amplitude error signal.

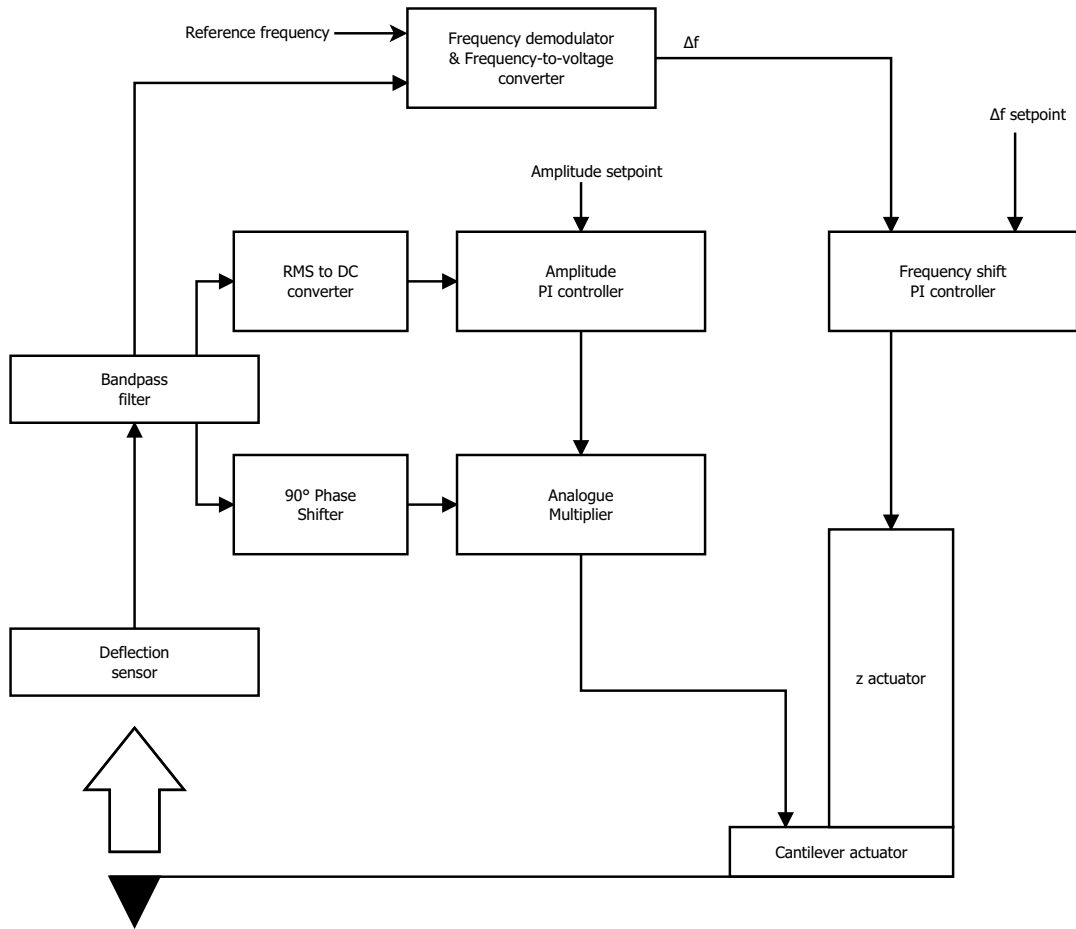


Figure 2.10: *Schematic of self-excitation method of FM-AFM feedback with constant amplitude and frequency shift.*

## 2.3.7 FM-AFM Electronics

### 2.3.7.1 Self excitation FM-AFM

One method for exciting the cantilever on resonance is called self excitation. In this the deflection signal (bandpass filtered to remove noise from frequencies far from resonance) is phase shifted by  $90^\circ$  and used as the excitation signal (see Figure 2.10).

The signal from the bandpass filter also goes into an RMS-to-DC converter to produce a voltage proportional to the RMS amplitude of the oscillation. This amplitude and a set-point amplitude are fed into the PI controller (see Section

## Instrumental Techniques

2.3.4) which adjusts the driving amplitude to reduce the amplitude error. The driving amplitude is adjusted by using an analogue multiplier to multiply the phase-shifted deflection signal with the PI controller output. The output of the PI controller can also be recorded as it is a measure of the damping felt by the cantilever.

The signal from the bandpass filter branches in a third direction towards a frequency-demodulator and a frequency-to-voltage converter, this compares the frequency from the bandpass-filtered signal with  $f_0$ , the cantilever's free resonant frequency, and outputs  $\Delta f = f - f_0$ . Many methods for this demodulation and voltage conversion can be used, from complicated phase detection processes to simply converting  $f$  and  $f_0$  to voltages with frequency-to-voltage converters and then calculating  $\Delta f$  with a differential amplifier.

The calculated  $\Delta f$  signal and a set-point  $\Delta f$  are fed into another PI controller which adjusts the tip sample separation to minimise the frequency error.

### 2.3.7.2 PLL-driven FM-AFM

The PLL-driven FM-AFM design, as its name suggests, uses a PLL (phase-locked loop) to drive the cantilever. An ideal PLL, explained below, produces a pure sinusoidal wave at the same frequency as its input signal, this can then be used as a spectrally clean driving waveform. However, the electronics are much more difficult to implement and problems can occur when the PLL fails to lock to the input signal.

#### Phase-locked loops (PLL)

A PLL produces a signal which is phase 'locked' to the input signal. In a simple PLL this phase is arbitrary, but in order to lock to a constant phase the output frequency must match the input frequency. A standard PLL has 4 components, as shown in Figure 2.11, these are a phase detector, low pass filter, amplifier and voltage-controlled oscillator (VCO).

The phase detector measures the phase between the VCO output and the input signal and outputs a voltage proportional to this phase. Ignoring feedback for a moment, if the two input signals have a different frequency then the phase will repeatedly ramp from 0 to  $2\pi$  over a period of  $T = \frac{1}{\delta f}$ , where  $\delta f$  is the

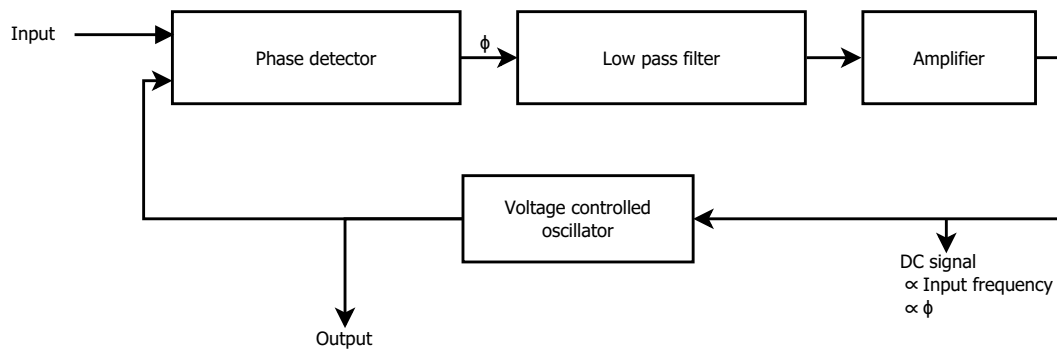


Figure 2.11: *Schematic of a simple PLL circuit.*

frequency differences between the input signals. The low pass filter is used to smooth the phase detector output into the expected linear voltage ramp, and the amplifier is simply to adjust the phase detector's output voltage to a sensible range for the VCO.

The VCO outputs a sinusoidal signal with frequency proportional to the input voltage. This means that if the filtered, amplified output of the phase detector is fed into the VCO then the frequency will change in response to the varying phase difference. Once the VCO varies to the correct frequency the phase difference will remain constant and the output frequency will be locked to the input frequency. This means that once locked the signal out of the amplifier is proportional both the frequency of the input signal, and proportional to the phase between the VCO output and the input signal. In other words the PLL will lock to a particular phase depending on the frequency. The phase detector is set up such that if the input frequency changes slightly the VCO will vary the correct way and lock very quickly.

### **PLL-driven FM-AFM design**

A PLL-driven FM-AFM needs the PLL output signal to be both equal in frequency to the input signal, and also  $90^\circ$  out of phase. This poses a problem, because for a simple PLL, the phase will change as the frequency changes. To solve this we have to add a frequency tracker to the PLL [47]. In Figure 2.12 is a schematic of the PLL driven design.

When the AFM starts (before approaching) the switch in Figure 2.12 starts

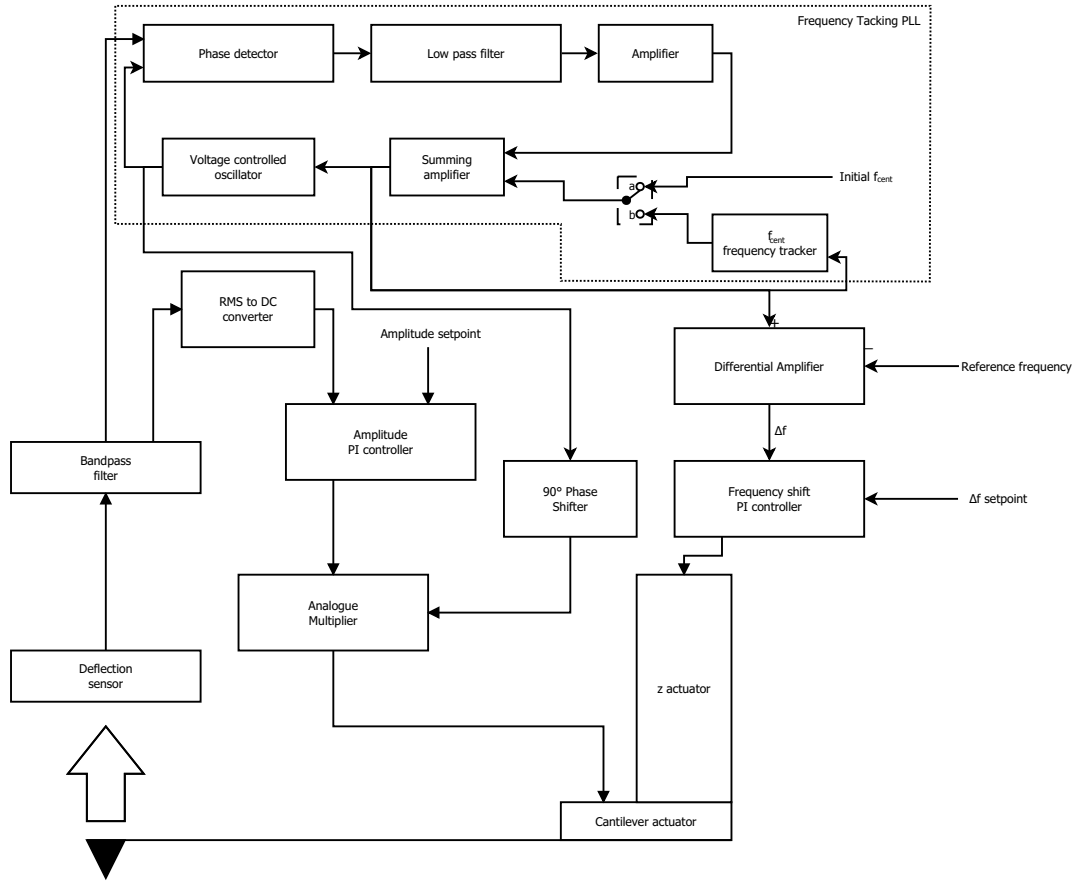


Figure 2.12: Schematic of a PLL driven FM-AFM circuit.

in position a. A voltage proportional<sup>9</sup> to a central frequency,  $f_{\text{cent}}$ , is added to the amplified phase detector output, and sent to the VCO. In this case when the PLL locks the frequency is

$$f_{\text{PLL}} = f_{\text{cent}} + f_{\text{PD}} \quad (2.65)$$

where  $f_{\text{PD}}$  is the frequency produced by the VCO for a voltage equal to the amplified output of the phase detector. In this case the phase difference between the cantilever deflection and the PLL signal is proportional to  $f_{\text{PD}}$  instead of  $f_{\text{PLL}}$  as before.

<sup>9</sup>Such that if the signal was fed into the VCO it would produce a signal with frequency  $f_{\text{cent}}$ .

## Instrumental Techniques

Once the PLL has locked the switch is switched to position b. Now the central frequency is coming from the frequency tracker. The frequency tracker is a device which updates discretely such that the voltage output is set to equal the voltage input. In this case at each iteration ( $n$ ) when the switch is at position b,

$$f_{\text{cent}}^n = f_{\text{cent}}^{n-1} + f_{\text{PD}} = f_{\text{PLL}} \quad (2.66)$$

and then when the PLL next locks using equation (2.65) we find that  $f_{\text{PD}} = 0$  and hence the phase difference between the cantilever deflection and the PLL signal is 0. The frequency tracker is set to update at a slower rate than the time for the PLL to lock so that the PLL has locked before each update. The switch remains at b for the experiment, and the frequency tracker tracks the cantilever frequency, allowing the PLL to constantly produce a signal in phase with the cantilever. This PLL signal is then phase shifted  $90^\circ$  to produce the resonance condition.

The voltage fed into the VCO is proportional to the cantilever's oscillation frequency  $f$ , this is fed into the positive terminal of a differential amplifier, and a voltage proportional to  $f_0$  (which is collected at the start of the experiment) is fed into the negative. The output ( $f - f_0 = \Delta f$ ) this is fed into a PI controller to maintain constant  $\Delta f$  as seen in the self excitation method.

Just as with the self excitation method the RMS amplitude of the cantilever is controlled by a second PI controller. The output of this is recorded as a damping signal, and also multiplied to the phase shifted PLL output used to drive the cantilever.

### Commercial “PLL”-driven FM-AFM design

Some, more recent, commercial FM-AFM, such as the Omicron Matrix controller and the Nanonis controller use a PI controller which varies the excitation frequency to try to maintain a set-point phase of  $90^\circ$ . Such PI controlled systems are referred to as PLLs, however, this is not strictly true as the loop does not *lock* to the input frequency due to the phase relationship, instead the loop *tracks* the phase and hence the resonant frequency. For this reason PLL has been included in quotes for this section title, a more accurate name for such systems would be

## Instrumental Techniques

a phase tracking loop or PTL.

# Chapter 3

## Literature Review

*“Science knows it doesn’t know everything; otherwise, it’d stop.”*

Dara Ó Briain

### Chapter Overview

The central aim of this thesis is a careful consideration of SPM experiments from an instrumental perspective to analyse accuracy and reproducibility. Much of this work, therefore, depends on the theory of the instrumental techniques discussed in the previous chapter. This work, however, as with all science, must be understood in the context of the relevant literature, an overview of which is presented in this chapter.

We start with discussing the materials studied in SPM experiments in this thesis. These are well-studied materials, the work presented does not aim to deepen our understanding of these material, but instead to exploit our understanding of the materials to test the SPM system.

The following sections discuss how AFM sensors have developed since the introduction of the technique and outline methods used to calibrate AFM sensors. This gives a perspective on the importance of the qPlus sensor, studied in detail in this thesis. More fundamentally it provides context for the new sensor design introduced in Chapter 6.

## 3.1 Materials

### 3.1.1 Highly Oriented Pyrolytic Graphite (HOPG)

Early work on automated tip conditioning (Chapter 7) was concentrated on highly oriented pyrolytic graphite (HOPG). HOPG was chosen as it is a surface which can be atomically resolved with the simplest of STM designs. Freshly cleaved HOPG can be imaged with atomic resolution in air for days without contamination or oxidation [48]. HOPG can be cleaved using adhesive tape, to reveal a fresh (0001) surface. This made HOPG ideal for early automation work as time-consuming processes, for example sample preparation, can be kept to a minimum.

The structure of HOPG consists of planes of carbon atoms arranged in a hexagonal lattice. The carbon atoms in the planes are  $sp^2$  hybridised, allowing C–C bonding to three nearest neighbours with bond length of 1.42 Å [49]. The planes are held by van der Waals forces, with a separation of 3.40 Å, and are stacked ABAB to form a crystal. The offset between the A and B planes is one atomic spacing, such that there are two types of atomic site:  $\alpha$ -sites where carbon atoms are present directly above and below in neighbouring layers, and  $\beta$ -sites directly above and below hole sites in adjacent layers. This leads to a primitive unit cell with four carbon atoms, 2  $\alpha$  and 2  $\beta$ .

Despite the simplicity of sample preparation, and the relatively simple surface structure, HOPG does produce some surprising STM results. STM images of the (0001) surface do not regularly produce the hexagonal lattice expected, but instead yield a trigonal lattice with spacing of 2.46 Å [50]. Simple geometry tells us that the lattices of just  $\alpha$  or  $\beta$ -sites are trigonal with spacings of  $2 \sin(60^\circ) \times 1.42 \text{ \AA} = 2.46 \text{ \AA}$ , implying that generally only the  $\alpha$  or  $\beta$ -sites are imaged. Theoretical models using the first integral of equation (2.37)<sup>1</sup>, have predicted that it is the  $\beta$ -sites which are imaged [51]. This result is due to the coupling between  $\alpha$ -states which produce energies further from the Fermi level, pushing many of these states out of the energy window imaged by the STM. However, despite these calculation dating from 1987, the wide variety of possible

---

<sup>1</sup>Assuming a flat LDOS for the tip in the tunnelling energy region

HOPG images and the theory behind them is still not fully explained [50].

Other interesting features in STM of HOPG include giant corrugations of up to 24 Å being measured [52]. The corrugations expected for total charge densities on graphite are 0.2 Å, whereas the corrugations for contours of LDOS is 0.8 Å. Thus the tip will move physically closer to the surface between atomic sites instead of tracking a constant tip-sample separation [53]. This is thought to cause an elastic deformation of the sample as the tip approaches (or retracts) further pushing (pulling) the sample away from its equilibrium position, amplifying the corrugation.

Not only have giant corrugations been imaged in STM but entire giant lattices in STM images with lattice constants of up to 77 Å [54, 55] have been observed. The lattices, commonly referred to as Moiré patterns, are thought to arise from a top layer of the graphite crystal having an angular offset from the bulk lattice orientation. This forms an interference pattern with lattice constant,  $D$ , dependent on the angular offset,  $\theta$ , between the top and second layers of the crystal, and  $d$  the lattice constant of the underlying surface, by [56]

$$D = \frac{d}{2 \sin\left(\frac{\theta}{2}\right)}. \quad (3.1)$$

### 3.1.2 Silicon(111)

Silicon, which dominates the semiconductor industry, is also widely studied in surface science, making it another good test substrate for automated SPM imaging. Silicon is a group IV semiconductor with an indirect band gap of 1.17 eV [17]. It forms  $sp^3$  hybridised orbitals producing crystals of diamond crystal structure and readily oxidises, so any SPM measurements of silicon must be performed in UHV. The most commonly studied silicon surfaces are Si(111) and Si(100). Si(111) was the first semiconductor surface studied by STM. This makes it an ideal benchmark for any automated SPM software.

Silicon cleaved along the (111) plane at room temperature will form a  $2 \times 1$  reconstruction, where the top double layer rearranges to bring chains of the higher and lower atoms together allowing the dangling bonds from the  $1 \times 1$  surface to  $\pi$ -bond chains lowering the surface energy [17]. These chains were first imaged

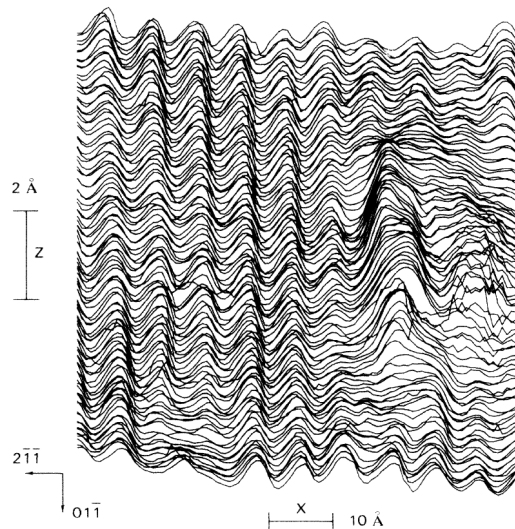


Figure 3.1: *First published STM image of the Si(111)  $2 \times 1$  reconstruction. The left hand side shows the  $\pi$  bonded chains formed in the reconstruction. Reproduced from [56]*

by Feenstra [56] and the first published image is reproduced in Figure 3.1.

However, the Si(111)  $2 \times 1$  reconstruction is only metastable. If the surface is annealed to above  $875^\circ\text{C}$  then the surface will form a stable  $7 \times 7$  reconstruction. This  $7 \times 7$  reconstruction was first discovered by LEED (low energy electron diffraction) experiments in 1959 [58]. No model had successfully been developed to explain the surface reconstruction when it was first imaged in real space in 1983 with STM by Binnig *et. al.* [57], revealing 12 adatoms per unit cell (See Figure 3.2). The same paper put forward a model to explain the images, but the model did not explain why half of the unit cell regularly appears lower in images with positive sample bias [59]. The currently accepted model was introduced in 1984 by Takayanagi [7] by combining these results and other previous data with new TEM and TED (transmission electron microscopy and diffraction) data. The result was the dimer-adatom-stacking-fault (DAS) model.

The DAS model (see Figure 3.3) consists of three dimers along each of the four sides of the unit cell, each half enclosed by the cell. Three more dimers are positioned along the short diagonal of the cell, marking the boundary of a partial stacking fault. This gives a total of nine dimers per unit cell, and a faulted and unfaulted half to each cell. The dimers form in the bottom half of the surface

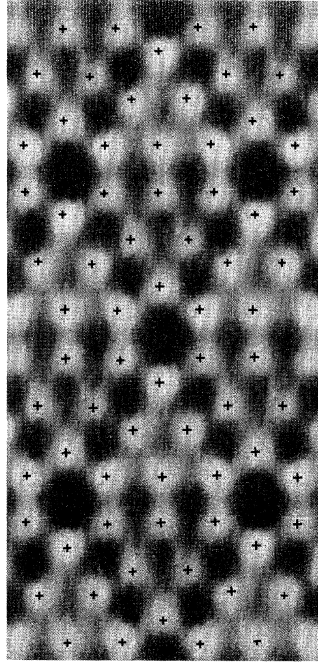


Figure 3.2: *First published STM imaged of the Si(111)  $7 \times 7$  reconstruction. The crosses indicate the position of the adatoms. Reproduced from [57]*

double layer of the crystal. Considering the edge of the unit cell in this layer the four remaining silicon atoms, each quarter enclosed by the corner of the cell, are lost revealing a dangling bond at the bottom of hole (referred to as a corner hole). Finally, twelve silicon adatoms adsorb to the surface, each bonding with three underlying atoms from the top half of the surface double layer. The final surface has 19 dangling bonds per unit cell: one on each of the 12 adatoms; one in each of the four corner holes, quarter enclosed by the unit cell; and 6 on the rest atoms, the atoms in the top half of the surface double layer which did not bond to an adatom.

Si(111)  $7 \times 7$  has also been an important surface for AFM. The first atomic resolution AFM image of the surface was produced by Giessibl in 1994 [60]. The  $7 \times 7$  surface was also used by Giessibl to demonstrate the abilities of the newly developed qPlus force sensor [61], and to produce the first AFM images with subatomic features [13] (see Figure 3.4). The subatomic features consisted of two crescents being imaged for each of the 12 adatoms. The distance between these features was too small ( $2.2 \text{ \AA}$ ) to be explained by a standard double tip

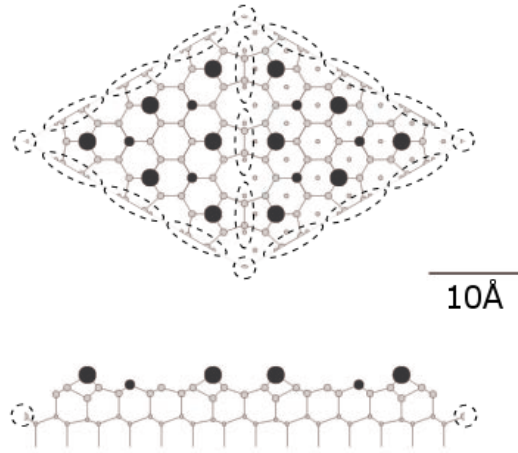


Figure 3.3: *Schematic of the DAS model of the Si(111)  $7 \times 7$  reconstruction. Where the large black dots are adatoms, the smaller black dots are rest atoms, the dotted circles enclose four different quarters of a corner hole, and the dotted ellipses enclose dimers, 12 of which are only half inside the unit cell. Adapted from [13]*

as the nearest neighbour distance in tungsten (the tip material) is  $3.16 \text{ \AA}$ , and as defects do not get repeated across the image this rules out the possibility of a double tip with a spacing of an integer number of silicon lattice vectors plus  $2.2 \text{ \AA}$ . The interpretation of these images is that the tip has picked up a cluster of silicon and the final atom is  $sp^3$  hybridised with two dangling bond, each of which acts as a ‘subatomic’ mini-tip forming chemical bonds with the dangling bond of the surface adatom.

### 3.1.3 $C_{60}$

A great number SPM studies of molecules adsorbed on surfaces have been performed, showing bonding geometries of individual molecules [62], the formation of molecular tilings [63], and the synthesis of covalently bonded networks [64], to mention just a few results. One of the molecules most studied in SPM is buckminsterfullerene ( $C_{60}$ ), a molecule consisting of a spherical cage of sixty carbon atoms [65] (Figure 3.5). Due to the spherically symmetric shape of  $C_{60}$ , it is used in this thesis to detect asymmetries of the tip motion in AFM studies (Chap-

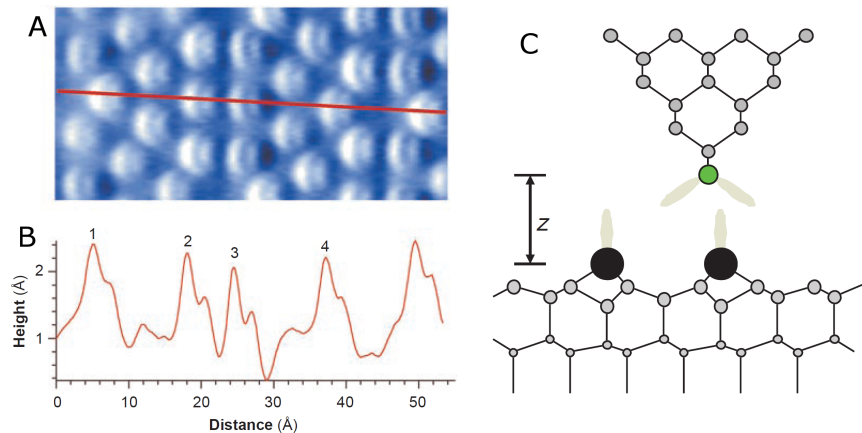


Figure 3.4: *Subatomic features in AFM image of Si(111)  $7 \times 7$  reconstruction. (A) AFM image, (B) line profile through (A), (C) schematic of proposed model to explain image. Adapted from [13]*

ter 5). For these experiments performed on the Si (111)  $7 \times 7$  reconstruction, the bonding geometry and stability of  $C_{60}$  adsorbed on silicon is of particular interest, as is the  $C_{60}$ - $C_{60}$  potential.

Individual  $C_{60}$  molecules were first imaged in STM on Si (100) [68] and S(111) [69] in 1992, just seven years after their discovery [65]. Subsequent studies showed island and monolayer growth of  $C_{60}$  on silicon [70, 71]. In 1995 Chen *et al.* showed that annealing  $C_{60}$  on Si(100) causes movement of the adsorption site from between dimer rows to on top of the rows [72]. Combining these measurements with theory it was suggested that before annealing the  $C_{60}$  is only physisorbed onto the silicon surface, and chemisorption happens after annealing. Three years later Moriarty *et al.* combined photoemission spectroscopy measurements with manipulations of  $C_{60}$  on Si (100) to show that the interaction was actually chemisorption, however the bond strength does increase for sites on top of the dimer rows [73]. This work furthered earlier work by the same group from 1995 which demonstrated the first controlled SPM manipulation at room temperature, by moving  $C_{60}$  on Si (111) [74]. One interesting difference in the later work on Si (100) was the ability to entirely remove  $C_{60}$  from the surface, transferring the molecule to the tip which improved image resolution. Further photoemission spectroscopy from Moriarty *et al.* in 1998 suggested that all  $C_{60}$ -

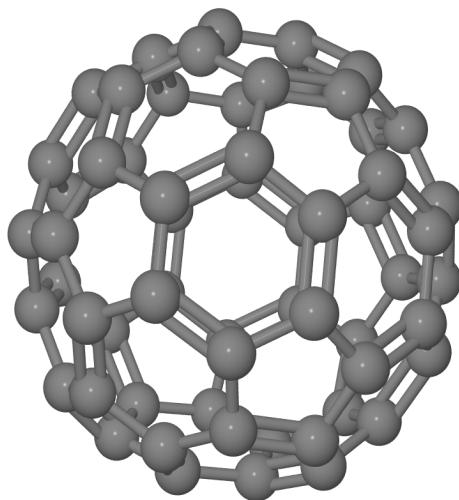


Figure 3.5: A rendering of a  $C_{60}$  molecule from Jmol [66] rendered in POV-Ray [67]

Si interactions were always chemisorbed for both Si (111) and Si (100) [75]. Two papers by Sakamoto *et al.* in the same and following year suggested otherwise [76, 77], with physisorbed  $C_{60}$  on Si (111) for coverages close to a monolayer measured with photoemission spectroscopy. In 2000, Pesci explained Sakamoto *et al.*'s results as arising from miscalibration of the surface coverage with physisorbed states resulting from coverages above one monolayer [78]. Following studies have confirmed these results [79, 80].

Due to the difficulties of imaging silicon in AFM, described in the previous section,  $C_{60}$  on silicon was not successfully imaged with AFM until 1999 [82]. Later theoretical AFM studies suggested that it should be possible to image orientation of  $C_{60}$  on silicon with a silicon terminated tip [83], and even perform thermally driven manipulation of  $C_{60}$  mediated by the AFM tip [84]. The precise orientation of  $C_{60}$  on a surface was first demonstrated on copper rather than silicon by STM imaging [85]. This work was extended to AFM where not only the orientation of the  $C_{60}$  was measured, but also the bond order [86]. Further investigations of  $C_{60}$  on Cu with a Cu tip via grid spectroscopy show clear asymmetry in the  $C_{60}$  molecule [81] (See Figure 3.6). The cause of this asymmetry is

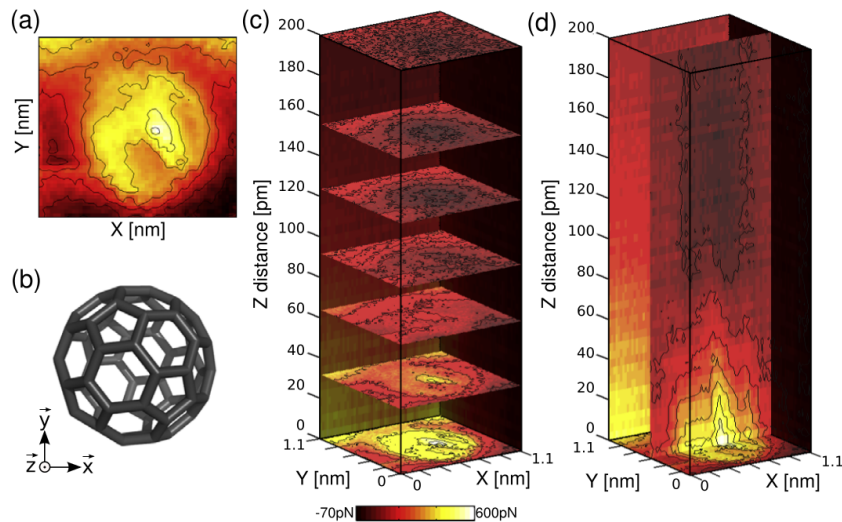


Figure 3.6: *Grid spectroscopy measurements of  $C_{60}$  with a Cu tip. The clear asymmetry in the  $C_{60}$  could be a result of asymmetry of the Cu tip apex. From [81]*

not discussed. However, as the precise structure of the Cu-terminated tip is not known this result could simply be a result of tip asymmetry.

In 2012 the theoretically predicted imaging of the precise orientation of  $C_{60}$  with silicon tip was demonstrated in a novel way. Chiutu *et al.* used  $C_{60}$  terminated tips to image the Si (111)  $7 \times 7$  reconstruction [12]. Due to the large adatom spacing and narrow spatial extent of the dangling bond orbitals, the individual atoms of the closest face of the  $C_{60}$  are clearly resolved (See Figure 3.7). With the precise orientation of the tip apex known, force spectroscopy measurements were performed on both the bare Si substrate to reliably calculate the interaction between a known orientation of  $C_{60}$  on a specific Si site. Further force spectroscopy measurements directly probed the  $C_{60}$ – $C_{60}$  interaction, showing excellent agreement with the analytical Girifalco potential [87]. Similar agreement to the Girifalco potential had previously been achieved using density functional theory studies [88]. Further experiments on  $C_{60}$  on Si (111) with  $C_{60}$  terminated tips in STM showed that by combining the known orientation of the molecule on the tip with theoretical STM images of the  $C_{60}$ – $C_{60}$  interaction [89, 90] the orientation of the surface molecule could also be determined [91].

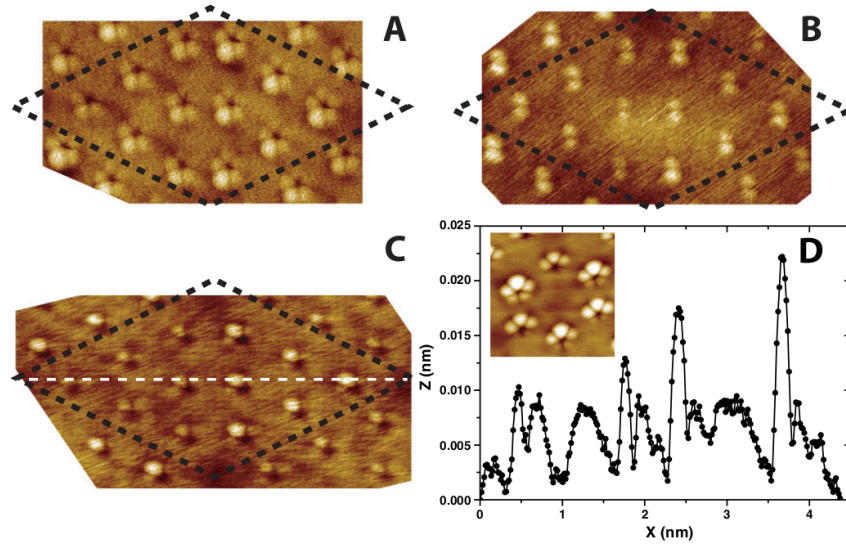


Figure 3.7: *Faces of a  $C_{60}$  molecule imaged on the adatoms of the Si (111)  $7 \times 7$  reconstruction. From [12]*

## 3.2 The Evolution of AFM Sensors

The heart of an AFM is its sensor, used to measure atomic forces. Three features are key to an AFM sensor: how forces affect the sensor's motion, how its deflection is measured, and (in the case of dynamic AFM) how the sensor is excited. The spring constant of the sensor controls how strongly forces affect the sensor's deflection. Calibration of spring constants is therefore a high priority for accurate force measurements. In dynamic AFM the sensor is oscillating and thus properties such as the resonant frequency and the Q of the sensor are important for understanding the sensor's dynamics.

The first AFM sensor, designed by Binnig *et al.* in 1986 [92], consisted of a diamond tip attached to a cantilever made from gold foil (with dimensions of  $800 \mu\text{m} \times 250 \mu\text{m} \times 25 \mu\text{m}$ ). This sensor used an STM to measure the deflection of the cantilever. The sensor was operated both in static and dynamic modes. Dynamic modes were mechanically excited with a separate piezoelectric actuator. The resonant frequency of the sensor is not given in Reference [92]. For the bare (tipless) cantilever, however, this can be estimated as  $\sim 13$  kHz using the dimensions, density, and Young's modulus [93] of the gold cantilever. The resonant frequency of the final sensor depends on the size of the diamond tip attached

## Literature Review

(also not given) and thus we can conclude only that the resonant frequency was less than (possibly much less, if the tip mass was significant compared to the cantilever mass) 13 kHz. The spring constant can also be estimated to be  $\sim 150 \text{ N.m}^{-1}$ .

As AFM experiments developed, so did the designs of the sensors. Early AFM experiments generally operated in a static mode. As such, the resonance characteristics (i.e. resonant frequency and  $Q$ ) were not considered as important as the spring constant of the sensor. Just one year after the seminal AFM paper, a considerably different AFM was built by Mate *et al.* [3]. It used etched tungsten wires, bent near the apex, to produce a sensor with an integrated tip. As this wire was conductive, STM measurements were possible with the same microscope. This AFM detected lateral deflection of the wire, thus introducing lateral force microscopy (LFM). The deflections were detected optically with an interferometer (see [94] for more detail), removing the need for a complicated second feedback loop and piezoelectric actuator needed for the tunnelling detection.

Optical detection was further simplified in 1988 when Meyer and Nabil introduced the optical lever technique [95]. This technique requires a surface on the rear of the sensor from which a laser can be reflected. The laser light is then collected by a position-sensitive detector. From the position of the deflected laser spot the angle of the sensor can be detected. This method, widely used in AFM, is dependent on the position of the laser spot, and is an indirect measure of the deflection. This must be considered carefully if using the deflection signal for quantitative measurements [96].

The same year, Albrecht *et al.* [97] produced silicon dioxide microcantilevers specifically designed for use in AFM. Both rectangular and V-shape cantilevers were produced and compared. Initially these were produced without tips. In fact some experiments were attempted with tip-free microcantilevers. Tips could then be attached with either glue or evaporated onto the cantilever through a small hole.

Günther *et al.* [98] developed a variant of the AFM, the scanning near-field acoustic microscope, in 1999. This measures forces due to gas coupling between a sensor oscillating on resonance and the sample. Despite not being a true AFM it introduced new concepts to scanning probe microscopy. Most notably it used

## Literature Review

quartz tuning forks from watches as its sensors, as these are inexpensive, mass produced resonators with a very high  $Q$ . They also do not require any external deflection detection (except a simple electronic amplifier) as quartz is piezoelectric and the tuning forks are produced with gold contacts for this purpose. Another advantage of the quartz tuning fork sensors was that their resonance can be excited electrically, removing the need for extra piezoelectric actuators for mechanical excitation signals.

Deflection detection methods continued to develop. In 1990 Göddenhenrich *et al.* [99] introduced capacitive detection. The capacitor consisted of a plate attached to the rear of the sensor and a second adjustable plate behind this. Capacitive detection allowed for deflection measurements with sub-Ångstrom precision without the difficulties inherent in optical detection.

In the early 1990s silicon microcantilevers (SMCs) quickly developed, eventually becoming the standard method of AFM sensing. In 1990 SMCs with integrated sharp tips were produced, removing the difficult process of tip attachment [100, 101] (Figure 3.8(a)). In the same year SMCs were used to combine AFM and LFM with both torsional and normal bending of the cantilever being measured [102]. Modified SMCs produced by Tortonese *et al.* [103] utilised the piezoresistive effect in silicon to produce cantilevers which detected deflection from a change in resistance (Figure 3.8(b)). The cantilever can be included as part of a Wheatstone bridge [104] to allow accurate detection of resistance changes. Due to the conductivity of piezoresistive SMCs they could also be used as STM sensors [105]. SMCs with integrated capacitive sensing [106] were also fabricated, adding to the choice of detection methods easily available for the SMC.

SMCs were used to make the first true atomic resolution AFM image [107] and the first true atomic image of a reactive (silicon) surface, in 1992 with a STM detected SMC and 1995 [60] with a piezoresistive SMC respectively.

As dynamic AFM in liquid became more popular a more direct way of exciting the cantilever was required to produce well behaved resonances. In 1994, Florin *et al.* [108] attached magnets to SMCs and directly excited the cantilever using an electromagnet located below the sample. Four years later a more elegant solution for direct cantilever excitation was developed by Ratcliff *et al.* [109] using a laser

## Literature Review

to photothermally excite SMCs with reflective coatings, already readily available for optical detection.

When dynamic modes of lateral force microscopy were introduced [110, 111], originally the sample was oscillated rather than the sensors. Soon development of sensors which could easily be excited with resonance motion parallel to the surfaces began. Jarvis *et al.* [112] introduced a specialised cantilever which consisted of two rectangular SMCs with a third microcantilever attached between them by a hinge (See Figure 3.8(c)). This third cantilever had a tip located between the hinges, and a magnet for magnetic excitation on the far end. Due to the tip location any excitation about the hinges caused lateral motion of the tip apex. The two support SMCs could also be excited to allow both normal and lateral measurements to be made simultaneously [113]. Pfeiffer *et al.* also achieved laterally excited sensors by exciting the torsional mode of standard rectangular SMCs, removing the requirement for specialist sensors. Indeed, the Q factor of torsional modes is much higher than for normal modes. This led to the development of T-shaped cantilevers with the tip located on the far arm of the T [114]. If driven torsionally these produce vertical tip oscillation, allowing the benefits of the torsional mode to be used in conventional AFM [115].

While SMCs became the standard AFM sensors in the early 1990s, development of piezoelectric sensors continued. In 1993, Bartzke *et al.* introduced the first piezoelectric sensors for conventional AFM, using a commercially available quartz oscillator, with a micro-tip deposited by chemical vapour deposition. The quartz oscillator was a length extensional resonator (LER), with a first resonance of 1 MHz and an effective stiffness of  $\sim 1 \text{ MN.m}^{-1}$  [116] (Figure 3.8(d)). Edwards *et al.* [117] reintroduced the quartz tuning fork sensor in 1997, but by attaching a small etched tungsten wire to one tine of the tuning fork, a sensor with a well defined tip was produced. This added mass, however, removes the symmetry of the tuning fork. The two tines with different resonant frequencies can no longer share their energy so efficiently, and as a result the Q factor drops.

A year after Edwards *et al.* introduced the tuning fork AFM with attached tip, Giessibl improved on the design by attaching the second tine of the tuning fork to the substrate on which the sensor was mounted [118] (Figure 3.8(e)). This effectively transforms the sensor into a quartz cantilever. While cantilevers do not

have Q factors which are as high as an ideal tuning fork, this was a great benefit over the unbalanced tuning fork, leading to this sensor being named the ‘qPlus’ sensor. qPlus sensors took just two years to show true atomic resolution [61].

Hyde *et al.*, 2004 [120], combined two tuning forks, in the qPlus configuration, at 90 degrees to each other, with a tip in the centre to produce V-shaped quartz cantilevers to limit other vibrational modes possible with the qPlus sensor (Figure 3.8(g)). The following year this sensor achieved true atomic resolution [121], as did the LER sensor [119] after a 12 year wait. Improvements to the LER and its amplifier have been commercialised as the KolibriSensor<sup>®</sup> [122]. The qPlus and Kolibri sensor have been compared in detail in [116].

Quartz sensors have also been used for lateral force microscopy, with the first true atomic resolution mapping of friction achieved with a qPlus sensor in a lateral configuration [8] (Figure 3.8(e)). Another interesting design for a quartz LFM sensor was introduced by Mühlshlege in 2006 [123]. This consisted of a sharp fiber probe normal to the surface held under tension against the side of a tuning fork. Tuning fork oscillations then drive the needle laterally. The lack of glued components allows tuning of the Q factor by changing the tension.

### 3.3 AFM Sensor Calibration

As previously mentioned, the spring constant of AFM sensors must be known to obtain quantitative data from an AFM. For simple rectangular cantilevers this can be easily derived from the Euler-Bernoulli beam equation. However, this requires a variety of assumptions:

- The dimensions of the cantilever are known accurately and the beams cross section is constant along the entire length.
- The beam is homogeneous and has a well defined Young’s modulus.
- The boundary conditions are perfect, both at the clamped and the free end.

AFM sensors, however, cannot just be simply treated as a rectangular cantilever. Metallic coatings for optical, capacitive or piezoelectric sensing affect

Literature Review

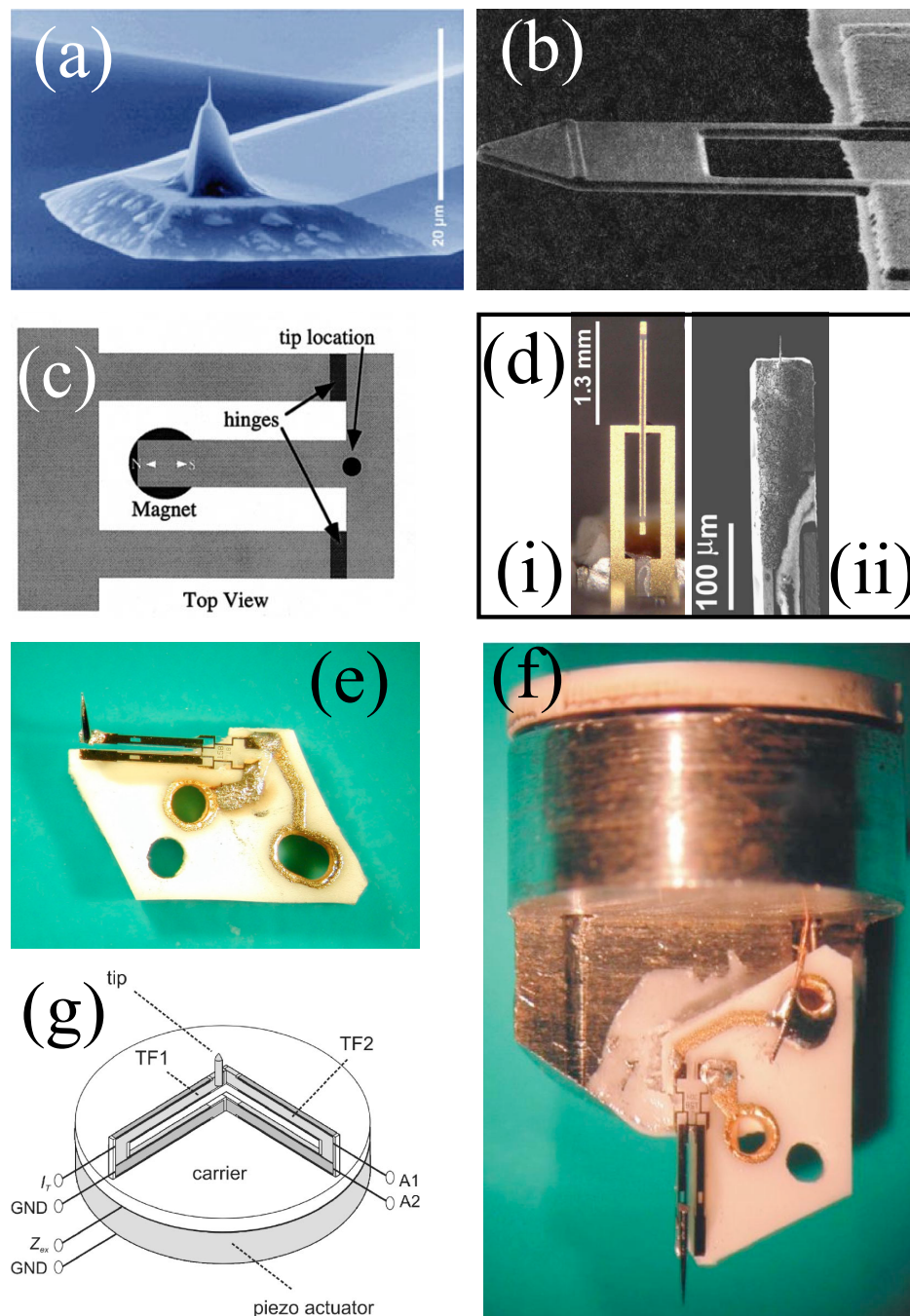


Figure 3.8: A range of AFM sensors. (a) A silicon microcantilever with integrated tip. (b) A piezoresistive cantilever. (c) A sensor specially designed for dynamic lateral force microscopy. (d)(i) A length extensional resonator (ii) and its integrated tip. (e) and (f) The qPlus sensor in conventional and lateral configurations. (g) A double tuning fork sensor. (Images (a),(b),(e) and (f) are reproduced from [2]; (c) from [113]; (d) from [119]; and (g) from [120])

the homogeneity and Young's modulus of the beam. The added mass of the tip also modifies the cross section near the free end of the cantilever. Other factors such as the accuracy of machining and the mounting of the sensor can affect the boundary conditions. For these reasons, for reliable force measurements the cantilever spring constant, wherever possible, should be measured rather than calculated.

Direct measurements of spring constants, however, are not always practical. Thus methods for calculating spring constants for sensors of other geometries have been introduced [124]. Both analytical [124,125] and finite element analysis [126] have been used to calculate other modes of sensors such as torsional modes not arising from a simple Euler-Bernoulli model.

Three methods of calibration are commonly used: the Cleveland method [127], thermal tuning [128], and the Sader method [129,130]. These are described below in detail, along with variants of the methods. Comparisons, corrections, and less commonly used methods are also discussed.

### 3.3.1 Cleveland Method

An ideal cantilever acts as a simple harmonic oscillator. Solving the boundary conditions for an ideal cantilever to give a natural frequency and a spring constant, however, does not agree with the resonances expected by Hooke's law ( $\omega_0^2 = \frac{k}{m}$ , where,  $m$  is the oscillating mass). This results from the fact that most of the cantilevers mass is not moving the full amplitude of oscillation. In the first eigenmode, however, the equations can be balanced using an effective mass of  $m_{\text{eff}}$  (See Appendix A.4.5) giving,

$$k = m_{\text{eff}}\omega_0^2. \quad (3.2)$$

Any mass,  $\Delta m$  added to the end of the cantilever, however, must be treated in full. Therefore, by adding masses to the cantilever the change in resonant frequency allows the spring constant,  $k$ , to be calculated as

$$k = \Delta m \frac{1}{(1/\omega_m^2) - (1/\omega_0^2)}, \quad (3.3)$$

where  $\omega_m$  is the resonant frequency of the loaded cantilever. Cleveland *et al.* [127] used this equation to calibrate cantilever spring constants by adding tungsten micro-spheres of varying size to the end of a cantilever and comparing the resonances to the unloaded resonance.

Variations of the Cleveland method have been implemented. Golovko *et al.* [131], repeated the Cleveland method using micro-droplets of water from a piezoelectric droplet generator. These droplets can be finely controlled, positioned accurately, and easily removed by evaporation. Shaw *et al.* [132] modified the method for qPlus cantilevers by electrochemically etching the tungsten tip to reduce the mass. Although the bare resonant frequency was left unknown, the spring constant can be measured simply from the gradient of a  $\omega_m^{-2}$  vs.  $\Delta m$  plot.

### 3.3.2 Thermal Tuning

From the equipartition theorem the average vibrational elastic potential energy of the sensors is equal to  $\frac{1}{2}k_B T$ . Combining with Hooke's law gives

$$\frac{1}{2}k\langle z^2 \rangle = \frac{1}{2}k_B T, \quad (3.4)$$

where  $\langle z^2 \rangle$  is the average deflection at the end of the cantilever. Hence, by simply measuring the average deflection and the temperature of the sensor in thermal equilibrium the spring constant can be calculated as

$$k = \frac{k_B T}{\langle z^2 \rangle}. \quad (3.5)$$

Butt and Jaschke [96] provided a more rigorous derivation to show that the mean deflection must include contributions from all modes of the cantilever to produce the static spring constant, or simply the deflection for one particular eigenmode to get the dynamic spring constant for that mode of oscillation. Stark *et al.* [133] used finite element analysis to analyse the thermal noise of a V-shaped cantilever as their extra modes complicate thermal tuning. A more detailed discussion of dynamic versus static spring constants was provided by Melcher *et al.* [134]. For rectangular cantilevers the error is  $\sim 3\%$ .

### 3.3.3 Sader Method

The Sader method [129] differs from thermal tuning and the Cleveland method as it requires finite element analysis to solve the Euler-Bernoulli equation for the beams normalised dimensions, to give the effective mass. This can then be used in Equation (3.2). Sader *et al.* [129] also provide corrections for tips not placed at the far end of the cantilever, gold coatings, and air damping.

This method was simplified for rectangular cantilevers by Sader *et al.* [130], for use in a range of fluids into a final equation depending on the density of the fluid ( $\rho_f$ ), the beam's width ( $b$ ) and length ( $L$ ), the Q factor of the beam in the fluid ( $Q_f$ ) and the resonant frequency of the beam in the fluid ( $\omega_f$ ):

$$k = 0.1906\rho_f b^2 L Q_f \Gamma_i(\omega_f) \omega_f, \quad (3.6)$$

where  $\Gamma_i(\omega_f)$  is the imaginary part of the cantilever's hydrodynamic function. The hydrodynamic function relates to the frequency dependent loading force of the cantilever due to the fluid, a detailed discussion of which is given in Reference [135].

### 3.3.4 Other Methods of Calibration

#### 3.3.4.1 Indentation

A more direct method for measuring spring constants it to use an indenter which loads the cantilever by applying a known force with a diamond stylus, and measures the deflection [132]. Theoretically the gradient of a displacement vs. force plot should give the spring constant. In practice, however, other factors must be considered, including the exact position of the loading, the angle between the cantilever and the loading force, the machine compliance of the indenter, and the contact compliance of the contact. This contact compliance is a factor of the maximum force applied, the indentation hardness of the cantilever's surface, both the Poisson ratio and the Young's modulus of the cantilever's surface material and diamond. The specialist equipment needed and the difficulties of calibrating the indenter limit its use for AFM calibration.

### 3.3.4.2 Reference Cantilever

Another direct method for measuring spring constants for AFM sensors is to use a reference cantilever of known spring constant [136]. This requires purchasing a cantilever with a well known spring constant which will have been measured using one of the above methods. These are available from national standards agencies such as NIST or NPL. The calibration procedure involves comparing the static deflection of the AFM cantilever when pressed against a stiff surface and the static deflection when pressed against the reference cantilever.

### 3.3.4.3 Tip Mass and Resonant Frequencies

Another method is to modify the boundary conditions of the Euler-Bernoulli beam equation such that the free end feels the inertial force of the tip mass. This has been studied in detail [137, 138], with two main effects. The dynamic spring constant of the first mode tends towards the static spring constant for increased tip mass, and the frequency ratios of the eigenmodes shift depending on the ratio of tip mass to cantilever mass ( $m^*$ ).

Lübbe *et al.* [139] used this effect to calibrate sensors, by measuring the frequencies of the first and second mode, and the dimensions of the tip. From the dimensions they estimated the tip mass, and from the ratio of the first and second eigenfrequencies they were able to determine  $m^*$ . Combining  $m^*$  with the tip mass gives the cantilever mass ( $m$ ). The ratio of the eigenfrequencies also gives a theoretical unique value for  $\beta_1 L$ , the characteristic length of the first eigenmode (See Appendix A.6). These are then combined with an equation from elementary beam dynamics:

$$k = \frac{3\omega_1^2 m}{(\beta_1 L)^4} \quad (3.7)$$

to give the spring constant.

Drawbacks to this method are that it requires an SEM to approximate the tip dimensions assuming perfect geometries which are far from accurate. It also assumes a constant profile of the beam, that the tip has no moment of inertia and is located directly on the cantilever's end (affecting the boundary conditions at the free end), and that the boundary conditions at the fixed end are that of a

perfect clamp. These assumptions are made by other methods too, however, due to the repeated dependence of deriving one value from another through theory these errors are difficult to quantify, especially as the relationships between the eigenmodes' properties are numerically derived and highly sensitive to boundary conditions. For example, Tung *et al.* [140] show very extreme changes in resonant frequencies of higher modes resulting from the moment of inertia of the tip.

### 3.3.5 Comparisons

Lévy and Maaloum [141], Cook *et al.* [142] and Ohler [143] compare thermal tuning and the Sader method showing good agreement for rectangular cantilevers. These values, however, differed significantly from the values quoted by the manufacturers. These inconsistencies varied significantly for 'identical' cantilevers produced on the same wafer. This highlights the need to calibrate individual sensors. Lévy and Maaloum [141] also used V-shaped cantilevers. These showed poor agreement between thermal tuning and the Sader method. This was attributed to the Sader method's assumption that the beam is of uniform thickness.

The Sader method and the Cleveland method were compared and shown to agree in Sader's original paper introducing the method [129]. This agreement was tested for both V-shaped and rectangular cantilevers.

## Chapter 4

# Calculation of the Effect of Tip Geometry on ncAFM Measurements with a qPlus Sensor

*“Several things are wrong here. The phrase “a moment after starting” is entirely superfluous, for Newton’s law applies just as well a moment before starting, or an hour after starting.”*

George A. Lindsay [144]

### Chapter Overview

In the first experimental chapter of this thesis we consider the sensors used in qPlus AFM. qPlus measurements use the same calibration procedures as other AFM measurements, these procedures generally being derived from treating the sensor as free cantilever. Taking a moment to consider geometry of the qPlus sensor (see Figure 3.8(e) on page 54), the tip size is no longer negligible. This chapter investigates the effect of this tip geometry on measurements with a qPlus sensor. This chapter was published in a slightly modified form in the Beilstein Journal of Nanotechnology [145].

## 4.1 Introduction

From imaging of individual chemical bonds [35] to subatomic imaging of the tip apex [13], many experiments have demonstrated the ability of qPlus atomic force microscopy (AFM) to produce unprecedented resolution. Other qPlus studies have measured both the forces necessary to perform atomic precision manipulations [33, 146, 147], and the strength of both atomic and molecular interactions [12, 148]. As with all forms of AFM, image resolution and force measurements ultimately depend on the structure of the last few Ångströms of the tip apex [2, 12, 13, 35, 146, 148, 149]. In the case of the qPlus sensor [61], however, the tip's macroscopic geometry cannot be ignored [140]. This is because in many cases the length of the tip is comparable to that of the tuning fork tine which forms the sensor.

An accurate value of the spring constant of the sensor is vital for any conversion from raw data to meaningful force measurements [29]. Despite the oft-quoted piconewton accuracy of qPlus measurements [33], the spring constant is often left unmeasured and is assumed to be  $k \approx 1800 \text{ N.m}^{-1}$  from the geometry of the bare tine [61]. Other measurements of the spring constants of qPlus sensors have produced conflicting results [132, 146], which highlights the need for more detailed analysis. Tung *et al.* [140] have shown that the dimensions of conical tips have large effects on the higher eigenmodes, suggesting careful consideration of tip geometry is necessary for sensors operated in the the second eigenmode or above.

Modelling the tine of the qPlus sensor as an Euler-Bernoulli beam [150] of length  $L$ , we can write

$$EI \frac{\partial^4 Z(x, t)}{\partial x^4} = f(x, t) - \rho A \frac{\partial^2 Z(x, t)}{\partial t^2}, \quad (4.1)$$

where  $E$ ,  $I$ ,  $\rho$ , and  $A$  are the Young's modulus, second moment of area, density, and cross sectional area of the tine respectively.  $f(x, t)$  is the external force per unit length acting on the tine, and  $Z(x, t)$  is the deflection along the length of the tine. Separating the spatial ( $\Phi_i(x)$ ) and temporal ( $\mathcal{T}_i(t)$ ) components of the

## Calculation of the Effect of Tip Geometry

deflection for all eigenmodes,  $i$ , we can write

$$Z(x, t) = \sum_{i=1}^{\infty} \Phi_i(x) \mathcal{T}_i(t), \quad (4.2)$$

where

$$\mathcal{T}_i = C_i \sin(\omega_i t + \delta_i). \quad (4.3)$$

As Equation 4.1 is fourth-order spatially we get the following general spatial solution:

$$\Phi_i(x) = b_1 \cos(\beta_i x) + b_2 \sin(\beta_i x) + b_3 \cosh(\beta_i x) + b_4 \sinh(\beta_i x) \quad (4.4)$$

where  $\beta_i$  is the spatial frequency of the  $i$ th mode governed by

$$\beta_i^4 = \frac{\rho A \omega_i^2}{EI}. \quad (4.5)$$

The tip connected to the tine, with mass  $m_{\text{tip}}$  and moment of inertia about the tip's point of rotation  $\mathcal{I}_{\text{tip}}$  (A stylised  $\mathcal{I}$  is used to differentiate between moments of inertia and moments of area  $I$ .), will produce a resulting force of  $m_{\text{tip}} \frac{\partial^2 Z(L, t)}{\partial t^2}$  and torque of  $-\mathcal{I}_{\text{tip}} \frac{\partial^3 Z(L, t)}{\partial x \partial t^2}$ . Thus, we can write the spatial boundary conditions as:

$$\Phi_i(0) = 0 \quad (4.6)$$

$$\frac{\partial \Phi_i(0)}{\partial x} = 0 \quad (4.7)$$

$$EI \frac{\partial^2 \Phi_i(L)}{\partial x^2} = \mathcal{I}_{\text{tip}} \omega_i^2 \frac{\partial \Phi_i(L)}{\partial x} \quad (4.8)$$

$$EI \frac{\partial^3 \Phi_i(L)}{\partial x^3} = -m_{\text{tip}} \omega_i^2 \Phi_i(L) \quad (4.9)$$

as the tine is fixed at  $x = 0$ . Under the assumption of uniform tip density we can write  $\mathcal{I}_{\text{tip}} = J m_{\text{tip}}$ , where  $J$  is a constant with units of length squared. The very small effect of the motion, normal to the tine, of the tip's center of mass due to the tip rotation has been ignored as this significantly increases the complexity of the problem for a negligible component of the motion unless the the tip's width becomes significant compared to its entire length, including the portion attached

## Calculation of the Effect of Tip Geometry

to the end of the tine.

From Equations B.1 and B.2, presented in Appendix B.1, the conditions  $b_1 = -b_3$  and  $b_2 = -b_4$  are apparent, and the ratio of  $b_1$  to  $b_2$  can be found from Equation B.3. From this ratio we get the analytical form of the spatial solution to be

$$\begin{aligned} \Phi_i(x) = & \left( \sin(\beta_i L) + \sinh(\beta_i L) - \frac{J\beta_i^2}{\gamma_i} (-\cos(\beta_i L) + \cosh(\beta_i L)) \right) \\ & \times (\cos(\beta_i x) - \cosh(\beta_i x)) \\ & - \left( \cos(\beta_i L) + \cosh(\beta_i L) - \frac{J\beta_i^2}{\gamma_i} (\sin(\beta_i L) + \sinh(\beta_i L)) \right) \\ & \times (\sin(\beta_i x) - \sinh(\beta_i x)) \end{aligned} \quad (4.10)$$

where  $\gamma_i$  is defined in equation B.5.

## 4.2 Effects on dynamic properties

As shown by Butt and Jaschke [96], properties of a cantilever (or tine) such as the dynamic spring constants and the proportion of energy in each eigenmode at thermal equilibrium can be found by considering the elastic potential energy of the tine. This becomes particularly important if calibration is done by thermal tuning, or if force measurements are done at higher modes [140]. The elastic potential energy of the tine is given by

$$W = \frac{EI}{2} \int_0^L \left( \frac{\partial^2 Z(x, t)}{\partial x^2} \right)^2 dx. \quad (4.11)$$

Again, separating into spatial and temporal components gives

$$W = \frac{EI}{2} \int_0^L \sum_{i=1}^{\infty} \left( \mathcal{T}_i^2(t) \frac{\partial^2 \Phi_i(x)}{\partial x^2} \right)^2 dx. \quad (4.12)$$

In Appendix B.2, we show that, just as for bare cantilevers [96], this reduces to

$$W = \frac{EI}{2} \sum_{i=1}^{\infty} \mathcal{T}_i^2(t) \int_0^L \left( \frac{\partial^2 \Phi_i(x)}{\partial x^2} \right)^2 dx. \quad (4.13)$$

## Calculation of the Effect of Tip Geometry

For brevity we define  $\Lambda_i = \int_0^L \left( \frac{\partial^2 \Phi_i(x)}{\partial x^2} \right)^2 dx$ . This allows us to write the average elastic potential energy for each eigenmode as

$$\langle W_i \rangle = \frac{EI}{2} \langle \mathcal{T}_i^2(t) \rangle \Lambda_i. \quad (4.14)$$

In thermal equilibrium, the equipartition theorem requires that  $\langle W_i \rangle = \frac{1}{2} k_B T$ . But, as  $\langle Z_i^2(L, t) \rangle = \langle \mathcal{T}_i^2(t) \rangle \Phi_i^2(L)$ , and including the static spring constant from Euler-Bernoulli beam theory,  $k_{\text{stat}} = 3EI/L^3$ , we get the mean square deflection of each mode in thermal equilibrium to be

$$\langle Z_i^2(L, t) \rangle = \frac{3k_B T \Phi_i^2(L)}{L^3 k_{\text{stat}} \Lambda_i}. \quad (4.15)$$

The full analytical form of  $L^3 \Lambda_i / \Phi_i^2(L)$  is derived in Appendix B.3 . Combined with solutions for Equation B.7, this could be used to measure the static spring constant of a qPlus sensor with a well defined tip geometry, by thermal tuning. However, thermal tuning of qPlus sensors with spring constants of order 2 kN.m<sup>-1</sup> remains a challenging experimental task as the rms amplitude of thermal excitation at 300 K is  $\sim 1.4$  pm.

For well calibrated force measurements, the dynamic spring constant for the excited eigenmode  $k_i$  must be calculated. By considering the equipartition theorem again, but with the dynamic spring constant and Hooke's law:  $\frac{1}{2} k_B T = \frac{1}{2} \langle Z_i^2(L, t) \rangle k_i$ . Combining with Equation 4.15 gives

$$\frac{k_i}{k_{\text{stat}}} = \frac{L^3 \Lambda_i}{3 \Phi_i^2(L)}. \quad (4.16)$$

Thus, as with the thermal tuning, and with the results given in Appendix B.3 , the dynamic spring constant for any eigenmode can be calculated, provided the tip geometry is well-defined and the static spring constant is known.

The tine of a qPlus sensor was modeled as a quartz beam of length  $L = 2.4$  mm, width  $w = 130$   $\mu\text{m}$ , and thickness  $t_{\text{TF}} = 214$   $\mu\text{m}$  (Figure 4.1(a)). The tip was modeled as a tungsten cylinder of diameter  $D_{\text{tip}}$  attached to the end of the tine of the tuning fork. The tip protrudes  $H$  from the tine giving the tip a total length of  $H + t_{\text{TF}}$ . The axis of rotation is located at the centre of the join between

## Calculation of the Effect of Tip Geometry

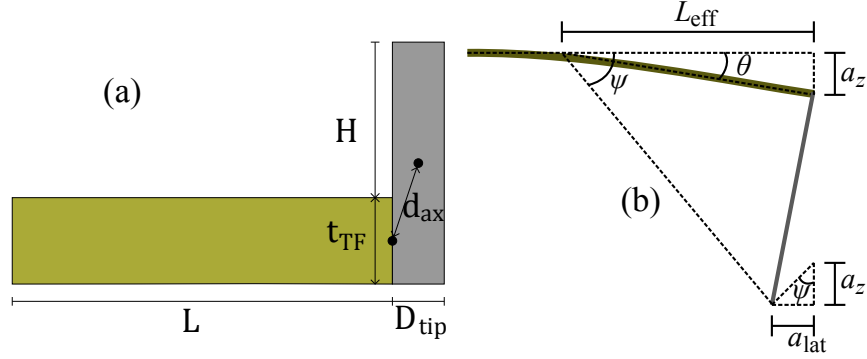


Figure 4.1: (a) Diagram of theoretical model.  $d_{ax}$  is the distance from the centre of mass of the tip to the axis of tip rotation. The tine of the tuning fork is assumed to be clamped at the left hand side. (b) Geometrical diagram of tip motion as cantilever deforms. Note the two  $\psi$  angles are not identical in this diagram as  $\theta$  is too large due to the exaggerated amplitude of deflection,  $a_z$ .

the tip and cantilever. By the parallel axis theorem the moment of inertia,  $\mathcal{I}_{tip}$ , can be calculated as  $\mathcal{I}_{tip} = \mathcal{I}_{tip}^{COM} + d_{ax}^2 m_{tip}$ , where  $\mathcal{I}_{tip}^{COM}$  is the moment of inertia through the centre of mass of the tip and  $d_{ax}$  is the distance from the axis of rotation to the centre of mass. The moment of inertia can be calculated as

$$\mathcal{I}_{tip}^{COM} = m_{tip} \left( \frac{D_{tip}^2}{16} + \frac{(H + t_{TF})^2}{12} \right). \quad (4.17)$$

The distance to the axis is  $d_{ax} = [(H/2)^2 + (D_{tip}/2)^2]^{1/2}$ . So, finally

$$\mathcal{I}_{tip} = \frac{m_{tip}}{48} (15D_{tip}^2 + 4(4H^2 + 2Ht_{TF} + t_{TF}^2)), \quad (4.18)$$

and thus

$$J = \frac{1}{48} (15D_{tip}^2 + 4(4H^2 + 2Ht_{TF} + t_{TF}^2)). \quad (4.19)$$

Using this model, dynamic spring constants have been calculated for the first four eigenmodes, relative to  $k_{stat}$  (Figure 4.2). The first two eigenmodes agree qualitatively with experimentally verified Hamiltonian calculations by Tung *et al.* for the first two eigenmodes of conical tips [140]. The sudden rises to infinite spring constant correspond to when a node of the vibrational mode is located at the end of the cantilever.

## Calculation of the Effect of Tip Geometry

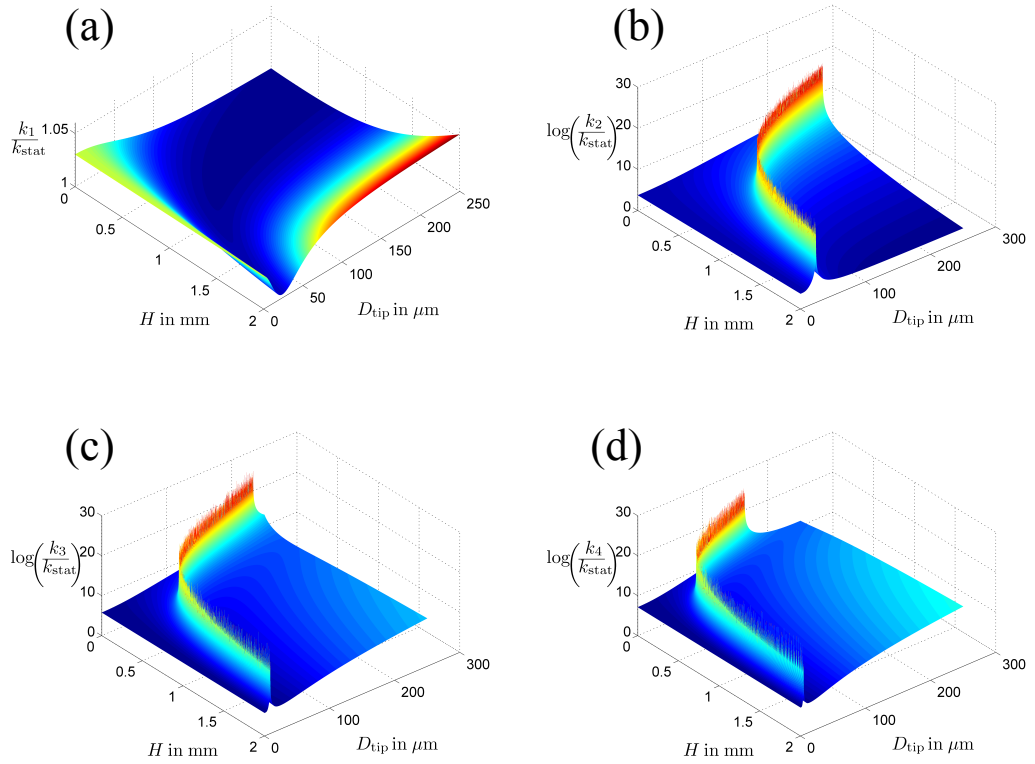


Figure 4.2: *The ratio of dynamic spring constants  $k_n$  to the cantilever static spring constant  $k_{\text{stat}}$  for  $n = 1, 2, 3, 4$ , plotted for a range of tip length and diameters. The sudden increases in the higher eigenmodes result from nodes positioned at the end of the tip resulting in infinite spring constants.*

### 4.3 Resulting lateral motion

The model presented above allows us to calculate the angle the tip is rotated through during the oscillation as

$$\theta = \arctan\left(\frac{\partial\Phi(L)}{\partial x} \frac{a_z}{\Phi(L)}\right) \quad (4.20)$$

$$= \arctan\left(a_z \frac{\beta_i \sin(\beta_i L) \sinh(\beta_i L)}{\Xi}\right) \quad (4.21)$$

where  $a_z$  is the amplitude of oscillation, and  $\Xi$  is a dimensionless parameter defined as

$$\begin{aligned} \Xi = & -\beta_i^3 J L m^* - \cos(\beta_i L) \sinh(\beta_i L) \\ & + \cosh(\beta_i L) (\beta_i^3 J L m^* \cos(\beta_i L) - \sin(\beta_i L)). \end{aligned} \quad (4.22)$$

This has been plotted in Figure 4.3(a) for the first eigenmode with an amplitude of 0.5 nm. The angle is extremely small,  $\sim (2 \times 10^{-5})^\circ$ , and nearly constant for different tip geometries. However, the lateral motion at the end of the tip will have an amplitude of

$$a_{\text{lat}} = \left(H + \frac{t_{\text{TF}}}{2}\right) \sin \theta = \left(H + \frac{t_{\text{TF}}}{2}\right) \sin\left(\arctan\left(\frac{\partial\Phi(L)}{\partial x} \frac{a_z}{\Phi(L)}\right)\right) \quad (4.23)$$

$$\approx \frac{\partial\Phi(L)}{\partial x} \frac{a_z (H + t_{\text{TF}}/2)}{\Phi(L)} \quad (4.24)$$

$$= a_z \left(H + \frac{t_{\text{TF}}}{2}\right) \frac{\beta_i \sin(\beta_i L) \sinh(\beta_i L)}{\Xi} \quad (4.25)$$

The amplitude of lateral vibrations has been plotted as a function of  $H$  in Figure 4.3(b). This has been plotted for  $D_{\text{tip}} = 50 \mu\text{m}$ , as the angular dependence on tip diameter is relatively small. It is apparent that this lateral motion can be significant compared with the normal motion, even for relatively short tips, reaching an equal amplitude at  $H = 1.389 \text{ mm}$ . We can define  $a$ , the total amplitude of oscillation at the apex, as

$$a = \sqrt{a_z^2 + a_{\text{lat}}^2}. \quad (4.26)$$

## Calculation of the Effect of Tip Geometry

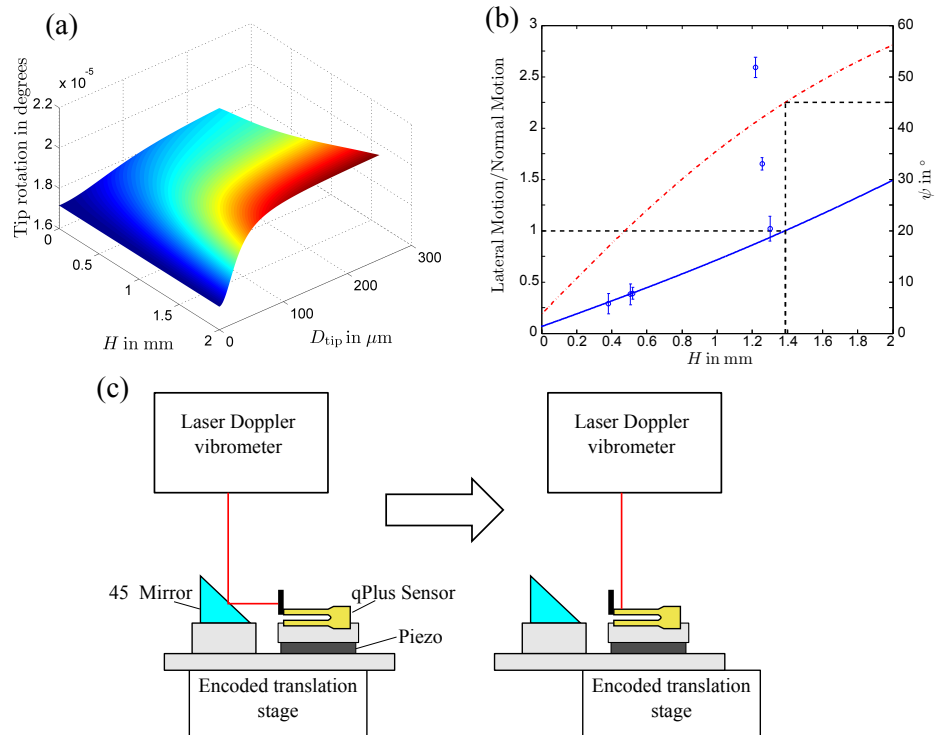


Figure 4.3: *Effect of tip geometry on tip movement for an arbitrary oscillation amplitude. (a) Angle of tip rotation plotted for varying tip sizes. (b) Amplitude of lateral motion of the tip apex plotted (solid line) for varying lengths with a tip diameter of  $50 \mu\text{m}$ . Circular data points represent experimentally measured values. Angle of resulting motion,  $\psi$  of the tip apex is also plotted (dot-dashed line). The dashed lines represent when the lateral amplitude equals the normal amplitude. (c) Schematic of experimental setup for measuring both normal and lateral motion of the qPlus sensor.*

## Calculation of the Effect of Tip Geometry

Defining the angle of tip motion as  $\psi$ , where  $\psi = 0$  corresponds to oscillation normal to the surface and  $\psi = 90^\circ$  to oscillation parallel to the surface, we get

$$\psi = \arctan\left(\frac{a_{\text{lat}}}{a_z}\right). \quad (4.27)$$

It is important to note that as the angle of tip rotation is so small, the motion of the tip apex should not be thought of as circular motion. Instead the tip apex is moving over a linear trajectory at an angle  $\psi$  to the surface, with no detectable rotation.

### 4.3.1 Experimental validation

The resulting lateral motion was measured experimentally for Omicron Nanotechnology qPlus sensors excited mechanically by a piezoelectric actuator located under the qPlus sensor (Figure 4.3(c)). The actuator was driven by a digital lock-in amplifier (Perkin Elmer 7280 DSP). The deflection of the qPlus sensor was measured using a laser Doppler vibrometer (Polytec OFV-522) connected to the lock-in amplifier. The qPlus sensor and piezoelectric actuator was mounted on an encoded translation stage, allowing deflection measurements to be recorded in multiple positions on the sensor. A  $45^\circ$  mirror positioned near the qPlus sensor allowed lateral deflection measurements of the tip to be made without remounting the sensor or interrupting the excitation, thus limiting changes to the transfer function.

Tungsten wire of  $50 \mu\text{m}$  in diameter was attached to the end of the bare qPlus sensor with EPO-TEK H21D electrically conductive silver epoxy. These were then etched to different tip lengths using potassium hydroxide.

For measurements of both normal and lateral motion the translation stage was used to collect multiple deflection readings at different positions along the sensor and tip respectively. These were then extrapolated to get the deflection at the end of the sensor and tip despite poor reflectivity at both regions of the sensor not covered by gold electrodes and the tip apex where it was etched.

The ratio of lateral to normal motion was measured for six sensors. Tip lengths were measured with an optical microscope and an encoded translation

## Calculation of the Effect of Tip Geometry

stage. These results are presented in Figure 4.3(b). Four of the six sensors show good agreement with the theoretical curve. The two remaining sensors show significantly higher lateral motion. This is most likely due to the elasticity of the epoxy used to connect the tip to the sensor allowing some rotation of the tip relative to the end of the sensor. These results confirm the prediction of large lateral motions on qPlus sensors.

Lateral amplitudes of this magnitude, at first glance, could be thought to limit the resolution of the AFM. However, it is important to consider that the lateral motion is perfectly correlated to the normal motion, unlike lateral motion resulting from torsional modes of the cantilever which will oscillate with much higher frequency causing blurring of the image. Simulated images and spectra can be generated to theoretically calculate the effect, however one must carefully consider both the amplitude calibration and the methods for calculating frequency shifts from a potential before continuing.

### 4.3.2 Effect on frequency shift

Under the assumption that the direction of motion of the tip apex is parallel to the motion of end of the cantilever (or tine) it can be shown [2] that

$$\Delta f = -\frac{f_0}{ka_z^2} \langle F_{ts} Z(L) \rangle, \quad (4.28)$$

where  $Z(L) = a_z \cos(\omega_0 t)$ , and  $F_{ts}$  is the force due to the tip sample interaction.

In the case that the motion of the tip is not parallel to the cantilever's oscillation, more care must be taken. Equation 4.28 can be derived from Newton's second law in the reference frame of the end of the cantilever

$$m_{\text{eff}} \frac{d^2 Z(L)}{dt^2} = -k_1 Z(L) + F_{ts}^C(Z(L)), \quad (4.29)$$

where  $F_{ts}^C$  is the force due to the tip-sample interaction as experienced at the end of the cantilever, and  $m_{\text{eff}}$  is the effective mass of the tip and cantilever. Thus, to modify Equation 4.28 to include lateral oscillations the amplitude terms will remain as  $a_z$ , as this is the oscillation amplitude of the beam. However, the tip-sample force must be modified from the interaction at the tip apex to the

## Calculation of the Effect of Tip Geometry

resulting force at the end of the cantilever.

For an amplitude of  $a_z$ , the end of the cantilever is angled by  $\theta$ , which can be treated as circular motion about an effective pivot at a distance of  $L_{\text{eff}} = a_z / \tan \theta$  from the end of the cantilever. Combining with Equations 4.23 and 4.27, and equating  $\sin \theta$  to  $\tan \theta$  due to the very small angle we can show

$$L_{\text{eff}} = \frac{H}{\tan \psi}. \quad (4.30)$$

Thus, the bending can be described by a torque of

$$\tau_B = \frac{H}{\tan \psi} F_{\text{ts}}^{\text{C}}. \quad (4.31)$$

In the reference frame of the tip apex the distance to the effective pivot is  $H / \sin \psi$  by simple geometry, and the measured tip sample force  $F_{\text{ts}}$  is perpendicular to the vector from the tip apex to the effective pivot such that

$$\tau_B = \frac{H}{\sin \psi} F_{\text{ts}}. \quad (4.32)$$

Hence,

$$F_{\text{ts}}^{\text{C}} = \frac{F_{\text{ts}}}{\cos \psi}, \quad (4.33)$$

and so the frequency shift can be calculated as

$$\Delta f = -\frac{f_0}{ka_z^2} \left\langle \frac{F_{\text{ts}}}{\cos \psi} Z(L) \right\rangle. \quad (4.34)$$

In the case that the lateral force is zero,

$$F_{\text{ts}} = F_{\text{ts}}^z \cos \psi \quad (4.35)$$

where  $F_{\text{ts}}^z$  is the  $z$  component of the tip-sample force. Thus, if the calibrated amplitude of the oscillation is  $a_z$ , rather than the total amplitude of oscillation at the tip apex  $a$ , then  $\Delta f$  is equal to the expected result for tip motion parallel to the cantilever oscillation. However, if lateral forces are present, then these will also affect the frequency shift.

### 4.3.3 Effect on calibration

Amplitude calibration in qPlus AFM is usually performed by measuring the  $z$  extension needed to maintain a constant value for  $\Delta f a_z^{3/2}$  [61]. It can be shown that for large amplitudes, by inserting

$$F_{ts}(q) = -Cq^{-n} \quad (4.36)$$

into Equation 4.34, where  $q$  is the position of the tip apex relative to the surface, that

$$\Delta f \approx \frac{f_0 C}{\sqrt{2\pi} \cos \psi k a_z^{3/2} d^{n-1/2}} I_1(n). \quad (4.37)$$

This follows from using the force conversion in Equation 4.33, and applying the method from [151].  $I_1(n)$  is an integral, dependent on  $n$ , but constant for the experiment, and  $d$  is the point of closest approach.

To maintain a constant  $\Delta f a_z^{3/2}$ , the point of closest approach must be kept constant. The recorded  $z$  extension to meet this condition will be equal to the change in  $a_z$ . Thus, the calibrated amplitude is not the amplitude of the complete motion tip apex, but  $a_z$ , the  $z$  component of this amplitude.

### 4.3.4 Effect on imaging and spectroscopy

Simulated AFM data were produced by creating a Lennard-Jones potential for a simple 2D square lattice, with a lattice constant of 3 Å, and a minimum potential of -3 eV at a distance of 0.5 Å (Figure 4.4(a)). For simplicity the simulated AFM was run in constant height mode to collect  $\Delta f$  images. These were calculated using Equation 4.34. Images were collected for both tips oscillating normal and at 45° to the sample (i.e. a qPlus sensor with a tip length of 1.389 mm). An oscillation amplitude of  $a_z = 0.5$  Å was used for both motions (Figure 4.4(b) and (c)), thus mimicking a calibration performed using the method described in Section 4.3.3. This leads to a total amplitude of  $a = 0.707$  Å, for the angled motion of the finite tip.

Qualitatively the images for both angled and normal tip motion look almost identical, and there is no noticeable reduction in resolution. Quantitatively the difference between the scans (Figure 4.4(d)), is  $\pm 2.5$  Hz for images with a  $\Delta f$

## Calculation of the Effect of Tip Geometry

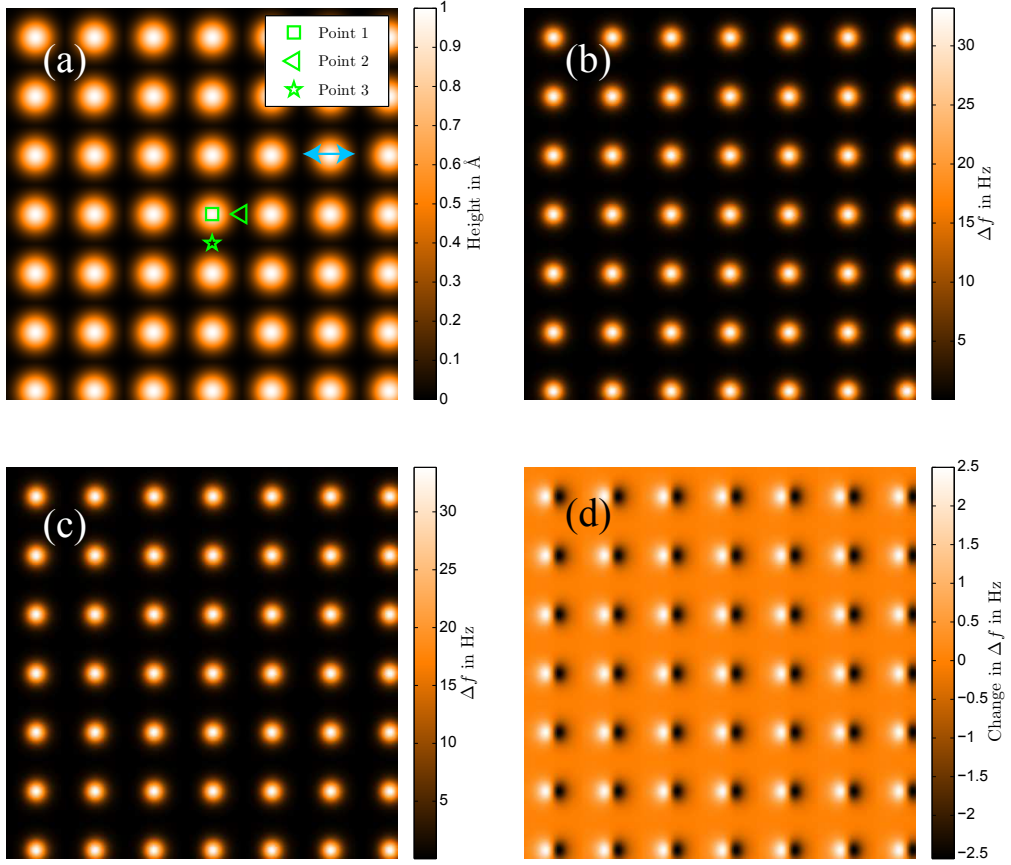


Figure 4.4: *Effect of tip motion on imaging for an oscillation amplitude of  $a_z = 5 \text{ \AA}$ . All image widths are  $2 \text{ nm} \times 2 \text{ nm}$ . (a) shows the model surface. (b) and (c) theoretical  $\Delta f$  images for constant height scans with tip motion normal and at  $45^\circ$  to the sample surface respectively. Lateral motion of the tip in (c) is aligned with the  $x$  axis of the scan as indicated by light blue arrow in (a). (d) is the difference between scans (b) and (c).*

range of approximately 34 Hz, giving rise to a relative error of less than 8%.

As the model potential has only one decay power rather than a combination of long range and short range forces, the relative changes between angled and normal oscillations are largely independent of the amplitude of oscillation. The change in sensitivity which arises from the different amplitudes will affect the absolute values of the frequency shift. As the simulation is not subject to experimental noise, however, limiting the frequency resolution, these absolute values are of little interest.

Following this, simulated  $z$  spectroscopy measurements were taken over three

## Calculation of the Effect of Tip Geometry

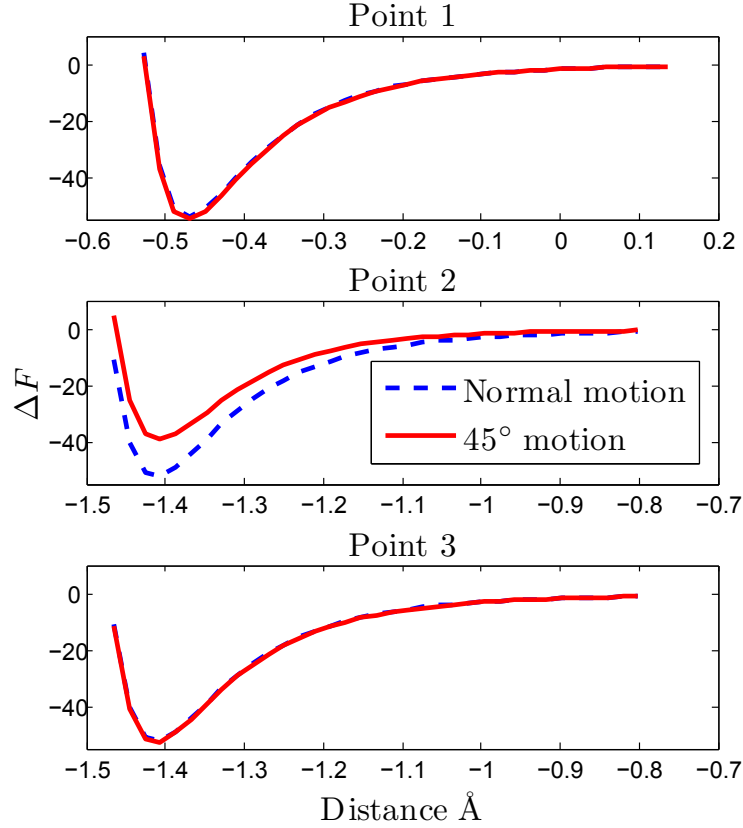


Figure 4.5: *Effect of lateral tip motion on spectroscopy for an oscillation amplitude of  $a_z = 5 \text{ \AA}$ . Simulated spectroscopy measurements taken at three points as marked on Figure 4.4(a). These show that only when the tip apex moves through significant lateral forces does the angle of scan have a noticeable effect on  $z$  spectroscopy.*

points (Marked on Figure 4.4(a).) for both images. The results, presented in Figure 4.5, show that for points 1 and 3, where the lateral force is near zero throughout the tip oscillation, the spectra align with a relative error of less than 3% at the point of highest interaction, as predicted in Section 4.3.2. However, for point 2 where the lateral force is significant as the tip moves diagonally over the adjacent atom there is a difference of 23% between the curves at the point of highest interaction.

## 4.4 Conclusion

We have shown that using a simple Euler-Bernoulli model for the tine of a qPlus sensor, and inserting boundary conditions which account for both the moment of inertia and mass of the tip, we were able to derive analytical results for a range of dynamic properties. When the moment of inertia of the tip is zero our results agree with previous results found in the literature for point mass weighted cantilevers [138]. After including the moment of inertia our results are in agreement with Tung *et al.* [140].

Further analysis of our model revealed large lateral motion at the tip apex for long tips. Due to the methods used for calibrating amplitude in AFM, this leads to no change in the z-component of the amplitude, but instead increases the overall amplitude of motion at the tip apex. If the lateral force is near zero throughout the tip oscillation then this has minimal effect on either imaging or spectroscopy measurements, thus explaining the ability of qPlus AFM to gain both sub-Ångstrom spatial resolution, and excellent agreement to theoretical force measurements [12]. However, the lateral motion has a large effect on any data when lateral forces are present, requiring both careful analysis of experimental results and knowledge of the tip geometry.

# Chapter 5

## 3D force mapping of $C_{60}$ – $C_{60}$ interactions

*“If you try and take a cat apart to see how it works, the first thing you have on your hands is a nonworking cat.”*

Douglas Adams

### Chapter Overview

In the last chapter we discussed the inherent coupling of lateral forces into ncAFM measurements with a qPlus sensor caused by the geometry of the tip. In this chapter we present the preliminary findings of work which uses grid spectroscopy measurements with a well defined tip and sample structure to directly measure and correct for these forces.

### 5.1 Introduction

The Girifalco potential [87] has been shown experimentally [12] to accurately describe the interaction potential landscape between two  $C_{60}$  molecules. With functionalised  $C_{60}$  tips it is not only possible to measure the orientation of the  $C_{60}$  tip, but that of also the  $C_{60}$  adsorbed on the surface [91]. This results in a well known tip-sample geometry and tip-sample potential. By using atom-tracking-corrected grid spectroscopy [41] this potential can be mapped experimentally in

### 3D force mapping of C<sub>60</sub>-C<sub>60</sub> interactions

3D. The Girifalco potential for two C<sub>60</sub> molecules is

$$U(r) = -\frac{60^2 A}{12d^6} \left( \frac{1}{s(s-1)^3} + \frac{1}{s(s+1)^3} - \frac{2}{s^4} \right) + \frac{60^2 B}{90d^{12}} \left( \frac{1}{s(s-1)^9} + \frac{1}{s(s+1)^9} - \frac{2}{s^{10}} \right), \quad (5.1)$$

where  $s = r/d$ ,  $d$  is the diameter of a C<sub>60</sub> (7.1 Å), and  $A$  and  $B$  are constants calculated from the energy of a C<sub>60</sub> computed using experimental results for the lattice constant and the heat of sublimation. Clearly due to the analytical form of the Girifalco potential the expected symmetry of the potential is radial. However, as Chapter 4 has shown, coupling of the lateral forces is possible in AFM due to the length of the tip causing tip motion which is no longer normal to the surface. This has the potential to distort the symmetry of the experimental results. Depending on the adsorption site of the C<sub>60</sub> on the tip, tip-asymmetry could also cause asymmetric results.

If the tip length is a significant fraction of the beam length of the sensor the angle of the tip's trajectory can be large, approaching 45° for tip lengths  $\sim 60\%$  of the beam length. While the tip trajectory angle has been measured experimentally, and the effect on AFM measurements has been calculated, no measurements have been performed which directly assess the effect of this motion.

Previous  $\Delta f(z)$  grid spectroscopy measurements on C<sub>60</sub> with an assumed Cu tip have shown asymmetry [81], however without detailed knowledge of the tip termination it is impossible to know if this results from asymmetry of the tip. Asymmetry has also been noted in repulsive imaging of pentacene [35] with a known CO termination, however this asymmetry has been attributed to the angle of the CO molecule.

C<sub>60</sub>-terminated tips allow a well known tip structure, which facilitates an accurate assessment of the asymmetry arising from the tip trajectory. In this chapter we combine C<sub>60</sub>-C<sub>60</sub> grid spectroscopy of this type with theoretical AFM data generated from the Girifalco potential to not only measure but also correct for such asymmetry.

## 5.2 Calculation of sensor properties

Experiments in this chapter were performed with the same qPlus sensor with two different length tips to vary the size of the lateral motion. The shorter tip was produced by etching the tip in 1M NaOH. For both tips the apex trajectory was calculated using the theoretical results from Chapter 4.

### 5.2.1 Measuring tip geometry from optical images

To determine the tip geometry backlit optical microscope images of the tip and the end of the tine were first acquired. These were read into MATLAB, binarised and reduced to an outline. Pixels in outline are listed as  $x$ - $y$  coordinates and are divided up as follows:

- Top of the top tine
- Bottom of top tine
- End of tines, where flat - not used for calculations on shorter tip
- Left side of tip, where flat - not used for calculations on shorter tip
- Right side of tip, where flat - not used for calculations on shorter tip

First order polynomials were then fitted to each of these sets of co-ordinates to get gradients  $m$  and intercepts  $c$  in units of pixels. These fitted lines are shown in Figure 5.1.

#### 5.2.1.1 Conversion from pixels to real units

Any measurements from the optical micrographs is in pixels, and so we must use known dimensions to calculate a conversion from pixels to real units. The equation for distance,  $d$  between two parallel lines

$$d = \frac{|c_1 - c_2|}{\sqrt{m^2 + 1}} \quad (5.2)$$

was used for the lines fitted either side of the tine to get the width of the tine in pixels. Two values are calculated: one using  $m$  from the fit for the top of the

## 3D force mapping of $C_{60}$ - $C_{60}$ interactions

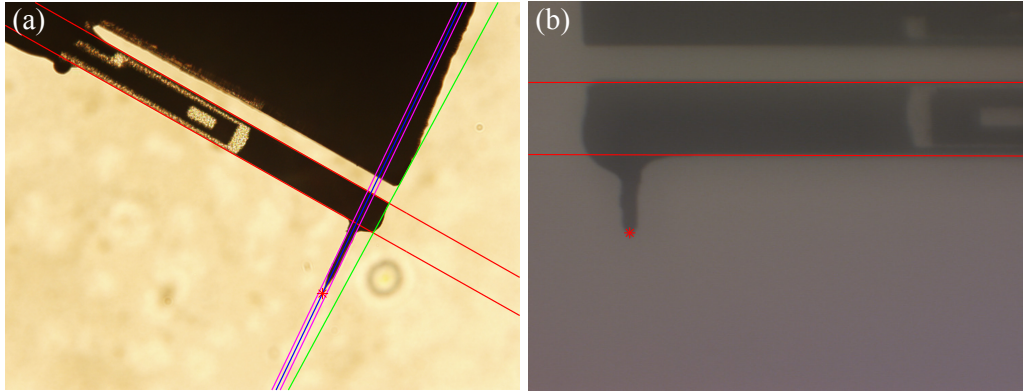


Figure 5.1: *a) Original tip. Red lines mark the sides of top tine, the green line the end of the tine, magenta lines the sides of the tip, blue line the centre line of the tip (calculated from magenta lines), and red asterisk the end of the tip. b) The same sensor as in (a) after tip is etched shorter. Red lines mark sides of the top tine, and the red asterisk the end of the tip.*

tine, another for  $m$  from the bottom. The same procedure is used with the fits for the sides of the tip, to get the width of the tip in pixels. As the diameter of the tip,  $d_{\text{tip}}$ , is known to be  $50 \mu\text{m}$ , and the width of the tine is known to be  $214 \mu\text{m}$  we can calculate four measured conversions for pixels to  $\mu\text{m}$  for the image. This is then averaged for a final value. A maximum error method is used to estimate the error on this value as only four, non-independent, measurements are available. This gives a value of  $2.37 \pm 0.04 \mu\text{m}/\text{pixel}$ .

For the shorter tip (Figure 5.1(b), taken on a different microscope due to equipment maintenance), the sides of the tip have also been etched during the process of etching to produce a shorter tip. As such measurements of the width of tip cannot be calibrated to a known values. In light of this only the top and bottom tine are used to calculate the conversion from pixels to  $\mu\text{m}$ . For this a conservative error estimate of 5% (compared to 1.6% for the other image) is used due to the lack of multiple corroborating measurements. This gives a value of  $2.0 \pm 0.1 \mu\text{m}/\text{pixel}$ .

### 5.2.1.2 Measuring the tip offset

The tip is not mounted directly on the end of the tine. To measure the offset of the tip we use Figure 5.1(a). The gradients and intercepts for the left and

## 3D force mapping of $C_{60}$ - $C_{60}$ interactions

right-hand sides of the tip were averaged to give an equation for the central line of the tip. The intercept of this line with the line for the top of the tine was then taken as the position of the tip attachment. The intercept between the line for the top of the tines and the line for the end of the tines was used to get a position for the end of the tine. The distance between these intercepts was calculated to be  $123 \pm 2 \mu\text{m}$ .

### 5.2.1.3 Tip angle

The angle of the tip relative to the beam is not significant and is therefore not accounted for in later calculations. For completeness this is calculated from Figure 5.1(a). The angle between the tip and the tine is calculated for four possible combinations of measured lines for top or bottom of tine with left or right of the tip. Again, a maximum error method was used to estimate error bars. This gives an angle of  $(3.81 \pm 0.09)^\circ$ . This angle is only known in the plane of the optical image, thus the small error bar is not really meaningful. We quote this angle as  $\sim 4^\circ$ , and thus a cosine error is less than 1%.

### 5.2.1.4 Tip length

As explained in Section 5.2.2, the critical measurement for this experiment is not the length of the tip wire, but the shortest distance from the tip apex to the top of the tine. As the tip is close ( $\sim 4^\circ$ ) to perpendicular to the beam of the tuning fork we will still refer to this value as tip length. For this the end of the tip was located by using the the final pixel in the binarised image. The shortest distance from this pixel to the line defining the top of the tine is used as the tip lengths. This gives apex to beam distances of  $487 \pm 8 \mu\text{m}$  and  $231 \pm 12 \mu\text{m}$  for the long and short tips respectively.

## 5.2.2 Calculating angle of apex motion from tip geometry

For this we can take advantage of some properties of the sensor to simplify the calculation. As apparent in Figure 4.3, for small changes in moments of inertia the gradient of the end tine is nearly constant. Therefore, a small shift of the tip from the apex to the end of the tine should have little effect on the mode

### 3D force mapping of $C_{60}$ - $C_{60}$ interactions

shape. Thus, we can use the mode shape as though the tip was located at the end. This saves very complex calculations for a beam loaded at an arbitrary location. Secondly, the gradient of the tine is approximately constant at the free end of the tine, so for a tip placed only a small distance from the free-end the calculated free-end gradients can be used. To convert from free end gradient to the angle of the tip apex the distance from the tip apex to the top of the tine is needed, as the tip wire is angled  $\sim 4^\circ$  we refer to this value as the tip length. As such, the angle of the tip apex can be calculated using the expressions from Chapter 4.

Using the length and diameter of the tips we calculate apex trajectory angles of  $(20.3 \pm 0.3)^\circ$  and  $(11.7 \pm 0.4)^\circ$  for the long and short tips respectively. These quoted uncertainties relate only to the uncertainty in the tip length and do not include other uncertainties arising from the mechanical properties of the tuning fork or the slightly modified geometry due to the offset tip placement.

For the qPlus sensor used, manufactured by Omicron Nanotechnology, the angle with which the tuning fork is mounted relative to the surface is  $(5^\circ)$ . Including this the final angle of the tip apex motion relative to the sample plane is  $25.3^\circ$  and  $16.7^\circ$  for the two tip lengths.

As well as the zenith angle of the tip trajectory relative to the plane of the sample, we also need the azimuth angle. For this we use the angle of rotation of the scan as recorded by our SPM, combined with the relative direction of the sensor mounting.

### 5.2.3 Other experimental considerations: spring constant and sensitivity

The spring constant of the qPlus sensor can be calculated using Euler-Bernoulli beam theory as

$$k = \frac{3EI}{L^3}, \quad (5.3)$$

where  $E$  is the Young's modulus,  $I$  is the second moment of area, and  $L$  is the length of the beam. The length used is the distance from the base to the point of tip attachment:  $L = (2400 - 123) \mu\text{m}$ . A value of 76.5 GPa was used for the

### 3D force mapping of C<sub>60</sub>-C<sub>60</sub> interactions

Young's modulus of quartz [152]. The second moment of area was calculated as

$$I = \frac{wt^3}{12}, \quad (5.4)$$

where  $t = 214 \mu\text{m}$  and  $w = 130 \mu\text{m}$  are the width ( $z$ -direction) and thickness of the beam respectively. This gives a value of  $k = 2064 \text{ N/m}$  at the tip position, and  $k = 1763 \text{ N/m}$  at the end of the tine.

This method is internally consistent with the model used to estimate the tip angle. A range of studies, however, have produced different measurements for the spring constant of quartz tuning forks. Shaw has statically measured the spring constant of tip free Omicron qPlus sensors using an indenter and  $150 \mu\text{m}$  from the end of the tine found  $k$  to be  $2639 \text{ N/m}$  [153], which extrapolates to  $k = 2175 \text{ N/m}$  at the end of the tine. Tung *et al.* have fitted measured mode shapes of qPlus sensors of the same geometry to the general solution for a cantilever beam to estimate spring constant at the free end [140]. These measurements, which were performed on three sensors with varying tip lengths and a fourth with no tip range from  $k = 1890 - 2379 \text{ N/m}$ , showing a wider range of variation than is expected for that caused by the tip. These variations could be explained by the mounting of the tuning fork, which has been shown to cause large variations in spring constant [154]. As such we will average the four results from Tung, the results of Shaw, and the geometric result to get a value of  $k = 2022 \text{ N/m}$  at the free end. Extrapolating to  $123 \mu\text{m}$  from the free end yields a final value of  $k = 2368 \text{ N/m}$ .

From the standard deviation of the above values the relative spread in spring constant for qPlus sensors can be estimated to be of order 11%. Thus, we use a spring constant as  $k = 2370 \pm 260 \text{ N/m}$  for all calculations.

Using the Giessibl normalised frequency shift method [61] we calculated the piezoelectric sensitivity of the qPlus sensor *in situ* after experimental results were taken. Our results give an inverse sensitivity of  $5.35 \pm 0.17 \text{ nm/V}$  for with long tip and  $4.42 \pm 0.14 \text{ nm/V}$  for the short tip. The increase in sensitivity ( $\text{V/nm}$ ) for the shorter tip results from the change in strain due to the the modified mode shape as predicted in Tung *et al.* [140]. It is important to note, as discussed in Chapter 4 that the distance here is the  $z$  component of the tip apex amplitude.

## 3D force mapping of $C_{60}$ - $C_{60}$ interactions

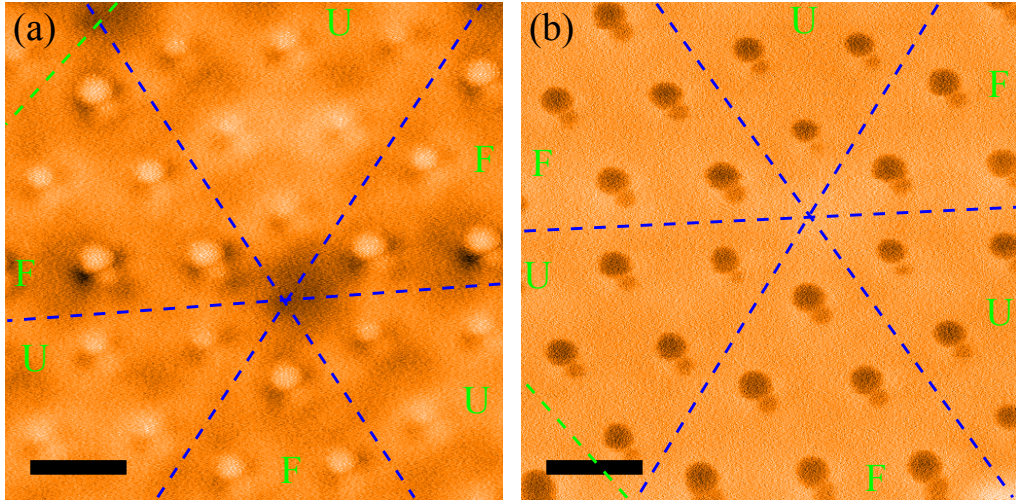


Figure 5.2: *Tip convolution imaging showing  $C_{60}$  tip on the Si (111)  $7 \times 7$  reconstruction in AFM. (a) Shows a constant  $\Delta f$  image (set-point 25.5 Hz). (b) Shows a constant height image. Blue dashed lines are to guide the eye to the unit cell of the reconstruction. Separation between faulted and unfaulted halves are marked by green dashed lines. Note how the tip contrast differs above adatoms in the faulted and unfaulted halves of the cell, the increased reactivity of the faulted half [155] has been used to identify the halves (A green “F” marks the faulted and a “U” the unfaulted half). For both images the  $z$ -component of the amplitude  $A_z = 268 \pm 9$  pm. No grid spectroscopy was performed with this tip termination.*

### 5.3 Measuring 3D potentials

For the experimental work we used an Omicron LT AFM/STM at a temperature of 77 K. Atom-tracking-corrected grid spectroscopy was performed with external control electronics designed by Rahe *et al.* [41] interfacing with the Omicron control electronics via the MATE scripting interface. The sample was a Si (111) wafer, flash annealed to produce the  $7 \times 7$  reconstruction. A low coverage of  $C_{60}$  was then evaporated onto the surface. The qPlus sensor was first conditioned to show atomic resolution in dynamic STM (dSTM) by controlled tip crashes into the Si surface, producing what is most likely a Si terminated tip. Controlled tip crashes above  $C_{60}$  molecules, or high current scanning over  $C_{60}$  molecules was used to produce  $C_{60}$  terminated tips.

To check for  $C_{60}$  termination, dSTM images of surface-adsorbed  $C_{60}$  were taken showing molecular orbital convolution described in Lakin *et al* [91]. A

### 3D force mapping of C<sub>60</sub>-C<sub>60</sub> interactions

second check was performed by spectroscopy measurements above the centre of a C<sub>60</sub>. These are expected to accurately reproduce the Girifalco potential. The accurate reproduction is expected even for a tip apex oscillating at an unknown angle but treated as oscillating vertically due to the lack of significant lateral forces at this position, as described in Section 4.3.4. Finally, ncAFM images of the Si adatoms can be taken to verify the orientation of the C<sub>60</sub> tip, see Figure 5.2. These ncAFM images, however, require very high tip sample forces which can often change the tip apex.

As for this work the precise orientation of the C<sub>60</sub> on the tip is not crucial, in that we are interested in the radially symmetric Girifalco potential, the  $\Delta f(z)$  grid spectra were recorded before adatom ncAFM images. ncAFM images were performed after the  $\Delta f(z)$  grid spectroscopy for completeness.

#### 5.3.1 Processing grid spectroscopy measurements

Using reference  $\Delta f(z)$  spectra, taken on a molecule-free region of the Si(111)  $7 \times 7$  surface just before the  $\Delta f(z)$  grid spectroscopy recordings were taken, the Girifalco contribution to the frequency shift was calculated using the following method. Taking only the points in the last (furthest from surface)  $\sim 0.6$  nm of the each spectra and the corresponding points from the reference spectrum, the experimental  $z$ -offset between these spectra was calculated by using a least squares method to find the offset which minimised the difference. After applying this calculated offset to the  $z$ -axis of the experimental curve the interaction frequency shift is calculated for measurements which overlap on the new  $z$  axis. This processing is shown graphically in Figure 5.3. Finally a grid is constructed from all measurements at  $z$  values which appear in all interaction  $\Delta f(z)$  spectra.

The experimental potential is then calculated by numerical integration of each interaction  $\Delta f(z)$  spectrum using the Sader-Jarvis method [29] under the substitution described in Section 2.2.3.3:

$$U(z) = \frac{4k}{f_0} \int_0^\infty \left( u^3 + \sqrt{\frac{A}{16\pi}} u^2 + \sqrt{\frac{A^3}{2}} \right) \Delta f(u^2 + z) du, \quad (5.5)$$

where  $f_0$  is the centre frequency of the phase tracking loop (see final paragraph

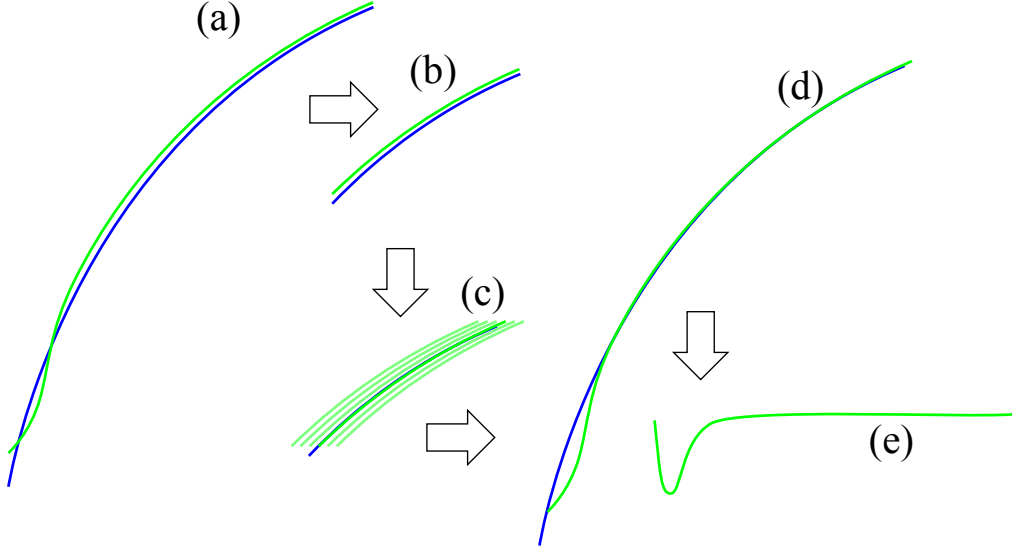


Figure 5.3: *Graphical explanation of spectra processing. a) Experimental spectrum (green) and reference spectrum (blue). b) Spectra cropped to just the tail end. c) Least squares fitting is used to determine the offset of the experimental spectra with respect to the reference. d) This offset is applied to the full experimental spectrum. e) The reference spectrum is subtracted from the experimental spectrum at all  $z$  which appear in both spectra to produce the interaction spectrum.*

of Section 2.3.7.2),  $A$  is the set-point amplitude, and  $u$  is a dummy integration value.

### 5.3.2 Simulating grid spectroscopy measurements

For simulated grid spectroscopy measurements the Girifalco potential is calculated for a grid of points slightly larger than the experimental grid, to allow for simulated tip oscillation. This grid is then differentiated along each dimension to calculate the force in the  $x$ ,  $y$ , and  $z$  directions. These force vectors are then combined to give the force,  $F_{ts}$ , in the direction of the calculated tip trajectory.

Next,  $\Delta f$  is calculated using Equation 4.34 in the form

$$\Delta f(\mathbf{r}_m) = -\frac{f_0}{kA_z^2} \left\langle \frac{F_{ts}(\mathbf{r}_m + \mathbf{q}(\theta))}{\cos \psi} q'_z(\theta) \right\rangle, \quad (5.6)$$

where  $A_z$  is the  $z$  components of the oscillation amplitude,  $\mathbf{r}_m$  is the point of

### 3D force mapping of $C_{60}$ - $C_{60}$ interactions

closest approach,  $\phi$  is the zenith angle of the tip apex motion relative to the surface,  $\theta$  is the phase angle of the oscillation, and  $\langle \rangle$  denotes the average over one oscillation ( $\theta = 0 \rightarrow 2\pi$ ). Here  $q'_z = A_z \cos(\theta)$  is the oscillation  $z$ -position relative to the centre of oscillation, and  $\mathbf{q}(\theta) = \hat{\mathbf{u}}_r A_t (1 + \cos(\theta))$  the vector position of the tip apex relative to the point of closest approach, where  $A_t$  is the full amplitude of tip apex, and  $\hat{\mathbf{u}}_r$  is a unit vector in the direction of the tip apex motion during oscillation away from the surface.

The average in Equation 5.6 is calculated over 100 points. As the force has not been calculated at the exact position of all 100 points linear 3D interpolation of the calculated force grid is used. This calculation is repeated for all positions  $\mathbf{r}_m$  required in the simulation. The final simulated  $\Delta f(z)$  grid is then processed identically to the experimental equivalent.

### 5.3.3 Correcting grid spectroscopy measurements

To correct the calculated experimental potential for the effects of tip angle we consider that if each spectrum had been taken in a direction parallel to the tip motion the force can be extracted by inverting equation 5.6. Thus, for each measured  $\Delta f$  point we interpolate all  $\Delta f$  values along a path parallel to the calculated tip apex motion, with the same spacing as the original  $z$  spacing for  $\Delta f$  measurements, up to the final  $z$  height of the grid. This interpolation is expected to be a reasonable estimate for all positions lying within the grid. For positions outside the grid the  $x$ - $y$  coordinates are replaced with the closest  $x$ - $y$  coordinates within the grid. This correction is thus of poor accuracy near the bottom of the side of the grid where most interpolated points fall outside the grid.

To deconvolve the force from these interpolated  $\Delta f$  measurements we use an equation analogous to the Sader-Jarvis method but to deconvolve Equation 5.6:

$$U(z) = \frac{4k \cos(\psi)}{f_0} \int_0^\infty \left( u^3 + \sqrt{\frac{A_z}{16\pi}} u^2 + \sqrt{\frac{A_z^3}{2}} \right) \Delta f(u^2 + z) du. \quad (5.7)$$

## 3D force mapping of $C_{60}$ - $C_{60}$ interactions

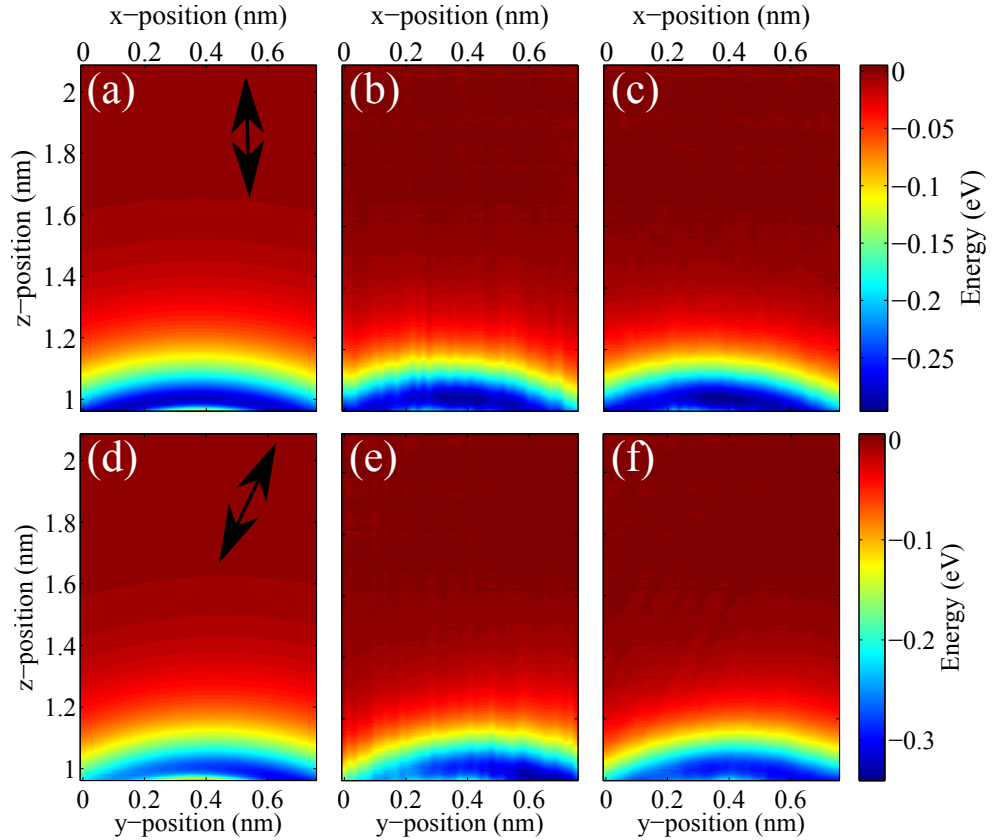


Figure 5.4: *Slices through the centre of the 3D experimental  $C_{60}$ - $C_{60}$  potential in  $x$ - $y$  and  $y$ - $z$  planes. (a) and (d) show simulated experiments with a tip-apex oscillating in the direction shown, with a  $z$  amplitude of  $A_z = 268 \pm 9$  pm. (b) and (e) show the experimentally measured potentials. (c) and (f) are the result of applying the correction for tip-apex oscillation angle to (b) and (e). Colour scale is consistent along rows.*

## 5.4 Results and Discussion

Figures 5.4(b) and (e) show slices through the centre of a the 3D potential measured in a grid spectroscopy measurement taken over a  $C_{60}$  molecule with a  $C_{60}$  tip termination. The direction of the lateral motion is  $94^\circ$  relative to the  $x$  axis,<sup>1</sup> and the resulting full tip apex oscillation direction has been noted

<sup>1</sup>We know image rotation relative to the normal scanner motion from the data files. The direction of the normal scanner motion with respect to the coarse motors has been measured by taking a sequence of large images with coarse motor steps taken between images. Finally, the orientation of the sensor with respect to the coarse motors has been measured by recording a video of the sensor moving as the coarse motors are moved a few millimeters. These videos were compared with technical drawing supplied by Omicron Nanotechnology.

### 3D force mapping of $C_{60}$ - $C_{60}$ interactions

with arrows in Figure 5.4. Figures 5.4(a) and (d) show the potential calculated from simulated spectra with an angled apex oscillation as described in Section 5.3.2. It is clear from comparing the simulated with experimental data that the results are in excellent agreement, not only in shape but in magnitude, as the colour scale is consistent along each row. By applying the correction described in Section 5.3.3, we generated Figures 5.4(c) and (f). From the direction of the tip oscillation it is important to note that at the right hand side of (f) the correction is not expected to be valid as the most of the interpolated points lie outside the measured grid and were replaced with the closest values inside the grid. It is clear, however, that the correction has produced a significant improvement of the potential.

Taking slices in  $z$  (Figure 5.5) through the lower region of potentials presented in Figure 5.4 we can further see the similarity between experiment (Figure 5.5(b,e,h,k)) and theory (Figure 5.5(a,d,g,j)), and the effect of the correction (Figure 5.5(c,f,i,l)). Here it is especially clear that, as expected, the correction does not perform well on the top side of the grid. Another observation which stands out is that the experimental work has a much slower onset of the repulsive regime of the potential. This effect has been seen before in measurements of the Girifalco potential and is attributed to relaxation of the tip and the surface under the applied force. The  $z$  scale used here is chosen such that at the centre point of the grid the minima in the analytical Girifalco potential align with the minima in the experiment. The centre of the grid is located as the point where the original and corrected experimental potentials best align.

To quantitatively confirm the agreement between the original and corrected experimental potentials and the Girifalco potential in Figure 5.6 we plot the potential at three points. Again the only fitting here is the aligning of the minima for the central point (Figure 5.6(b)), for the offset points the analytical potential is calculated as

$$U(z) = U(\sqrt{r^2 + y_{\text{off}}}), \quad (5.8)$$

where  $y_{\text{off}}$  is the magnitude of the offset from the centre. The experimental and analytical potential minima still align well without any further fitting. The

### 3D force mapping of $C_{60}$ - $C_{60}$ interactions

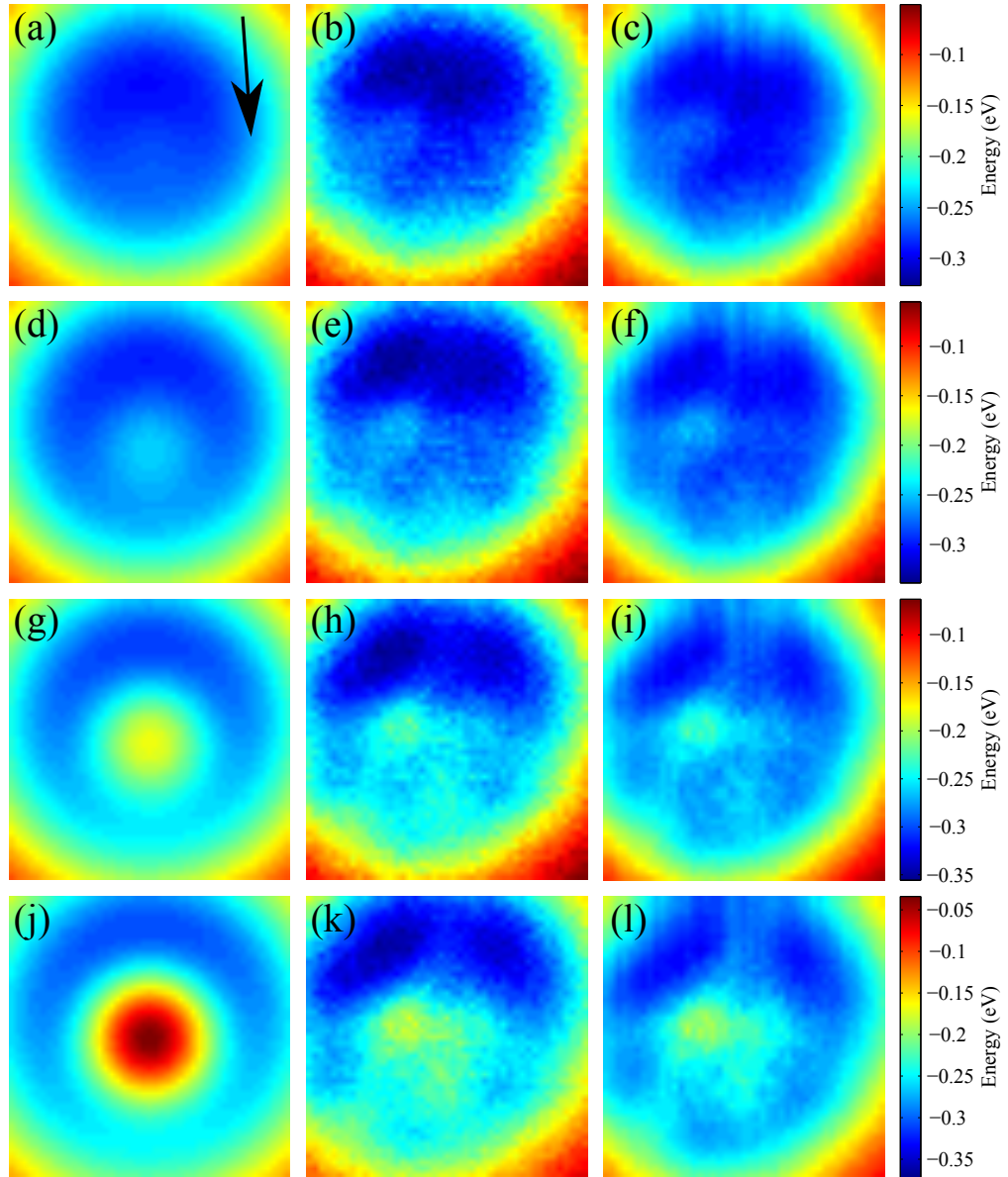


Figure 5.5: *Slices through the 3D  $C_{60}$ - $C_{60}$  potential in the  $x$ - $y$  plane at a range of heights. The black arrow represents the direction of the lateral component tip-apex oscillation during the motion towards the sample, the lateral amplitude  $A_{\text{lat}} = 127 \pm 4$  pm. The first column is the shows simulated experiment. The second and third column show the experimentally measured potential in original and corrected form respectively. Colour scale is consistent along rows. All images are  $0.75 \times 0.75$  nm<sup>2</sup>.*

### 3D force mapping of $C_{60}$ - $C_{60}$ interactions

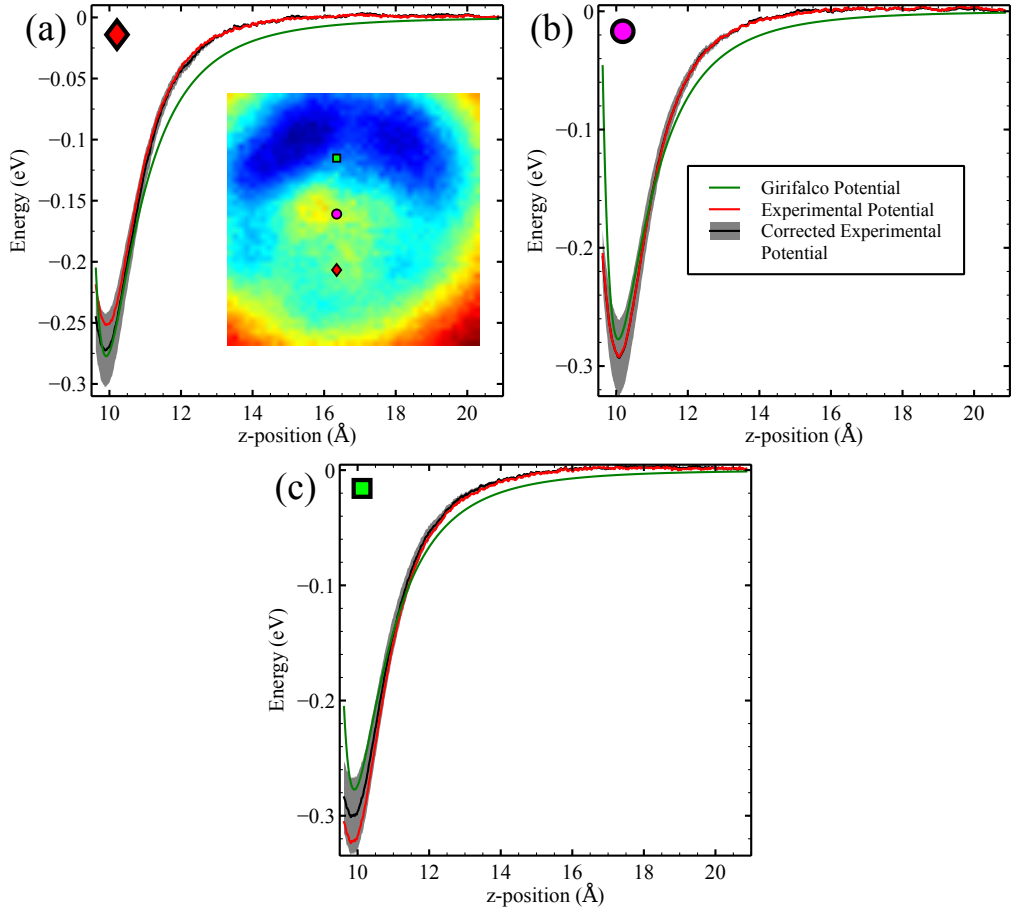


Figure 5.6: *Individual spectra measurements of  $C_{60}$ - $C_{60}$  interaction potential. The grey error bar for the corrected potential only includes the contribution from the uncertainty in the spring constant of the sensor. (a) Spectra from a negative  $y$  offset of  $1.7 \text{ \AA}$  from centre of  $C_{60}$ , shows the corrected potential aligns well with the analytical Girifalco potential. Inset shows the position of the three spectra on the molecule. (b) shows the potential at the centre of the  $C_{60}$ , corrected and raw spectra align well as expected. (c) Spectra from a positive  $y$  offset of  $1.7 \text{ \AA}$  from centre of  $C_{60}$ , correction does not perform as well as for a negative offset due to using interpolated values which fall outside the measurement grid. For all measurements  $A_z = 268 \pm 9 \text{ pm}$ .*

uncertainty presented in Figure 5.6 results from the one standard deviation uncertainty in the spring constant, other uncertainties arising from other factors such as the sensitivity are not included. For the central point the agreement between the magnitude of the minima in the experimental and analytical potentials is well within the experimental uncertainty. Further the corrected and analyti-

### 3D force mapping of $C_{60}$ - $C_{60}$ interactions

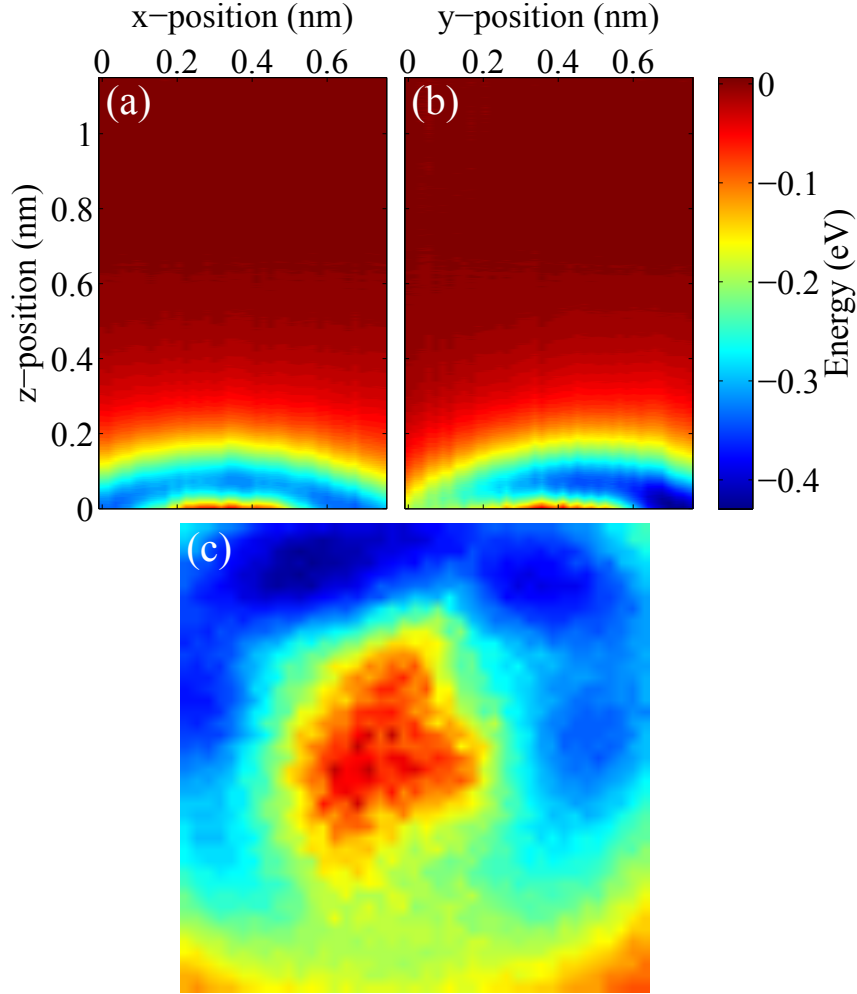


Figure 5.7: A second measurement of  $C_{60}$ - $C_{60}$  interaction potential for a different surface molecule and tip termination. (a) and (b) show slices in the  $x$ - $z$  and  $y$ - $z$  planes respectively. (c) is a slice in the  $x$ - $y$  plane taken at the lowest recorded  $z$  position. Colour scale is consistent throughout the figure. For all measurements  $A_z = 268 \pm 9$  pm

cal potential show good agreement for a negative offset in the  $y$ -axis, while the original experimental result is unreliable due to the tips motion. Again we see that the correction does not perform well for a positive offset in the  $y$ -axis for reasons previously explained. We notice, however, that the correction while not complete does represent a significant improvement over the original potential.

The results are consistent with a second grid spectroscopy measurement taken over a different  $C_{60}$  on the surface. Between experiments a change in contrast consistent with a tip change was observed and the tip was then modified until

### 3D force mapping of $C_{60}$ - $C_{60}$ interactions

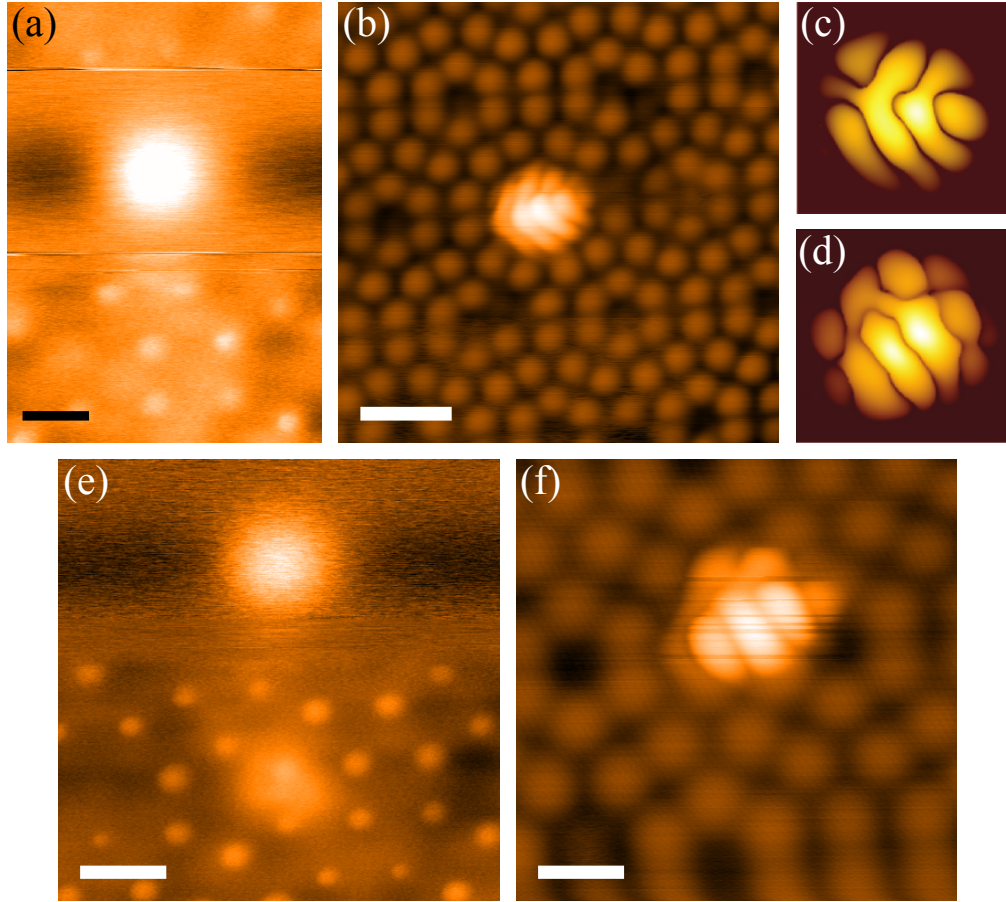


Figure 5.8: (a) ncAFM of surface  $C_{60}$  used for grid spectroscopy measurements presented in Figure 5.7. For areas where surface is visible the  $\Delta f$  set-point is  $-38$  Hz this is lowered to  $-9$  Hz where the  $C_{60}$  molecule is to raise the tip height by  $\sim 6$  Å. (b) dSTM image of  $C_{60}$  molecule in (a) showing sub-molecular contrast similar to (c). (c) and (d) are reproduced from Lakin et al. [91], showing simulated STM images of a  $C_{60}$  with a  $C_{60}$  tip termination for different orientations. (e) ncAFM of surface  $C_{60}$  used for grid spectroscopy measurements presented in Figures 5.4–5.6. For areas where surface is visible the  $\Delta f$  set-point is  $-36.5$  Hz this is lowered to  $-9.5$  Hz where the  $C_{60}$  molecule is to raise the tip height by  $\sim 5$  Å. (f) dSTM image of  $C_{60}$  molecule in (e) showing sub-molecular contrast similar to (d). Scale bars are (a):  $6$  Å, (b)  $15$  Å, (e)  $8$  Å, and (f)  $15$  Å. For (a), (e), and (f)  $A_z = 268 \pm 9$  pm for (b)  $A_z = 1510 \pm 50$  pm.

resolution consistent with a  $C_{60}$  termination was again visible. These results, presented in Figure 5.7, were taken with the same rotation as the data presented in Figures 5.4 and 5.5. It is clear that the same symmetry is visible in the repeat measurement.

### 3D force mapping of C<sub>60</sub>-C<sub>60</sub> interactions

To verify the termination of the tip in these experiments we could point to the agreement between experiment and theory for the potentials. Further evidence is however gathered via imaging. Figures 5.8(b) and (f) show dSTM images of the surface C<sub>60</sub> with the tip termination used for the grids shown in Figures 5.7 and 5.4 respectively. These images show strong agreement to theoretical C<sub>60</sub>-C<sub>60</sub> STM images from Lakin *et al.* [91], reproduced in (c) and (d). (c) corresponds to the interaction between C<sub>60</sub> molecules where a pentagon face on one is closest and a single carbon atom on the other, (d) corresponds to a double bond and closest to a single carbon atom. AFM measurements in 5.8(a) and (e) show they are taken with the same tip and surface molecules as (b) and (f) respectively. The  $\Delta f$  set-point is lowered significantly over the region with the C<sub>60</sub> to allow imaging of the surface and molecule in the same image. The image is also flattened line by line rather than with a plane otherwise the significant  $z$  change, due to the modification of the set-point, masks all contrast. Neither image shows sub-molecular contrast which we attribute to the C<sub>60</sub> molecule having a single carbon atom down. This is consistent with the orientations suggested from dSTM. We also note the feature in (e) on the surface, this could be contamination on the surface, it could also however result from a tip double. As these features are separated by almost 2 nm in the  $x$ - $y$  plane and by a further 5 Å in  $z$  this possible tip double should have no effect on the force spectra.

After the tip was etched shorter further experiments with the same sensor were performed. Due to the macroscopically blunt tip (See Figure 5.1), however, these experiments were significantly more difficult to perform. One grid spectroscopy measurement was performed, however, during the analysis of the results it became clear that the spectra taken prior to the grid show a significantly reduced potential to what would be expected for a C<sub>60</sub>-C<sub>60</sub> interaction (Figure 5.9(e)). By comparing dSTM images (Figures 5.9(a-c)) with this tip termination and a C<sub>60</sub> we get good agreement to an image from Lakin *et al.* [91] for an s-wave type tip (Figure 5.9(d)). This gives further evidence that the tip was not C<sub>60</sub> terminated. Furthermore the extraction of the potential is difficult due to minor tip changes which are not visible in the raw  $\Delta f$  data but become visible when the background is subtracted. We note however that asymmetry in the expected direction is present in the background subtracted  $\Delta f$  data (Figures

### 3D force mapping of $C_{60}$ - $C_{60}$ interactions

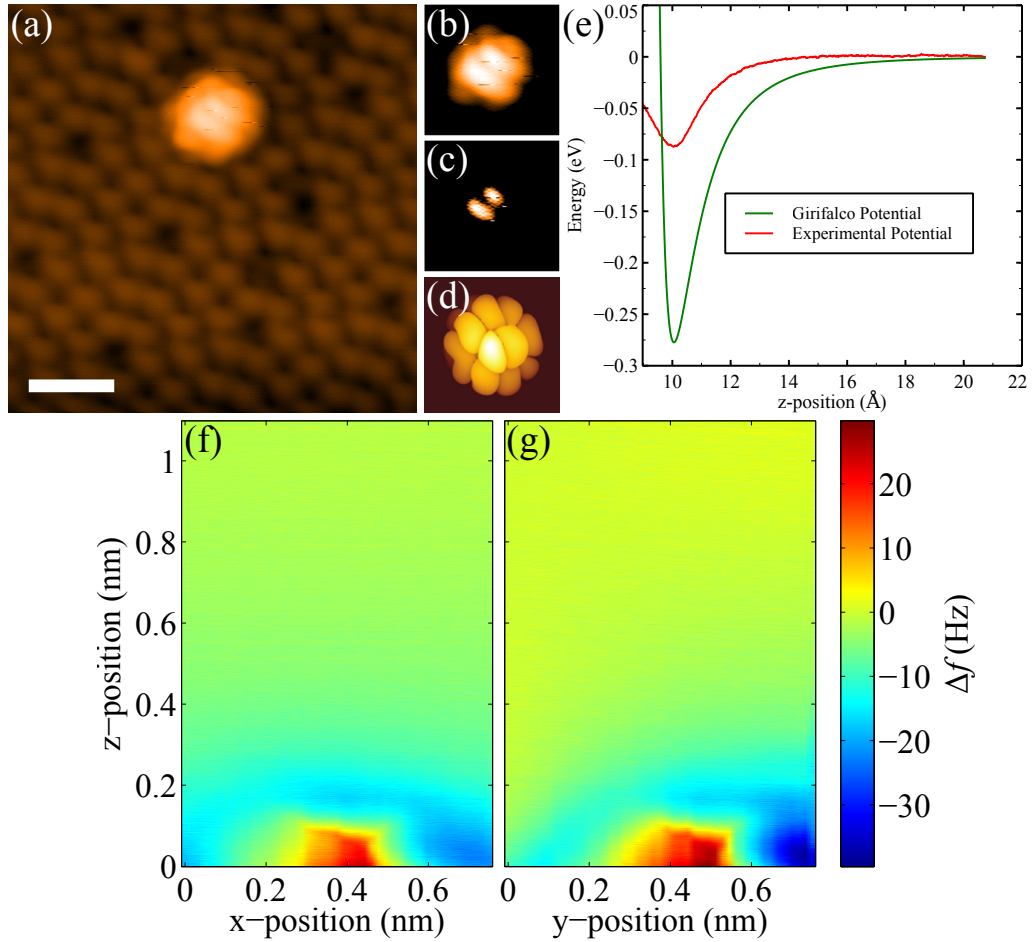


Figure 5.9: Identification of a tip not terminated with a  $C_{60}$  molecule. (a) dSTM image of surface  $C_{60}$  molecule shows sub-molecular contrast. (b) and (c) are zooms of (a) with colour scale adjusted to better identify contrast in molecule. (d) A simulated STM image of a  $C_{60}$  with an s-wave type tip from Lakin et al. [91], showing similar structure to (a)–(c). (e) Potential from  $\Delta f$  spectrum taken above the centre of  $C_{60}$  before grid measurement. These data show a much reduced potential. (f) and (g) show  $x$ - $z$  and  $y$ - $z$  plane slices through the background subtracted 3D  $\Delta f$  data. Asymmetry shows same orientation as Figures 5.4 and 5.7, however, due to the unknown tip termination this could arise from an asymmetric tip. For all measurements  $A_z = 221 \pm 7$  pm.

5.9(f–g), but due to the unknown tip termination and the known minor contrast variation during the measurement we are not confident assigning this asymmetry to the motion of the tip apex. As such, further experiments with varying tip lengths are required to confirm that the observed asymmetry is a result of tip length.

## 5.5 Conclusion

We have shown the presence of asymmetry in  $C_{60}$ - $C_{60}$  interactions measured with a qPlus sensor would appear to be in good agreement with the expected asymmetry predicted in Chapter 4. Confirmation of varying levels of asymmetry for different tip lengths on the same sensor was not achieved due to the challenging nature of these experiments.

As experimental measurements were performed in 3D it is possible to integrate the potential in the direction of tip motion to correct the interaction potential. Results for this correction were promising, however, for more accurate results the measurement would need to be extended further in the  $x$ - $y$  plane as otherwise data must be interpolated.

# Chapter 6

## Optimal geometry for a quartz multi-purpose SPM sensor

*“Only one thing is impossible for God: to find any sense in any copyright law on the planet.”*

Mark Twain

### Chapter Overview

In the previous two chapters we have discussed how the geometry of the qPlus sensor can cause inaccurate measurements due to the large tip and the asymmetry of the cantilever. In this chapter this topic is further developed to suggest a new sensor design which not only solves these issues, but also opens doors for new measurements with the same sensor. This chapter is adapted from work published in the Beilstein Journal of Nanotechnology [156].

### 6.1 Introduction

The type of measurements possible for scanning probe microscope (SPM) depend entirely on its sensory probe. For a scanning tunnelling microscope (STM) this is simply an electrically conducting wire with an atomically sharp apex. For atomic force microscopes (AFM) and lateral force microscopes (LFM), however, the sensor is more complex. The atomically sharp probe must be combined with

a force sensor, usually a cantilever, with either piezoelectric or optical deflection detection. For non-contact AFM (NC-AFM) and dynamic LFM (DLFM), where the sensor is excited at or near one of its eigenfrequencies, properties such as the Q factor, eigenfrequencies, effective spring constant [140] and other geometrical attributes [145] of the eigenmodes become important.

AFM and LFM sensors have evolved from gold foil with a diamond tip [92] and bent tungsten wires [3] respectively, into a wide range of specialised sensors. The most common NC-AFM sensors — namely, silicon microcantilevers [97], and quartz sensors such as the qPlus sensor (tuning fork) [118] or KolibriSensor<sup>®</sup> [122], have all been used for combined AFM/STM [61, 105, 122]. Combined AFM/LFM sensors have been constructed from silicon cantilevers by exciting torsional modes to generate the lateral motion needed for the LFM [157]. The qPlus sensor has been used as an LFM by rotating the tip on the end of the quartz tuning fork [8], but no combined AFM/LFM qPlus system has been developed due to the magnitude of the torsion constant for the tine of the sensor. A combined AFM/LFM sensor, operated in frequency modulation mode, would enable measurements of conservative and non-conservative forces simultaneously in the normal and lateral direction. Such measurements could be used to further important investigations in single-asperity friction [9], where the relationship between normal and lateral force is of interest. In this chapter we suggest the optimum geometry of a quartz sensor to produce a combined AFM/LFM/STM from a quartz crystal resonator with many theoretical benefits over other sensors.

### 6.1.1 Combining NC-AFM and DLFM

For a sensor to image as both an NC-AFM and a DLFM it must be able to oscillate both normal to and parallel to the surface it is scanning. The simplest method for achieving this is a single oscillator which will oscillate in different directions depending on the eigenmode excited. Ideally for atomic resolution imaging the effective spring constant of the excited eigenmode should be low [158]. However, as the spring constant normal to the surface lowers, the risk of the probe snapping to contact with the surface increases. This produces a problem for combined AFM/LFM using the principal and first torsional eigenmode of a

## Optimal geometry for a quartz multi-purpose SPM sensor

cantilever, as the torsional mode can have an effective spring constant of up to approximately two orders of magnitude higher than the principal mode [157]. This results in a difficult trade off. To avoid snap to contact, the following condition must be satisfied: [151]

$$A_0 k_N + F_{\text{TS},N} > 0, \quad (6.1)$$

where  $A_0$  and  $k_N$  are the amplitude and effective spring constant of the principal eigenmode, and  $F_{\text{TS},N}$  is the tip-sample force normal to the sample.

For high resolution AFM imaging  $A_0$  should be as low as possible [158]. However, the signal-to-noise ratio, which is a function of  $A_0$ , [116] limits the minimum amplitude. Experimentally some groups have achieved stable imaging with amplitudes as low as 20pm [35]. Thus, to be safe from snap to contact for atomic forces of order -3 nN, it is required that  $k_N > 150 \text{ N.m}^{-1}$ . If imaging, however, is only in DLFM mode, then  $A_0$  is ideally zero. Obviously, Equation 6.1 doesn't hold in this case as it would suggest that we require an infinite spring constant to stop snap to contact. In this example  $A_0$  must be considered as the distance the tip has moved from its equilibrium position due to  $F_{\text{TS},N}$ . Therefore, if trying to image in DLFM mode, the error in z-position due to normal forces is inversely proportional to  $k_N$ , requiring higher minimum normal spring constants of  $k_N \gtrsim 1\text{--}3 \text{ kN.m}^{-1}$ . This would result in torsional constants of order of hundreds of  $\text{kN.m}^{-1}$ , which is not ideal for LFM imaging.

The torque required to torsionally twist a beam of length  $L$  through an angle  $\theta$  is given by

$$T = \frac{\theta JG}{L}, \quad (6.2)$$

where  $J$  and  $G$  are the torsion constant and shear modulus of the beam. In the case of a cantilever beam with a tip of length  $L_{\text{tip}}$  (measured from the central axis of the beam), the lateral displacement of the tip apex,  $A_{\text{lat}}$ , is  $L_{\text{tip}}\theta$ . Replacing the torque with the lateral tip sample force  $F_{\text{TS},L}$  multiplied by the tip length we get

$$F_{\text{TS},L} = \frac{A_{\text{lat}} JG}{L L_{\text{tip}}^2}. \quad (6.3)$$

Hence, the lateral spring constant

$$k_L = \frac{JG}{LL_{\text{tip}}^2}, \quad (6.4)$$

is inversely proportional to the square of the tip length. Thus, the tip length becomes an important parameter to consider alongside the more typical geometrical constants associated with the normal spring constant.

For quartz sensors the obvious choice of cantilever is the standard qPlus sensor with a normal spring constant of approximately  $1.8 \text{ kN.m}^{-1}$  [154, 159]. For commercially available silicon cantilevers the spring constants are usually less than  $50 \text{ N.m}^{-1}$ , with resonant frequencies of 200–300 kHz. The resonant frequency of the cantilever scales with  $L^{-4}$  and the spring constant with  $L^{-3}$ . Considering that the torsional eigenfrequency can be approximately two orders of magnitude larger than the normal eigenfrequency, achieving the necessary normal spring constant by length reduction could push the torsional eigenfrequency into GHz which is impractical. We instead will consider different rectangular cross sections for a  $200 \mu\text{m}$  long silicon beam.

A range of rectangular cross sections which would produce a normal spring constant of  $2 \text{ kN.m}^{-1}$  for a  $200 \mu\text{m}$  long beam have been calculated using Euler-Bernoulli beam theory, see Table 6.1. The frequency of the first eigenmode has also been calculated. Using Equation 6.4, the tip length needed for  $k_L = 2 \text{ kN.m}^{-1}$  was calculated, using previously tabulated values for  $J$  [160]. This tip length was also calculated for the qPlus sensor.

The calculated tip lengths range from approximately 10% to 70% of the beam length. As has previously been shown, AFM sensors with tip lengths of similar scale to the length of the beam exhibit a large lateral component to the motion of the tip apex in the first eigenmode [145]. This lateral component is perpendicular to the torsional eigenmode, thus making it impossible to truly separate the normal and lateral forces. This problem is exacerbated if the tip length is further increased to increase sensitivity to lateral forces by reducing the lateral spring constant as snap to contact is not an issue in the lateral direction. Increasing the ratio of thickness to width reduces the required tip length, but at the expense of introducing normal eigenfrequencies above 1 MHz, pushing

## Optimal geometry for a quartz multi-purpose SPM sensor

Name	$L$ ( $\mu\text{m}$ )	$w$ ( $\mu\text{m}$ )	$T$ ( $\mu\text{m}$ )	$k_N$ ( $\text{N.m}^{-1}$ )	$f_N$ (Hz)	$L_{\text{tip}}$ ( $\mu\text{m}$ )	$L_{\text{tip}}/L$
Si1	200	112.2	15.0	2 000	515 913	139.1	0.696
Si2	200	47.3	20.0	2 000	687 884	124.6	0.623
Si3	200	24.2	25.0	2 000	859 856	93.1	0.466
Si4	200	14.0	30.0	2 000	1 031 827	57.2	0.286
Si5	200	8.8	35.0	2 000	1 203 798	33.7	0.168
Si6	200	5.9	40.0	2 000	1 375 769	20.5	0.102
qPlus	2 400	130.0	214.0	1 763	32 246	772.9	0.322

Table 6.1: *Dimensions and dynamic properties of silicon microcantilevers which would provide normal spring constants of  $2 \text{ kN.m}^{-1}$ .  $L_{\text{tip}}$  is the tip length required to provide a lateral spring constant of  $2 \text{ kN.m}^{-1}$ . qPlus sensor is also included (the frequency is not  $32\,768 \text{ Hz}$  as some features, such as base deformations and gold contacts, were neglected in the calculations).*

torsional eigenfrequencies to ranges which most AFM electronics cannot handle.

## 6.2 Non-cantilever geometries

Due to the large difference between the operating frequencies of normal and torsional modes, and the coupling of unwanted lateral motion into the normal eigenmode for sensors with the tip lengths needed to produce low lateral spring constants, we propose a new sensor geometry. The proposed design, see Figure 6.1, is to attach a tungsten tip to the centre of a quartz beam. The design exploits the intrinsic symmetry of the sensor to remove any unwanted lateral motion in the principal eigenmode (Figure 6.1(b)), thus allowing for longer tips. By exciting the second eigenmode of the beam, lateral motion can be generated (Figure 6.1(c)). The effective spring constant and eigenfrequency can be calculated, and thus tuned, far more simply than for torsional modes, by solving the Euler-Bernoulli beam equation with the appropriate boundary conditions. In principle, by also exciting a torsional mode, a perpendicular lateral oscillation could be generated allowing simultaneous measurements in *all three dimensions*. This chapter will, however, concentrate on just the first and second eigenmode.

## Optimal geometry for a quartz multi-purpose SPM sensor

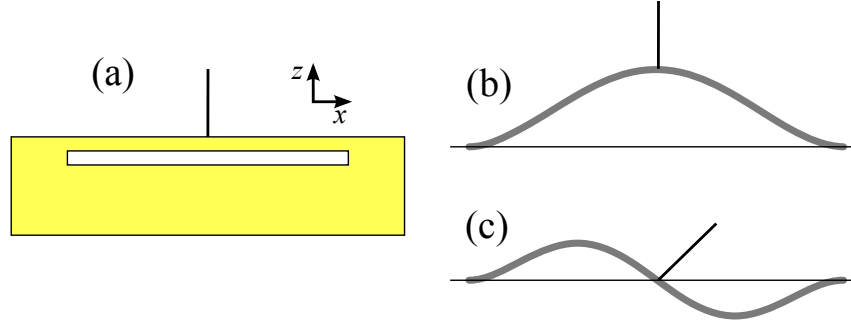


Figure 6.1: (a) *Proposed geometry of new sensor. A tungsten tip connected to the centre of a quartz bar clamped at both ends. (b) and (c) First and second eigenmode of the sensor. The symmetry provides pure normal motion in the first eigenmode and lateral motion of the tip apex in the second eigenmode due to the rotation of the tip about the node of the beam.*

### 6.2.1 Dynamic properties of symmetrical sensors

#### 6.2.1.1 Spring constants

The two most fundamental properties to consider for dynamic force sensors are the effective spring constants and the eigenfrequencies of each imaging mode. For simplicity we will begin with effective spring constants as the influence of the tip's inertia has only the effect of moving the dynamic spring constant closer to the static constant [138], removing the  $\sim 3\%$  error. (Note that this is not true in higher eigenmodes for cantilever geometries as the inertia shifts the position of the antinodes [140] In this system, however, the antinodes are pinned due to the symmetry of the system.)

As in Chapter 4, we use the dynamic Euler-Bernoulli beam equation

$$EI \frac{\partial^4}{\partial x^4} \left( \sum_{i=1}^{\infty} \Phi_i(x) \mathcal{T}_i(t) \right) = f(x, t) - \rho A \frac{\partial^2}{\partial t^2} \left( \sum_{i=1}^{\infty} \Phi_i(x) \mathcal{T}_i(t) \right), \quad (6.5)$$

to describe the dynamic deformations of a beam, where  $E$  and  $\rho$  are the Young's modulus and density of the material respectively.  $A$  and  $I$  are the area and second moment of area of the beam's cross section.  $f(x, t)$  is the applied force per unit length acting on the beam,  $\Phi_i(x)$  and  $\mathcal{T}_i(t)$  are the spatial and temporal components of the beam's deformation for the  $i$ th eigenmode.

As any effect from the tip must be considered at the centre of the beam we

## Optimal geometry for a quartz multi-purpose SPM sensor

will consider only one half of the beam and use symmetry (or anti-symmetry in the case of even eigenmodes) to construct the full spatial solution. For both even and odd modes the boundary conditions

$$\Phi_i(0) = 0 \quad (6.6)$$

$$\frac{\partial\Phi_i(0)}{\partial x} = 0 \quad (6.7)$$

are valid. Equation 6.5 is spatially fourth order, therefore two further conditions are required. For odd modes:

$$\frac{\partial\Phi_{i,\text{odd}}(L/2)}{\partial x} = 0 \quad (6.8)$$

$$EI \frac{\partial^3\Phi_{i,\text{odd}}(L/2)}{\partial x^3} = \frac{F_{\text{norm}}}{2}, \quad (6.9)$$

and for even modes:

$$\Phi_{i,\text{even}}(L/2) = 0 \quad (6.10)$$

$$EI \frac{\partial^2\Phi_{i,\text{even}}(L/2)}{\partial x^2} = -\frac{T}{2}. \quad (6.11)$$

$L$  is the length of the entire beam, and  $F_{\text{norm}}$  and  $T$  are the force and torque applied to the centre of the beam.

Entering these boundary conditions into the general static spatial solution of Equation 6.5 (i.e the final term is zero), gives the spring constant of the first eigenmode as

$$k_{\text{norm}} = \frac{192EI}{L^3}. \quad (6.12)$$

Considering the torque on the centre of the beam  $T = L_{\text{tip}}F_{\text{lat}}$ , where  $F_{\text{lat}}$  is a lateral force applied in the  $x$  direction at the far end of the tip, the effective lateral spring constant of the second eigenmode is

$$k_{\text{lat}} = \frac{16EI}{LL_{\text{tip}}^2}. \quad (6.13)$$

Full derivations are provided in Appendix C.

Thus, just as in the case of the torsional mode, the effective spring constant

in the lateral mode can be tuned by tip length. However, due to the symmetry of the sensor this will not cause unwanted lateral motion at the tip apex in the first eigenmode.

### 6.2.1.2 Eigenfrequencies

When considering the eigenfrequencies of the sensor, the inertia of the tip plays a very strong role which cannot be ignored. Solving Equation 6.5 for the dynamic case, the same boundary conditions (Equations 6.6–6.11) hold, where

$$F_{\text{norm}} = -m_{\text{tip}}\omega_{i,\text{odd}}^2 \Phi_{i,\text{odd}}(L/2) \quad (6.14)$$

and

$$T = -\mathcal{I}_{\text{tip}}\omega_{i,\text{even}}^2 \frac{d\Phi_{i,\text{even}}(L/2)}{dx}. \quad (6.15)$$

$\omega_i$  is the angular eigenfrequency of the  $i$ th eigenmode. By combining the general spatial solution with the four boundary conditions as a matrix equation, equal to a zero vector, we see that resonance occurs when the determinant is equal to zero (See Appendix C for full derivation). This yields the following resonance conditions:

$$\begin{aligned} & \cosh(\beta_{i,\text{odd}}L/2) \sin(\beta_{i,\text{odd}}L/2) + \cos(\beta_{i,\text{odd}}L/2) \sinh(\beta_{i,\text{odd}}L/2) \\ & + \frac{1}{2\gamma_{i,\text{odd}}} \left( -1 + \cos(\beta_{i,\text{odd}}L/2) \cosh(\beta_{i,\text{odd}}L/2) \right) = 0, \end{aligned} \quad (6.16)$$

and

$$\begin{aligned} & \cosh(\beta_{i,\text{even}}L/2) \sin(\beta_{i,\text{even}}L/2) - \cos(\beta_{i,\text{even}}L/2) \sinh(\beta_{i,\text{even}}L/2) \\ & + \frac{\epsilon_{i,\text{even}}}{2} \left( -1 + \cos(\beta_{i,\text{even}}L/2) \cosh(\beta_{i,\text{even}}L/2) \right) = 0, \end{aligned} \quad (6.17)$$

where

$$\beta_i^4 = \frac{\rho A \omega_i^2}{EI}, \quad \gamma_i = \frac{EI \beta_i^3}{m_{\text{tip}} \omega_i^2}, \quad \epsilon_i = \frac{\mathcal{I}_{\text{tip}} \omega_i^2}{EI \beta_i}. \quad (6.18)$$

## Optimal geometry for a quartz multi-purpose SPM sensor

These equations can be solved numerically in terms of dimensionless quantities ( $\beta_i L, m^*, \mathcal{I}^*$ , discussed in Appendix C), and dimensions can be added later to get a value for  $\omega_i$ . In the case of no tip, the ratio between the second and first eigenmode is 2.757. Whether this ratio rises or falls when a tip is added depends on the dimensions of both the tip and sensor. It is clear, however, that such a low ratio between the eigenmodes is another advantage of the symmetrical sensor over torsional designs as both modes can be tuned to near the optimal frequency of the detection system.

### 6.2.2 Optimal geometry for a symmetrical sensor

In order for the sensor to be used in currently available commercial UHV combined AFM/STM systems, it should be similar in size to the qPlus sensor. However, as the normal spring constant per unit beam length (with the same cross section) is 64 times higher than for a cantilever geometry, a greater length than the 2.4 mm beam of the qPlus sensor is advisable.

Choosing a 3 mm long beam, and a normal spring constant of  $2 \text{ kN}\cdot\text{m}^{-1}$ , as previously suggested, we calculate that the second moment of area of the cross section should be  $I=3.68 \times 10^{-18} \text{ m}^4$ . A width (y-direction),  $w$  of  $100 \text{ }\mu\text{m}$ , would result in a thickness (z-direction) of  $t = 76.1 \text{ }\mu\text{m}$ , as  $I = wt^3/12$ . Such a beam would have first and second eigenfrequencies of 46.7 kHz and 128.8 kHz respectively. These frequencies will reduce when the tip is added to the centre of the beam.

Before considering the mass or moment of inertia of the tip and its effect on the eigenfrequencies of the sensor, it is important to consider the spring constant of the tip itself. Any bending of the tip will not be detected by the piezoelectric quartz sensor. Thus, treating the tip as a cantilever, its spring constant must be much greater than the effective lateral spring constant for the sensor ( $k_{\text{lat}}$ ), otherwise this will result in incorrect force measurements in the LFM mode. Considering a maximum tip length of 1.73 mm, the length which would give  $k_{\text{lat}} = 500 \text{ N}\cdot\text{m}^{-1}$ , to keep the tip's spring constant above  $10 \text{ kN}\cdot\text{m}^{-1}$  the diameter of the tungsten wire must be greater than  $144 \text{ }\mu\text{m}$ .

We will consider a tip diameter,  $D_{\text{tip}}$ , of  $150 \text{ }\mu\text{m}$ , an easily available diameter

## Optimal geometry for a quartz multi-purpose SPM sensor

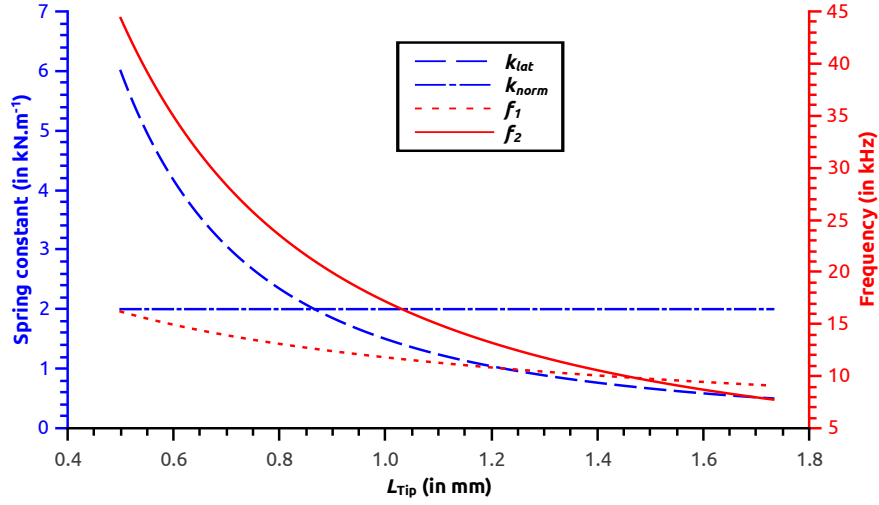


Figure 6.2: The effective spring constants ( $k_{\text{lat}}$  for mode 2, and  $k_{\text{norm}}$  for mode 1) and eigenfrequencies of the first two eigenmodes of a symmetrical sensor. Plotted for 150  $\mu\text{m}$  tungsten tips of varying lengths.

of tungsten wire. The moment of inertia of the tip for the even modes should be calculated about the centre of the beam,  $t/2$  from the bottom of the tip, and hence a distance of  $(L_{\text{tip}} + t)/2$  from the tip's centre of mass. Thus the moment of inertia of the tip can simply be calculated by the parallel axis theorem as  $\mathcal{I}_{\text{tip}} = m_{\text{tip}}(D_{\text{tip}}^2/16 + L_{\text{tip}}^2/3 + L_{\text{tip}}t/2 + t^2/4)$ . Using Equations 6.13 and 6.16–6.18, the spring constants and eigenfrequencies of the first two modes have been plotted in Figure 6.2 for a range of tip lengths. For plotted tip lengths the ratio of the spring constant of the tip to  $k_{\text{lat}}$  is at minimum 23.5.

Examining the plot it is clear that tip lengths near 1.47 mm are unusable as the two eigenfrequencies are too close. This would make it difficult to selectively excite them, as well as requiring long averaging times in bimodal operation to remove any correlation between the modes.

The benefit of increasing the tip length is a reduction in lateral spring constant which comes at the price of lower eigenfrequencies. A tip length of 1 mm would provide eigenfrequencies of  $f_1=11.8$  kHz and  $f_2=17.2$  kHz, with  $k_{\text{lat}}= 1.50$  kN.m<sup>-1</sup>. As these frequencies are of the same order of magnitude as qPlus sensors with long tips, the sensor could be used in commercially available qPlus systems with no modifications to the electronics.

It is also important to consider the minimum amplitudes achievable by the sensor, particularly in the lateral mode. As little is known about the optimum amplitudes in DLFM, the issue will be treated approximately. The lateral amplitude of the tip apex is

$$A_{\text{lat}} = L_{\text{tip}} \frac{d\Phi_2(L/2)}{dx}. \quad (6.19)$$

By considering that the tip is approximately half the length of the beam ( $L/2$ ), and  $\frac{d\Phi_2(L/2)}{dx} \approx \frac{4A_{\text{anti-node}}}{L}$  (approximating Figure 6.1(c) as 3 straight lines), where  $A_{\text{anti-node}}$  is the amplitude of the anti-node. Thus, the ratio between  $A_{\text{lat}}$  and  $A_{\text{anti-node}}$  is of order 2. Other detection parameters are also of the same order of magnitude as for a qPlus sensor. Thus, as qPlus sensors have achieved imaging with amplitudes as low as 20pm [35], similar amplitudes are in theory possible for the LFM mode of the symmetrical sensor. Such amplitudes are an order of magnitude smaller than inter-atomic distances.

### 6.2.3 Experimental viability

The experimental viability of this method depends on the equipment available to produce the sensor. Firstly, no quartz crystal resonators of the proposed geometry are commercially available. The closest commercially available sensor is a double-ended tuning fork available from Statek (DETF Force Sensor, [statek.com](http://statek.com)). By fixing the bottom tine it is possible to reproduce the required symmetry. However, these sensors are too large for most commercial qPlus systems with a total width of 15.2 mm and a beam length of 8.44 mm. Also the beams are recessed with respect to the top of the resonator by 0.86 mm, preventing tip lengths below this. A second possible option would be to attach two identical tuning forks end-to-end using a similar method to Heyde *et al.* [120]. However, the glue used to attach the tines will have different mechanical properties to the quartz, which also depend on the quantity, placement, and curing conditions. This will affect the repeatability, as well shape of the eigenmodes, and hence the spring constant. Thus, ideally custom resonators would need to be made.

Secondly, the correct placement of the tungsten wire is vital. The tip needs to be positioned in the centre of the 3 mm beam, which is just  $100 \times 76.1 \mu\text{m}$  in cross section, and needs to be mounted perfectly normal to the beam. Misplacement of the tip breaks the symmetry, thus affecting operation. Reproducible tip placement requires three dimensional micro-manipulators, which can be prohibitively expensive for some groups.

A final consideration should be taken regarding the connection of a separate electrode for the tunnel current. Two options are available. First a thin ( $\sim 15\text{-}50\mu\text{m}$ ) loose wire could be attached to the tungsten tip, as is often done for qPlus sensors. This is inadvisable as it also breaks the symmetry of the sensor. Another method would be to add a thin insulating layer to the top side of the resonator and on top of that a new electrode, such as the method developed by Nauga Needles [161]. Although this maintains the symmetry, great care needs to be taken to consider the possibility of capacitive cross-talk between the tunnelling and deflection channels [162].

### 6.3 Conclusion

We have proposed a new geometry of a piezoelectric sensor for use in combined AFM/LFM, which utilises symmetry to bring the eigenfrequencies and spring constants of the two modes closer together. This allows both modes to be tuned to the optimal parameters for operation. The symmetry also removes issues with unwanted lateral motion in normal oscillating modes, allowing longer tips for tuning the lateral spring constant of the LFM operation. By attaching an extra electrode, the sensor can also be used for STM providing a truly multi-purpose SPM sensor.

# Chapter 7

## Automated Tip Conditioning

*“I think a nerd is a person who uses the telephone to talk to other people about telephones. And a computer nerd therefore is somebody who uses a computer in order to use a computer.”*

Douglas Adams

### Chapter Overview

Chapter 5 detailed experiments which fundamentally depend on the state of the AFM tip. More generally, all AFM and STM experiments rely on the tip state to achieve the desired resolution, even if the exact termination is not important. In this chapter we detail our efforts to automate conditioning of the tip apex, with the end goal being an SPM which can both determine and modify its own tip apex. Early work in this chapter on HOPG was published in Applied Physics Letters [163]. Later work on Silicon is largely unpublished with one result being presented in a separate paper [164] on the SPM image analysis described in Chapter 8.

### 7.1 Introduction

In any SPM experiment, before any useful data can be collected the tip (probe) itself must be in a good state. Reliable methods for tip conditioning become of even more importance when experiments require specific molecular tip termina-

## Automated Tip Conditioning

tions [12, 35]. Often a large proportion of time is spent initially conditioning the tip, or re-conditioning a tip which has lost the desired resolution. Therefore, it makes sense that any approach to automating SPM experiments must be able to perform this conditioning. This chapter describes efforts taken to automatically condition SPM tips. All the work been performed using STMs, but with the aim to port these procedures to qPlus AFM.

To emphasise the need for tip conditioning Figure 7.1 shows some examples of the types of images regularly acquired during STM imaging. The difficulty with STM tip preparation is that it is not only difficult to identify the cause of bad images, but even if the cause has been identified it is generally impossible to correct it in any controlled manner. For example Figure 7.1(a), shows image features changing almost every scan line. This suggests that the tip is unstable and changing as the image is produced. Perhaps the user hypothesises there is a small flake of graphite on the tip which changes orientation almost every scan line. Even if this hypothesis is correct, there is no direct method for removing the graphite. Common procedures for tip conditioning are: voltage pulses, high current scanning and tip crashing. Each of these procedures can change the termination of the tip, but the induced change is arbitrary and regularly just changes the problem rather than solving it.

For a voltage pulse the sample bias is suddenly raised to of order 10 V. Considering that the tip is approximately 5 Å from the surface this will produce an electric field of order  $2 \times 10^{10} \text{ Vm}^{-1}$ . Such a field can move adsorbed molecules or rearrange atoms at the end of the tip.

High current scanning in the constant current STM mode requires the tip to be very near to the surface. If this is combined with low feedback gains or high scan speeds then the feedback controller does not always have time to track the surface adequately. This can lead to material being removed from the end of the tip, or the tip picking up pieces of the surface, leading to a change in tip state.

Tip crashing involves using the  $z$  actuator to drive the tip a controlled distance into the sample. This can cause the sample to become bonded to the tip. This can be performed on clean surfaces with the aim that as the tip and sample separate the resulting tip structure will be sharper than the initial tip structure, leading to clear imaging. This can also be performed above molecules

## Automated Tip Conditioning

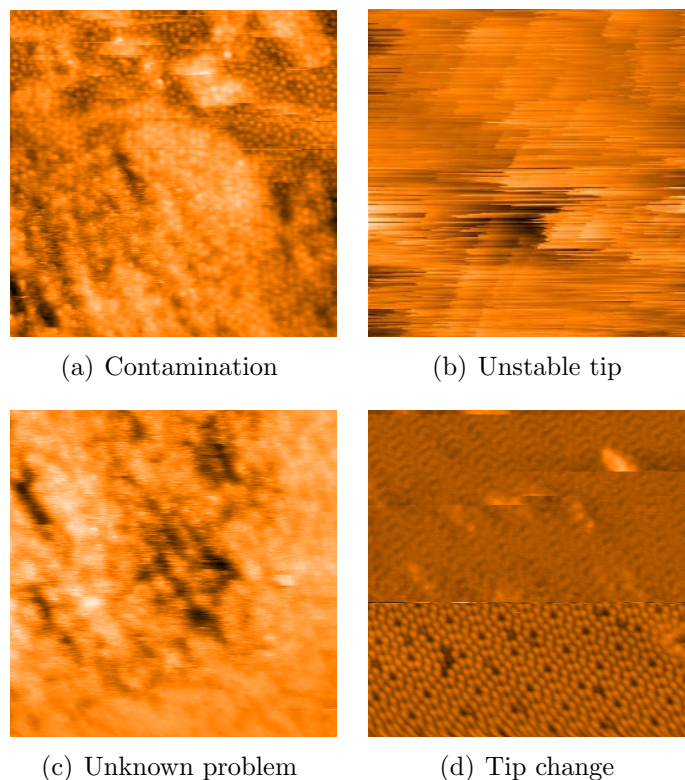


Figure 7.1: *A series of poor quality STM images which would never normally make it into a publication. Identifying the cause of the problem can be a difficult task even for experienced STM users.*

on the surface to attempt to coerce the molecule to bond to the tip if molecular termination is desired (as was described in Chapter 5).

The first attempts at automated tip conditioning were performed with an entry level ambient STM (Nanosurf EasyScan 2), scanning HOPG with Pt/Ir tips. HOPG, as mentioned in Section 3.1.1, is an ideal surface to be studied with such a microscope as it is easy to prepare and can be scanned with atomic resolution in air for days without quality degrading. Another advantage of HOPG is that images often result from a sliding of one layer over another causing an averaged image free of step edges and defects [165]. As such, these HOPG images are not true atomic resolution images. Nonetheless, the uniformity of the images allows for simple metrics to determine quality while tip conditioning algorithms are developed. However, despite the simplicity of the final HOPG images it is not the easiest surface to scan, as the layers of graphite are only bonded by van

## Automated Tip Conditioning

der Waals forces, and tip conditioning procedures can therefore lead to flakes of graphite becoming attached to the tip. These flakes bond weakly to the tip resulting in a physically unstable termination.

Further work on automated tip conditioning has been performed under room temperature UHV conditions on the Si(111)  $7 \times 7$  reconstruction. This is a more difficult surface for image analysis, as features such as corner holes, defects, contamination, and step edges can be present in high quality images. For this work more specialised image analysis routines were developed. These routines are discussed in detail in Chapter 8.

## 7.2 Image Analysis for HOPG images

To automate an optimisation process one must be able to assess the current state of the process. In the case of automated SPM tip conditioning this requires the quality of the tip apex for imaging to be assessed. To do this the collected images need to be analysed. For optimisation on HOPG it was decided that the best method was to compare collected scans with ideal images generated from theory. Data from Cisternas *et. al.* [50] was used to generate ideal scans.

For simplicity, the automation software only collected images with one of four sizes:  $200 \times 200 \text{ nm}^2$ ,  $50 \times 50 \text{ nm}^2$ ,  $20 \times 20 \text{ nm}^2$ , and  $4 \times 4 \text{ nm}^2$ . The image analysis of  $200 \times 200 \text{ nm}^2$  and  $50 \times 50 \text{ nm}^2$  was generally the same and served simply to check for a flat image, not specific structure. Smaller images of size  $20 \times 20 \text{ nm}^2$  and  $4 \times 4 \text{ nm}^2$  scans each had their own analysis methods to check for structure. Sample tilt was removed from all images via plane subtraction before any further processing was performed.

### 7.2.1 Large Size Image Analysis

Scans of graphite with a width in excess of 50 nm are not expected to show clear atomic structure at the pixel densities used ( $256 \times 256 \text{ px}^2$ ). Instead, a good scan should be flat with a surface roughness measured in Ångstroms. To account for distortions often seen on large scale scans, surface roughness was estimated from the residuals of second order polynomial lines fitted through each row and

## Automated Tip Conditioning

column of the final image. This was performed for simplicity compared to fitting second order polynomial planes [166]. Polynomial plane fitting was introduced into the image analysis code after the HOPG project was completed.

Images which were determined not to be flat were then divided into one of two different classes of bad images which we defined as “cloudy” and “streaky” images. Streaky images (for example, Figure 7.1(b)) are images where there is a clear tip instability, whereas cloudy images (for example Figure 7.1(c)), result from an unknown cause, but tend to show less fast changes in image contrast. These two types of images were compared using the universal similarity metric (USM) [167]. The USM compares the information needed to compress the image under analysis with and without the information contained in target images. Smaller compressed files relate to images being more closely related to the target. The USM, however, is not discussed in more detail in this thesis as its performance on analysing STM images was poor and was eventually removed from the image analysis.

### 7.2.2 Target-Driven Image Analysis

For images with a width of 20 nm or less it is possible to resolve carbon atoms in a  $256 \times 256$  px<sup>2</sup> image. Before comparing such images to target images they were checked for the expected periodicity by applying a 2D fast Fourier transform (FFT). If the measured spatial frequency was below the expected frequency then the image is classified as not having atomic resolution; if it is above then this suggests a low signal-to-noise ratio. This simple test for atomic resolution was possible due to the lack of contamination and defects on HOPG images, combined with the simplicity of the Fourier space image.

Further analysis was performed on images with recognised atomic resolution. The logarithm of the measured power spectra of the scans was correlated with expected power spectra calculated from the target images. The correlation coefficients were used to further define the quality of the resolution. For  $20 \times 20$  nm<sup>2</sup> scans this was the final test, as further analysis of scan quality is difficult as the atomic spacings are only  $\sim 3$  pixels.

$4 \times 4$  nm<sup>2</sup> images were further analysed by counting the peaks in the power

## Automated Tip Conditioning

spectrum. Due to the trigonal symmetry of the lattice six Fourier peaks are expected. Extra peaks are often found in noisy or doubled images, which sometimes could pass the correlation test.

Scans passing all tests up to this point have atomic resolution, with the correct symmetry for graphite. To accurately classify the quality of the image it needs to be compared to the target in real space. For this the atomic positions and rotation of the lattice must be calculated, so that the ideal image can be positioned correctly for comparison. Atomic positions were found by convolving the image with a  $5 \times 5$  pixel Gaussian with a standard deviation of one pixel to remove noise. After noise removal, all regional maxima are found. After removing the lower of any pairs of maxima too close together to be neighbouring atoms these positions are recorded as the atomic positions. The rotation of the lattice can be found simply by a Radon transform [168]. Once the atomic positions and lattice rotation have been found the image can be compared with a correctly rotated unit cell of the ideal image at every atomic position. The comparison was done by calculating the robust mutual information (RMI) [169] of the images, as explained in Appendix D.1. The average of the RMI values for each point is used as a measure of image quality. Figure 7.2 shows a selection of scans and their RMI scores.

As mentioned in Section 3.1.1, two types of image can be formed in STM of HOPG, either images with trigonal symmetry showing just  $\beta$ -sites in the lattice, or images with a honeycomb structure showing all images in the lattice. All methods above are calculated for both trigonal and honeycomb ideal images. This allows not only the quality to be assessed but also the type of resolution to be ascertained (see Figure 7.2).

## 7.3 Image Analysis for Silicon

As the project moved into UHV conditions using the Silicon (111)  $7 \times 7$  reconstruction as a test surface a decision was made to move away from target driven image analysis to metrics which could be applied to a much wider variety of surfaces. This was done to make the tip conditioning protocol more easily portable to other surfaces without sweeping changes to the analysis. The code for this new

## Automated Tip Conditioning

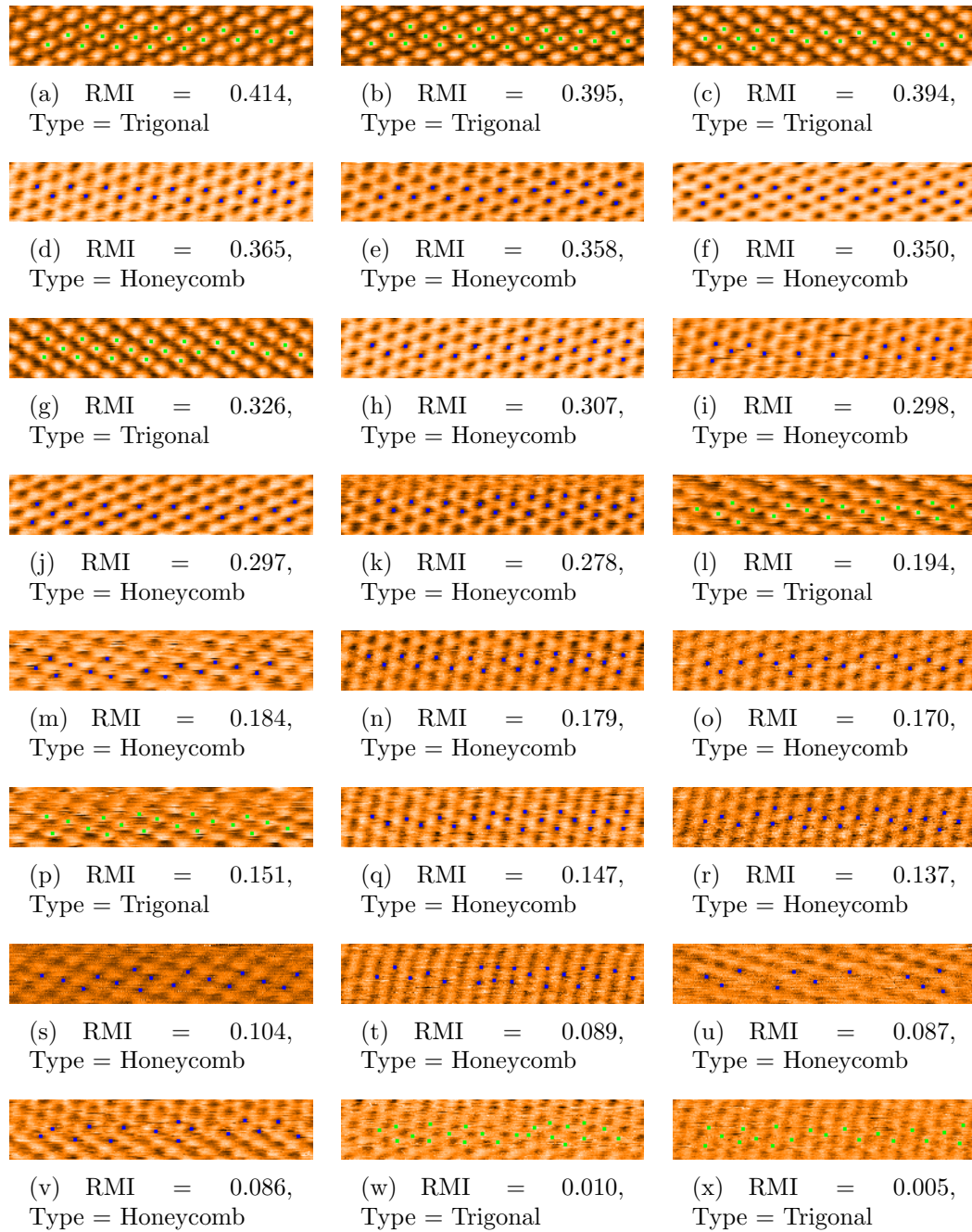


Figure 7.2: *RMI scores for a selection of STM scans. The same program was run for all images, calculating the RMI for a trigonal and a honeycomb target. The highest RMI has been output along with the image type detected. Green dots indicate image registration points (atoms) for trigonal images, blue dots indicate image registration points (local minima) for honeycomb images.*

generalised automated SPM image analysis was made into an open-source MATLAB toolbox called SPIW (scanning probe image wizard). As SPIW is discussed in detail in Chapter 8, this section will concentrate on how SPIW features were applied to classify images rather than how the image analysis was performed.

### 7.3.1 Analysing large scale images

As with HOPG, for images of large areas (in this case images with widths of 128 nm or 64 nm with 512 points per line) surface roughness was used to determine images of sufficient quality (see Section 8.2.4). However, due to the presence of contamination, large surface defects, and step edges the entire image cannot be assessed at once. Instead, if step edges were located (Section 8.2.2) the image was divided into terraces which (if above a threshold size) were each analysed separately. When analysing individual terraces, they were flattened with high and low regions masked (Section 8.2.1), surface roughness was then determined only for non-masked regions. Figure 7.3 shows examples of this image analysis being performed. Information on the surface roughness of terraces and on the positions of located step edges were passed back to the optimisation software.

### 7.3.2 Target-Free Small Image Analysis

While target-free image analysis was used to assess the quality of the Si(111)  $7 \times 7$  reconstruction image, some information about the surface was still required, including, for example, the expected number of atoms per unit area and expected corrugation heights. As for the large scale images, steps, defects, and contaminated regions in the image must be detected and handled separately from the clean areas of the sample.

A separate method for finding the step edges is used instead of the method used for larger images. This is due to the steep gradients present in atomic resolution images which can get misidentified as step edges. This new method, described in full in 8.3.1, first detects atomic positions and uses only the heights of atomic maxima to create a new image which can be analysed for steps.

Once terraces have been separated, contamination and defects can be removed from the image again by thresholding. For this thresholding method maxima

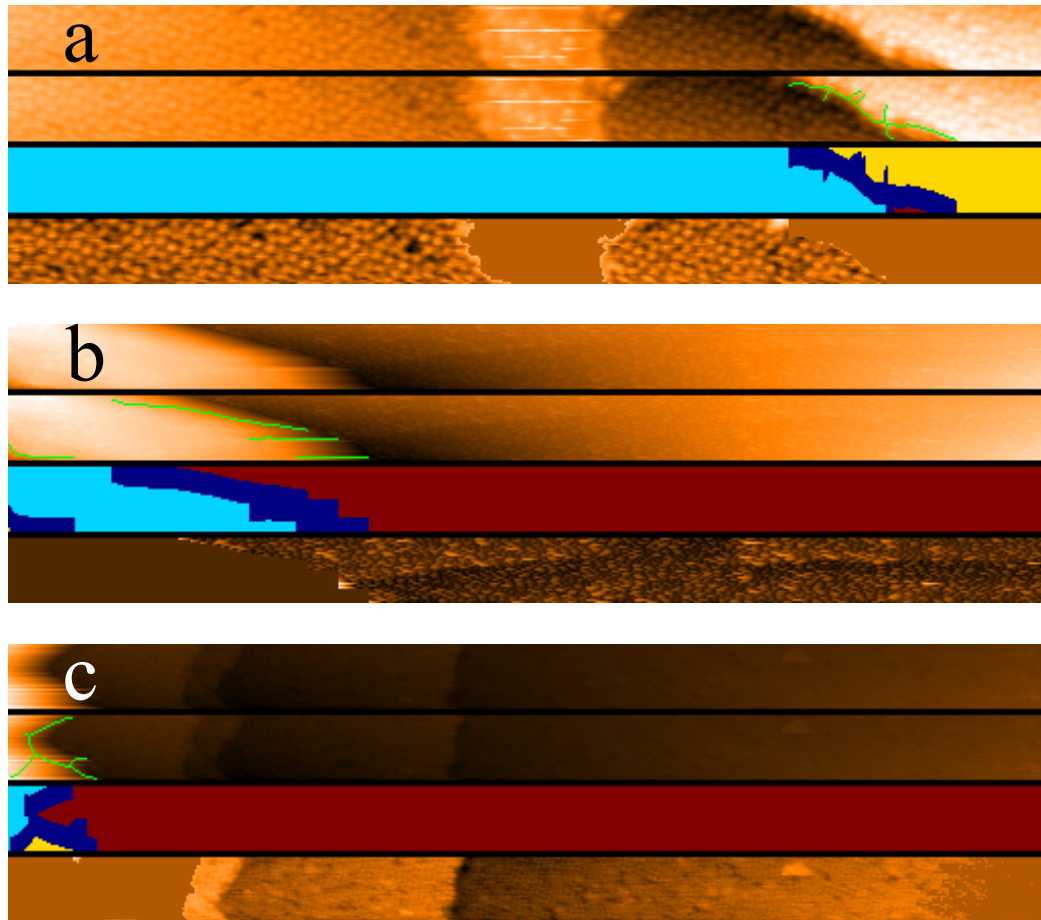


Figure 7.3: *Finding flat regions of large scans. The four sub-images in (a), (b), and (c) correspond to: The raw STM scan after plane fitting (Top). The position of step edges or the edges of large contamination, traced in green (Second). A colourmap representation of areas in the image where blue represents edges, and other colours define separate regions (Third). Plane fitted image of the largest region with any further contamination removed.*

and minima are located, and the median maxima and minima heights are used to define the atomic corrugation. Anything significantly higher or lower can be masked as contamination or surface defects. More detail on this method is provided in Section 8.2.1.

From the remaining image the quality has to be assessed. This is done by masking and analysing features located at the position of located maxima. This is done using the features described in Section 8.2.3. From these located features the height and the circularity of the atoms are returned to the optimisation

## Automated Tip Conditioning

software. Only clearly resolved features are used for generating these statistics, and features appearing merged are ignored (see Figure 7.4). The number of atoms used for these statistics is also returned to the optimisation software. An image with only a few-resolved, highly-circular atoms is most likely a highly contaminated surface, image with a good tip. Whereas an image with a number of resolved atoms close to the number expected in an ideal image, but with low circularity would imply a clean surface convolved with the structure of the tip.

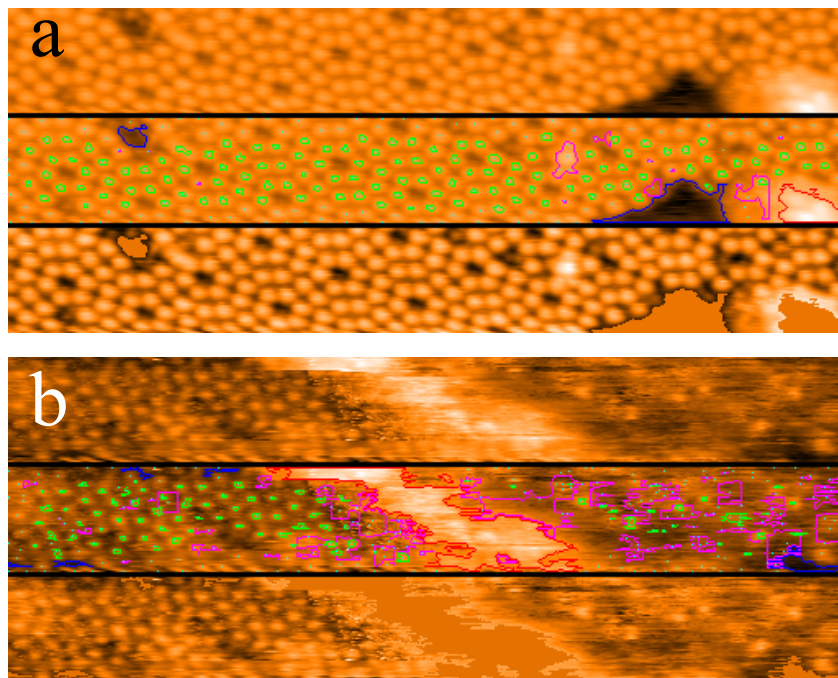


Figure 7.4: *Computer vision interpretation of a scan of Si(111)  $7 \times 7$  reconstruction. Cyan pixels represent maxima, green traces represent atoms, magenta traces represent areas in which atomic structure appears merged, red traces represent contamination and blue traces surface defects. Final image shows scan after contamination and defects are masked out. (a) shows that if the scan is uniform the contrast is greatly increased, however (b) shows that treating the image as a whole can lead to poor analysis.*

## 7.4 Optimisation protocols

Optimising the scan quality requires not only the ability to measure the quality of the scan but also to make decisions about how to improve the quality. This

## Automated Tip Conditioning

has been broken down into two tasks which are solved separately. Firstly, coarse conditioning, i.e. taking the STM tip from a state where images are purely tip artefacts to the point where atomic resolution can be seen. Secondly, fine tuning where the quality of atomic resolution is improved until an acceptable image quality is achieved.

### 7.4.1 Deterministic Coarse Conditioning

The coarse conditioning procedure is a series of rules specified to the software which decide how it will act when it scans certain image types recognised by the image analysis software. Consecutive scans of the same type increment counters so the software can perform more aggressive tip conditioning if the current method is having little to no effect. It is described as deterministic as, given the same sequence of images, it will always make the same decisions.

This method has been successfully applied to scanning HOPG and the Si(111)  $7 \times 7$ . The decision trees have been significantly changed between the two surfaces. This does not necessarily indicate that standard procedures could not be developed, but instead that when changing from HOPG, where surface defects and contamination are so rare, to Si(111), where they are common, major changes to the method were needed. However, for this method to truly be effective and general the system will need to be able to change the decision trees to learn from the past.

#### 7.4.1.1 HOPG Coarse Conditioning

Coarse conditioning on HOPG was started by taking  $200 \times 200 \text{ nm}^2$  scans. Once a flat area was found  $50 \times 50 \text{ nm}^2$  scans were taken to check the area was still flat. After this,  $20 \times 20 \text{ nm}^2$  scans were taken until an image with periodicity was obtained. Finally  $4 \times 4 \text{ nm}^2$  scans were taken until scan quality reached a level with good Fourier correlations, and with 5–7 peaks in the power spectrum of the scan. Full  $256 \times 256$  scans were taken before analysis as the Nanosurf software does not give access to the raw data stream to external software. Due to other issues interfacing with the Nanosurf software, delays were so long that it was decided to take full square images rather than rectangular images of just

## Automated Tip Conditioning

a few scan lines.

At each stage, if the criteria for progressing was not met the system would either rescan, move, or apply tip cleaning procedures depending on how far from the criteria the image was. On HOPG, tip pulsing and high current images were regularly used for large scans, once flat regions were found smaller tip pulses were used.

This coarse conditioning method has been shown to work for approximately 91% of probes. An example of a successful run is shown in Figure 7.5.

### 7.4.1.2 Si(111) $7 \times 7$ Coarse Conditioning

Coarse conditioning on Si(111) was done in UHV with an Omicron VT STM. This Omicron Matrix control software does not allow external programs access to the raw data but the images can be accessed quickly once the scan is complete. To speed up optimisation only a few lines are taken per image. Three different image sizes are taken:  $128 \times 8 \text{ nm}^2$  with  $512 \times 32$  pixels,  $64 \times 4 \text{ nm}^2$  with  $512 \times 32$  pixels, and  $32 \times 4 \text{ nm}^2$  with  $512 \times 64$  pixels. For the two larger size images, if surface roughness was below an acceptable level, a decision was made to zoom in to the next level. If a high proportion of the image was covered with contamination or steps the scan area was moved. For other images, tip conditioning was performed. For the smaller size images similar procedures were taken to try to maximise the number of atoms (up to the limit of the maximum number expected for an ideal scan) resolved and the circularity of these atoms. Tip conditioning methods used were less severe for small images as if the first two stages of optimisation had been completed, the tip state is assumed to be closer to an ideal state. If atomic resolution is not detected for multiple consecutive scans the optimisation procedure will zoom out again to only check for flat regions.

To complete automated tip conditioning on Si(111) takes a matter of hours. As such no runs on Si(111) are short enough to be reproduced in full in this thesis. Figure 7.6, however, shows representative images taken during a successful optimisation run.

## Automated Tip Conditioning

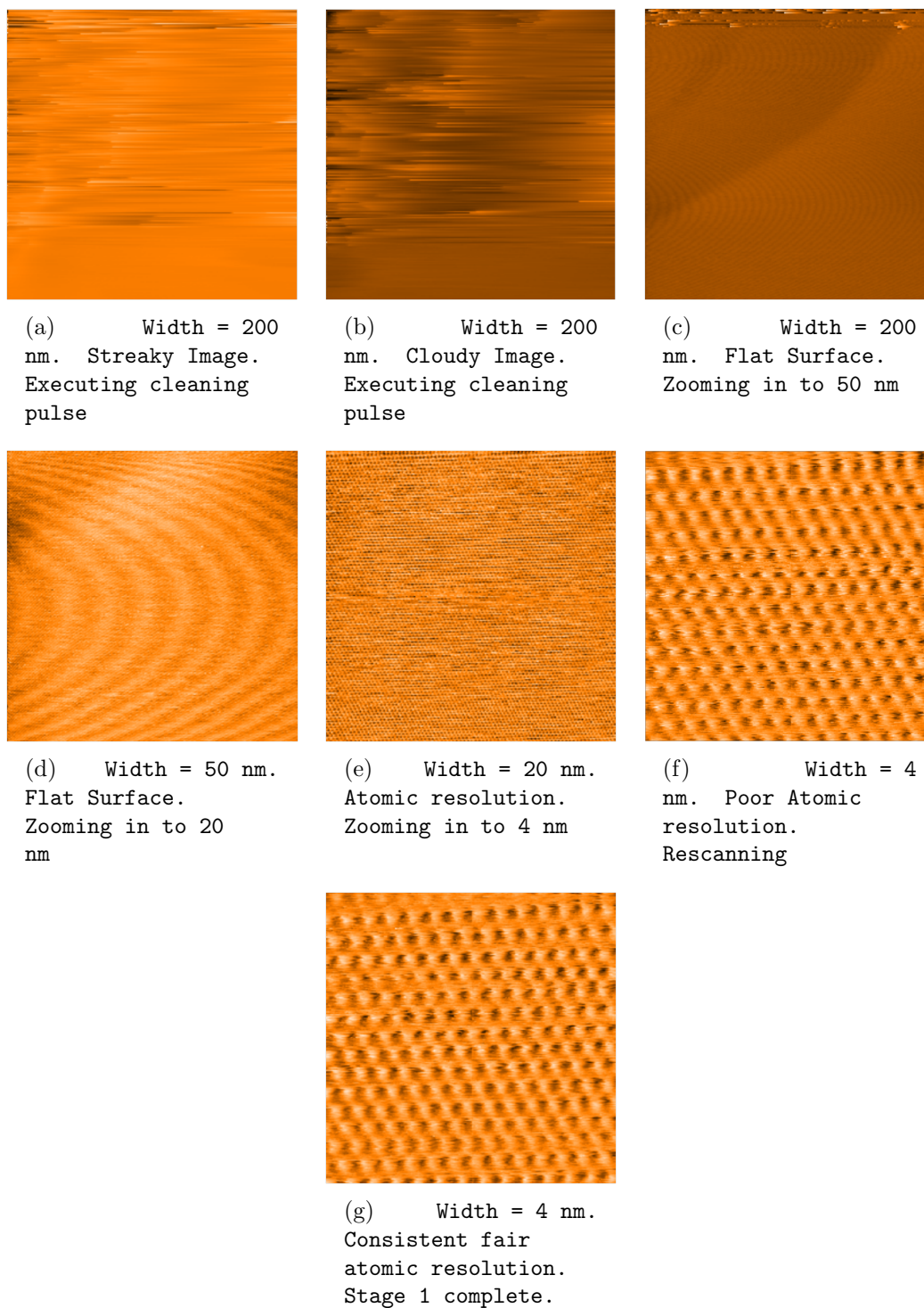


Figure 7.5: A sequence of scans on HOPG showing coarse optimisation. These have been produced sequentially as taken by the microscope complete with the output from the software. There was no human intervention once the tip was approached to the sample.

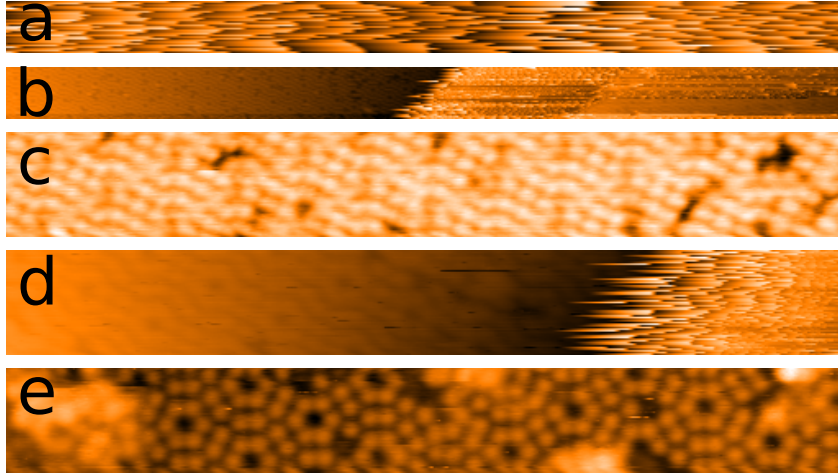


Figure 7.6: *A sequence of images from automated STM tip conditioning on the Si(111)  $7 \times 7$  surface, image widths are 128 nm for a) and b), and 32 nm for c)–e). a) First scan, shows an unstable tip. b) Less than 7 minutes into the run, a flat area is detected, despite the presence of a step in the scan region. The automation algorithm zooms in for finer tuning. Poor quality atomic resolution is detected (c), as are steps in atomic resolution images (d). After less than 80 minutes good quality imaging is detected, despite surface contamination being present.*

### 7.4.2 Evolutionary Fine Tuning

To fine tune the scan parameters to acquire images of high quality is a complex task which requires a large multi-dimensional parameter space to be explored. Fine tuning of the scan parameters using evolutionary algorithms was performed to produce images of the desired resolution on HOPG. This method has not currently been implemented in UHV. Instead, engineering the molecular tip terminations has taken priority for the researchers still working on this project. Because of this, the following section on evolutionary fine tuning refers only to ambient STM images of HOPG.

For our experiments, four parameters were modified during fine tuning: sample bias,  $V$ ; set-point current,  $I$ ; proportional gain,  $K_p$ ; and integral gain,  $K_i$ . Fully exploring this entire parameter space systematically is not possible due to the sheer number of possible combinations. Instead a machine learning process, the cellular genetic algorithm (cGA) was chosen to control the fine tuning.

A standard genetic algorithm (GA) starts with a population of different in-

## Automated Tip Conditioning

dividuals. In this case an individual is a set of four scan parameters. These individuals are tested for fitness, i.e. the quality of the resulting scan. Individuals with the lowest fitness are replaced by slightly mutated (small changes to the scan parameters) offspring of fitter individuals. The cGA modifies this process so the individuals are arranged on a grid and are only compared and replaced by their direct neighbours. More detail is given in Appendix D.2.

In our experiment 24 initial parameter sets are generated randomly within a set range. Combined with the parameter set from the final image of the coarse conditioning this makes a population of 25 individuals. Images are recorded with each of these 25 scan parameters. To save time only a  $256 \times 50$  pixel image is taken for each individual. Due to the time overhead between scans on the Nanosurf system 5 full images are recorded  $256 \times 256$  images are recorded, with the scan parameters modified every 51 lines. The quality of each of these image segments is assessed from the RMI compared to a target image. These qualities are fed into the cGA algorithm which then generates 25 sets of scan parameters for the next generation.

This fine tuning automatically begins when the tip conditioning algorithm completes the coarse conditioning stage on HOPG. The method successfully generates high quality images of HOPG as shown in Figure 7.7. It is possible to engineer a particular imaging state by only using trigonal or honeycomb targets, or to simply aim for any high quality images by using the highest fitness score from either target.

## Automated Tip Conditioning

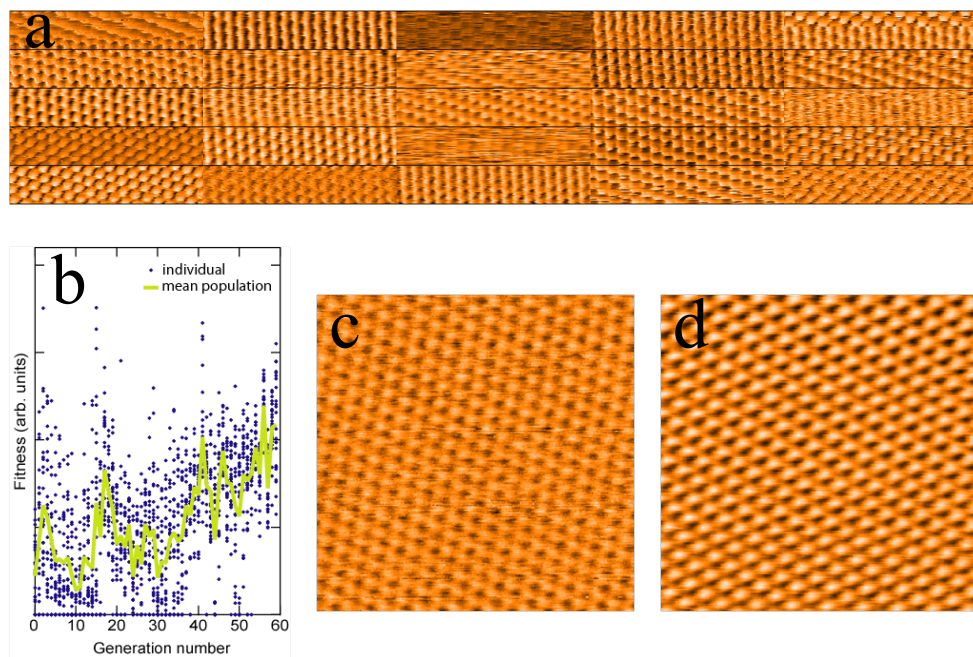


Figure 7.7: *Evolutionary optimisation of HOPG imaging using a cellular genetic algorithm. a) A generation of individuals. b) Fitness trend over multiple generations of the cGA. c) Initial image before cGA, and d) the final image after the cGA.*

## Chapter 8

# SPIW: A toolbox for automated scanning probe microscopy data analysis

*“Part of the inhumanity of the computer is that, once it is competently programmed and working smoothly, it is completely honest.”*

Isaac Asimov

### Chapter Overview

In the previous chapter routines for automating SPM tip conditioning were described. That work heavily relied on specialised image analysis to analyse the image quality to help determine the tip state. These image analysis routines are equally applicable to offline analysis of SPM data, and, as such, have been packaged into an open-source toolbox for MATLAB named SPIW (scanning probe image wizard). This chapter is a slightly edited form of a publication in the Review of Scientific Instruments which gives an overview of SPIW’s capabilities [164].

## 8.1 Introduction

Analysis of scanning probe microscope (SPM) data, a standard tool for investigating nanoscale surface structure in real space, can be a very time consuming task. A huge portion of researcher time is invested in manual data analysis, often in multiple software packages, or in writing custom analysis scripts. Considering, also, the considerable time taken to perform SPM experiments, we believe that automation of both data collection and analysis are of high priority.

While software packages, including Gwyddion [170], WSXM [171], and SPIP<sup>1</sup>, are available for manipulating SPM images, such packages require a user to decide how to process and extract statistics from the data. This can consume a large portion of an SPM researcher's time. Time can be saved by batch processing (for example, the Gwyddion libraries can be accessed through `gwybatch`), such as subtracting a fitted plane from all images and exporting to a suitable image file. While this greatly improves the speed of processing for sets of similar images, it still requires time to manually sort the images, and decide on the processing needed. In addition, as the libraries were designed with human interaction in mind, only a limited amount of batch processing is possible.

Often further data analysis is needed to extract the desired information from the image. This ranges from measuring lattice constants or step heights, to more complicated feature location, counting, and measuring. The standard SPM processing software mentioned above has little support for such analysis, instead concentrating on plane subtraction, filtering, and basic roughness statistics [172]. Some support for this analysis is available in software such as ImageJ [173]. ImageJ, however, is designed for conventional optical images and electron microscopy images, and thus many SPM specific analysis functions are not natively supported. Due to this limitation a great deal of SPM data analysis is performed by purpose written scripts [174,175], or even manual counting and masking in conventional image manipulation software. It is difficult to estimate the researcher-time wasted on avoidable manual processing or on duplicated script functionality, when so many groups write their own analysis code.

---

<sup>1</sup><http://www.imagemet.com>

We present Scanning Probe Image Wizard (SPIW)<sup>2</sup> a new open source software toolbox built entirely around the concept of automated scanning probe data processing. SPIW is written as a MATLAB toolbox, allowing the user to easily combine standard SPM image processing functions with new feature-locating functions designed specifically for SPM images. For more complicated or specialised analysis it is possible for researchers to combine SPIW functionality with their own code as well as with any of the great range of data processing operations already included in MATLAB.

## 8.2 Overview of capabilities

SPIW was originally written as part of a wider project to fully automate scanning probe experiments, as described in Chapter 7. This project combines SPIW image analysis with machine learning techniques to successfully automate STM tip conditioning. Initial experiments in ambient conditions with highly oriented pyrolytic graphite (HOPG) samples [163], relied heavily on prior knowledge of the expected images. Moreover, as STM images of HOPG often result from the sliding of graphite layers [165], this causes an averaging effect and thus step edges, lattice defects, and contamination are rarely seen. The STM automation project has since moved to ultra high vacuum (UHV) conditions, with a Si(111)  $7 \times 7$  surface. In such conditions the image analysis must reliably recognise step edges with flat terraces, process images accurately in the presence of contamination, and identify atomic resolution even on areas of the surface with a high defect density. This work is presented in Chapter 7.

As no human is present during the automation process, the image analysis must work autonomously with a wide range of images. Successful tip conditioning was achieved with no specific information of the surface reconstruction and without target images. Below we provide detailed explanation of the most important of SPIW's capabilities.

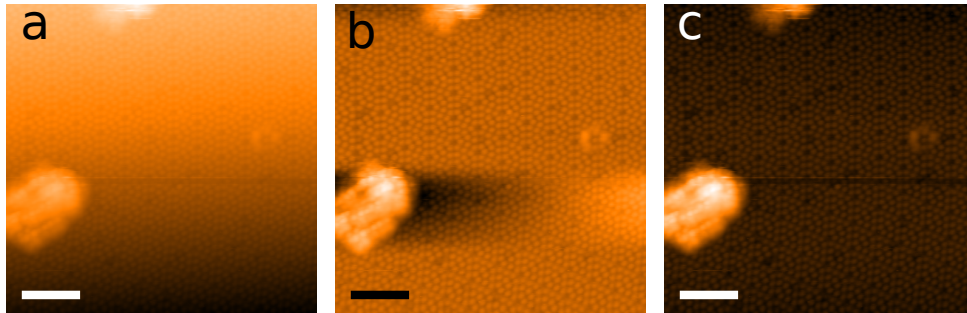


Figure 8.1: *a) Raw STM image of Si(111) 7×7 reconstruction. b) Line-by-line flattening of the same image, resulting in distortion of the surface near contamination. c) Iterative plane flattening (with masking) of same image using a SPIW algorithm. (Scale bars 6 nm.)*

### 8.2.1 Adaptive masking and flattening

Raw SPM images show the topography traced by the probe. As the height of the features in an image are generally much smaller than the width or length of the image, a very small sample tilt can result in an image where features are very difficult to recognise (Figure 8.1a). Most SPM software avoids this problem by line fitting and subtracting from each line of data in the fast scan direction, which we will refer to as line-by-line fitting. Although this allows the user to see structure more clearly, large surface features such as contamination and adsorbates can have a strong effect on only certain lines, causing previously flat areas to become bowed (Figure 8.1b). Final processed images are usually plane-fitted, to provide a realistic impression of the scanned surface (Figure 8.1c). Certain scanners (such as tube scanners) can exhibit a bowed motion. To correct for this, one can subtract second, or higher, order polynomial planes. Again, large surface features affect the plane fitting algorithm, in this case causing the surface to remain tilted or (for higher order planes) to even become distorted. As such, the user must mask large features from the surface before fitting.

Erickson *et al.* [176] have produced an automatic method of adaptive thresholding to produce masks and then used second order polynomial planes to flatten images [166]. This method does not translate well to images with atomic scale surface corrugation or molecular networks. SPIW offers similar capabilities, but

<sup>2</sup><https://sourceforge.net/projects/spiw/>

it also offers more powerful methods in the case of these corrugated surfaces. The method involves locating every atom/molecule on the surface, via the methods described in Section 8.2.3. By comparing the median maxima and minima of the surface the corrugation height can be calculated. High and low areas are defined as any part of the surface which is a user defined fraction of the corrugation height above/below the median maxima/minima height (Figure 8.2a). These pixels are added to a mask (Figure 8.2c, and e), and will not be included in the plane fitting. Before the plane fitting algorithm is executed, the mask is processed to remove any small areas which can arise from artefacts such as feedback instabilities.

The full flattening procedure is as follows. The image is first flattened with a first order polynomial plane (as the distortions of higher polynomials are undesirable). Next a mask is produced using the method described above, and the surface is again flattened, ignoring any masked pixels. This process can be iterated until the mask does not change within a given tolerance (Figure 8.2b–e).

A final improvement to the flattening can optionally be applied. In this method we fit a second order polynomial plane through just the surface maxima which are not inside the masked region (Figure 8.2f–g). This removes the effect of scanner bow, without less densely packed areas of the surface appearing lower and thus distorting the final image.

## 8.2.2 Step edge finding

Other features which commonly appear in high resolution SPM images are step edges (Figure 8.3). Step edges pose problems for both flattening routines and for generating statistics about images. SPIW detects step edges using Sobel filtering to calculate the square magnitude of the pixel height gradient [177]. These areas are thresholded with respect to the mean square gradient, to create masks of high gradient regions. The subsequent masks are thinned to single pixel lines. Further processing consisting of hole filling and dilation followed by re-thinning to single pixel. This improves the continuity of the single pixel mask along the step edge.

Once steps have been located, they can be taken into account during flat-

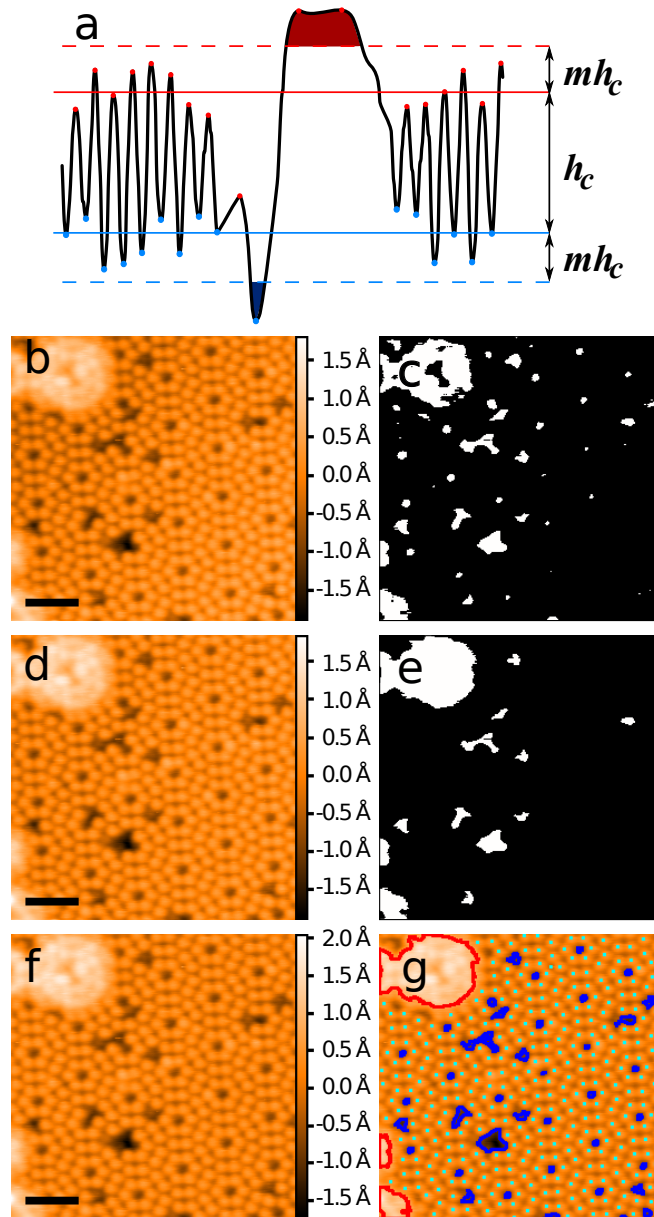


Figure 8.2: a) 2D schematic of masking procedure. Maxima/minima are marked with red/blue points, their means by solid lines.  $h_c$  is the calculated corrugation height, and  $m$  is the fraction of  $h_c$  above/below which features are masked. b) STM image of Si(111)  $7 \times 7$  reconstruction flattened using a first order polynomial plane. c) Resulting mask of high and low areas of (b), using surface corrugations to set threshold height. d) Result of 5 iterations of flattening non-masked regions, and re-masking. e) Processed mask of (d). f) Result of second order polynomial flattening only unmasked peaks in (d). g) Computer vision image of (f). Cyan points represent atoms, red/blue outlines high/low masked areas. Note that the image is now flat enough that all defects and corner holes are masked. (Scale bars 3 nm.)

tening by using a specially designed plane-flattening routine. The routine does not fit the whole image, instead it carries out line fits to each line separately, as in line-by-line fitting. If a line is broken by a step then each line segment is fitted separately. This is repeated for both the fast and slow scan directions. A weighted average of all gradients in each direction is used to produce a first order polynomial plane. As no line segment contains a step, the step does not affect the calculated gradients, leaving correctly flattened images. The advantage of this method over defining a plane from three points in the image, a feature available in most SPM software, is that this be applied automatically, rather than using manually selected points.

Locating the positions of step edges opens up another opportunity for automated image processing, as the image has now been divided into terraces. SPIW can be set to divide the image ordering terraces by size, and removing terraces smaller than a set area. These terraces then can be flattened and processed separately, to give statistics specific to each terrace.

### 8.2.3 Atom/molecule recognition

Locating the position of surface features such as atoms and molecules is an essential part of many of the SPIW routines. For images with atomic or molecular resolution the process of locating the molecule is relatively simple. The image is first filtered using a 2D Gaussian kernel. The aim of this filtering is to remove white noise, not to significantly alter the image. As such, the default Gaussian kernel has a standard deviation of just one pixel width. After this, local maxima in the filtered image are used as a first approximation of atom/molecule positions. Local minima can also be located as they are required for certain functions such as calculating corrugation heights. Both lists of points can be improved by removing any points which falls within a masked region. To accurately resolve atoms/molecules the peak to peak separation should be  $\gtrsim 5$  pixels. For images with a low signal to noise ratio the size of the Gaussian kernel may need to be increased for better results.

Fitting of peaks is not used to improve the accuracy of the atomic positions, as this was found to considerably increase the time to process images for no

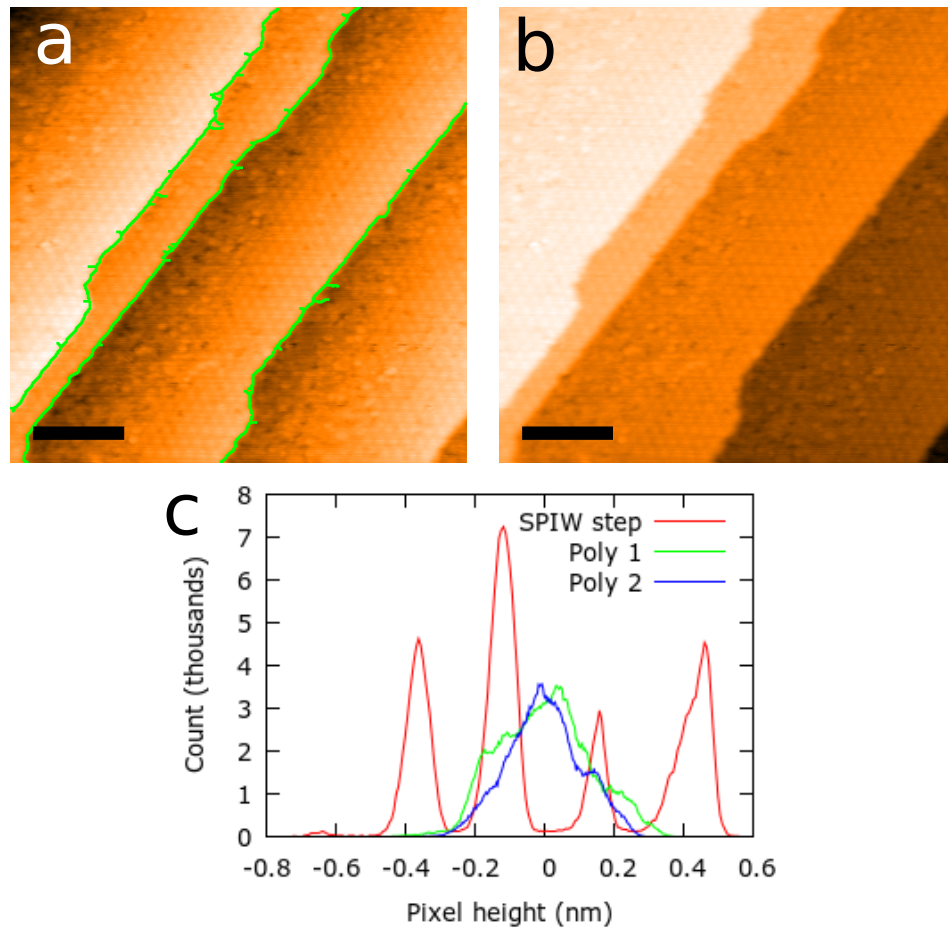


Figure 8.3: *a) STM image of Si(111) step edges flattened using a first order polynomial plane, with computer vision overlay of located step edges. b) Image flattened in SPIW with steps taken into account. c) Histogram of pixel heights for image flattened with the SPIW step method (red), compared compared to first and second order polynomial plane methods (green and blue respectively).  $z$ -heights not yet calibrated, see Section 8.2.4. (Scale bars 20 nm.)*

measurable improvement. Moreover, fitting algorithms were found to regularly fail to provide a good fit when image features overlap, causing a decrease in accuracy.

Further properties of the features can be analysed, such as the shape and the area. This is done by looping through all maxima, and comparing to their closest local minima. A local section of the image is then masked at some fraction of the minima-to-maxima height (Figure 8.4). The user has control of both the height

threshold and the local area size, but both are related to image features rather than set values to improve the applicability of the routine to multiple surfaces. Any masked feature which is not entirely contained in the local image is removed from the statistics. Thus, badly resolved molecules or spuriously defined points do not affect the final statistics. Features too close to the edge of the image are also not included as they may overlap the edge of the image, which would distort the statistics.

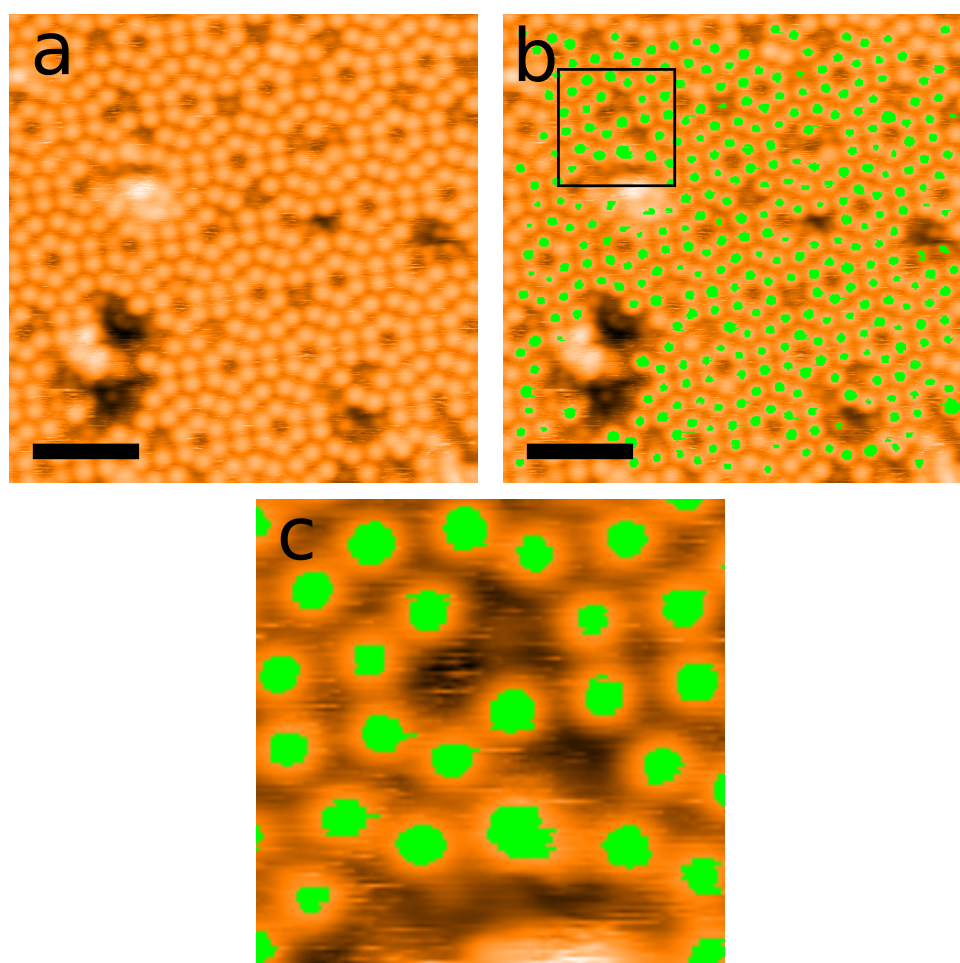


Figure 8.4: *a) STM image of Si(111)  $7\times 7$  reconstruction flattened using SPIW mask and flatten routines. b) Computer vision image of (a) with all well-resolved atoms masked for shape. c) Zoom of boxed region of (b). (Scale bars 3 nm.)*

### 8.2.4 Generating image statistics

The previous section touched upon SPIW's ability to generate image statistics. With SPIW it is possible to generate statistics for specific sections of the image defined by masks. Thus contamination, surface defects, and steps have minimal effect on the final results.

Lattice periodicity and step heights can also be measured automatically and used to calibrate images. Step edge heights can be measured using a function which fits Gaussian functions to each terrace identified in a histogram of pixel heights. For example, for Figure 8.3c, the mean step height detected was 2.67 Å, giving a calibration factor of 1.17, as the bilayer step height between Si(111) planes is 3.135 Å. Lattice periodicity can be measured without knowledge of the expected lattice structure by calculating the distance between each detected atom/molecule and its nearest neighbour. In the case of adatoms of the Si(111)  $7 \times 7$  reconstruction, the closest pairing is 6.71 Å across the divide between the faulted and unfaulted halves of the unit cell [178]. SPIW measures an average closest distance of 6.88 Å for Figure 8.2f, and 6.64 Å for Figure 8.5c. These values not only have percentage error of less than 3%, the absolute error is also much smaller than the pixel width of 0.625 Å. This method was chosen over using a Fourier transform, as many surface structures produce a number of peaks in  $k$ -space, which are best analysed with specific routines for the expected structure. The relative intensities and clarity of Fourier peaks can also be affected significantly by contamination and defects. These problems are removed by directly using the atomic positions in real space.

RMS surface roughness ( $R_{\text{RMS}}$ ) can be calculated as a simple standard deviation of the surface heights. As an example, the RMS roughnesses of the four detected terraces in Figure 8.3b, from left to right are  $R_{\text{RMS}} = 53$  pm, 29 pm, 39 pm, and 58 pm, after  $z$ -calibration. Compare these values to  $R_{\text{RMS}} = 353$  pm for the whole image, or  $R_{\text{RMS}} = 152$  pm for the plane flattened image Figure 8.3a. Surface corrugation,  $h_c$ , can also be measured for atomic resolution images using the method explained in Section 8.2.1 (see also Figure 8.2a).

Another benefit of writing SPIW in MATLAB is for more specialised statistics it is easy to pass data from areas located or masked in SPIW into the wide range

SPIW: A toolbox for automated scanning probe microscopy data analysis

of built-in MATLAB functions or home-written scripts. This can dramatically speed up script writing for very specialised image analysis not available ‘out of the box’ in any software package.

### **8.2.5 Computer vision outputs**

Generating image statistics is of little use without being able to verify that the image analysis they rely on is working correctly. With this in mind, SPIW is able to produce computer vision outputs which allow the user to see what features were recognised, the positions of steps or masks, and how the image was flattened. SPIW can easily be set to loop through a large batch of images and save image files with the computer vision outputs along with the statistics. These computer vision outputs can be used to monitor script behaviour to ensure accuracy. All SPM images in this thesis are examples of the possible outputs in SPIW.

## **8.3 Performance under different conditions**

### **8.3.1 Step edges with atomic resolution**

A particularly difficult test for any step edge locating routine is to find step edges in an image with atomic resolution. The problem arises from edge-finding techniques’ use of gradients. Often the gradient from the atomic corrugations is as strong as the gradient at the step edge. SPIW has tools to create images where each pixel is the height of the nearest located atom. This image can then be fed into the step edge locating routine with excellent results (Figure 8.5).

### **8.3.2 Feature locating for molecular networks**

This chapter has concentrated on UHV STM images of Si(111)  $7 \times 7$  as this is a key prototype. The same routines, however, apply equally well to a number of more complex surfaces. In Figure 8.6, we have used the same routines as for Figure 8.4 but on a liquid STM image of a quaterphenyl-tetracarboxylic acid and terphenyl benzene assembly on HOPG [179]. The only changes were the size of the kernel used to generate the peak locations: the standard deviation

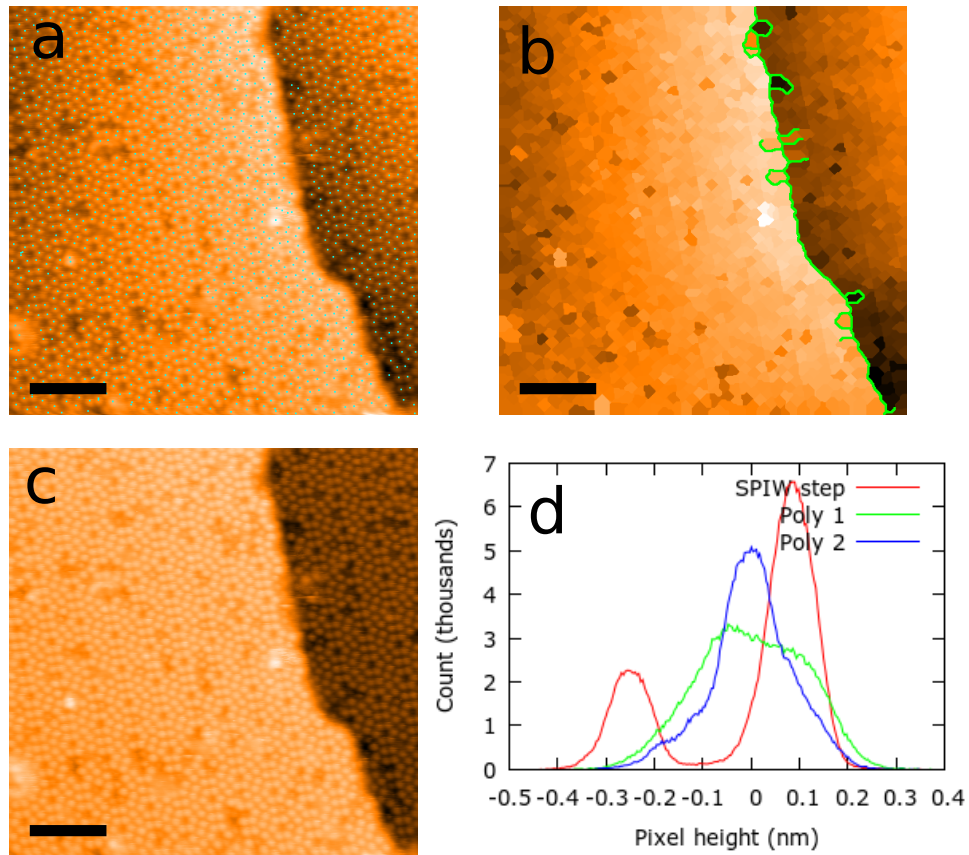


Figure 8.5: *a) STM image of Si(111) step edge flattened using a first order polynomial plane, with computer vision overlay showing located atoms in cyan. b) Image constructed such that each pixel height is equal to the height of the nearest located atom, with computer vision overlay of located step edge. c) Image flattened in SPIW with step taken into account. d) Histogram of pixel heights for image flattened with the SPIW step method (red), compared to first and second order polynomial plane methods (green and blue respectively). (Scale bars 6 nm.)*

was increased from one to 3 pixels due to the more complex shapes of the surface features. The results compare favourably to the results for masking atoms previously presented.

### 8.3.3 Known issues

SPM image processing presents a number of very specific image processing challenges. This is due to the process by which the image is acquired. Image artifacts which can arise from improper imaging parameters, such as feedback gains, can be difficult to separate from real surface features. Changes at the apex of the

scanning probe can cause sudden changes in height and/or resolution in the middle of an image. Sample drift or piezoelectric creep from the scanners can cause distortions not only in the  $x$ - $y$  plane but also in  $z$ . Images with periodic structure can be corrected in the  $x$ - $y$  plane [180], a method not currently implemented in SPIW. However, images dominated by drift or creep in  $z$  are very difficult to process in SPIW as flattening the image is near impossible, and no tools exist to reliably correct such distortions automatically. Line by line fitting can give visually pleasing results, yet a combination of inherent distortion and added distortion from the fitting result in images which cannot be used with any degree of confidence for most purposes. SPIW can be used to output such images to alert the user to interesting features, yet the raw data will still need manual processing elsewhere.

## 8.4 Conclusion

We have presented a number of tools from SPIW that can be used to automatically perform SPM data analysis. The tools are applicable to a wide range of SPM data sets, and can be used in numerous ways from simply flattening SPM images and saving to image files which can be easily browsed for interesting data, to scripted routines which select only certain images to be processed and analysed statistically. SPIW, like all software projects, is an ongoing development. We hope that by releasing it as an open source project, SPM and image processing experts also can share their acquired knowledge to improve the toolbox for the benefit of the entire SPM community<sup>3</sup>.

---

<sup>3</sup>As of the 12 of December 2013, the toolbox has been downloaded a total of 967 times from either sourceforge or softpedia (a site mirroring the SPIW content).

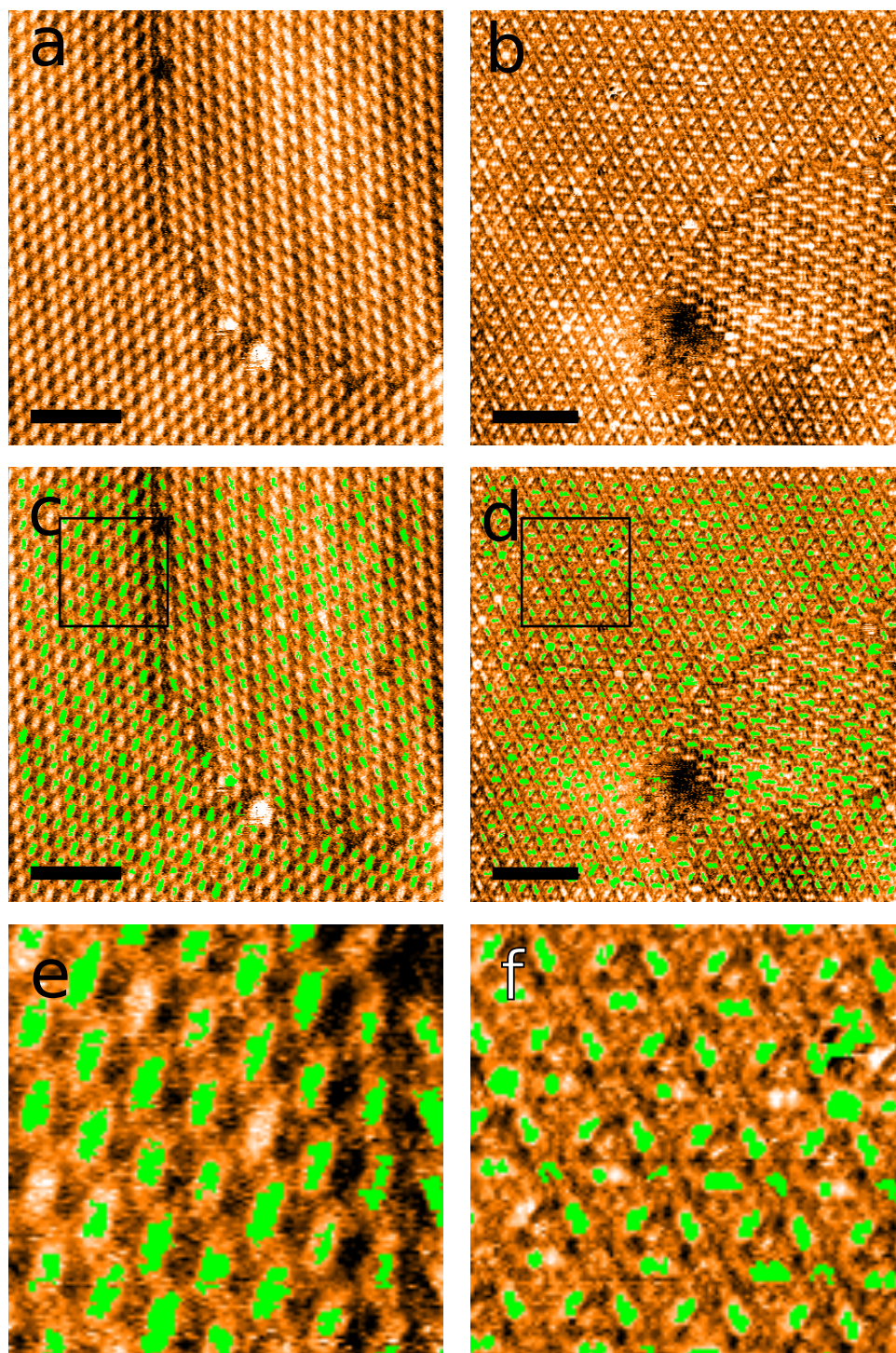


Figure 8.6: *a) and b) Liquid STM image of quaterphenyl-tetracarboxylic acid and terphenyl benzene assembly on HOPG. c) and d) Computer vision image of (a) and (b) respectively with all well resolved molecules masked for shape. e) and f) Zoom of boxed region of (c) and (d) respectively. (Scale bars 10 nm.)*

# Chapter 9

## Control theory for scanning probe microscopy revisited

*“Those people who think they know everything are a great annoyance to those of us who do.”*

Isaac Asimov

### Chapter Overview

The final results chapter of this thesis describes theoretical work on methods developed for modelling SPM feedback controllers. The first section on analytical modelling of SPM feedback describes a correction to the prevailing method in the literature, and has been submitted to the Beilstein Journal of Nanotechnology [181]. The later section on numerical feedback loops describes a simulator to generate theoretical SPM images of nanoparticles. This will form one of the central arguments of a paper in preparation discussing the apparent striped morphology of thiol-capped nanoparticles [182].

### 9.1 Introduction

Scanning probe microscope (SPM) images rely on feedback loops to maintain a constant interaction between the the tip and the sample [16, 92]. Many well known artefacts can arise from improper feedback settings [14, 15]. Thus, for

reliable SPM operation and analysis the characteristics and behaviour of feedback loops must be considered [183, 184]. SPM feedback loops usually employ a proportional-integral (PI) controller, equivalent to the common proportional-integral-differential (PID) controller with the differential gain set to zero to avoid amplification of noise. Other groups have successfully modelled and implemented proportional-differential controllers [185], but these are not commonly used. Previous work has used control theory to analyse the behaviour of PI and PID feedback loops in the context of SPM [17, 47, 186, 187], and these models are still being applied in the current literature [188]. However, the details of the operation of the feedback loop have been incorrectly modelled, resulting in decreased stability and exaggerated ringing at the resonant frequency of the piezoelectric actuator. Due to these errors, the feedback controller often cannot maintain tracking without a high derivative component [188], which is entirely at odds with experimental observations. This chapter employs analysis of specific SPM PI controllers to provide a more appropriate method for modelling such systems.

## 9.2 Analytical Models for SPM Feedback

When modelling an SPM feedback loop we must first consider the workings of the PI controller under perfect conditions. First, assume that the tip is stationary above a sample of height  $Z$ , and that the  $z$ -piezoelectric actuator for tip positioning is extended by  $X$ . For this perfect model  $X$  is considered to be the output of the PI controller; consideration of amplifier bandwidths and mechanical resonances are added later. For our original simplified model we will consider a generic SPM which tracks to a set-point tip-sample distance (Note that the exact mechanism to detect this distance is not relevant). Referring to the set-point distance as  $P$ , and the tip-sample distance as  $Z - X$ , then the error signal input to the PI controller,  $E$ , is

$$E = Z - (X + P). \quad (9.1)$$

After a time  $t$  in feedback the output of a standard PI controller would be

$$X(t) = K_p E(t) + K_i \int_0^t E(\tau) d\tau, \quad (9.2)$$

where  $K_p$  and  $K_i$  are the proportional and integral gains of the PI controller respectively and  $\tau$  is a dummy integration variable. It is clear that such a system is intrinsically unstable, by considering the case that  $E(t_0) = 0$ . As the tip-sample distance is equal to the set-point distance there should be no movement, however, evaluating Equation 9.2, the output to the piezo  $X(t_0 + dt)$  will be zero (where the  $dt$  is used to clarify that the system was not initiated at 0 but the first output after initiation will be zero.). Thus, the tip will return to the zero piezo extension position, rather than staying static (because the error signal being zero). At the next time step, there will be a large error signal and the tip will move back towards its correct position. This rudimentary problem has apparently gone unnoticed to date because it has been ‘disguised’ by the more complicated modelling of the response of the various other electrical and electromechanical components of the SPM (amplifiers, piezoelectric actuators).

It is helpful to draw an analogy with the most commonly considered control system, namely a temperature controller. A conventional PI controller in essence calculates the heat to be added to the system under control. If the set-point matches the measured temperature an output of zero is required. However, an SPM directly controls the extension of the piezoelectric actuator which is analogous to directly controlling the temperature. To correct for this one must consider that the output of a the PI controller in an SPM is the *change* in the extension. Thus, for the final output of feedback controller to be the extension we must integrate the PI controller output since the start of the experiment (with  $X(0) = 0$ ):

$$X(t) = K_p \int_0^t E(t^*) dt^* + K_i \int_0^t \int_0^{t^*} E(\tau) d\tau dt^*, \quad (9.3)$$

where  $t^*$  is another dummy integration variable. This integration effectively stores all previous feedback response. Comparing to Equation 9.2 we see that if initiated under the same conditions, where  $X(0) = 0$ , the integral term does store the previous response as a proportional controller. Thus, the controller

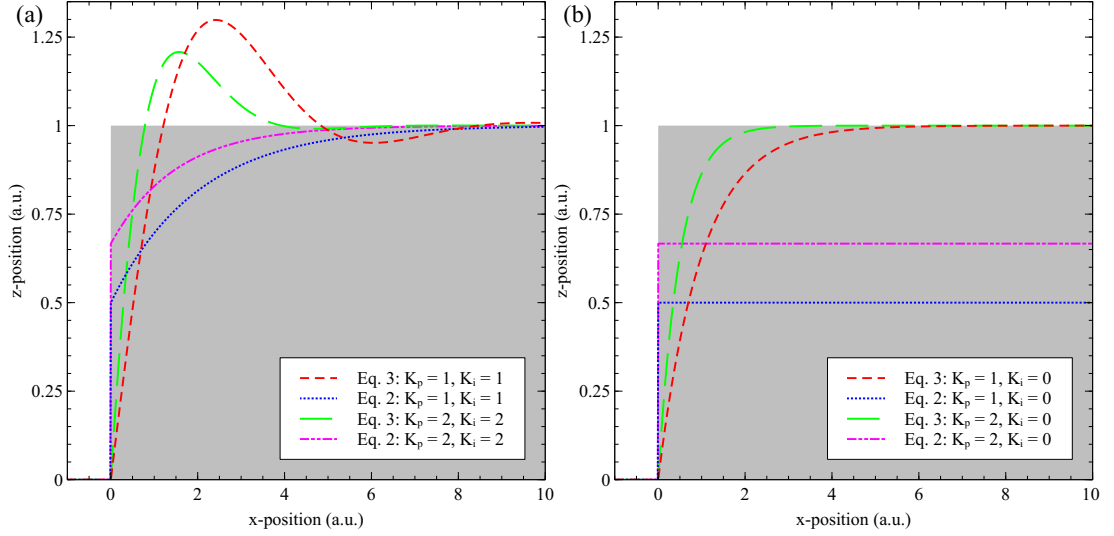


Figure 9.1: *Direct comparison of our model (Equation 9.3, red and green lines) with the model from the current literature (Equation 9.2, blue and pink lines), without modelling of electrical or mechanical components. The comparison is performed for a full PI controller (a) and a simple proportional controller (b), where the grey area represents the surface being tracked with a set-point of 0. Equation 2, shows unexpected discontinuities and does not track the set-point for a proportional controller, instead only reacting to the initial impulse. Equation 9.3 produces the expected results from elementary control theory. All gain units are arbitrary.*

implemented by Equation 9.2 would perform as a proportional-differential controller.

Figure 9.1 directly compares the response of Equations 9.2 and 9.3 to a unit step, analytically solved using a Laplace transform, with a set-point of zero. For a PI controller, Figure 9.1(a), modelled using Equation 9.2 there is a discontinuity in the extension at the time of the step, this results from the incorrectly modelled proportional controller acting as a derivative controller. This discontinuity can go unnoticed if the equations are solved numerically, if a frequency cut-off is modelled [17], or if the mechanical response of the  $z$ -piezo is modelled. Additionally, the controller modelled using Equation 9.2 does not experience the expected overshoot of the set-point for a PI controller, this can also go unnoticed when mechanical response of the  $z$ -piezo is modelled as its resonance can be mistaken for feedback ringing [17]. By further examining Equation 9.2 for a proportional controller ( $K_i = 0$ ), we see (Figure 9.1(b)) that in addition to the

discontinuity the controller settles to a value which is a  $1/(K_p + 1)$  of the required extension. This has previously been mistaken as a steady state error common to proportional controllers [17], however when plotted without any the modelling of other components it becomes clear that it results from the controller only acting to the initial impulse.

From Figure 9.1(b) it becomes apparent there will be no steady state offset when evaluating the response of Equation 9.3 to a static surface ( $Z(t) = E + X + P = \text{constant}$ ), for a simple proportional controller ( $K_i = 0$ ). This initially appears at odds with both experiments and elementary control theory. However, this is due to the simplicity of the system we are modelling. Again considering our analogous temperature controller it is well known that the cause of steady state error is that the heat input into the system is equal to the heat lost to (or gained from) outside the system. Now we see that steady state errors in SPM feedback result from sample drift in the  $z$ -direction or a scanning a sample with a tilt. Thus, any system not modelling  $z$ -drift or sample tilt should not expect a steady state error.

### 9.2.1 Complete model of SPM feedback

Before running simulations of our simplified SPM system we will first derive the model for the full SPM feedback system, and then set the transfer functions of unmodelled components to unity, to reduce the possibility for errors following their introduction. To avoid unnecessary generalisations we will discuss the feedback loop as it applies to the scanning tunnelling microscope (STM). The results are, however, equally applicable to other forms of SPM. For analysis of the full feedback loop of an STM (Figure 9.2) we start by considering that at any time  $t$  the tip will be above a particular area of the sample with height  $Z$ . Thus, the tip encounters the topography as a time changing function  $Z(t)$ . Using the extension of the  $z$ -axis of the piezoelectric scanner ( $z$ -piezo),  $X(t)$  (Note that when modelling a complete SPM  $X(t)$  is no longer simply the output of the PI controller, as described in Equation 9.7), we can express the tip-sample,  $D(t)$ , distance as

$$D(t) = Z(t) - X(t). \quad (9.4)$$

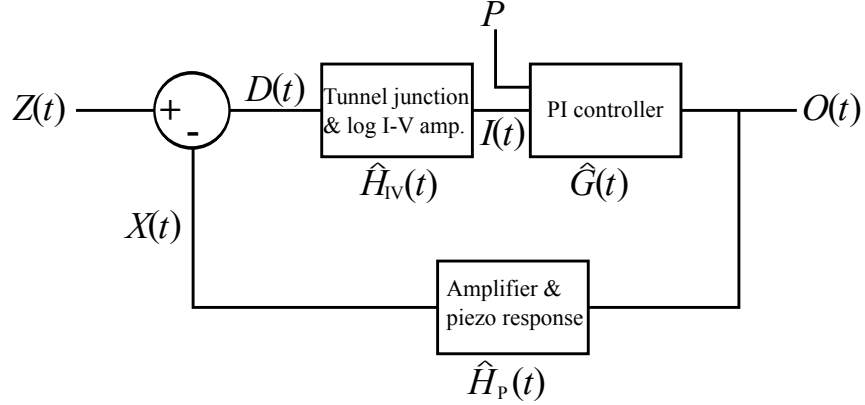


Figure 9.2: Schematic of an STM feedback loop.  $Z(t)$  and  $X(t)$  represent the sample height and  $z$ -piezo extension at time  $t$  respectively, and  $P$  is the set-point current. Other SPM systems can be modelled using the same feedback system by replacing the operator  $\hat{H}_{\text{IV}}$ , with an operator which describes the tip sample interaction and signal amplification of the SPM to be modelled.

The measured tunnelling current is a function of this distance, and also of the properties of the current-to-voltage (I-V) amplifier of the STM. As the tunnel current is exponentially dependent on the tip-sample distance the logarithm of the tunnel current is used for the feedback to improve the linearity of the feedback response. We can refer to this log tunnel current as

$$I(t) = \hat{H}_{\text{IV}}(t)D(t), \quad (9.5)$$

where  $\hat{H}_{\text{IV}}(t)$  is the time dependent operator fully describing the tunnel junction, the I-V amplifier, and the logarithm operation.

The feedback controller then compares  $I(t)$  with a set-point,  $P$ , and tries to correct for discrepancies by modifying the output,  $O(t)$ , to the  $z$ -piezo. We can write the feedback controller as the time dependent operator  $\hat{G}(t)$ , and hence

$$O(t) = \hat{G}(t)[P - I(t)]. \quad (9.6)$$

Finally, we can link the  $z$ -piezo extension to the feedback controller output with an operator,  $\hat{H}_{\text{P}}(t)$ . This describes both the high voltage amplifier used for

the piezoelectric actuator and the mechanical response of the z-piezo itself:

$$X(t) = \hat{H}_P(t)O(t). \quad (9.7)$$

As the set-point acts as only a linear offset to the system we can set  $P = 0$ . Thus, combining Equations 9.5 and 9.6 under this condition we get

$$O(t) = -\hat{H}_{IV}(t)\hat{G}(t)D(t). \quad (9.8)$$

Combining this with Equation 9.7:

$$X(t) = -\hat{H}_{IV}(t)\hat{H}_P(t)\hat{G}(t)D(t) = -\hat{H}_{IV}(t)\hat{H}_P(t)\hat{G}(t)[Z(t) - X(t)], \quad (9.9)$$

and applying a Laplace transform we get

$$\tilde{X}(s) = -\tilde{H}_{IV}(s)\tilde{H}_P(s)\tilde{G}(s)[\tilde{Z}(s) - \tilde{X}(s)], \quad (9.10)$$

where  $\tilde{X}(s) = \mathcal{L}\{X(t)\}$  and  $\mathcal{L}$  is the Laplace transform. Some minor rearrangement gives

$$\tilde{X}(s) = \frac{-\tilde{H}_{IV}(s)\tilde{H}_P(s)\tilde{G}(s)\tilde{Z}(s)}{1 - \tilde{H}_{IV}(s)\tilde{H}_P(s)\tilde{G}(s)}. \quad (9.11)$$

We are interested, however, in the output signal to the z-piezo, not its physical extension, as this is what the SPM controller records for the image. By simply considering the Laplace transform of Equation 9.7 ( $\tilde{X}(s) = \tilde{H}_P(s)\tilde{O}(s)$ ) we arrive at a final result of

$$\tilde{O}(s) = \frac{-\tilde{H}_{IV}(s)\tilde{G}(s)}{1 - \tilde{H}_{IV}(s)\tilde{H}_P(s)\tilde{G}(s)}\tilde{Z}(s). \quad (9.12)$$

For this chapter we are working in arbitrary units, thus the simulation needs to provide the relative response to change in gain settings rather than a response in physical units. Thus we can set  $\hat{H}_{IV}(t) = -1$  ( $\tilde{H}_{IV}(s) = -1$ ) as the logarithm should cancel the exponential dependence of the tunnel junction, and the gain of the I-V amplifier is simply linear, which is irrelevant if we are working in arbitrary units. To specifically consider the effect of the bandwidth of the SPM

pre-amplifier, the functional form of  $\hat{H}_{IV}(t)$  must be considered in more detail. More detail on modelling of such electrical components is given in the Section 9.2.3. Under this condition we can simplify Equation 9.12 to

$$\tilde{O}(s) = \frac{\tilde{G}(s)}{1 + \tilde{H}_P(s)\tilde{G}(s)} \tilde{Z}(s). \quad (9.13)$$

By applying the same argument used to derive Equation 9.3 we can write the operator for the PI-controller acting on an arbitrary function  $f(t)$  as

$$\hat{G}(t) = K_p \int_0^t f(t^*) dt^* + K_i \int_0^t \int_0^{t^*} f(\tau) d\tau dt^*, \quad (9.14)$$

and thus in  $s$ -space this becomes

$$\tilde{G}(s) = \frac{K_p}{s} + \frac{K_i}{s^2}. \quad (9.15)$$

## 9.2.2 Feedback performance - without mechanical modelling

Initially we will study the stability of the STM feedback without modelling the mechanical resonances of the SPM system. For this we can substitute  $\tilde{H}_P(s) = 1$  and Equation 9.15 into Equation 9.13. The feedback behaviour has been studied for four simulated surfaces:

$$Z(t) = 1, \quad Z(t) = 1 + t/10, \quad Z(t) = t/10, \quad Z(t) = \sin(t) \exp(-t), \quad (9.16)$$

which correspond to a unit step, a ramp added to a unit step, a ramp, and a smooth topographical feature respectively. The results for a range of different feedback parameters are plotted in Figure 9.3. As the system is modelled in arbitrary units, time and  $x$ -position are equivalent if the tip is moving at a constant speed in  $x$ . It is clear from Figure 9.3 that the system behaves as expected. Steady state offsets appear for proportional only controllers if there is a  $z$  ramp present, but is corrected by an integral controller.

When discussing the stability of the system, qualitatively one can see that tracking is maintained for a wide range of proportional and integral gains. For

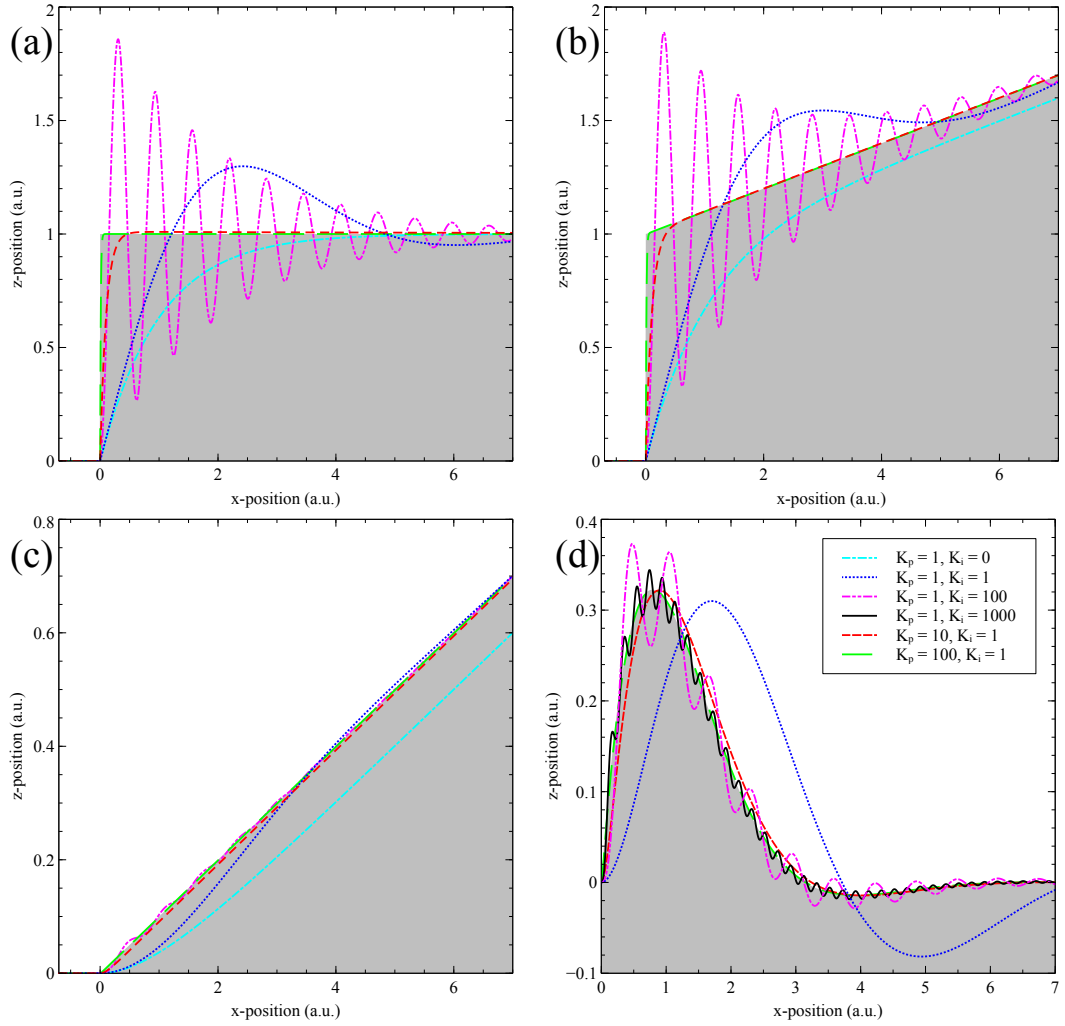


Figure 9.3: *The feedback response of an SPM, without the inclusion of mechanical resonances, calculated for four different topographies, and for a range of feedback gains. Not all gains are plotted for all topographies to avoid overcrowding.*

large integral gains the system oscillates, as expected. For all plotted gains oscillations always ring-off, never resulting in positive feedback. To further investigate the stability in the case of the unit step the full system output in  $s$ -space can be analysed for poles. The final output in  $s$ -space is:

$$\tilde{O}(s) = \frac{K_p s + K_i}{s(s^2 + K_p s + K_i)}, \quad (9.17)$$

which results in three poles:

$$s = 0, \quad s = \frac{-K_p \pm \sqrt{K_p^2 - 4K_i}}{2}. \quad (9.18)$$

From this it is clear that if  $K_p$  and  $K_i$  are always positive (true for a feedback loop) no pole ever has a positive real value, and thus the system is always stable. We can also calculate that the feedback output will not oscillate if  $4K_i \leq K_p^2$ .

### 9.2.3 Feedback performance - with mechanical and electrical modelling

For a more realistic model of SPM feedback one should also model the response of electrical and mechanical components. Equations for such extra components should be tested individually and added sequentially to reduce the possibility of error as equations in  $s$ -space are rarely intuitive. To build up a full electrical and mechanical model of an arbitrary system is of little use when discussing stability as the system becomes too complicated to analytically derive the poles. Instead, the above equations should be used in conjunction with real physical values from a SPM system to understand its stability.

As an example we will include a mechanical resonance for the  $z$ -piezo relative to its equilibrium position at its input voltage

$$\tilde{H}_P(s) = \frac{1}{1 + \frac{s}{Q\omega_0} + \frac{s^2}{\omega_0^2}}, \quad (9.19)$$

where  $Q$  is the quality factor of the resonance and  $\omega_0$  is the angular eigenfrequency. It is important to note that this equation differs from that used in Reference [17], as this text mistakenly uses the mechanical response to a force rather than to a coupled mechanical offset. It is possible to model the transfer function of the  $z$ -piezo for an input voltage by replacing the numerator with the relevant piezoelectric coefficient. This is not done as it has no effect for a model in arbitrary units, and also as in this form Equation 9.19 can equally be used as the response of an AFM cantilever. It is, however, important to note that for some geometries of piezoelectric scanners, such as the tube scanner, the motion

of the principle eigenmode is perpendicular to the  $z$ -axis [189], and thus cannot be included into our one dimensional model.

Substituting Equations 9.19 and 9.15 into Equation 9.13, along with the equation for a unit step, the response of the full system in  $s$ -space is given by

$$\tilde{O}(s) = \frac{K_p Q s^3 + (K_i Q + K_p \omega_0) s^2 + (K_i \omega_0 + K_p Q \omega_0^2) s + K_i Q \omega_0^2}{s(Q s^4 + \omega_0 s^3 + Q \omega_0^2 s^2 + K_p Q \omega_0^2 s + K_i Q \omega_0^2)}. \quad (9.20)$$

As the denominator is fifth order there are 5 poles. One pole at  $s = 0$  shows the final response to the step. The functional form of the other 4 poles is too long to be qualitatively useful. However, the trend in pole positions can be qualitatively understood. Two poles correspond to the ringing oscillations from the system without the mechanical resonance, though the frequency and decay times are affected by the modelled resonance. Two further poles represent the excitation of the mechanical resonance. These poles can move into the unstable region if excited by high gains. The system can be made stable under higher gains by increasing the eigenfrequency or decreasing the  $Q$  of the resonator. For these reasons components with a high quality factor and a low resonant frequency are unsuitable as part of SPM scanners.

In Figure 9.4(a) the PI controller output for a range of mechanical eigenfrequencies with a constant quality factor is plotted against time. Arbitrary units are used for both time and the PI output as the evolution under increasing eigenfrequency is valid for any magnitude. The  $y$ -axis is labelled PI output, not extension, as these are no longer equivalent when mechanical resonance is modelled. For all plotted outputs the bandwidth of the high voltage (HV) amplifier driving the  $z$ -piezo was assumed to be infinite, and hence Equation 9.19 was used without modification.

The evolution of the output under varying  $Q$  of the mechanical resonance is shown in Figure 9.4(b). Again, in agreement with the polar analysis, the stability increases for lower  $Q$ . For higher  $Q$  the resulting instability can be diminished or eradicated by reducing the bandwidth of the HV amplifier. The transfer function of an amplifier with a finite bandwidth can be accurately modelled as a first order low-pass filter [190]

$$\tilde{H}_{\text{amp}}(s) = \frac{1}{s/\omega_c + 1}, \quad (9.21)$$

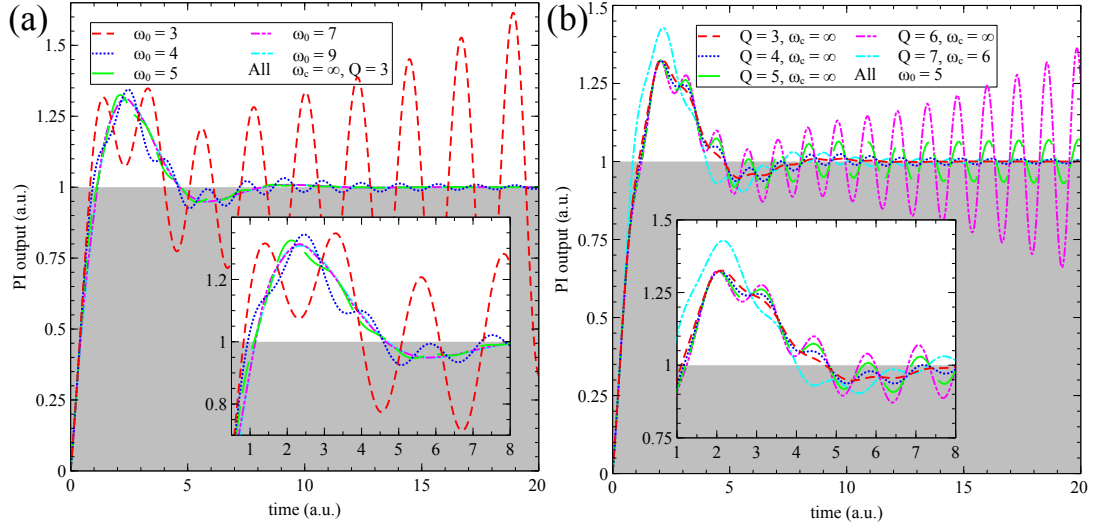


Figure 9.4: *The feedback response of an SPM, including mechanical resonance. (a) Shows the evolution of the feedback output for varying eigenfrequency of the mechanical resonance. The stability improves for increasing resonant frequency. For all plots the bandwidth of the HV amplifier is infinite and the  $Q$  of the resonance does not vary. (b) Shows similar evolution in feedback output for varying  $Q$  of the resonance at a constant eigenfunction, with lower  $Q$  values stabilising the output. The cyan line shows the same resonance properties as the pink line, however by limiting the bandwidth of the HV amplifier to near that of the resonance, the stability is improved significantly. Both insets are zooms of the most important region of their respective plots.*

where  $\omega_c$  is the cut-off angular frequency (3dB point) of the amplifier. As we are working in arbitrary units this amplifier has a gain of 1, the numerator of the transfer function can be replaced with the desired gain if needed. Including this, the full transfer function of the amplifier and piezo becomes

$$\tilde{H}_P(s) = \frac{1}{(s/\omega_c + 1) \left(1 + \frac{s}{Q\omega_0} + \frac{s^2}{\omega_0^2}\right)}. \quad (9.22)$$

The cyan line in 9.4(b) shows the significant improvement in stability resulting from a cut-off frequency just above that of the mechanical eigenfrequency. This, however, comes at the cost of an increased overshoot. One also must be careful not to lower the cut-off frequency below the resonance, nor to use an over-damped ( $Q < 1/2$ ) mechanical component as this can introduce a significant phase lag, causing new instabilities.

The MATLAB code used to generate the data for Figures 9.3 and 9.4 is included as supplementary information. This can be used to further explore the parameter space of the SPM PI controller.

The only component in Figure 9.2 not modelled, is the tunnel junction and logarithmic amplifier,  $\hat{H}_{IV}(t)$ . Considering the tunnel junction as an exponential decay with distance, producing a current which is first amplified by an I-V preamp with a finite bandwidth. The logarithm of this output voltage is then taken either by a logarithmic amplifier or calculated numerically by the SPM controller. This results in a functional form for the time-domain operator action on the tunnel gap  $D(t)$  being

$$\hat{H}_{IV}(t) = \log \left( \hat{H}_{\text{amp}}[\exp\{-\kappa D(t)\}] \right) \quad (9.23)$$

where  $\kappa$  is the characteristic decay length of the tunnel junction, and  $\hat{H}_{\text{amp}}$  is the time-domain operator corresponding to the transfer function in Equation 9.21.

To calculate the s-space transfer function of Equation 9.23, one would need to calculate the Laplace transform of the exponential of an arbitrary function  $D(t)$ . This may be possible for the specific functional forms of  $D(t)$  but is not generally applicable. One can approximate  $\hat{H}_{IV}(t)$  under the approximation that the logarithm and  $\hat{H}_{\text{amp}}$  commute:

$$\hat{H}_{IV}(t) \sim \hat{H}_{\text{amp}}(\log[\exp\{-\kappa D(t)\}]) = \hat{H}_{\text{amp}}(-\kappa D(t)) \quad (9.24)$$

in arbitrary units  $\kappa$  can be ignored and the transfer function of the tunnel junction approximates to  $\tilde{H}_{IV}(s) = -\tilde{H}_{\text{amp}}(s)$ . Under this approximation we ignore the effect of higher harmonics of frequencies present in  $D(t)$  being generated by the exponential dependence in the tunnel junction.

### 9.3 Numerical implementation of feedback simulations

As a real SPM controller records the control interaction at a specific sample rate rather than continuously, and as all feedback calculations are performed numer-

ically, it is arguably more appropriate to model the system numerically. For this we have built a simulation SPM in MATLAB. Again, for general application the feedback is performed directly on the tip-sample distance, and neither mechanical or electromechanical components are modelled.

This simulation is performed using arbitrary units. However, as the numerical simulation's performance is dependent on both sample rate and scan speed the arbitrary units of the gains are not equivalent to those from the analytical feedback model. Rather than describing the numerical model as a large and unintuitive equation, an algorithmic explanation of the feedback simulation is provided as pseudocode in Algorithm 1, where text inside braces represents comments.

In this simulation a sample topography is fed in. Two nested for loops simulate the raster scan. The code Algorithm 1 simulates trace and retrace in the fast scan direction but only a single trace in the slow scan direction, and all scan parameters must remain constant throughout the scan. This is done to make the pseudocode more understandable. The full code allows arbitrarily timed changes in scan parameters and continuous scanning.

An advantage of this numerical simulation is that it allows us to more accurately replicate the conditions of a real STM. We simulate experimental noise by adding normally distributed random numbers to each measurement. The amplitude the simulated noise can be modified to monitor performance at a range of signal-to-noise ratios. As well as the options to change the proportional and integral gains, the scan speed, and the set-point height common to most SPM controllers, extra options can be modified. The sample rate of the STM controller can be modified, to investigate how this affects imaging performance and particular scan speeds. Finally, an option to modify the method for the PI controller is available. This method named wind-up protection resets the integral term after each pixel. This method will stop the built up integral gains causing large oscillations, but similarly will limit the ability of the PI controller to combat steady state errors.

This simulator has been used as part of an ongoing project to understand STM images of thiol-capped nanoparticles. For particles capped with a mixture of two thiols, it has been suggested that the ligands spontaneously phase separate

---

**Algorithm 1** Pseudocode for STM simulation algorithm. Braces indicate comments.

---

**Input:** The topography *topog* (an  $N \times N$  array), time per line *Tline*, Sample Rate *SR*, Set-Point *SetPoint*, Proportional gain *Pgain* and Integral gain *Igain*, Wind-up protection (boolean) *Protect*.

**Output:** The simulated STM outputs *scan* and *scanR*.

```

1: spp = ROUND(Tline*SR/N) {Calculate the number of PID iterations taken
   per pixel}
2: height = topog(1,1) + SetPoint
3: I=0 {Initialise integral term}

4: {Using loops to simulate raster scan}
5: for m = 1 to N do
6:   for n = 1 to 2*N do
7:     if Protect then
8:       I = 0 {Reset integral term if wind-up protection is on.}
9:     end if
10:    {Calculate if on trace or retrace}
11:    if n > N then
12:      n2 = 2*N + 1 - n; {If on retrace, new x position is calculated from
   n}
13:    else
14:      n2 = n; {If on trace x position is simply n}
15:    end if
16:    for i = 1 to spp do
17:      {Calculating error and adding normally distributed noise}
18:      err = topog(m,n2) + SetPoint - height + RANDN
19:      I = I + err
20:      {Using feedback to adjust height.}
21:      height = height + Pgain*err + Igain*(I/SR)
22:    end for
23:    {Scan data is the last height, must be written to either scan or scanR
   depending on if tip motion is trace or retrace}
24:    if n > N then
25:      scanR(m,n2) = height
26:    else
27:      scan(m,n2) = height
28:    end if
29:  end for
30: end for

31: return scan, scanR

```

---

into ordered striped domains which can be imaged in STM [191]. However, other work has suggested that these features are the result of improper scan parameters causing feedback oscillations which cause the apparent striped morphology [14]. The full details of the striped nanoparticle controversy are outside the scope of this thesis [14, 192, 193], however, preliminary results of the feedback simulations are of relevance to this chapter.

Figure 9.5(a) shows a real STM image of mixed thiol-capped nanoparticles with stripes of a clearly defined width all aligned perpendicular to the fast scan direction and continuous between particles. Similar results are obtained with the simulation SPM presented in Figure 9.5(c)–(h), with stripe widths which vary for different gains. As predicted in the analytical model, by reducing the integral gain these oscillating features are no longer generated (Figure 9.5(i)). This suggests a simple test for images with striped morphologies: repeated measurements on the same areas with varying integral gain. If these features arise from feedback instabilities the stripe spacing should be dependent on the integral gain.

## 9.4 Conclusion

We have derived an appropriate updated model to understand SPM feedback in the context of control theory. This model shows the intrinsic stability of the SPM feedback controller in an ideal environment. We further discuss methods to include modelling of mechanical resonances showing low frequency components to cause instabilities. By introducing amplifiers with bandwidths just above the mechanical eigenfrequency these instabilities can be controlled. The method presented here uses arbitrary units to show a generalised approach, but can be combined with real parameters from SPM systems to understand and model performance under a range of conditions. We also present a numerical SPM simulation which can be used to understand the effect of SPM feedback on apparent morphologies in SPM images.

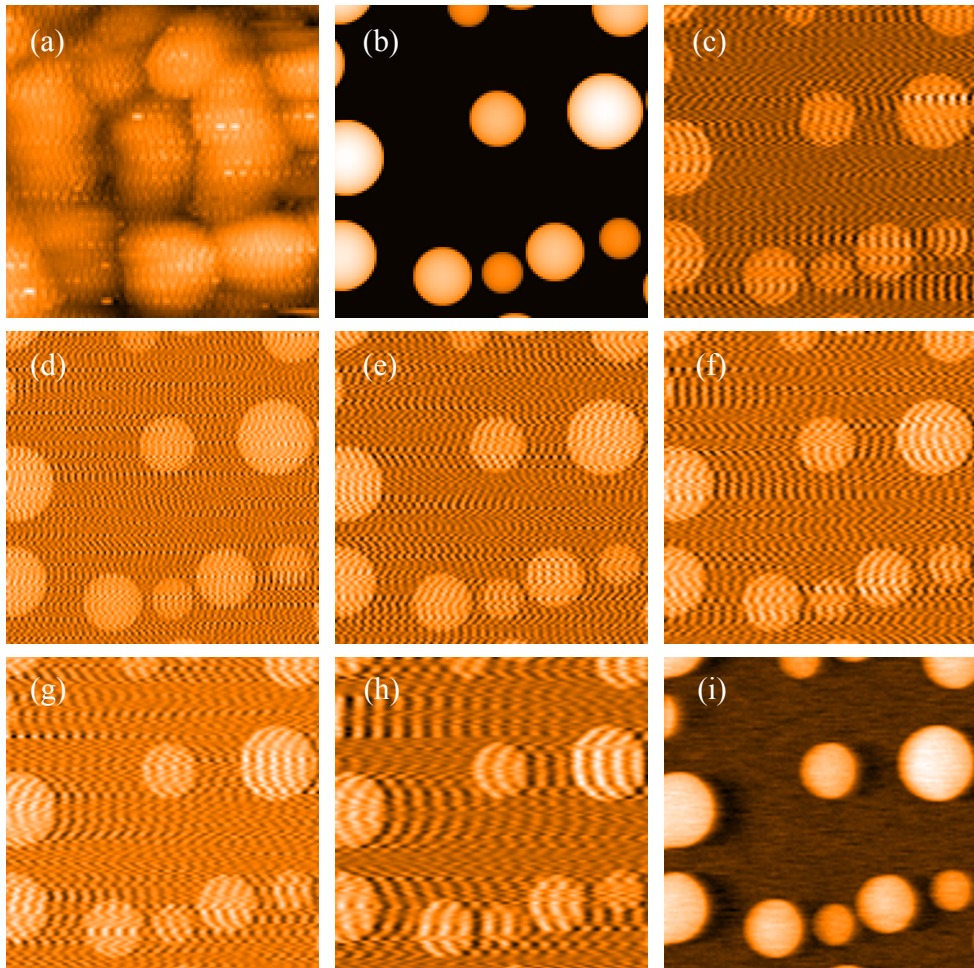


Figure 9.5: *a) An real STM image of mixed thiol-capped nanoparticles, raw data equivalent to Figure 1(a) from [191], but processed in SPIW [164] showing the full topography range on a linear scale. b) Shows the surface topography used in all numerical simulations. d–h) Show numerically simulated images with  $K_p = 50$  and  $K_i = 8000, 5000, 3000, 2000,$  and  $1000$  respectively. i) The same simulation with more appropriate parameters  $K_p = 500$  and  $K_i = 100$ . c) is the retrace image recorded while recording image (f). Note the arbitrary units are not consistent between the analytical simulation in Figure 9.3 and the numerical simulations (c)–(h).*

# Chapter 10

## Conclusion

*“Only on the edge of the grave can man conclude anything.”*

Henry Adams

This thesis has broadly concentrated on the effect of instrumentation on SPM measurements, showing that three decades in to scanning probe microscopy there are still instrumental artefacts which are not well understood. Both STM and AFM operation have been considered, and topics ranging from feedback performance and tip termination effects on imaging to the accuracy of force spectroscopy measurements have been studied.

Early chapters concentrated on accurate force extraction from ncAFM measurements with a qPlus sensor. Here, we considered how the tip geometry, while having little effect on the spring constant of the sensor, can introduce significant lateral motion to the trajectory of the tip apex. This lateral motion results in a coupling of lateral and normal forces into the measurements. The lateral motion was confirmed experimentally, and the effect this has on imaging, calibration, and force spectroscopy measurements was calculated. We progressed to use the well defined  $C_{60}$ - $C_{60}$  interaction potential and the technique of grid spectroscopy measurements to experimentally record the effects of this lateral motion in 3D. Furthermore we were able to use the 3D data to attempt to correct for the effects of the coupled lateral forces. Preliminary data suggests this can improve the accuracy of the measured potential. Finally on the topic of force measurements a new quartz sensor geometry was proposed which uses symmetry to eliminate

## Conclusion

lateral motion arising from cantilever geometry. A further advantage of this symmetrical design is that for the second eigenmode of the sensor the position of tip attachment is at a node of the sensor, and thus the direction of the tip-apex oscillation is normal to the surface. This allows LFM measurements without introducing torsional modes.

The next section of the thesis concentrated on automatic methods for instrument operation and data analysis. Initially we considered the researcher-time wasted on preparing the apex of the probe before SPM measurements can be performed. Using a combination of prescribed methods and genetic algorithms we developed methods to automatically optimise STM image resolution in both vacuum and ambient conditions. This work relied heavily on advanced methods developed to automatically process and analyse SPM data. This algorithms have been packaged into an open-source toolbox for offline SPM data analysis.

Finally, we considered methods of simulating SPM feedback which are currently used in the literature. We found that the prevalent method for performing feedback calculations analytically showed a highly decreased stability for the SPM loop than is expected. This arises from a mistake in the application of control theory for the PI controller, instead the system models a proportional differential controller. Combining this with incorrect modelling of the piezoelectric actuator for  $z$  position, the feedback loop heavily excites the eigenmode of the piezo causing oscillation which was mistaken as feedback ringing. We go further to discuss numerical models of feedback performance showing them to be in agreement with our the analytical model.

## 10.1 Future work

### 10.1.1 Accuracy of force extraction

Much work is needed for accurate and reproducible force extraction. The proposed symmetrical sensor needs to be fabricated and tested. If the sensor performs as expected this will eliminate the lateral motion present from sensors with cantilever style sensors. The accuracy of force measurements, however, is affected by the high uncertainty in the spring constant of the fabricated sensors. As such,

## Conclusion

once the sensor is fabricated it is important to find methods to experimentally probe the spring constant for each individual sensor. Methods such as thermal tuning and the Cleveland method could easily be applied to this sensor.

### 10.1.2 Automated SPM image acquisition and analysis

The automated SPM image acquisition needs to be extended in several directions. The tip optimisation software needs to be tested on a wider variety of surfaces. Currently it is possible by configuration files to modify the prescribed tip modification procedures if some are known to perform badly on a particular surface, in future this needs to be extended so that the system can learn and modify its methods autonomously. Other desirable extensions of the tip optimisation software is to extend it to qPlus ncAFM operation, and to engineer a specific molecular tip termination. Both of these will require extensive work. ncAFM operation can be very unstable, especially when surface contamination invisible in STM can cause tip crashes. The software will therefore need to be modified to monitor the scan live. This is not possible with many commercial SPM controllers and thus may require additional interfacing electronics. Recognising specific tip terminations introduces further complications. The ‘fingerprints’ of specific tip terminations are difficult for experienced operators to identify given time and theoretical images to compare to. As such, the image recognition software needs to perform as well as a human operator, something which will require significant investment of time into developing state-of-the-art image recognition.

Future work for the automated SPM image acquisition should not be limited to tip optimisation. As the system is capable of recognising high quality images, modification to collect many high quality images of different scales in different areas of a surface automatically should not be too time consuming. Combined with masking and recognising features it should be possible to automatically characterise surface reconstructions and molecular assemblies. This work will rely on extending the tip optimisation to more surfaces as if atomic/molecular resolution is lost the tip will need re-preparing.

For automated SPM image analysis further work is also needed to extend the software to open a wider range of SPM image formats, and to improve methods

## Conclusion

of exporting processed data. It may also be desirable to develop a user-friendly graphical user interface to help in the building and testing of analysis scripts before they are batch applied to data.

### **10.1.3 Feedback loop modelling**

The analytical model presented is purposefully simplified to allow isolated testing of the transfer function of the PI controller. This work could be extended to investigate the effect on imaging and stability caused by components such as amplifier bandwidths and mechanical resonances. For example, by modelling the resonance of an AFM cantilever it could be possible to investigate if the feedback causes excitation of the cantilever above that expected from the drive piezo. This would require modelling of the AFM control electronics as described by Nony *et al.* [47].

# Bibliography

- [1] G. Binnig, H. Rohrer, C. Gerber, and E. Weibel, *Applied Physics Letters* **40**, 178 (1982).
- [2] F. J. Giessibl, *Rev. Mod. Phys.* **75**, 949 (2003).
- [3] C. Mate, G. McClelland, R. Erlandsson, and S. Chiang, *Physical Review Letters* **59**, 1942 (1987).
- [4] J. J. Sáenz *et al.*, *Journal of Applied Physics* **62**, 4293 (1987).
- [5] U. Dürig, D. W. Pohl, and F. Rohner, *Journal of Applied Physics* **59**, 3318 (1986).
- [6] C. D. Bugg and P. J. King, *Journal of Physics E: Scientific Instruments* **21**, 147151 (1988).
- [7] K. Takayanagi, Y. Tanishiro, M. Takahashi, and S. Takahashi, *J. Vac. Sci. Technol. A* **3**, 1502 (1985).
- [8] F. J. Giessibl, M. Herz, and J. Mannhart, *Proceedings of the National Academy of Sciences of the United States of America* **99**, 12006 (2002).
- [9] I. Szlufarska, M. Chandross, and R. W. Carpick, *Journal of Physics D: Applied Physics* **41**, 123001 (2008).
- [10] F. Atamny and a. Baiker, *Surface Science* **323**, L314 (1995).
- [11] P. Markiewicz and M. C. Goh, *Review of Scientific Instruments* **66**, 3186 (1995).
- [12] C. Chiutu *et al.*, *Phys. Rev. Lett.* **108**, 268302 (2012).

## Bibliography

- [13] F. J. Giessibl, *Science* **289**, 422 (2000).
- [14] Y. Cesbron, C. P. Shaw, J. P. Birchall, P. Free, and R. Lévy, *Small* (Weinheim an der Bergstrasse, Germany) **8**, 3714 (2012).
- [15] T. Lenihan, a.P. Malshe, W. Brown, and L. Schaper, *Thin Solid Films* **270**, 356 (1995).
- [16] G. Binnig, H. Rohrer, C. Gerber, and E. Weibel, *Physical Review Letters* **49**, 5761 (1982).
- [17] J. Stroscio and W. Kaiser, editors, *Scanning Tunneling Microscopy* (Academic Press Limited, London, 1994).
- [18] D. Lide, editor, *CRC Handbook of Chemistry and Physics, 90th Edition (Internet Version)* (CRC Press/Taylor and Francis, Boca Raton, Florida, 2010), chap. 12.
- [19] R. Wiesendanger, *Scanning Probe Microscopy and Spectroscopy* (Cambridge University Press, Cambridge, 1994).
- [20] J. Bardeen, *Phys. Rev. Lett.* **6**, 57 (1961).
- [21] J. Tersoff and D. R. Hamann, *Physical Review B* **31**, 805 (1985).
- [22] C. J. Chen, *Physical Review B* **42**, 8841 (1990).
- [23] J. Tersoff, *Physical Review B* **41**, 1235 (1990).
- [24] C. J. Chen, *Journal of Vacuum Science & Technology A: Vacuum, Surfaces, and Films* **6**, 319 (1988).
- [25] A. Proctor and P. M. A. Sherwood, *Analytical Chemistry* **54**, 13 (1982).
- [26] A. Schwarz, H. Hölscher, S. M. Langkat, and R. Wiesendanger, *AIP Conference Proceedings* **696**, 68 (2003).
- [27] M. L. Goldstein, S. a. Morris, and G. G. Yen, *The European Physical Journal B* **41**, 255 (2004).

## Bibliography

- [28] F. J. Giessibl, *Applied Physics Letters* **78**, 123 (2001).
- [29] J. Sader and S. Jarvis, *Applied Physics Letters* **84**, 1801 (2004).
- [30] J. Welker, E. Illek, and F. J. Giessibl, *Beilstein journal of nanotechnology* **3**, 238 (2012).
- [31] A. Stannard and A. M. Sweetman, A considered approach to force extraction from dynamic force microscopy measurements, in *TBC*, edited by TBC, Springer, *In preparation*.
- [32] C. W. Groetsch, *The American Mathematical Monthly* **105**, 320 (1998).
- [33] M. Ternes, C. P. Lutz, C. F. Hirjibehedin, F. J. Giessibl, and A. J. Heinrich, *Science* **319**, 1066 (2008).
- [34] G. Langewisch, J. Falter, H. Fuchs, and a. Schirmeisen, *Physical Review Letters* **110**, 036101 (2013).
- [35] L. Gross, F. Mohn, N. Moll, P. Liljeroth, and G. Meyer, *Science* **325**, 1110 (2009).
- [36] D. W. Pohl and R. Moller, *Review of Scientific Instruments* **59**, 840 (1988).
- [37] E. Hill, B. Freelon, and E. Ganz, *Physical Review B* **60**, 15896 (1999).
- [38] B. Swartzentruber, *Physical review letters* **76**, 459 (1996).
- [39] X. Qin, B. Swartzentruber, and M. Lagally, *Physical review letters* **85**, 3660 (2000).
- [40] M. Abe, Y. Sugimoto, O. Custance, and S. Morita, *Nanotechnology* **16**, 3029 (2005).
- [41] P. Rahe *et al.*, *The Review of scientific instruments* **82**, 063704 (2011).
- [42] Z. Popović and B. Popović, *Introductory Electromagnetism* (Prentice Hall, New Jersey, 2000), pp. 247–248.
- [43] G. Binnig and D. Smith, *Rev. Sci. Instrum.* **57**, 1688 (1986).

## Bibliography

- [44] C. Chen, *Appl. Phys. Lett.* **60**, 132 (1992).
- [45] D. Pohl, *Rev. Sci. Instrum.* **58**, 54 (1987).
- [46] C. Chen, *Introduction to Scanning Tunneling Microscopy* (Oxford University Press, Oxford, 1993), chap. 12.
- [47] L. Nony *et al.*, *Physical Review B* **74**, 1 (2006).
- [48] S.-I. Park and C. F. Quate, *Appl. Phys. Lett.* **48**, 112 (1986).
- [49] B. K. Vainshtein, V. M. Fridkin, and V. L. Indenbom, *Structure of Crystals (3rd Edition)* (Springer-Verlag, Berlin, 2000), pp. 130–131.
- [50] E. Cisternas, F. Stavale, M. Flores, C. Achete, and P. Vargas, *Phys. Rev. B* **79**, 205431 (2009).
- [51] D. Tománek *et al.*, *Phys. Rev. B* **35**, 7790 (1987).
- [52] H. Mamin, E. Ganz, D. Abraham, R. Thomson, and J. Clarke, *Phys. Rev. B* **34**, 9015 (1986).
- [53] J. Soler, A. Baro, N. García, and H. Rohrer, *Phys. Rev. Lett.* **57**, 444 (1986).
- [54] M. Kuwabara, D. R. Clarke, and D. a. Smith, *Appl. Phys. Lett.* **56**, 2396 (1990).
- [55] J. Xhie, K. Sattler, M. Ge, and N. Venkateswaran, *Phys. Rev. B* **47**, 15835 (1993).
- [56] R. M. Feenstra, W. A. Thompson, and A. P. Fein, *Phys. Rev. Lett.* **56**, 608 (1986).
- [57] G. Binnig, H. Rohrer, and C. Gerber, *Physical Review Letters* **50**, 120 (1983).
- [58] R. E. Schlier and H. E. Farnsworth, *J. Chem. Phys.* **30**, 917 (1959).
- [59] R. J. Hamers, R. M. Tromp, and J. E. Demuth, *Phys. Rev. Lett.* **56**, 1972 (1986).

## Bibliography

- [60] F. J. Giessibl, *Science* **267**, 68 (1995).
- [61] F. J. Giessibl, *Appl. Phys. Lett.* **76**, 1470 (2000).
- [62] B. C. Stipe, M. A. Rezaei, and W. Ho, *Science* **279**, 1907 (1998).
- [63] A. Stannard *et al.*, *Nature chemistry* **4**, 112 (2012).
- [64] L. Grill *et al.*, *Nature nanotechnology* **2**, 687 (2007).
- [65] H. W. Kroto, A. W. Allaf, and S. P. Balm, *Chemical Reviews* **91**, 1213 (1991).
- [66] E. Willighagen, E. Willighagen, and M. Howard, Fast and Scriptable Molecular Graphics in Web Browsers without Java3D, in *Nature Precedings*, 2007.
- [67] P. of Vision Pty. Ltd. (2004), Persistence of vision raytracer (version 3.6), [Computer software] Retrieved from <http://www.povray.org/download/>.
- [68] T. Hashizume *et al.*, *Japanese Journal of Applied Physics* **31**, L880 (1992).
- [69] X.-D. Wang *et al.*, *Japanese Journal of Applied Physics* **31**, L983 (1992).
- [70] X.-D. Wang *et al.*, *Physical Review B* **47**, 15923 (1993).
- [71] D. Klyachko and D. Chen, *Physical Review Letters* **75**, 3693 (1995).
- [72] D. Chen and D. Sarid, *Surface Science* **329**, 206 (1995).
- [73] P. Moriarty, Y. Ma, M. Upward, and P. Beton, *Surface Science* **407**, 27 (1998).
- [74] P. H. Beton, a. W. Dunn, and P. Moriarty, *Applied Physics Letters* **67**, 1075 (1995).
- [75] P. Moriarty *et al.*, *Physical Review B* **57**, 362 (1998).
- [76] K. Sakamoto *et al.*, *Physical Review B* **58**, 13951 (1998).
- [77] K. Sakamoto *et al.*, *Journal of Electron Spectroscopy and Related Phenomena* **101-103**, 413 (1999).

## Bibliography

- [78] A. Pesci *et al.*, *Surface Science* **454-456**, 832 (2000).
- [79] J. N. OShea *et al.*, *The Journal of Chemical Physics* **119**, 13046 (2003).
- [80] S. Gangopadhyay *et al.*, *Surface Science* **603**, 2896 (2009).
- [81] R. Pawlak, S. Kawai, S. Fremy, T. Glatzel, and E. Meyer, *Journal of physics. Condensed matter : an Institute of Physics journal* **24**, 084005 (2012).
- [82] K. Kobayashi, H. Yamada, T. Horiuchi, and K. Matsushige, *Applied Surface Science* **140**, 281 (1999).
- [83] C. Hobbs and L. Kantorovich, *Surface Science* **600**, 551 (2006).
- [84] N. Martsinovich and L. Kantorovich, *Nanotechnology* **20**, 135706 (2009).
- [85] R. Pawlak, S. Kawai, S. Fremy, T. Glatzel, and E. Meyer, *ACS nano* **5**, 6349 (2011).
- [86] L. Gross *et al.*, *Science (New York, N.Y.)* **337**, 1326 (2012).
- [87] L. A. Girifalco, *The Journal of Physical Chemistry* **96**, 858 (1992).
- [88] J. Pacheco and J. Prates Ramalho, *Physical Review Letters* **79**, 3873 (1997).
- [89] A. J. Lakin, H. S. Alqannas, and J. L. Dunn, *Journal of Physics: Conference Series* **428**, 012001 (2013).
- [90] J. L. Dunn, A. J. Lakin, and I. D. Hands, *New Journal of Physics* **14**, 083038 (2012).
- [91] A. J. Lakin, C. Chiutu, A. M. Sweetman, P. Moriarty, and J. L. Dunn, *Physical Review B* **88**, 035447 (2013).
- [92] G. Binnig, C. F. Quate, and C. Gerber, *Physical Review Letters* **56**, 930 (1986).
- [93] G. Kaye and T. Laby, *Tables of Physical & Chemical Constants, 16th Edition* (Longman, Essex, 1995).

## Bibliography

- [94] R. Erlandsson, G. M. McClelland, C. M. Mate, and S. Chiang, *Journal of Vacuum Science & Technology A: Vacuum, Surfaces, and Films* **6**, 266 (1988).
- [95] G. Meyer and N. M. Amer, *Applied Physics Letters* **53**, 1045 (1988).
- [96] H. J. Butt and M. Jaschke, *Nanotechnology* **6**, 1 (1995).
- [97] T. R. Albrecht and C. F. Quate, *Journal of Vacuum Science & Technology A: Vacuum, Surfaces, and Films* **6**, 271 (1988).
- [98] P. Günther, U. C. Fischer, and K. Dransfeld, *Applied Physics B* **48**, 89 (1989).
- [99] T. Göddenhenrich, H. Lemke, U. Hartmann, and C. Heiden, *Journal of Vacuum Science & Technology A: Vacuum, Surfaces, and Films* **8**, 383 (1990).
- [100] T. R. Albrecht, S. Akamine, T. Carver, and C. F. Quate, *Journal of Vacuum Science & Technology A: Vacuum, Surfaces, and Films* **8**, 3386 (1990).
- [101] S. Akamine, R. C. Barrett, and C. F. Quate, *Applied Physics Letters* **57**, 316 (1990).
- [102] O. Marti, J. Colchero, and J. Mlynek, *Nanotechnology* **1**, 141 (1990).
- [103] M. Tortonese, H. Yamada, R. C. Barrett, and C. F. Quate, *Atomic force microscopy using a piezoresistive cantilever* (IEEE, 1991), pp. 448–451.
- [104] M. Tortonese, R. C. Barrett, and C. F. Quate, *Applied Physics Letters* **62**, 834 (1993).
- [105] F. J. Giessibl and B. M. Trafas, *Review of Scientific Instruments* **65**, 1923 (1994).
- [106] J. Brugger, R. A. Buser, and N. F. d. Rooij, *Journal of Micromechanics and Microengineering* **2**, 218 (1992).

## Bibliography

- [107] F. J. Giessibl and G. Binnig, *Ultramicroscopy* **42-44**, 281 (1992).
- [108] E.-L. Florin, M. Radmacher, B. Fleck, and H. E. Gaub, *Review of Scientific Instruments* **65**, 639 (1994).
- [109] G. C. Ratcliff, D. a. Erie, and R. Superfine, *Applied Physics Letters* **72**, 1911 (1998).
- [110] K. Yamanaka and E. Tomita, *Japanese Journal of Applied Physics* **34**, 2879 (1995).
- [111] K. Yamanaka, H. Takano, E. Tomita, and M. Fujihira, *Japanese Journal of Applied Physics* **35**, 5421 (1996).
- [112] S. P. Jarvis, H. Tokumoto, H. Yamada, K. Kobayashi, and A. Toda, *Applied Physics Letters* **75**, 3883 (1999).
- [113] S. P. Jarvis, H. Yamada, K. Kobayashi, A. Toda, and H. Tokumoto, *Applied Surface Science* **157**, 314 (2000).
- [114] O. Sahin, S. Magonov, C. Su, C. F. Quate, and O. Solgaard, *Nature nanotechnology* **2**, 507 (2007).
- [115] N. Mullin *et al.*, *Applied Physics Letters* **94**, 173109 (2009).
- [116] F. J. Giessibl, F. Pielmeier, T. Eguchi, T. An, and Y. Hasegawa, *Physical Review B* **84**, 1 (2011).
- [117] H. Edwards, L. Taylor, W. Duncan, and A. J. Melmed, *Journal of Applied Physics* **82**, 980 (1997).
- [118] F. J. Giessibl, *Applied Physics Letters* **73**, 3956 (1998).
- [119] T. An, T. Eguchi, K. Akiyama, and Y. Hasegawa, *Applied Physics Letters* **87**, 133114 (2005).
- [120] M. Heyde, M. Kulawik, H.-P. Rust, and H.-J. Freund, *Review of Scientific Instruments* **75**, 2446 (2004).

## Bibliography

- [121] M. Heyde, M. Sterrer, H.-P. Rust, and H.-J. Freund, *Applied Physics Letters* **87**, 083104 (2005).
- [122] S. Torbrügge, O. Schaff, and J. Rychen, *Journal of Vacuum Science & Technology B: Microelectronics and Nanometer Structures* **28**, C4E12 (2010).
- [123] P. Mühlischlegel, J. Toquant, D. W. Pohl, and B. Hecht, *Review of Scientific Instruments* **77**, 016105 (2006).
- [124] J. M. Neumeister and W. A. Ducker, *Review of Scientific Instruments* **65**, 2527 (1994).
- [125] U. D. Schwarz, P. Koster, and R. Wiesendanger, *Review of Scientific Instruments* **67**, 2560 (1996).
- [126] R. Cain, S. Biggs, and N. Page, *Journal of colloid and interface science* **227**, 55 (2000).
- [127] J. P. Cleveland, S. Manne, D. Bocek, and P. K. Hansma, *Review of Scientific Instruments* **64**, 403 (1993).
- [128] J. L. Hutter and J. Bechhoefer, *Review of Scientific Instruments* **64**, 1868 (1993).
- [129] J. E. Sader, I. Larson, P. Mulvaney, and L. R. White, *Review of Scientific Instruments* **66**, 3789 (1995).
- [130] J. E. Sader, J. W. M. Chon, and P. Mulvaney, *Review of Scientific Instruments* **70**, 3967 (1999).
- [131] D. S. Golovko, T. Haschke, W. Wiechert, and E. Bonaccorso, *The Review of scientific instruments* **78**, 043705 (2007).
- [132] G. A. Shaw, J. R. Pratt, and Z. J. Jabbour, *Conference Proceedings of the Society for Experimental Mechanics Series* **2**, 49 (2011).
- [133] R. W. Stark, T. Drobek, and W. M. Heckl, *Ultramicroscopy* **86**, 207 (2001).
- [134] J. Melcher, S. Hu, and A. Raman, *Applied Physics Letters* **91**, 053101 (2007).

## Bibliography

- [135] J. E. Sader, *Journal of Applied Physics* **84**, 64 (1998).
- [136] P. J. Cumpson, C. a. Clifford, and J. Hedley, *Measurement Science and Technology* **15**, 1337 (2004).
- [137] M. S. Allen, H. Sumali, and P. C. Penegor, *Journal of Dynamic Systems, Measurement, and Control* **131**, 064501 (2009).
- [138] J. R. Lozano, D. Kiracofe, J. Melcher, R. Garcia, and A. Raman, *Nanotechnology* **21**, 465502 (2010).
- [139] J. Lübbe, L. Doering, and M. Reichling, *Measurement Science and Technology* **23**, 045401 (2012).
- [140] R. C. Tung *et al.*, *Journal of Applied Physics* **107**, 104508 (2010).
- [141] R. Lvy and M. Maaloum, *Nanotechnology* **13**, 33 (2002).
- [142] S. M. Cook *et al.*, *Nanotechnology* **17**, 2135 (2006).
- [143] B. Ohler, *The Review of scientific instruments* **78**, 063701 (2007).
- [144] G. A. Lindsay, *American Journal of Physics* **11**, 319 (1943).
- [145] J. Stirling and G. A. Shaw, *Beilstein Journal of Nanotechnology* **4**, 10 (2013).
- [146] A. Sweetman *et al.*, *Phys. Rev. Lett.* **106**, 136101 (2011).
- [147] A. Sweetman *et al.*, *Phys. Rev. B* **84**, 085426 (2011).
- [148] C. Chiutu, A. Stannard, A. M. Sweetman, and P. Moriarty, *Chem. Commun.* **47**, (2011).
- [149] A. Sweetman, S. Jarvis, R. Danza, and P. Moriarty, *Beilstein Journal of Nanotechnology* **3**, 25 (2012).
- [150] S. Rao, *Mechanical vibrations* (Addison-Wesley, 1995).
- [151] F. J. Giessibl, *Phys. Rev. B* **56**, 16010 (1997).

## Bibliography

- [152] Y. H. Yang and W. Z. Li, *Applied Physics Letters* **98**, 041901 (2011).
- [153] G. A. Shaw, Improvement in Uncertainty of Tuning Fork-Based Force Sensor Stiffness Calibration via the Indentation Method Using Direct Determination of Contact and Machine Compliance, in *Proceedings of the 2013 Annual Conference on Experimental and Applied Mechanics*, edited by G. A. Shaw, B. C. Prorok, L. Starman, and C. Furlong, pp. 125–128, Springer, 2014.
- [154] D. van Vrden, M. Lange, M. Schmuck, N. Schmidt, and R. Mller, *Beilstein Journal of Nanotechnology* **3**, 809 (2012).
- [155] M. Piancastelli, N. Motta, A. Sgarlata, A. Balzarotti, and M. De Crescenzi, *Physical Review B* **48**, 17892 (1993).
- [156] J. Stirling, *Beilstein journal of nanotechnology* **4**, 370 (2013).
- [157] S. Kawai, S.-i. Kitamura, D. Kobayashi, and H. Kawakatsu, *Applied Physics Letters* **87**, 173105 (2005).
- [158] F. J. Giessibl, H. Bielefeldt, S. Hembacher, and J. Mannhart, *Applied Surface Science* **140**, 352 (1999).
- [159] J. Berger *et al.*, *Beilstein Journal of Nanotechnology* **4**, 1 (2013).
- [160] J. Gere and B. Goodno, *Mechanics of Materials, 8th Edition* (Cengage Learning, 2013).
- [161] NaugaNeedles, <http://nauganeedles.com>, Private Communication.
- [162] Z. Majzik *et al.*, *Beilstein Journal of Nanotechnology* **3**, 249 (2012).
- [163] R. A. J. Woolley, J. Stirling, A. Radocea, N. Krasnogor, and P. Moriarty, *Appl. Phys. Lett.* **98**, 253104 (2011).
- [164] J. Stirling, R. A. J. Woolley, and P. Moriarty, *Review of Scientific Instruments* **84**, 113701 (2013).
- [165] J. Pethica, *Physical Review Letters* **57**, 3235 (1986).

## Bibliography

- [166] J. Starink and T. M. Jovin, *Surface Science* **359**, 291305 (1996).
- [167] G. Terrazas, P. Siepman, G. Kendall, and N. Krasnogor, *Journal of Cellular Automata* **2**, 77 (2007).
- [168] S. Deans, *The Radon transform and some of its applications* A Wiley-Interscience publication (Wiley, New York City, 1983).
- [169] F. Maes, A. Collignon, D. Vandermeulen, G. Marchal, and P. Suetens, *Medical Imaging, IEEE Transactions on* **16**, 187 (1997).
- [170] D. Nečas and P. Klapetek, *Central European Journal of Physics* **10**, 181188 (2011).
- [171] I. Horcas *et al.*, *Rev. Sci. Instrum.* **78**, 013705 (2007).
- [172] M. Raposo, Q. Ferreira, and P. A. Ribeiro, *A Guide for Atomic Force Microscopy Analysis of Soft- Condensed Matter* (Formatex, 2007), p. 758769.
- [173] C. a. Schneider, W. S. Rasband, and K. W. Eliceiri, *Nature Methods* **9**, 671675 (2012).
- [174] A. Liscio, *Chemphyschem* **14**, 128392 (2013).
- [175] N. Zaki *et al.*, *Physical Review B* **83**, 205420 (2011).
- [176] B. W. Erickson, S. Coquoz, J. D. Adams, D. J. Burns, and G. E. Fantner, *Beilstein Journal of Nanotechnology* **3**, 747 (2012).
- [177] R. C. Gonzalez and R. E. Woods, *Digital Image Processing (2nd Edition)* (Prentice-Hall, Inc., 2002), p. 137.
- [178] K. Brommer, M. Needels, B. Larson, and J. Joannopoulos, *Physical Review Letters* **68**, 13551358 (1992).
- [179] M. Blunt *et al.*, *Chemical communications* , 23046 (2008).
- [180] M. J. Lawler *et al.*, *Nature* **466**, 34751 (2010).
- [181] J. Stirling, *Submitted* (2013).

## Bibliography

- [182] J. Stirling *et al.*, *In Preparation* .
- [183] T. Wutscher, J. Niebauer, and F. J. Giessibl, The Review of scientific instruments **84**, 073704 (2013).
- [184] O. Payton, a. R. Champneys, M. E. Homer, L. Picco, and M. J. Miles, Proceedings of the Royal Society A: Mathematical, Physical and Engineering Sciences **467**, 1801 (2010).
- [185] K. K. Leang and S. Devasia, IEEE Transactions on Control Systems Technology **15**, 927 (2007).
- [186] a. I. Oliva, E. Anguiano, N. Denisenko, M. Aguilar, and J. L. Pena, Review of Scientific Instruments **66**, 3196 (1995).
- [187] E. Anguiano, a. I. Oliva, and M. Aguilar, Review of Scientific Instruments **69**, 3867 (1998).
- [188] F. Biscarini *et al.*, Langmuir : the ACS journal of surfaces and colloids *Just Accepted* (2013).
- [189] G. Schitter and a. Stemmer, IEEE Transactions on Control Systems Technology **12**, 449 (2004).
- [190] T. H. Glisson, *Introduction to Circuit Analysis and Design* (Springer-Verlag, 2011), chap. 18.
- [191] A. M. Jackson, J. W. Myerson, and F. Stellacci, Nature materials **3**, 330 (2004).
- [192] M. Yu and F. Stellacci, Small **8**, 3720 (2012).
- [193] S. Hadlington, Striped nanoparticle controversy blows up, 2012, Chemistry World,  
<http://www.rsc.org/chemistryworld/2012/12/stripped-nanoparticles-self-assembly-stm-controversy>.
- [194] S. Rao, *Mechanical Vibrations, Third Edition* (Addison–Wesley Publishing Company, Inc, Reading, Massachusetts, 1995), chap. 8.

# Appendix A

## Derivations of key equations in AFM

*“Moderation is a fatal thing. Nothing succeeds like excess.”*

Oscar Wilde

### Appendix Overview

This appendix contains many very complete derivations of the key equation needed to understand the motion of the cantilever in AFM. It is included as the form of these derivations is vital to much of the work presented in this thesis which modifies the standard calculations to take into account for elements such as tip geometry, and other sensor geometries. Much of it could be described as bookwork, however having it all together, cross-referenced and where possible derived from first principles is considered preferable to citing a range of textbooks and papers with less complete derivations.

### A.1 Free simple harmonic oscillator

A freely oscillating damped cantilever with spring constant  $k$ , and displacement  $z$  has equation of motion:

$$F = ma \tag{A.1}$$

$$-kz - c\dot{z} = m\ddot{z} \tag{A.2}$$

where  $c$  is the viscous damping coefficient.

By suggesting the oscillating, exponentially decreasing, solution

$$z = Ae^{-dt}e^{i\omega t} = Ae^{(i\omega-d)t} \tag{A.3}$$

Derivations of key equations in AFM

equation (A.2) becomes

$$-kz = c(i\omega - d)z + m(i\omega - d)^2z \quad (\text{A.4})$$

$$-k = ic\omega - dc - m\omega^2 - 2im\omega d + md^2 \quad (\text{A.5})$$

however by imposing the condition that  $k$  must be real we get

$$c = 2md \quad (\text{A.6})$$

taking the real part of equation (A.5) and substituting in equation (A.6) we get

$$-k = -md^2 - m\omega^2 \quad (\text{A.7})$$

$$\frac{k}{m} = d^2 + \omega^2 = \omega_0^2 \quad (\text{A.8})$$

we can now rewrite equation (A.2) as

$$0 = \omega_0^2 z + 2d\dot{z} + \ddot{z} \quad (\text{A.9})$$

by writing  $d$  in terms of the damping ratio  $\zeta = \frac{d}{\omega_0}$

$$0 = \omega_0^2 z + 2\zeta\omega_0\dot{z} + \ddot{z}. \quad (\text{A.10})$$

This is the equation of motion for the damped harmonic oscillator.

## A.2 Quality Factor

The quality factor,  $Q$ , is defined as

$$Q = 2\pi \frac{\text{Energy stored}}{\text{Energy dissipated per oscillation}}, \quad (\text{A.11})$$

therefore the fraction of energy after  $Q$  cycles is

$$\frac{E_Q}{E_0} = \left(1 - \frac{2\pi}{Q}\right)^Q = \left(\frac{Q - 2\pi}{Q}\right)^Q. \quad (\text{A.12})$$

By generalising  $Q$  to  $z$  and  $2\pi$  to  $a$ , we get

$$\left(\frac{z - a}{z}\right)^z = \frac{(z - a)^z}{z^z} \quad (\text{A.13})$$

## Derivations of key equations in AFM

then by performing a binomial expansion on the top

$$= 1 + \binom{z}{1} \frac{z^{z-1}}{z} (-a) + \binom{z}{2} \frac{z^{z-2}}{z} (-a)^2 + \binom{z}{3} \frac{z^{z-3}}{z} (-a)^3 + \dots \quad (\text{A.14})$$

where  $\binom{n}{k}$  are binomial coefficients, which can be written as  $\frac{n!}{k!(n-k)!}$

$$= 1 + \frac{z!}{(z-1)!z} (-a) + \frac{z!}{2(z-2)!z^2} (-a)^2 + \frac{z!}{3!(z-3)!z^3} (-a)^3 + \dots \quad (\text{A.15})$$

but

$$\frac{z!}{(z-n)!} = z(z-1)(z-2)\dots(z-n) \quad (\text{A.16})$$

$$\approx z^n \quad \text{for } z \gg n \quad (\text{A.17})$$

so if for large  $z$

$$\left(\frac{z-a}{z}\right)^z = 1 + (-a) + \frac{1}{2}(-a)^2 + \frac{1}{3!}(-a)^3 + \dots \quad (\text{A.18})$$

$$= e^{-a} \quad (\text{A.19})$$

so from equation (A.12) for large  $Q$  the fraction of energy after  $Q$  cycles is

$$\frac{E_Q}{E_0} = e^{-2\pi} \quad (\text{A.20})$$

The energy of the oscillation is equal to the work done against the restoring force of the cantilever to move from no deflection to maximum deflection,

$$E = \int_0^A zkdz = \frac{1}{2}kA^2. \quad (\text{A.21})$$

Considering the exponential decay of the amplitude derived in Appendix A.1

$$A = A_0 e^{-\omega_0 \zeta t} \quad (\text{A.22})$$

Derivations of key equations in AFM

after  $Q$  cycles of period  $T$

$$\frac{E_Q}{E_0} = \frac{A_Q^2}{A_0^2} = (e^{-\omega_0 \zeta QT})^2 = e^{-2\pi} \quad (\text{A.23})$$

$$\therefore 2\omega_0 \zeta QT = 2\pi \quad (\text{A.24})$$

But  $\omega_0 = \frac{2\pi}{T}$ , hence

$$Q = \frac{1}{2\zeta} \quad (\text{A.25})$$

### A.3 Driving Amplitude

It can be useful to consider any driving force in terms of a corresponding amplitude without any resonance effects. Consider Hooke's law with a constant force  $F$ .

$$F = -kz \quad (\text{A.26})$$

dividing through by the mass and using equation (A.8) we get

$$\frac{F}{m} = -\omega_0^2 z \quad (\text{A.27})$$

we can rename the deflection amplitude  $z$  as  $A_{\text{drive}}$  getting the relation.

$$A_{\text{drive}} = -\frac{F}{m\omega_0^2} \quad (\text{A.28})$$

## A.4 The Cantilever

### A.4.1 Equation of Motion of a Cantilever

Consider a simple cantilever as shown in figure A.1. We will consider an element of length  $dx$  deflected by  $z$ . It has opposing shear forces  $V$  and  $V + dV$ , and opposing bending moments  $M$  and  $M + dM$  at either end and a force per unit length of  $f(x, t)$ .

By resolving forces in the direction of deflection and using Newton's second law

$$V - (V + dV) + f(x, t)dx = \rho A dx \frac{\partial^2 z}{\partial t^2} \quad (\text{A.29})$$

Derivations of key equations in AFM

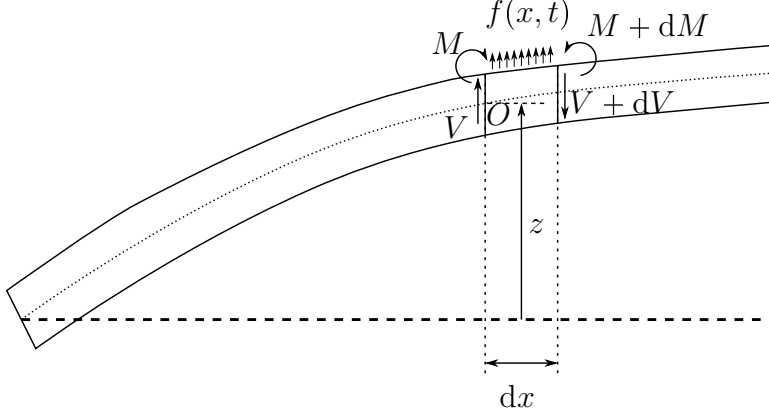


Figure A.1: A simple cantilever. With shear force  $V$ , bending moment  $M$  and force per unit area  $f$ .

and balancing the moments

$$(M + dM) - M - (V + dV)dx + f dx \frac{dx}{2} = 0 \quad (\text{A.30})$$

Considering

$$dM = \frac{\partial M}{\partial x} dx \quad dV = \frac{\partial V}{\partial x} dx \quad (\text{A.31})$$

therefore equation (A.29) becomes

$$-\frac{\partial V}{\partial x} dx + f(x, t) dx = \rho A dx \frac{\partial^2 z}{\partial t^2} \quad (\text{A.32})$$

$$-\frac{\partial V}{\partial x} + f(x, t) = \rho A \frac{\partial^2 z}{\partial t^2} \quad (\text{A.33})$$

and balancing the moments

$$\frac{\partial M}{\partial x} dx - V dx - \frac{\partial V}{\partial x} dx dx + f dx \frac{dx}{2} = 0 \quad (\text{A.34})$$

any terms with  $dx^2$  terms are considered vanishing, and hence

$$\frac{\partial M}{\partial x} = V. \quad (\text{A.35})$$

Combining equations (A.33) and (A.35) we get

$$-\frac{\partial^2 M}{\partial x^2} + f(x, t) = \rho A \frac{\partial^2 z}{\partial t^2} \quad (\text{A.36})$$

## Derivations of key equations in AFM

According to Euler-Bernoulli theory [194] the bending moment of a thin beam is related to the bending<sup>1</sup> by

$$M = EI \frac{\partial^2 z}{\partial x^2}, \quad (\text{A.37})$$

where  $E$  is the Young's modulus and  $I$  is the second moment of area of the cantilever through the bending axis.

Thus equation (A.36) becomes

$$EI \frac{\partial^4 z}{\partial x^4} = f(x, t) - \rho A \frac{\partial^2 z}{\partial t^2} \quad (\text{A.38})$$

the dynamic Euler-Bernoulli equation.

### A.4.2 Second moment of area

At each cantilever segment beam bends through an axis located halfway through the beams thickness (parallel to the deflection). The axis of bending is perpendicular to both the beams length and deflection. By defining the beams width as  $w$  ( $y$  direction) and thickness as  $h$  ( $z$  direction) the second moment of area can be calculated as

$$I_y = \int_A z^2 dA = \int_{-\frac{h}{2}}^{\frac{h}{2}} \int_0^w z^2 dy dz \quad (\text{A.39})$$

$$= \int_{-\frac{h}{2}}^{\frac{h}{2}} z^2 w dz = \left[ \frac{z^3}{3} w \right]_{-\frac{h}{2}}^{\frac{h}{2}} \quad (\text{A.40})$$

$$= \frac{h^3 w}{24} - \left( \frac{-h^3 w}{24} \right) = \frac{h^3 w}{12} \quad (\text{A.41})$$

### A.4.3 Spring Constant

Starting with equation (A.38) and considering a force,  $F$ , to be located directly on the end of the cantilever, we can use a Dirac delta function and get

$$EI \frac{\partial^4 z}{\partial x^4} = F \delta(x - L) - \rho A \frac{\partial^2 z}{\partial t^2} \quad (\text{A.42})$$

---

<sup>1</sup>Second derivative of the beam deflection with respect to position along the beams length ( $\frac{\partial^2 z}{\partial x^2}$ )

Derivations of key equations in AFM

and for a static deflected cantilever  $\frac{\partial^2 z}{\partial t^2} = 0$

$$EI \frac{\partial^4 z}{\partial x^4} = F\delta(x - L) \quad (\text{A.43})$$

$$\int EI \frac{\partial^4 z}{\partial x^4} dx = \int F\delta(x - L) dx \quad (\text{A.44})$$

$$EI \frac{\partial^3 z}{\partial x^3} = F + c \quad (\text{A.45})$$

$c = 0$  as if  $F = 0$  is applied the beam will relax and  $\frac{\partial^3 z}{\partial x^3} = 0$

$$EI \frac{\partial^3 z}{\partial x^3} = F \quad (\text{A.46})$$

We can now write the differential equation as

$$EI \frac{\partial^4 z}{\partial x^4} = 0 \quad \text{for } 0 \leq x < L \quad (\text{A.47})$$

and we have 4 boundary conditions

$$z|_{x=0} = 0 \quad \text{Beam clamped at } x = 0. \quad (\text{A.48})$$

$$EI \frac{\partial z}{\partial x} \Big|_{x=0} = 0 \quad \text{Beam clamped at } x = 0. \quad (\text{A.49})$$

$$EI \frac{\partial^2 z}{\partial x^2} \Big|_{x=L} = 0 \quad \text{No force at } x > L \text{ to cause it to bend.} \quad (\text{A.50})$$

$$EI \frac{\partial^3 z}{\partial x^3} \Big|_{x=L} = F \quad \text{From equation (A.46).} \quad (\text{A.51})$$

A general solution for equation (A.47) is

$$z = A + Bx + Cx^2 + Dx^3 \quad (\text{A.52})$$

from equations (A.48) and (A.49) we get

$$A = 0 \quad \text{and} \quad B = 0. \quad (\text{A.53})$$

Therefore with equation (A.50) we get

$$2C + 6DL = 0 \quad (\text{A.54})$$

Derivations of key equations in AFM

and finally using equation (A.51) we can show

$$D = \frac{F}{6EI} \quad (\text{A.55})$$

combining this with equation (A.54)

$$C = \frac{-3FL}{6EI} \quad (\text{A.56})$$

Therefore giving the solution of  $z$  for these boundary conditions as

$$z = \frac{F}{6EI} (x^3 - 3Lx^2) . \quad (\text{A.57})$$

Considering the deflection a  $z = L$

$$F = \frac{-3EI}{L^3} z \quad (\text{A.58})$$

Therefore using Hooke's law the spring constant of a cantilever is

$$k = \frac{3EI}{L^3} \quad (\text{A.59})$$

#### A.4.4 Natural Frequencies

Again starting with equation (A.38) this time with no force

$$EI \frac{\partial^4 z}{\partial x^4} + \rho A \frac{\partial^2 z}{\partial t^2} = 0 \quad (\text{A.60})$$

the solution  $z(x, t)$  can be considered separable as

$$z(x, t) = \Phi(x)T(t) \quad (\text{A.61})$$

$$\therefore EIT(t) \frac{\partial^4 \Phi(x)}{\partial x^4} + \rho A \Phi(x) \frac{\partial^2 T(t)}{\partial t^2} = 0 \quad (\text{A.62})$$

$$\frac{\partial^2 T(t)}{\partial t^2} = - \underbrace{\frac{EI}{\rho A \Phi(x)} \frac{\partial^4 \Phi(x)}{\partial x^4}}_{\omega_0^2} T(t) \quad (\text{A.63})$$

Derivations of key equations in AFM

From this we can get a differential equation for  $\Phi(x)$

$$\frac{\partial^4 \Phi(x)}{\partial x^4} = \frac{\rho A \omega^2}{EI} \Phi(x) \quad (\text{A.64})$$

$$\text{Let } \beta^4 = \frac{\rho A \omega^2}{EI} \quad (\text{A.65})$$

$$\frac{\partial^4 \Phi(x)}{\partial x^4} = \beta^4 \Phi(x) \quad (\text{A.66})$$

$$(\text{A.67})$$

This has a general solution of

$$\Phi(x) = B_1 e^{\beta x} + B_2 e^{-\beta x} + B_3 e^{i\beta x} + B_4 e^{-i\beta x} \quad (\text{A.68})$$

which is equivalent to

$$\Phi(x) = b_1 \cos(\beta x) + b_2 \sin(\beta x) + b_3 \cosh(\beta x) + b_4 \sinh(\beta x) \quad (\text{A.69})$$

For this system there is no external force so the boundary conditions are

$$z|_{x=0} = 0 \quad \text{Beam clamped at } x = 0. \quad (\text{A.70})$$

$$EI \frac{\partial z}{\partial x} \Big|_{x=0} = 0 \quad \text{Beam clamped at } x = 0. \quad (\text{A.71})$$

$$EI \frac{\partial^2 z}{\partial x^2} \Big|_{x=L} = 0 \quad \text{No force at } x > L \text{ to cause it to bend.} \quad (\text{A.72})$$

$$EI \frac{\partial^3 z}{\partial x^3} \Big|_{x=L} = 0 \quad \text{From equation (A.46) } (F = 0). \quad (\text{A.73})$$

Hence, from these four boundary conditions we get 4 simultaneous equations

$$b_1 + b_3 = 0 \quad (\text{A.74})$$

$$\beta b_2 + \beta b_4 = 0 \quad (\text{A.75})$$

$$-\beta^2 b_1 \cos(\beta L) - \beta^2 b_2 \sin(\beta L) + \beta^2 b_3 \cosh(\beta L) + \beta^2 b_4 \sinh(\beta L) = 0 \quad (\text{A.76})$$

$$\beta^3 b_1 \sin(\beta L) - \beta^3 b_2 \cos(\beta L) + \beta^3 b_3 \sinh(\beta L) + \beta^3 b_4 \cosh(\beta L) = 0 \quad (\text{A.77})$$

dividing each equation through to remove all  $\beta$  terms and then writing as a matrix we get

$$\underbrace{\begin{pmatrix} 1 & 0 & 1 & 0 \\ 0 & 1 & 0 & 1 \\ -\cos(\beta L) & -\sin(\beta L) & \cosh(\beta L) & \sinh(\beta L) \\ \sin(\beta L) & -\cos(\beta L) & \sinh(\beta L) & \cosh(\beta L) \end{pmatrix}}_{\underline{D}} \begin{pmatrix} b_1 \\ b_2 \\ b_3 \\ b_4 \end{pmatrix} = \begin{pmatrix} 0 \\ 0 \\ 0 \\ 0 \end{pmatrix} \quad (\text{A.78})$$

Derivations of key equations in AFM

Considering the case where

$$\det(\underline{\underline{D}}) \neq 0 \quad (\text{A.79})$$

Then  $\underline{\underline{D}}^{-1}$  exists and hence

$$\begin{pmatrix} b_1 \\ b_2 \\ b_3 \\ b_4 \end{pmatrix} = \underline{\underline{D}}^{-1} \begin{pmatrix} 0 \\ 0 \\ 0 \\ 0 \end{pmatrix} \quad (\text{A.80})$$

which would give a trivial solution

$$b_1 = b_2 = b_3 = b_4 = 0 \quad (\text{A.81})$$

Therefore the condition for a non-trivial solution is

$$\begin{vmatrix} 1 & 0 & 1 & 0 \\ 0 & 1 & 0 & 1 \\ -\cos(\beta L) & -\sin(\beta L) & \cosh(\beta L) & \sinh(\beta L) \\ \sin(\beta L) & -\cos(\beta L) & \sinh(\beta L) & \cosh(\beta L) \end{vmatrix} = 0 \quad (\text{A.82})$$

We can solve this to get

$$\underbrace{\sin^2(\beta L) + \cos^2(\beta L)}_1 + \underbrace{\cosh^2(\beta L) - \sinh^2(\beta L)}_1 + 2 \cos(\beta L) \cosh(\beta L) = 0 \quad (\text{A.83})$$

$$\therefore 1 + \cos(\beta L) \cosh(\beta L) = 0 \quad (\text{A.84})$$

This can be solved numerically using the Newton-Raphson method see figure A.2, giving the solutions

$$\beta L = 1.875104, 4.694091, 7.854757, 10.995541, 14.137168, \dots \quad (\text{A.85})$$

From the definition of  $\beta$  in equation (A.65) we can calculate that

$$\omega = (\beta L)^2 \sqrt{\frac{EI}{mL^3}} \quad (\text{A.86})$$

## Derivations of key equations in AFM

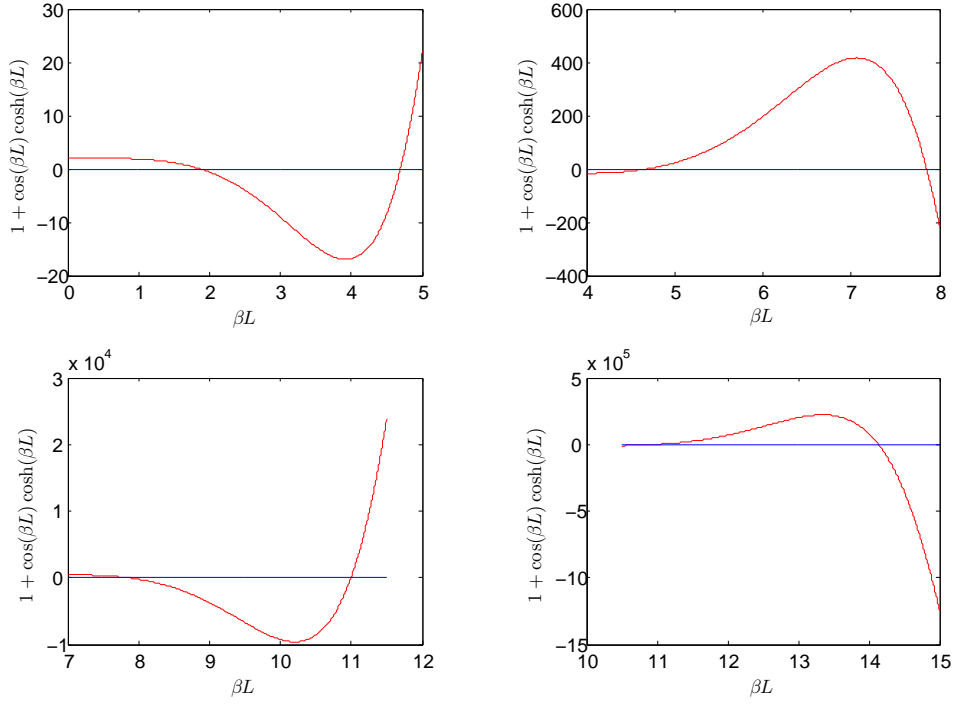


Figure A.2: *The first 5 roots of  $1 + \cos(\beta L) \cosh(\beta L) = 0$ .*

hence we get the following resonant frequencies for our cantilever

$$\begin{aligned}
 \omega_1 &= 3.516015 \sqrt{\frac{EI}{mL^3}} & f_1 &= 0.559591 \sqrt{\frac{EI}{mL^3}} = 1f_1 \\
 \omega_2 &= 22.034492 \sqrt{\frac{EI}{mL^3}} & f_2 &= 3.506898 \sqrt{\frac{EI}{mL^3}} = 6.266893f_1 \\
 \omega_3 &= 61.697214 \sqrt{\frac{EI}{mL^3}} & f_3 &= 9.819417 \sqrt{\frac{EI}{mL^3}} = 17.547482f_1 \\
 \omega_4 &= 120.901916 \sqrt{\frac{EI}{mL^3}} & f_4 &= 19.242138 \sqrt{\frac{EI}{mL^3}} = 34.386061f_1 \\
 \omega_5 &= 199.859530 \sqrt{\frac{EI}{mL^3}} & f_5 &= 31.808632 \sqrt{\frac{EI}{mL^3}} = 56.842623f_1
 \end{aligned}$$

### A.4.5 Effective Mass of Cantilever

From Hooke's law we get

$$\frac{k}{m} = \omega_0^2 \tag{A.87}$$

Derivations of key equations in AFM

as shown in (A.8). Using the value for  $k$  derived in equation (A.59) we expect a first resonance at

$$\omega_0 = \sqrt{\frac{k}{m}} = \sqrt{\frac{3EI}{L^3m}} = 1.732051\sqrt{\frac{EI}{L^3m}} \quad (\text{A.88})$$

Does not agree with the first resonance as calculated in Appendix A.4.4 because in Hooke's law all the mass is moved over the entire deflection which is not true for a cantilever. By defining the effective mass,  $m_{\text{eff}}$ , of a cantilever as its as a fraction of its mass such that it follows the resonant frequency as derived by Hooke's law, we can say

$$\omega_0 = 1.732051\sqrt{\frac{EI}{L^3Rm}} = 3.516015\sqrt{\frac{EI}{mL^3}} \quad (\text{A.89})$$

where  $R = \frac{m_{\text{eff}}}{m}$

$$1.732051R^{-1/2}\sqrt{\frac{EI}{L^3m}} = 3.516015\sqrt{\frac{EI}{mL^3}} \quad (\text{A.90})$$

$$R = \left(\frac{1.732051}{3.516015}\right)^2 = 0.242672 \quad (\text{A.91})$$

Thus the cantilever behaves as though it has an effective mass of

$$m_{\text{eff}} = 0.242672m \quad (\text{A.92})$$

In the case of an AFM cantilever, with a tip, the effective mass would be

$$m_{\text{eff}} = 0.242672m_{\text{cant}} + m_{\text{tip}} \quad (\text{A.93})$$

under the assumption the tip is a point mass at the far end of the cantilever.

## A.5 Driven Cantilever

Taking the equation of motion derived for a free cantilever (equation (A.10)) and including a sinusoidal force  $F \sin(\omega t)$ , we get

$$\frac{F}{m_{\text{eff}}} \sin(\omega t) = \omega_0^2 z + 2\zeta\omega_0\dot{z} + \ddot{z} \quad (\text{A.94})$$

## Derivations of key equations in AFM

we now have a response with both an in phase and out of phase component

$$z = A_1 \sin(\omega t) + A_2 \cos(\omega t) \quad (\text{A.95})$$

$$\dot{z} = A_1 \omega \cos(\omega t) - A_2 \omega \sin(\omega t) \quad (\text{A.96})$$

$$\ddot{z} = -A_1 \omega^2 \sin(\omega t) - A_2 \omega^2 \cos(\omega t) \quad (\text{A.97})$$

Taking the  $\sin(\omega t)$  coefficients of equation (A.94)

$$\frac{F}{m_{\text{eff}}} = \omega_0^2 A_1 - 2\zeta \omega_0 \omega A_2 - \omega^2 A_1 \quad (\text{A.98})$$

and then from the  $\cos(\omega t)$  coefficients of equation (A.94)

$$0 = \omega_0^2 A_2 + 2\zeta \omega_0 \omega A_1 - \omega^2 A_2 \quad (\text{A.99})$$

$$\therefore A_1 = -\frac{(\omega_0^2 - \omega^2)}{2\zeta \omega_0 \omega} A_2 \quad (\text{A.100})$$

By combining equations (A.98) and (A.100) to eliminate  $A_1$

$$\frac{F}{m_{\text{eff}}} = -\frac{(\omega_0^2 - \omega^2)^2}{2\zeta \omega_0 \omega} A_2 - 2\zeta \omega_0 \omega A_2 \quad (\text{A.101})$$

$$= -\frac{(\omega_0^2 - \omega^2)^2 + (2\zeta \omega_0 \omega)^2}{2\zeta \omega_0 \omega} A_2 \quad (\text{A.102})$$

$$A_2 = -\frac{2\zeta \omega_0 \omega (F/m_{\text{eff}})}{(\omega_0^2 - \omega^2)^2 + (2\zeta \omega_0 \omega)^2} \quad (\text{A.103})$$

Also combining equations (A.98) and (A.100) to eliminate  $A_2$

$$\frac{F}{m_{\text{eff}}} = (\omega_0^2 - \omega^2) A_1 - \frac{(2\zeta \omega_0 \omega)^2}{\omega_0^2 - \omega^2} A_1 \quad (\text{A.104})$$

$$A_1 = -\frac{(\omega_0^2 - \omega^2) (F/m_{\text{eff}})}{(\omega_0^2 - \omega^2)^2 + (2\zeta \omega_0 \omega)^2} \quad (\text{A.105})$$

Now from elementary trigonometry

$$A \sin(\omega t + \phi) = A \sin(\omega t) \cos \phi + A \cos(\omega t) \sin \phi \quad (\text{A.106})$$

Therefore

$$A_1 = \cos \phi \quad \text{and} \quad A_2 = \sin \phi, \quad (\text{A.107})$$

and thus

$$A_1^2 + A_2^2 = A^2(\cos^2 \phi + \sin^2 \phi) = A^2. \quad (\text{A.108})$$

## Derivations of key equations in AFM

Using this and the equations for  $A_1$  and  $A_2$  ((A.105) and (A.103)) we can say

$$A^2 = \left( \frac{F}{m_{\text{eff}}} \right)^2 \frac{(\omega_0^2 - \omega^2)^2 + (2\zeta\omega_0\omega)^2}{((\omega_0^2 - \omega^2)^2 + (2\zeta\omega_0\omega)^2)^2} \quad (\text{A.109})$$

$$\boxed{|A| = \frac{|F/m_{\text{eff}}|}{(\sqrt{\omega_0^2 - \omega^2})^2 + (2\zeta\omega_0\omega)^2}} \quad (\text{A.110})$$

Using  $Q = \frac{1}{2\zeta}$  from equation (A.25) and  $\left| \frac{F}{m_{\text{eff}}} \right| = |A_{\text{drive}}| \omega_0^2$  from equation (A.28) we can rewrite this as

$$|A| = \frac{|A_{\text{drive}}| \omega_0^2}{(\sqrt{\omega_0^2 - \omega^2})^2 + \frac{1}{Q^2} \omega_0^2 \omega^2} \quad (\text{A.111})$$

and this rearranges to

$$\boxed{|A| = \frac{|A_{\text{drive}}|}{\sqrt{\left(1 - \frac{\omega^2}{\omega_0^2}\right)^2 + \frac{1}{Q^2} \frac{\omega^2}{\omega_0^2}}}}, \quad (\text{A.112})$$

as it is commonly expressed [2].

From from the equations in (A.107) and from the equations ((A.105) and (A.103)) for  $A_1$  and  $A_2$  we can say

$$\frac{A_2}{A_1} = \frac{\sin \phi}{\cos \phi} = \tan \phi = \frac{-2\zeta\omega_0\omega}{\omega_0^2 - \omega^2} \quad (\text{A.113})$$

hence

$$\boxed{\phi = \arctan\left(\frac{2\zeta\omega_0\omega}{\omega^2 - \omega_0^2}\right)} \quad (\text{A.114})$$

and again using  $Q = \frac{1}{2\zeta}$  from equation (A.25)

$$\boxed{\phi = \arctan\left(-\frac{\omega}{Q\omega_0\left(1 - \frac{\omega^2}{\omega_0^2}\right)}\right)}. \quad (\text{A.115})$$

This means that when the drive frequency  $\omega$  is equal to  $\omega_0$  the phase shift is  $-90^\circ$ , such that the AFM tip is lagging quarter of a cycle behind the driving force.

## A.6 Full equations of motion for the cantilever.

Using the differential equation in equation (A.63), the solution for the time dependent part is simply,

$$T(t) = \sin(\omega_0 t + \phi). \quad (\text{A.116})$$

Then for position dependent part, the simultaneous equations (A.74–A.77) can be solved for each eigenfrequency, using the values for  $\beta L$  given in equation (A.85) and the corresponding resonant frequencies can be found on page 182. From (A.74) and (A.75) we get

$$b_1 = -b_3 \qquad b_2 = -b_4 \quad (\text{A.117})$$

putting these into (A.76) gives

$$b_1 = -\frac{\sin(\beta L) + \sinh(\beta L)}{\cos(\beta L) + \cosh(\beta L)} \quad (\text{A.118})$$

from this we can calculate the ratio between  $b_1, b_2, b_3$ , and  $b_4$  for equation (A.69) for each  $\beta L$ . The fourth simultaneous equation is not needed as for our  $\beta L$  values the determinant of the equations in matrix form is zero, leading to infinitely many solutions with three solutions for the relative sizes of the terms<sup>2</sup>.

Thus, by solving (A.118) for each eigenfrequency, we can write the full time

---

<sup>2</sup> The fourth equation (eq (A.76)), combined with equation (A.117), can be used to verify the result in equation (A.118), for each value of  $\beta L$ .

Derivations of key equations in AFM

dependent solution for our cantilever deflection as

$$\begin{aligned}
z(x, t) = & A_1 \sin \left( 3.516015 \sqrt{\frac{EI}{mL^3}} t \right) \\
& [1.362221(\cos(\beta_1 x) - \cosh(\beta_1 x)) - \sin(\beta_1 x) + \sinh(\beta_1 x)] + \\
& A_2 \sin \left( 22.034490 \sqrt{\frac{EI}{mL^3}} t \right) \\
& [0.981868(\cos(\beta_2 x) - \cosh(\beta_2 x)) - \sin(\beta_2 x) + \sinh(\beta_2 x)] + \\
& A_3 \sin \left( 61.697208 \sqrt{\frac{EI}{mL^3}} t \right) \\
& [1.000776(\cos(\beta_3 x) - \cosh(\beta_3 x)) - \sin(\beta_3 x) + \sinh(\beta_3 x)] + \\
& A_4 \sin \left( 120.901922 \sqrt{\frac{EI}{mL^3}} t \right) \\
& [0.999966(\cos(\beta_4 x) - \cosh(\beta_4 x)) - \sin(\beta_4 x) + \sinh(\beta_4 x)] + \\
& A_5 \sin \left( 199.859519 \sqrt{\frac{EI}{mL^3}} t \right) \\
& [1.000001(\cos(\beta_5 x) - \cosh(\beta_5 x)) - \sin(\beta_5 x) + \sinh(\beta_5 x)] + \\
& \dots
\end{aligned} \tag{A.119}$$

Noticeably for higher eigenfrequencies  $b_1 \rightarrow -b_2$ , as  $\cosh(x) \rightarrow \sinh(x)$  for large  $x$ , and  $\cosh(x), \sinh(x) \gg \cos(x), \sin(x)$  for large<sup>3</sup>  $x$ . The first 5 eigenfrequencies have been plotted out in figure A.3

## A.7 Frequency shift in AFM

This section covers a simple first order approximation for the for the frequency shift resulting from a force felt by the end of a cantilever for low amplitudes where the force gradient is considered constant. Following this a formula for arbitrary amplitudes is derived, an equation which is used extensively in this thesis. Another approximation which is not covered here is an equation which is true in the limit of large amplitudes which assumes only the force at the closest point of approach dominates the frequency shift. This method is not covered in detail as the derivation in Reference [151] covers the topic very clearly.

---

<sup>3</sup>Large in this case is  $\gtrsim 10$ .

## Derivations of key equations in AFM

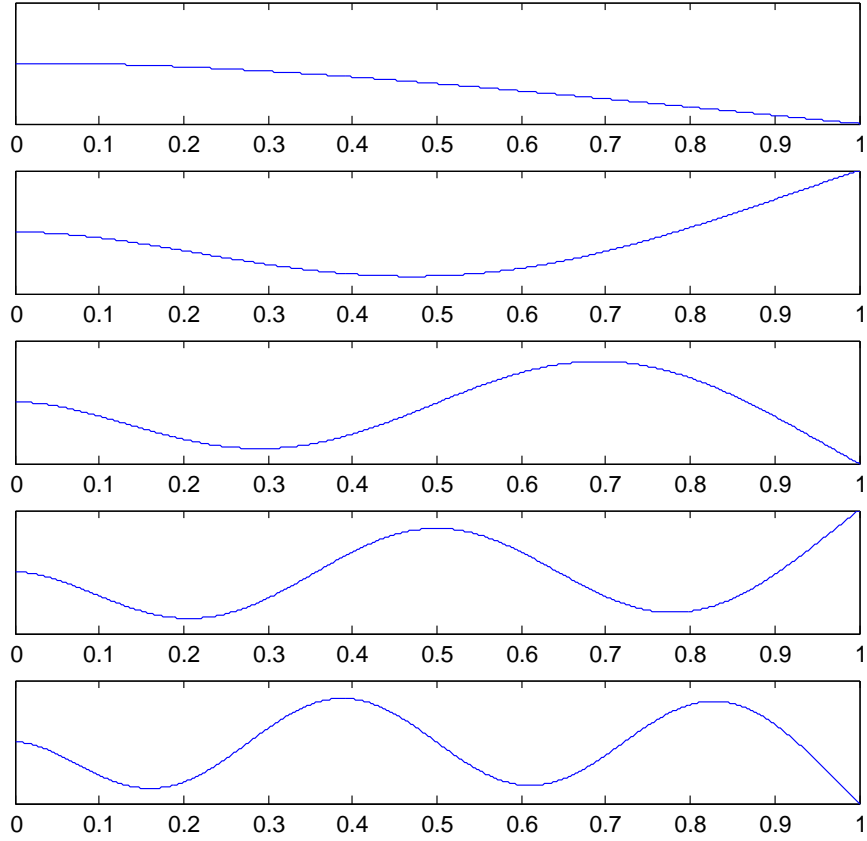


Figure A.3: *From top to bottom, the first 5 eigenfrequencies of a freely oscillating cantilever.*

### A.7.1 First order frequency shift (Low amplitude)

When an AFM approaches a surface it experiences a force from the surface related to the tip-sample potential,  $V_{ts}$ , by

$$F_{ts} = -\frac{\partial V_{ts}}{\partial z}. \quad (\text{A.120})$$

Hence by Hooke's law

$$F + F_{ts} = -k_{\text{eff}}z = -(k + k_{ts})z \quad (\text{A.121})$$

$$\therefore F_{ts} = -k_{ts}z \quad (\text{A.122})$$

$$k_{ts} = -\frac{\partial F_{ts}}{\partial z}. \quad (\text{A.123})$$

Derivations of key equations in AFM

Therefore if we assume a constant force gradient then the natural frequency of the cantilever becomes

$$\omega_0 + \Delta\omega = \sqrt{\frac{k_{\text{eff}}}{m_{\text{eff}}}} \quad (\text{A.124})$$

as  $m_{\text{eff}}$  is unchanged

$$= \sqrt{\frac{k + k_{\text{ts}}}{m_{\text{eff}}}} \quad (\text{A.125})$$

$$\sqrt{m_{\text{eff}}}(\omega_0 + \Delta\omega) = \sqrt{k + k_{\text{ts}}} \quad (\text{A.126})$$

by Taylor expansion taking just the first two terms (assuming  $k \gg k_{\text{ts}}$ )

$$= \sqrt{k} + \frac{1}{2\sqrt{k}}k_{\text{ts}} \quad (\text{A.127})$$

$$\omega_0 + \Delta\omega = \underbrace{\sqrt{\frac{k}{m_{\text{eff}}}}}_{\omega_0} + \frac{1}{2} \underbrace{\sqrt{\frac{k}{m_{\text{eff}}}}}_{\omega_0} \frac{k_{\text{ts}}}{k} \quad (\text{A.128})$$

$$\Delta\omega = \frac{k_{\text{ts}}}{2k}\omega_0 \quad (\text{A.129})$$

As derived by Giessibl in Ref [28]. However, as previously mentioned this is only valid for a constant force gradient which is not a good approximation for large amplitude AFM.

## A.7.2 Frequency shift for arbitrary amplitudes

Starting with Newton's second law

$$-kz + F_{\text{ts}}(z) = m_{\text{eff}} \frac{\partial^2 z}{\partial t^2} \quad (\text{A.130})$$

and considering the cantilever's motion as periodic we can describe its deflection as a Fourier series [2]

$$z(t) = \sum_{n=0}^{\infty} a_n \cos(n\omega t) \quad (\text{A.131})$$

inserting this into equation (A.130)

$$\sum_{n=0}^{\infty} a_n [k - (n\omega)^2 m_{\text{eff}}] \cos(n\omega t) = F_{\text{ts}}(z) \quad (\text{A.132})$$

Derivations of key equations in AFM

Multiplying by  $\cos(l\omega t)$  and integrating from over one oscillation gives

$$\int_0^{2\pi/\omega} \sum_{n=0}^{\infty} a_n [k - (n\omega)^2 m_{\text{eff}}] \cos(n\omega t) \cos(l\omega t) dt = \int_0^{2\pi/\omega} F_{\text{ts}}(z) \cos(l\omega t) dt \quad (\text{A.133})$$

but

$$\int_0^{2\pi/\omega} \cos(n\omega t) \cos(l\omega t) dt = \frac{\pi}{\omega} \delta_{nl} (1 + \delta_{n0}) \quad (\text{A.134})$$

which reduces equation (A.133) to

$$a_n [k - (n\omega)^2 m_{\text{eff}}] \pi (1 + \delta_{n0}) = \omega \int_0^{2\pi/\omega} F_{\text{ts}}(z) \cos(n\omega t) dt. \quad (\text{A.135})$$

Considering a weak perturbation where  $\Delta\omega \ll \omega_0$ , and  $z \approx A \cos(\omega t)$  then we can just consider the case were  $n = 1$  and  $a_n = A$ , hence

$$\omega \int_0^{2\pi/\omega} F_{\text{ts}}(z) \cos(\omega t) dt = A (k - \omega^2 m_{\text{eff}}) \pi \quad (\text{A.136})$$

$$= A \left( k - \omega^2 k \underbrace{\frac{m_{\text{eff}}}{k}}_{\frac{1}{\omega_0^2}} \right) \pi = Ak \left( 1 - \frac{\omega^2}{\omega_0^2} \right) \pi \quad (\text{A.137})$$

$$= Ak\pi \left( 1 - \frac{\omega_0^2 + 2\omega_0\Delta\omega + \Delta\omega^2}{\omega_0^2} \right) \quad (\text{A.138})$$

$$\approx -2Ak\pi \frac{\Delta\omega}{\omega_0} \quad (\text{A.139})$$

as  $\frac{\Delta\omega^2}{\omega_0^2} \approx 0$  when  $\Delta\omega \ll \omega_0$ . So to a good approximation

$$\Delta\omega(z) = -\frac{\omega\omega_0}{2\pi Ak} \int_0^{2\pi/\omega} F_{\text{ts}}(z) \cos(\omega t) dt \quad (\text{A.140})$$

if we substitute in  $q' = A \cos(\omega t)$

$$\Delta\omega(z_0) = -\frac{\omega\omega_0}{2\pi A^2 k} \int_0^{2\pi/\omega} F_{\text{ts}}(z_0 - q') q' dt, \quad (\text{A.141})$$

where  $z_0$  is the average tip position. Finally considering

$$\langle f(x) \rangle = 1/X \int_0^X f(x) dx \quad (\text{A.142})$$

Derivations of key equations in AFM

we can say

$$\Delta\omega(z_0) = -\frac{\omega\omega_0}{2\pi A^2 k} \frac{2\pi}{\omega} \langle F_{\text{ts}}(z_0 - q')q' \rangle \quad (\text{A.143})$$

hence

$$\boxed{\Delta\omega = -\frac{\omega_0}{A^2 k} \langle F_{\text{ts}}(z_0 - q')q' \rangle} \quad (\text{A.144})$$

As derived by Giessibl in Ref [151].

# Appendix B

## Derivations from Calculation of Effects of Tip Geometry

*“I rarely end up where I was intending to go, but often I end up somewhere I needed to be.”*

Douglas Adams

### Appendix Overview

Some derivation of results in Chapter 4 were too long too detailed to included in the main text. They are presented here for completeness.

## B.1 Boundary Conditions of a Loaded Cantilever

The boundary conditions in Equations 4.6–4.9 allow us to form four simultaneous equations for the factors  $b_{1..4}$  of  $\Phi_i(x)$  from Equation 4.4.

$$b_1 + b_3 = 0 \quad (\text{B.1})$$

$$b_2 + b_4 = 0 \quad (\text{B.2})$$

$$b_1 \left( -\cos(\beta_i L) + \frac{J\beta_i^2}{\gamma_i} \sin(\beta_i L) \right) + b_2 \left( -\sin(\beta_i L) - \frac{J\beta_i^2}{\gamma_i} \cos(\beta_i L) \right) \\ + b_3 \left( \cosh(\beta_i L) - \frac{J\beta_i^2}{\gamma_i} \sinh(\beta_i L) \right) + b_4 \left( \sinh(\beta_i L) - \frac{J\beta_i^2}{\gamma_i} \cosh(\beta_i L) \right) = 0 \quad (\text{B.3})$$

$$b_1 (\gamma_i \sin(\beta_i L) + \cos(\beta_i L)) + b_2 (-\gamma_i \cos(\beta_i L) + \sin(\beta_i L)) \\ + b_3 (\gamma_i \sinh(\beta_i L) + \cosh(\beta_i L)) + b_4 (\gamma_i \cosh(\beta_i L) + \sinh(\beta_i L)) = 0 \quad (\text{B.4})$$

where  $\gamma_i$  is a dimensionless parameter defined as

$$\gamma_i = \frac{EI\beta^3}{m_{\text{tip}}\omega_i^2}. \quad (\text{B.5})$$

Writing Equations B.1, B.2, B.3, and B.4 as a matrix equation in the form

$$\underline{\underline{D}} \begin{pmatrix} b_1 \\ b_2 \\ b_3 \\ b_4 \end{pmatrix} = \begin{pmatrix} 0 \\ 0 \\ 0 \\ 0 \end{pmatrix} \quad (\text{B.6})$$

it becomes clear that if  $\det(\underline{\underline{D}}) \neq 0$ , then the solution would trivially be  $b_{1..4} = 0$ , a stationary beam. Hence,  $\det(\underline{\underline{D}}) = 0$ , giving the following condition for  $\beta_i$ :

$$\begin{aligned} & 1 + m^{*2}\beta_i^4 JL^2 - (1 + m^{*2}\beta_i^4 JL^2) \cos(\beta L) \cosh(\beta_i L) \\ & + m^* \beta_i L [(1 - J\beta_i^2) \cos(\beta_i L) \sinh(\beta_i L) - (1 + J\beta_i) \cosh(\beta_i L) \sin(\beta_i L)] = 0 \end{aligned} \quad (\text{B.7})$$

using

$$\gamma_i = \frac{\rho A}{\beta_i m_{\text{tip}}} = \frac{1}{\beta_i L m^*}, \quad (\text{B.8})$$

from Equations 4.5 and B.5, where  $m^*$  is the ratio of the tip mass to the mass of the tine. Equation B.7 can be numerically solved simply and quickly using the Newton-Raphson method.

## B.2 Elastic Potential Energy of a Loaded Cantilever

Equation 4.12 can be expanded to give

$$\begin{aligned} W = \frac{EI}{2} & \left[ \sum_{i=1}^{\infty} \mathcal{T}_i^2(t) \int_0^L \left( \frac{d^2\Phi_i(x)}{dx^2} \right)^2 dx \right. \\ & \left. + \sum_{i=1}^{\infty} \sum_{k=1, k \neq i}^{\infty} \mathcal{T}_i(t) \mathcal{T}_k(t) \int_0^L \frac{d^2\Phi_i(x)}{dx^2} \frac{d^2\Phi_k(x)}{dx^2} dx \right] \end{aligned} \quad (\text{B.9})$$

Butt and Jaschke [96] use

$$\frac{d^4\Phi_i(x)}{dx^4} = \beta_i^4 \Phi_i(x) \quad (\text{B.10})$$

(which is clearly still true for our boundary conditions from the general form of  $\Phi$  given in equation 4.4) to show that the integral with mixed ( $\Phi_i(x)$  and  $\Phi_k(x)$ )

second derivatives can be written as

$$\int_0^L \frac{d^2\Phi_i(x)}{dx^2} \frac{d^2\Phi_k(x)}{dx^2} dx = \frac{1}{\beta_i^4 - \beta_k^4} \left[ \beta_i^4 \frac{d^2\Phi_k(x)}{dx^2} \frac{d\Phi_i(x)}{dx} - \beta_i^4 \frac{d^3\Phi_k(x)}{dx^3} \Phi_i(x) - \beta_k^4 \frac{d^2\Phi_i(x)}{dx^2} \frac{d\Phi_k(x)}{dx} + \beta_k^4 \frac{d^3\Phi_i(x)}{dx^3} \Phi_k(x) \right]_0^L. \quad (\text{B.11})$$

If we combine equations B.5 and B.8 to give

$$\beta_i^4 L m^* = \frac{m_{\text{tip}} \omega_i^2}{EI} \quad (\text{B.12})$$

then we can rewrite boundary conditions 4.8 and 4.9 as

$$\frac{\partial^2 \Phi_i(L)}{\partial x^2} = \beta_i^4 J L m^* \frac{\partial \Phi_i(L)}{\partial x} \quad (\text{B.13})$$

$$\frac{\partial^3 \Phi_i(L)}{\partial x^3} = -\beta_i^4 L m^* \Phi_i(L). \quad (\text{B.14})$$

From these conditions it becomes clear that the first and third terms in the square brackets of equation B.11 cancel, as do the the second and fourth. Thus,

$$\int_0^L \frac{d^2\Phi_i(x)}{dx^2} \frac{d^2\Phi_k(x)}{dx^2} dx = 0, \quad (\text{B.15})$$

and

$$W = \frac{EI}{2} \sum_{i=1}^{\infty} \mathcal{T}_i^2(t) \int_0^L \left( \frac{\partial^2 \Phi_i(x)}{\partial x^2} \right)^2 dx. \quad (\text{B.16})$$

### B.3 Analytical Solution for $\Lambda_i$

To solve  $\Lambda_i$  we first integrate by parts twice to give

$$\Lambda_i = \left[ \frac{d\Phi_i(x)}{dx} \frac{d^2\Phi_i}{dx^2} - \Phi_i(x) \frac{d^3\Phi_i(x)}{dx^3} \right]_0^L + \int_0^L \Phi_i(x) \frac{d^4\Phi_i(x)}{dx^4} dx. \quad (\text{B.17})$$

The square brackets can be evaluated using boundary conditions 4.6, 4.7, B.13, and B.14. Furthermore, with equation B.10 the integral can be written in terms of  $\Phi_i(x)$  only:

$$\Lambda_i = \beta_i^4 L J m^* \left( \frac{d\Phi_i(L)}{dx} \right)^2 + \beta_i^4 L m^* \Phi_i^2(L) + \beta_i^4 \int_0^L \Phi_i(x)^2 dx. \quad (\text{B.18})$$

Derivations from Calculation of Effects of Tip Geometry

The integral can be solved by substituting in  $\zeta = x/L$ , and writing  $\beta_i L$  as  $\alpha_i$ ,

$$\int_0^L \Phi_i^2 dx = L \int_0^1 \left\{ \left[ \sin(\alpha_i) + \sinh(\alpha_i) - \frac{J\beta_i^2}{\gamma_i} \left( -\cos(\alpha_i) + \cosh(\alpha_i) \right) \right] \right. \\ \times \left( \cos(\alpha_i \zeta) - \cosh(\alpha_i \zeta) \right) \\ \left. - \left[ \cos(\alpha_i) + \cosh(\alpha_i) - \frac{J\beta_i^2}{\gamma_i} \left( \sin(\alpha_i) + \sinh(\alpha_i) \right) \right] \right. \\ \left. \times \left( \sin(\alpha_i \zeta) - \sinh(\alpha_i \zeta) \right) \right\}^2 d\zeta \quad (\text{B.19})$$

$$= L \left( \sin(\alpha_i) + \sinh(\alpha_i) \right)^2 \\ + \frac{3L}{\alpha_i} \left( 1 + \cos(\alpha_i) \cosh(\alpha_i) \right) \\ \times \left( -\cosh(\alpha_i) \sin(\alpha_i) + \cos(\alpha_i) \sinh(\alpha_i) \right) \\ - \frac{J\beta_i^2}{\gamma_i} L \left\{ \frac{1}{\alpha_i} \left[ -4 + \cos(2\alpha_i) + \left( 1 + 2\cos(2\alpha_i) \right) \cosh(2\alpha_i) \right] \right. \\ \left. - 2(\cos(\alpha_i) - \cosh(\alpha_i))(\sin(\alpha_i) + \sinh(\alpha_i)) \right\} \\ + \frac{J^2\beta_i^4}{\gamma_i^2} L \left[ \left( \cos(\alpha_i) - \cosh(\alpha_i) \right)^2 \right. \\ + \frac{3}{\alpha_i} \left( -1 + \cos(\alpha_i) \cosh(\alpha_i) \right) \\ \left. \times \left( \cosh(\alpha_i) \sin(\alpha_i) + \cos(\alpha_i) \sinh(\alpha_i) \right) \right]. \quad (\text{B.20})$$

## Derivations from Calculation of Effects of Tip Geometry

Returning back to notation without  $\alpha_i$  or  $\gamma_i$  and using equation B.7 to replace  $(1 + \cos(\beta_i L) \cosh(\beta_i L))$  in the second term, after some manipulation gives

$$\begin{aligned}
&= L \left( \sin(\beta_i L) + \sinh(\beta_i L) \right)^2 \\
&\quad - 3Lm^* \left( \cosh(\beta_i L) \sin(\beta_i L) - \cos(\beta_i L) \sinh(\beta_i L) \right)^2 \\
&\quad - \beta_i^2 Jm^* L \left[ -\frac{5}{2} + \cos(2\beta_i L) + \cosh(2\beta_i L) \right. \\
&\quad \left. + \frac{1}{2} \cos(2\beta_i L) \cosh(2\beta_i L) \right. \\
&\quad \left. - 2\beta_i L \left( \cos(\beta_i L) - \cosh(\beta_i L) \right) \left( \sin(\beta_i L) + \sinh(\beta_i L) \right) \right. \\
&\quad \left. - 3m^* \beta_i L \left( 1 - \cos(\beta_i L) \cosh(\beta_i L) \right) \right. \\
&\quad \left. \times \left( \cosh(\beta_i L) \sin(\beta_i L) - \cos(\beta_i L) \sinh(\beta_i L) \right) \right] \\
&\quad + \beta_i^6 J^2 m^{*2} L^3 \left[ \left( \cos(\beta_i L) - \cosh(\beta_i L) \right)^2 \right] \\
&\quad + 3\beta_i^5 J^2 m^{*2} L^2 \left[ \left( -1 + \cos(\beta_i L) \cosh(\beta_i L) \right) \right. \\
&\quad \left. \times \left( \cosh(\beta_i L) \sin(\beta_i L) + \cos(\beta_i L) \sinh(\beta_i L) \right) \right]. \tag{B.21}
\end{aligned}$$

Using equation B.7 again, this time to replace  $\beta_i^3 Jm^* L(\cosh(\beta_i L) \sin(\beta_i L) + \cos(\beta_i L) \sinh(\beta_i L))$  in the final term, rearranging will give

$$\begin{aligned}
\int_0^L \Phi_i^2 dx &= L \left( \sin(\beta_i L) + \sinh(\beta_i L) \right)^2 \\
&\quad - 3Lm^* \left( \cosh(\beta_i L) \sin(\beta_i L) - \cos(\beta_i L) \sinh(\beta_i L) \right)^2 \\
&\quad - \beta_i^2 Jm^* L \left[ \sin^2(\beta_i L) \sinh^2(\beta_i L) \right. \\
&\quad \left. - 2\beta_i L \left( \cos(\beta_i L) - \cosh(\beta_i L) \right) \times \left( \sin(\beta_i L) + \sinh(\beta_i L) \right) \right. \\
&\quad \left. - 6m^* \beta_i L \left( 1 - \cos(\beta_i L) \cosh(\beta_i L) \right) \right. \\
&\quad \left. \times \left( \cosh(\beta_i L) \sin(\beta_i L) - \cos(\beta_i L) \sinh(\beta_i L) \right) \right] \\
&\quad + \beta_i^6 J^2 m^{*2} L^3 \left[ \left( \cos(\beta_i L) - \cosh(\beta_i L) \right)^2 \right. \\
&\quad \left. - 3m^* \left( 1 - \cos(\beta_i L) \cosh(\beta_i L) \right)^2 \right]. \tag{B.22}
\end{aligned}$$

## Derivations from Calculation of Effects of Tip Geometry

It can be shown simply that

$$\left(\frac{d\Phi_i(L)}{dx}\right)^2 = 4\beta_i^2 \sin^2(\beta_i L) \sinh^2(\beta_i L), \quad (\text{B.23})$$

and that

$$\begin{aligned} \Phi_i^2(L) = 4 & \left[ \left( \cosh(\beta_i L) \sin(\beta_i L) - \cos(\beta_i L) \sinh(\beta_i L) \right)^2 \right. \\ & - 2\beta_i^3 J m^* L \left( 1 - \cos(\beta_i L) \cosh(\beta_i L) \right) \\ & \times \left( \cosh(\beta_i L) \sin(\beta_i L) - \cos(\beta_i L) \sinh(\beta_i L) \right) \\ & \left. + \beta_i^6 J^2 m^{*2} L^2 \left( 1 - \cos(\beta_i L) \cosh(\beta_i L) \right)^2 \right]. \quad (\text{B.24}) \end{aligned}$$

Note that this form of  $\Phi_i^2(L)$  appears in equation B.22, allowing us to reduce it to

$$\begin{aligned} \int_0^L \Phi_i^2 dx = L & \left( \sin(\beta_i L) + \sinh(\beta_i L) \right)^2 - \frac{3Lm^*}{4} \Phi_i^2(L) \\ & - \beta_i^2 J m^* L \left[ \sin^2(\beta_i L) \sinh^2(\beta_i L) \right. \\ & - 2\beta_i L \left( \cos(\beta_i L) - \cosh(\beta_i L) \right) \left( \sin(\beta_i L) + \sinh(\beta_i L) \right) \left. \right] \\ & + \beta_i^6 J^2 m^{*2} L^3 \left( \cos(\beta_i L) - \cosh(\beta_i L) \right)^2. \quad (\text{B.25}) \end{aligned}$$

Combining equations B.23, B.24, and B.25 after some manipulation gives

$$\begin{aligned} \Lambda_i = \frac{\beta_i^4 L m^*}{4} & \Phi_i^2(L) + \beta_i^4 L \left( \sin(\beta_i L) + \sinh(\beta_i L) \right)^2 \\ & - \beta_i^6 J m^* L \left[ -3 \sin^2(\beta_i L) \sinh^2(\beta_i L) \right. \\ & - 2\beta_i L \left( \cos(\beta_i L) - \cosh(\beta_i L) \right) \left( \sin(\beta_i L) + \sinh(\beta_i L) \right) \left. \right] \\ & + \beta_i^{10} J^2 m^{*2} L^3 \left( \cos(\beta_i L) - \cosh(\beta_i L) \right)^2. \quad (\text{B.26}) \end{aligned}$$

Which for simplicity, can be written as

$$\Lambda_i = \frac{\beta_i^4 L m^*}{4} \Phi_i^2(L) + \beta_i^4 L \left( \sin(\beta_i L) + \sinh(\beta_i L) \right)^2 + \beta_i^6 J m^* L f(m^*, J), \quad (\text{B.27})$$

## Derivations from Calculation of Effects of Tip Geometry

where

$$\begin{aligned}
 f(m^*, J) = & 3 \sin^2(\beta_i L) \sinh^2(\beta_i L) \\
 & + 2\beta_i L \left( \cos(\beta_i L) - \cosh(\beta_i L) \right) \left( \sin(\beta_i L) + \sinh(\beta_i L) \right) \\
 & + \beta_i^4 J m^* L^2 \left( (\cos(\beta_i L) - \cosh(\beta_i L)) \right)^2. \quad (\text{B.28})
 \end{aligned}$$

By substituting equation B.7 into B.24 and rearranging we get

$$\begin{aligned}
 \Phi_i^2(L) = & 4 \left( \sin(\beta_i L) + \sinh(\beta_i L) \right)^2 \\
 & - 8\beta_i L m^* \sin(\beta_i L) \sinh(\beta_i L) \\
 & \times \left( \cosh(\beta_i L) \sin(\beta_i L) - \cos(\beta_i L) \sinh(\beta_i L) \right) \\
 & + 8\beta_i^3 L J m^* \left[ - \left( 1 - \cos(\beta_i L) \cosh(\beta_i L) \right) \right. \\
 & \times \left( \cosh(\beta_i L) \sin(\beta_i L) - \cos(\beta_i L) \sinh(\beta_i L) \right) \\
 & - \sin(\beta_i L) \sinh(\beta_i L) \left( \cosh(\beta_i L) \sin(\beta_i L) + \cos(\beta_i L) \sinh(\beta_i L) \right) \\
 & \left. + \beta_i L m^* \left( 1 - \cos(\beta_i L) \cosh(\beta_i L) \right) \sin(\beta_i L) \sinh(\beta_i L) \right] \\
 & + 4\beta_i^6 L^2 J^2 m^{*2} \left( 1 - \cos(\beta_i L) \cosh(\beta_i L) \right)^2. \quad (\text{B.29})
 \end{aligned}$$

Initially this form appears to be more complicated. However, as will be demonstrated, because it contains the boundary conditions it produces a final result which is more physically understandable. For simplicity it can be written as

$$= 4 \left[ \left( \sin(\beta_i L) + \sinh(\beta_i L) \right)^2 - \beta_i L m^* \left( 2g + \beta_i^2 J h(m^*, J) \right) \right], \quad (\text{B.30})$$

where

$$g = \sin(\beta_i L) \sinh(\beta_i L) \left( \cosh(\beta_i L) \sin(\beta_i L) - \cos(\beta_i L) \sinh(\beta_i L) \right) \quad (\text{B.31})$$

## Derivations from Calculation of Effects of Tip Geometry

and

$$\begin{aligned}
h(m^*, J) = & 2 \left[ - \left( 1 - \cos(\beta_i L) \cosh(\beta_i L) \right) \right. \\
& \times \left( \cosh(\beta_i L) \sin(\beta_i L) - \cos(\beta_i L) \sinh(\beta_i L) \right) \\
& - \sin(\beta_i L) \sinh(\beta_i L) \left( \cosh(\beta_i L) \sin(\beta_i L) + \cos(\beta_i L) \sinh(\beta_i L) \right) \\
& + \beta_i L m^* \left( 1 - \cos(\beta_i L) \cosh(\beta_i L) \right) \sin(\beta_i L) \sinh(\beta_i L) \left. \right] \\
& + \beta_i^3 L J m^* \left( 1 - \cos(\beta_i L) \cosh(\beta_i L) \right)^2
\end{aligned} \tag{B.32}$$

Thus finally we can write

$$\begin{aligned}
\frac{\Lambda_i L^3}{\Phi_i^2(L)} = & \frac{\beta_i^4 L^4}{4} \left( m^* \right. \\
& \left. + \frac{\left( \sin(\beta_i L) + \sinh(\beta_i L) \right)^2 + \beta_i^2 J m^* f(m^*, J)}{\left( \sin(\beta_i L) + \sinh(\beta_i L) \right)^2 - \beta_i L m^* \left( 2g + \beta_i^2 J h(m^*, J) \right)} \right).
\end{aligned} \tag{B.33}$$

It is clear that in the case of no tip,  $m^* = 0$ , this reduces to just  $\frac{\beta_i^4 L^4}{4}$ . Inserting this into equation 4.16 is consistent with Melcher *et al.* [134]. Further consistency with the literature can be shown in the case of the point mass, where  $J = 0$  but  $m^* \neq 0$ . Inserting Equation B.33 into Equation 4.16 with these conditions, agrees with the results of Lozano *et al.* [138].

A final test of the accuracy of this equation can be done by considering equipartition theorem with Hooke's law in terms of the static spring constant:

$$\frac{1}{2} k_B T = \frac{1}{2} k_{\text{stat}} \sum_{i=1}^{\infty} \langle Z_i^2(L) \rangle \tag{B.34}$$

and inserting equation 4.15 we get

$$\sum_{i=1}^{\infty} \frac{L^3 \Lambda_i}{\Phi_i^2(L)} = 3. \tag{B.35}$$

Using the same model qPlus sensor as described in section 4.2, this has been plotted in figure B.1, for  $i = 1..8$  showing excellent agreement with theory, and faster convergence for larger tips.

## Derivations from Calculation of Effects of Tip Geometry

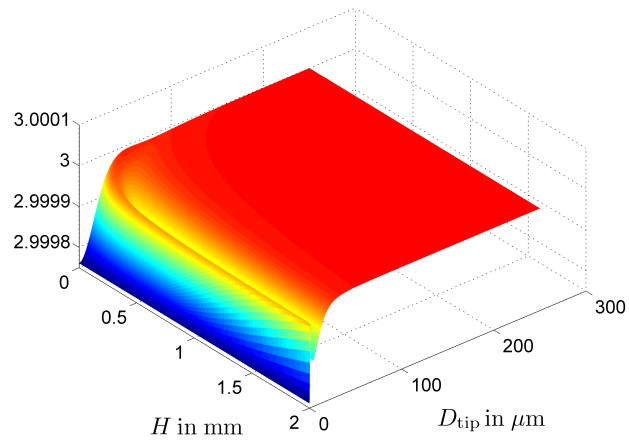


Figure B.1: Agreement with  $\lim_{N \rightarrow \infty} \sum_{i=1}^N \frac{L^3 \Lambda_i}{\Phi_i^2(L)} = 3$ , plotted for  $N = 8$  roots to show that the equation is consistent with equipartition theorem. Where  $H$  is the length and  $D_{\text{tip}}$  is the diameter of a cylindrical tip.

# Appendix C

## Full derivations of dynamic properties for a symmetrical sensor

*“Math is the language of the universe. So the more equations you know, the more you can converse with the cosmos.”*

Neil de Grasse Tyson

### Appendix Overview

Here is presented method used to derive the results in Chapter 6. This was not included in the main text to improve readability of the chapter.

### C.1 Harmonics of the symmetrical sensor

Considering the boundary conditions for a symmetrical sensor is a little more difficult than for a cantilever, as once the effects of the tip or interactions are included they will occur at the centre of the beam. The best method to account for this is to consider that for odd modes the cantilever will be symmetrical and for even modes anti-symmetrical. Now we can consider the boundary conditions at one of the clamped ends and at the centre of the beam.

Full derivations of dynamic properties for a symmetrical sensor

### C.1.1 Odd modes

Not including tip mass for simplicity the boundary conditions for the odd modes are

$$\Phi_i(0) = 0 \quad (\text{C.1})$$

$$\frac{d\Phi_i(0)}{dx} = 0 \quad (\text{C.2})$$

$$\frac{d\Phi_i(L/2)}{dx} = 0 \quad (\text{C.3})$$

$$\frac{d^3\Phi_i(L/2)}{dx^3} = 0 \quad (\text{C.4})$$

Thus, considering the normalised spatial solution as

$$\Phi_i(x) = b_1 \cos(\beta_i x) + b_2 \sin(\beta_i x) + b_3 \cosh(\beta_i x) + b_4 \sinh(\beta_i x), \quad (\text{C.5})$$

where

$$\beta_i^4 = \frac{\rho A \omega_i^2}{EI}. \quad (\text{C.6})$$

This can be written as the following matrix equation

$$\underline{\underline{D}} \begin{pmatrix} b_1 \\ b_2 \\ b_3 \\ b_4 \end{pmatrix} = \begin{pmatrix} 0 \\ 0 \\ 0 \\ 0 \end{pmatrix}, \quad (\text{C.7})$$

where

$$\underline{\underline{D}} = \begin{pmatrix} 1 & 0 & 1 & 0 \\ 0 & 1 & 0 & 1 \\ -\sin(\beta_i L/2) & \cos(\beta_i L/2) & \sinh(\beta_i L/2) & \cosh(\beta_i L/2) \\ \sin(\beta_i L/2) & -\cos(\beta_i L/2) & \sinh(\beta_i L/2) & \cosh(\beta_i L/2) \end{pmatrix}. \quad (\text{C.8})$$

Now for a non-trivial solution  $\det \underline{\underline{D}} = 0$ . This gives the resonance conditions

$$\cosh(\beta_i L/2) \sin(\beta_i L/2) + \cos(\beta_i L/2) \sinh(\beta_i L/2) = 0 \quad (\text{C.9})$$

From equations (C.1) and (C.2) we can see that

$$b_1 = -b_3 \quad b_2 = -b_4 \quad (\text{C.10})$$

and from equation (C.3) we can get the ratio between the constants:

$$\frac{b_1}{b_2} = \frac{\cos(\beta_i L/2) - \cosh(\beta_i L/2)}{\sin(\beta_i L/2) + \sinh(\beta_i L/2)} \quad (\text{C.11})$$

Full derivations of dynamic properties for a symmetrical sensor

### C.1.2 Even modes

For the even modes the boundary conditions are slightly different

$$\Phi_i(0) = 0 \quad (\text{C.12})$$

$$\frac{d\Phi_i(0)}{dx} = 0 \quad (\text{C.13})$$

$$\Phi_i(L/2) = 0 \quad (\text{C.14})$$

$$\frac{d^2\Phi_i(L/2)}{dx^2} = 0 \quad (\text{C.15})$$

thus for these cases

$$\underline{\underline{D}} = \begin{pmatrix} 1 & 0 & 1 & 0 \\ 0 & 1 & 0 & 1 \\ \cos(\beta_i L/2) & \sin(\beta_i L/2) & \cosh(\beta_i L/2) & \sinh(\beta_i L/2) \\ -\cos(\beta_i L/2) & -\sin(\beta_i L/2) & \cosh(\beta_i L/2) & \sinh(\beta_i L/2) \end{pmatrix}. \quad (\text{C.16})$$

giving a condition for resonance of

$$\cosh(\beta_i L/2) \sin(\beta_i L/2) - \cos(\beta_i L/2) \sinh(\beta_i L/2) = 0 \quad (\text{C.17})$$

As before, from equations (C.12) and (C.13) we can see that

$$b_1 = -b_3 \quad b_2 = -b_4 \quad (\text{C.18})$$

but equation (C.14) gives a slightly different ratio between the constants:

$$\frac{b_1}{b_2} = \frac{\sinh(\beta_i L/2) - \sin(\beta_i L/2)}{\cos(\beta_i L/2) - \cosh(\beta_i L/2)} \quad (\text{C.19})$$

### C.1.3 Odd modes - including tip

Including the mass of the tip requires a simple change of the 4th boundary condition to

$$EI \frac{d^3\Phi_i(L/2)}{dx^3} = -\frac{m_{\text{tip}}}{2} \omega_i^2 \Phi_i(L/2) \quad (\text{C.20})$$

Again, writing this as a matrix equation,

$$\underline{\underline{D}} \begin{pmatrix} b_1 \\ b_2 \\ b_3 \\ b_4 \end{pmatrix} = \begin{pmatrix} 0 \\ 0 \\ 0 \\ 0 \end{pmatrix}, \quad (\text{C.21})$$

Full derivations of dynamic properties for a symmetrical sensor

where

$$\underline{\underline{D}} = \begin{pmatrix} 1 & 0 & & \\ 0 & 1 & & \\ -\sin(\beta_i L/2) & \cos(\beta_i L/2) & \dots & \\ \sin(\beta_i L/2) + \frac{1}{2\gamma_i} \cos(\beta_i L/2) & -\cos(\beta_i L/2) + \frac{1}{2\gamma_i} \sin(\beta_i L/2) & & \\ \dots & \dots & \dots & \dots \\ 1 & 0 & & \\ 0 & 1 & & \\ \dots & \dots & \dots & \dots \\ \sinh(\beta_i L/2) & \cosh(\beta_i L/2) & & \\ \sinh(\beta_i L/2) + \frac{1}{2\gamma_i} \cosh(\beta_i L/2) & \cosh(\beta_i L/2) + \frac{1}{2\gamma_i} \sinh(\beta_i L/2) & & \end{pmatrix} \quad (\text{C.22})$$

where

$$\gamma_i = \frac{EI\beta_i^3}{m_{\text{tip}}\omega_i^2} \quad (\text{C.23})$$

Now for a non-trivial solution  $\det \underline{\underline{D}} = 0$ . This gives the resonance conditions

$$\begin{aligned} & \cosh(\beta_i L/2) \sin(\beta_i L/2) + \cos(\beta_i L/2) \sinh(\beta_i L/2) \\ & + \frac{1}{2\gamma_i} (-1 + \cos(\beta_i L/2) \cosh(\beta_i L/2)) = 0. \end{aligned} \quad (\text{C.24})$$

To calculate the frequencies we must first combine Equation C.23 with Equation C.6 to remove the  $\omega_i$  dependence in the definition of  $\gamma_i$ :

$$\gamma_i = \frac{m_b}{m_{\text{tip}}\beta_i L} = \frac{1}{m^*\beta_i L}, \quad (\text{C.25})$$

where  $m_b$  is the mass of the beam, and  $m^*$  is the ratio of the tip mass to the beam mass. Using this form of  $\gamma_i$  in Equation C.24 allows the the dimensionless quantity  $\beta_i L$  to be solved for any  $m^*$  by a simple numerical method such as Newton-Raphson. Dimensions can be subsequently added to calculate  $\omega_i$ .

As equations (C.1), (C.2) and (C.3) are still valid the ratio between the constants remains as

$$\frac{b_1}{b_2} = \frac{\cos(\beta_i L/2) - \cosh(\beta_i L/2)}{\sin(\beta_i L/2) + \sinh(\beta_i L/2)} \quad (\text{C.26})$$

#### C.1.4 Even modes - including tip

For the even modes the first three boundary conditions are also unaffected by the tip, the fourth changes to

$$EI \frac{d^2\Phi_i(L/2)}{dx^2} = \frac{\mathcal{I}_{\text{tip}}}{2} \omega_i^2 \frac{d\Phi_i(L/2)}{dx}, \quad (\text{C.27})$$

where  $\mathcal{I}_{\text{tip}}$  is the moment of inertia of the tip.

Full derivations of dynamic properties for a symmetrical sensor

Writing the new four conditions as a matrix

$$\underline{\underline{D}} = \begin{pmatrix} 1 & 0 & & \\ 0 & 1 & & \dots \\ \cos(\beta_i L/2) & \sin(\beta_i L/2) & & \\ -\cos(\beta_i L/2) + \frac{\epsilon_i}{2} \sin(\beta_i L/2) & -\sin(\beta_i L/2) - \frac{\epsilon_i}{2} \cos(\beta_i L/2) & & \\ 1 & 0 & & \\ 0 & 1 & & \\ \dots & \cosh(\beta_i L/2) & \sinh(\beta_i L/2) & \\ \cosh(\beta_i L/2) - \frac{\epsilon_i}{2} \sinh(\beta_i L/2) & \sinh(\beta_i L/2) - \frac{\epsilon_i}{2} \cosh(\beta_i L/2) & & \end{pmatrix}, \quad (\text{C.28})$$

where

$$\epsilon_i = \frac{\mathcal{I}_{\text{tip}} \omega_i^2}{EI \beta_i} \quad (\text{C.29})$$

This gives a resonance condition of

$$\begin{aligned} & \cosh(\beta_i L/2) \sin(\beta_i L/2) - \cos(\beta_i L/2) \sinh(\beta_i L/2) \\ & + \frac{\epsilon_i}{2} (-1 + \cos(\beta_i L/2) \cosh(\beta_i L/2)) = 0. \end{aligned} \quad (\text{C.30})$$

To calculate the frequencies we must first combine Equation C.29 with Equation C.6 to remove the  $\omega_i$  dependence in the definition of  $\epsilon_i$ :

$$\epsilon_i = \frac{\mathcal{I}_{\text{tip}} (\beta_i L)^3}{L^2 m_b} = \mathcal{I}^* (\beta_i L)^3, \quad (\text{C.31})$$

where  $\mathcal{I}^*$  is the ratio of the moment of inertia of the tip to the beam mass multiplied by the beams length squared. This ratio while physically meaningless, as  $m_b L^2$  is not the moment of inertia of the beam for any relevant rotational axis, provides a dimensionless constant to solve Equation C.30. Again  $\beta_i L$  can be solved for any  $\mathcal{I}^*$  by the Newton-Raphson method and dimensions can be added to calculate  $\omega_i$ .

Again as equations (C.12), (C.13) and (C.14) are still valid the ratio between the constants remains as

$$\frac{b_1}{b_2} = \frac{\sinh(\beta_i L/2) - \sin(\beta_i L/2)}{\cos(\beta_i L/2) - \cosh(\beta_i L/2)} \quad (\text{C.32})$$

## C.2 Static Spring Constants

Static spring constants are not normally (by definition) linked to the modes. However they are linked to the symmetry and boundary conditions. Thus, the even and odd modes relate to two separate static spring constants. One for the end of the tip being pushed normal to the beam ( $k_{\text{norm}}$ ), and the other for the tip being pushed parallel to the beam ( $k_{\text{lat}}$ ).

Full derivations of dynamic properties for a symmetrical sensor

### C.2.1 Calculating $k_{\text{norm}}$

In the normal case our boundary conditions are now

$$\Phi_i(0) = 0 \quad (\text{C.33})$$

$$\frac{d\Phi_i(0)}{dx} = 0 \quad (\text{C.34})$$

$$\frac{d\Phi_i(L/2)}{dx} = 0 \quad (\text{C.35})$$

$$EI \frac{d^3\Phi_i(L/2)}{dx^3} = \frac{F_{\text{norm}}}{2} \quad (\text{C.36})$$

where  $F_{\text{norm}}$  is the force on the tip normal to the beam. The factor of two is because we are only considering the force felt by half of the beam.

The general static spatial solution is

$$\Phi_i = A + Bx + Cx^2 + Dx^3 \quad (\text{C.37})$$

from equations (C.33) and (C.34) we get

$$A = 0 \quad \text{and} \quad B = 0. \quad (\text{C.38})$$

With equation (C.35) we get

$$C = -\frac{3DL}{4} \quad (\text{C.39})$$

and finally using equation (C.36) we can show

$$D = \frac{F_{\text{norm}}}{12EI} \quad (\text{C.40})$$

combining this with equation (C.39)

$$C = \frac{-F_{\text{norm}}L}{16EI} \quad (\text{C.41})$$

Therefore giving the solution of  $x$  for these boundary conditions as

$$z = \frac{F_{\text{norm}}}{4EI} \left( \frac{1}{3}x^3 - \frac{1}{4}Lx^2 \right). \quad (\text{C.42})$$

Considering the deflection at  $x = L/2$

$$F_{\text{norm}} = \frac{-192EI}{L^3} A_{\text{norm}} \quad (\text{C.43})$$

Full derivations of dynamic properties for a symmetrical sensor

Therefore using Hooke's law the static spring constant of the normal mode of a double-ended tuning fork sensor is

$$k_{\text{norm}} = \frac{192EI}{L^3}. \quad (\text{C.44})$$

### C.2.2 Calculating $k_{\text{lat}}$

In the lateral case our boundary conditions are now

$$\Phi_i(0) = 0 \quad (\text{C.45})$$

$$\frac{d\Phi_i(0)}{dx} = 0 \quad (\text{C.46})$$

$$\Phi_i(L/2) = 0 \quad (\text{C.47})$$

$$EI \frac{d^2\Phi_i(L/2)}{dx^2} = -\frac{F_{\text{lat}}H}{2} \quad (\text{C.48})$$

where  $F_{\text{lat}}$  is the force on the tip parallel to the beam, and  $H$  is the tip length. The factor of two is because we are only considering the force felt by half of the beam.

The general static spatial solution is still

$$\Phi_i = A + Bx + Cx^2 + Dx^3 \quad (\text{C.49})$$

from equations (C.45) and (C.46) we get

$$A = 0 \quad \text{and} \quad B = 0 \quad (\text{C.50})$$

as before. With equation (C.47) we get

$$C = -DL \quad (\text{C.51})$$

and finally using equation (C.48) we can show

$$D = \frac{-F_{\text{lat}}H}{4EIL} \quad (\text{C.52})$$

combining this with equation (C.51)

$$C = \frac{F_{\text{lat}}H}{8EI} \quad (\text{C.53})$$

Therefore giving the solution of  $x$  for these boundary conditions as

$$z = \frac{F_{\text{lat}}H}{4EI} \left( \frac{1}{2}x^2 - \frac{1}{L}x^3 \right). \quad (\text{C.54})$$

Full derivations of dynamic properties for a symmetrical sensor

Considering the deflection a  $x = L/2$ ,  $z = 0$ , as expected. Considering the first derivative of the deflection

$$\frac{dz}{dx} = \frac{F_{\text{lat}}H}{4EI} \left( x - \frac{3}{L}x^2 \right). \quad (\text{C.55})$$

at  $x = L/2$

$$\frac{dz(L/2)}{dx} = \frac{F_{\text{lat}}HL}{16EI}. \quad (\text{C.56})$$

However as  $A_{\text{lat}} = -H \frac{dz(L/2)}{dx}$

$$F_{\text{lat}} = -\frac{16EI}{H^2L} A_{\text{lat}} \quad (\text{C.57})$$

Therefore using Hooke's law the static spring constant of the lateral mode of a double-ended tuning fork sensor is

$$k_{\text{lat}} = \frac{16EI}{H^2L}. \quad (\text{C.58})$$

# Appendix D

## Computer Science Techniques

*“The question of whether computers can think is like the question of whether submarines can swim.”*

Edsger W. Dijkstra

### Appendix Overview

The work on automated tip conditioning in Chapter 7 has large overlaps with computer science. As this is a physics PhD thesis details of these methods are not presented in the main text. Detailed explanations of techniques, however, are relevant to the thesis and have thus been included in this appendix.

## D.1 Robust Mutual Information (RMI)

### D.1.1 Mutual Information (MI)

The mutual information (MI) between two data sets is a measure of how much the images depend on a mutual source of information. This can be calculated between two STM scans (henceforth image A and image B) by reshaping the image arrays into a 1D arrays of pixel values. The images are reduced in quality to  $N$  colour levels ( $N = 32$  was used for all analysis in this project), the probability of a pixel in image A having a particular colour value is calculated for each value,  $n$ , to give  $p_A(n)$ :

$$p_A(n) = \frac{\# \text{ of pixels } \in \text{ A, with value } n}{\# \text{ of pixels } \in \text{ A}}. \quad (\text{D.1})$$

$p_B(m)$  can be calculated in a similar way for all colour values  $m$  in image B. Also  $p_{AB}(n, m)$  is calculated which corresponds to the joint probability of a pixel in image A having value  $n$  and the corresponding pixel in image B having value  $m$ . Thus, it is clear that if image A and image B are completely independent then  $p_{AB}(n, m) = p_A(n)p_B(m)$ , if they do share some dependence then  $p_{AB}(n, m) >$

$p_A(n)p_B(m)$ . This means that the logarithm of  $\frac{p_{AB}(n,m)}{p_A(n)p_B(m)}$  is a useful quantity for measuring dependence as it goes to zero for no dependence. The full formula for the MI is [169]

$$MI(A, B) = \sum_n \sum_m p_{AB}(n, m) \log \left( \frac{p_{AB}(n, m)}{p_A(n)p_B(m)} \right) \quad (\text{D.2})$$

The extra factor of  $p_{AB}(n, m)$  is to scale by the regularity pixels with these dependence values.

### D.1.2 Calculating RMI from MI

The robust mutual information (RMI) is a more robust measure of MI. Occasionally images with no mutual dependence will get MI values above zero due to artefacts in the calculation. By calculating the MI of a randomly reordered second image image  $B'$ , this gives an idea of the portion of the MI resulting from these artefacts. This MI is calculated for a number,  $R$ , of random rearrangements and averaged. The RMI can then be calculated as

$$RMI(A, B) = MI(A, B) - \sum_{r=1}^R \frac{MI(A, B^r)}{R} \quad (\text{D.3})$$

## D.2 Cellular Genetic Algorithms

The nature of a cGA is to inherit parameters from fitter neighbours rather than from across the entire population, this is shown in Figure D.1. This slows the convergence of parameters across the population, allowing the algorithm to explore more of the parameter space, thus giving it a greater chance to find the global maximum fitness rather than concentrating around one of many local maxima.

A generation can consist of any number,  $n$ , of individuals,  $I_n$ , each having a particular set of parameters (genotype). In this particular example we have 25 individuals in one generation, represented by a 5 by 5 matrix. Each individual genotype is described by four imaging parameters  $I_n(i, V, G_I, G_P)$  where  $i$ ,  $V$ ,  $G_I$ , and  $G_P$  are the tunnel current setpoint, the sample bias voltage, integral gain, and proportional gain respectively.

One image per individual is collected and given a fitness score describing the image quality. During the selection and reproduction phase of the genetic algorithm each individual is compared to its neighbours. If the individual is fitter than its neighbours its genotype remains unchanged, however, if any of its neighbours have a higher fitness score it inherits the genotype of its fittest neighbour, plus a random mutation to allow it to explore a new area of the local parameter space.

Good images can evolve quite quickly, and it is interesting to note that the

## Computer Science Techniques

final generation shown here has ‘pockets’ of particular image, or phenotype. Once the desired level of image quality and type is achieved the cGA ends.

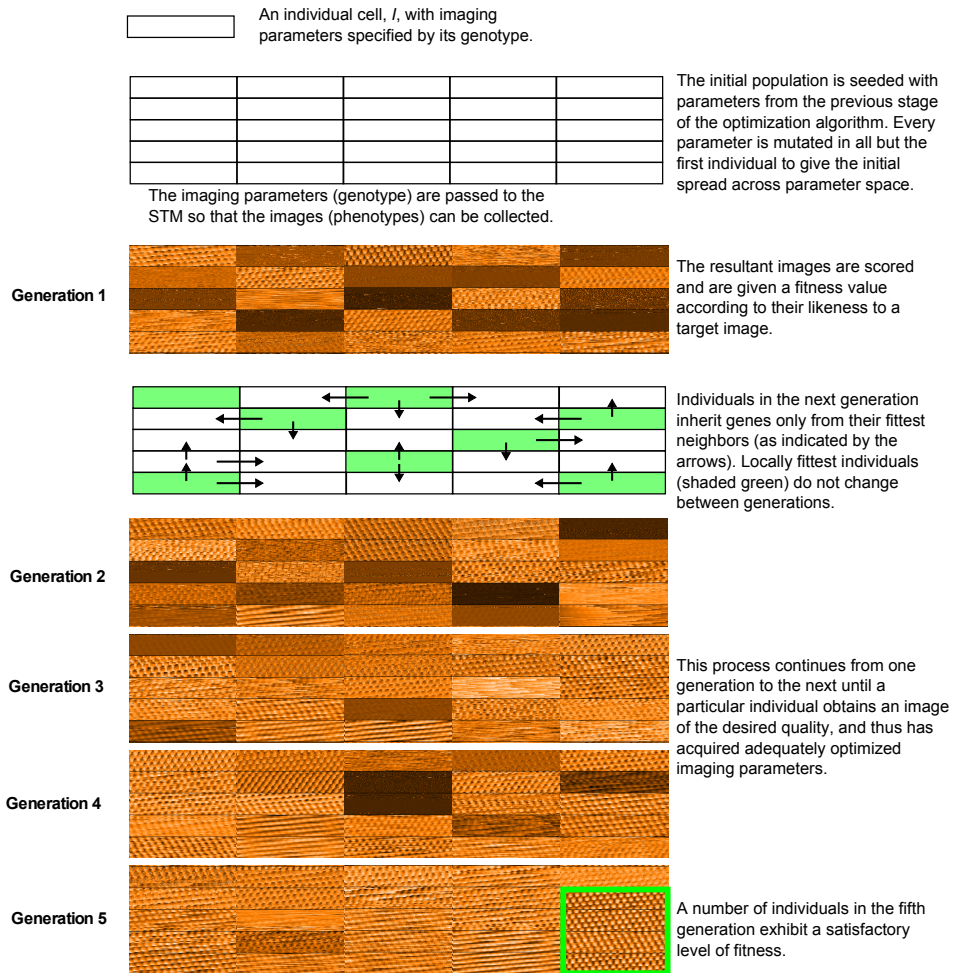


Figure D.1: Typical evolution of a cGA run showing the progression towards a good quality image as defined by a target. The initial population's parameters are seeded from a set of parameters that lie within the physical boundaries of the system. After 5 generations the desired image quality is obtained and thus so are the 'ideal' imaging parameters.

# List of Figures

2.1	Schematic diagram of an STM scan. . . . .	5
2.2	1D representations of the tip-sample tunnel junction. . . . .	6
2.3	Comparing calculated transmittance of a 1D potential barrier to exponentially decreasing approximation. . . . .	9
2.4	Response of a free cantilever and a cantilever experiencing an attractive potential to being externally driven. . . . .	16
2.5	The frequency response of vibrational isolation due to mechanical vibration. . . . .	25
2.6	Diagram of a piezoelectric tube scanner. . . . .	27
2.7	Design of an inertial slider. . . . .	28
2.8	Path taken by P and PI controllers, feeding back to a setpoint while experiencing a constant drift. . . . .	31
2.9	Schematic of STM electronics. . . . .	32
2.10	Schematic of self-excitation method of FM-AFM feedback with constant amplitude and frequency shift. . . . .	34
2.11	Schematic of a simple PLL circuit. . . . .	36
2.12	Schematic of a PLL driven FM-AFM circuit. . . . .	37
3.1	First published STM image of the Si(111) $2 \times 1$ reconstruction. . .	43
3.2	First published STM imaged of the Si(111) $7 \times 7$ reconstruction. .	44
3.3	Schematic of the DAS model of the Si(111) $7 \times 7$ reconstruction. .	45
3.4	Subatomic features in AFM image of Si(111) $7 \times 7$ reconstruction.	46
3.5	Rendering of $C_{60}$ . . . . .	47
3.6	Grid spectroscopy measurements of $C_{60}$ with a Cu tip. . . . .	48
3.7	Faces of a $C_{60}$ molecule imaged on Si adatoms. . . . .	49
3.8	A range of AFM sensors . . . . .	54
4.1	Theoretical model of the qPlus sensor and a geometrical diagram of tip motion as cantilever deforms. . . . .	65
4.2	The ratio of dynamic spring constants to the cantilever static spring constant. . . . .	66
4.3	Effect of tip geometry on tip movement for an arbitrary oscillation amplitude. . . . .	68
4.4	Effect of tip motion on imaging . . . . .	73

## List of Figures

4.5	Effect of lateral tip motion on force spectroscopy measurements . . . . .	74
5.1	Measuring qPlus sensor geometry. . . . .	79
5.2	Tip convolution imaging showing C <sub>60</sub> tip. . . . .	83
5.3	Graphical explanation of spectra processing. . . . .	85
5.4	Measured and simulated C <sub>60</sub> -C <sub>60</sub> potential in the $x$ - $y$ and $y$ - $z$ planes. . . . .	87
5.5	Measured and simulated C <sub>60</sub> -C <sub>60</sub> potential in the $x$ - $y$ plane. . . . .	89
5.6	Individual spectra measurements of C <sub>60</sub> -C <sub>60</sub> interaction potential. . . . .	90
5.7	A second measurement of C <sub>60</sub> -C <sub>60</sub> interaction potential for a different surface molecule and tip termination. . . . .	91
5.8	dSTM and ncAFM images of C <sub>60</sub> molecules used for grid spectroscopy experiments. . . . .	92
5.9	Identifying a non-C <sub>60</sub> terminated tip . . . . .	94
6.1	Proposed geometry of new sensor. . . . .	101
6.2	The effective spring constants and eigenfrequencies of the first two eigenmodes of a symmetrical sensor. . . . .	105
7.1	A series of poor quality STM images which would never normally make it into a publication. . . . .	110
7.2	RMI scores for a selection of STM scans. . . . .	114
7.3	Finding flat regions of large scans. . . . .	116
7.4	Computer vision interpretation of a scan of Si(111) 7 × 7 reconstruction. . . . .	117
7.5	A sequence of scans on HOPG showing coarse optimisation. . . . .	120
7.6	A sequence of images from automated STM tip conditioning on the Si(111) 7 × 7 surface. . . . .	121
7.7	Evolutionary optimisation on HOPGE using a cGA . . . . .	123
8.1	The distorting effects of line-by-line flattening on SPM images . . . . .	127
8.2	Iterative masking and flattening of an SPM image. . . . .	129
8.3	Automated step edge detecting and image flattening. . . . .	131
8.4	Automated masking of atoms on the Si(111) 7×7 reconstruction. . . . .	132
8.5	Automated step edge detection on images with atomic resolution. . . . .	135
8.6	Automated masking of a molecular reconstruction. . . . .	137

## List of Figures

9.1	Direct comparison of our model (Equation 9.3, red and green lines) with the model from the current literature (Equation 9.2, blue and pink lines), without modelling of electrical or mechanical components. The comparison is performed for a full PI controller (a) and a simple proportional controller (b), where the grey area represents the surface being tracked with a set-point of 0. Equation 2, shows unexpected discontinuities and does not track the set-point for a proportional controller, instead only reacting to the initial impulse. Equation 9.3 produces the expected results from elementary control theory. All gain units are arbitrary. . . . .	141
9.2	Schematic of an STM feedback loop . . . . .	143
9.3	The feedback response of an SPM, without the inclusion of mechanical resonances. . . . .	146
9.4	The feedback response of an SPM, including mechanical resonance. (a) Shows the evolution of the feedback output for varying eigenfrequency of the mechanical resonance. The stability improves for increasing resonant frequency. For all plots the bandwidth of the HV amplifier is infinite and the Q of the resonance does not vary. (b) Shows similar evolution in feedback output for varying Q of the resonance at a constant eigenfunction, with lower Q values stabilising the output. The cyan line shows the same resonance properties as the pink line, however by limiting the bandwidth of the HV amplifier to near that of the resonance, the stability is improved significantly. Both insets are zooms of the most important region of their respective plots. . . . .	149
9.5	Numerically simulated SPM feedback results. . . . .	154
A.1	A simple cantilever. With shear force $V$ , bending moment $M$ and force per unit area $f$ . . . . .	176
A.2	The first 5 roots of $1 + \cos(\beta L) \cosh(\beta L) = 0$ . . . . .	182
A.3	From top to bottom, the first 5 eigenfrequencies of a freely oscillating cantilever. . . . .	188
B.1	Convergence of model to equipartition theorem. . . . .	200
D.1	Typical evolution of a cGA run showing the progression towards a good quality image as defined by a target. . . . .	212